

**EFFECT OF EQUAL CHANNEL ANGULAR EXTRUSION ON  
MICROSTRUCTURE MECHANICAL PROPERTIES AND CORROSION  
BEHAVIOR OF WROUGHT AZ-MAGNESIUM ALLOYS**

Thesis

Submitted in partial fulfillment of the requirements for the degree of

DOCTOR OF PHILOSOPHY

By

**GAJANAN M NAIK**

**(ME16P05)**



DEPARTMENT OF MECHANICAL ENGINEERING

NATIONAL INSTITUTE OF TECHNOLOGY KARNATAKA, SURATHKAL,

MANGALORE -575025

JUNE - 2020

**EFFECT OF EQUAL CHANNEL ANGULAR EXTRUSION ON  
MICROSTRUCTURE MECHANICAL PROPERTIES AND CORROSION  
BEHAVIOR OF WROUGHT AZ-MAGNESIUM ALLOYS**

Thesis

Submitted in partial fulfillment of the requirements for the degree of

DOCTOR OF PHILOSOPHY

by

**GAJANAN M NAIK**

**(ME16P05)**

Under the guidance of

**Dr. NARENDRANATH S**

Professor

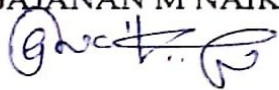


DEPARTMENT OF MECHANICAL ENGINEERING  
NATIONAL INSTITUTE OF TECHNOLOGY KARNATAKA, SURATHKAL,  
MANGALORE - 575025

JUNE – 2020

## DECLARATION

I hereby declare that the Research Thesis entitled **EFFECT OF EQUAL CHANNEL ANGULAR EXTRUSION ON MICROSTRUCTURE MECHANICAL PROPERTIES AND CORROSION BEHAVIOR OF WROUGHT AZ-MAGNESIUM ALLOYS** Which is being submitted to the **National Institute of Technology Karnataka, Surathkal** in partial fulfilment of the requirements for the award of the Degree of **Doctor of Philosophy** in Mechanical Engineering is a bonafide report of the research work carried out by me. The material contained in this Research Thesis has not been submitted to any University or Institution for the award of any degree.

Register Number : 168004-ME16P05  
Name of the Research Scholar : GAJANAN M NAIK  
Signature of the Research Scholar: 

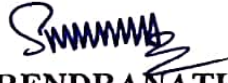
Department of Mechanical Engineering

Place: NITK-Surathkal  
Date: 16-06-2020

CERTIFICATE

This is to certify that the Research Thesis entitled **EFFECT OF EQUAL CHANNEL ANGULAR EXTRUSION ON MICROSTRUCTURE MECHANICAL PROPERTIES AND CORROSION BEHAVIOR OF WROUGHT AZ-MAGNESIUM ALLOYS** submitted by **Mr. GAJANAN M NAIK** (Reg. No: 168004-ME16P05) as the record of the research work carried out by him, is accepted as the Research Thesis submission in partial fulfilment of the requirements for the award of degree of **Doctor of Philosophy**.

Research Guide



**Dr. NARENDRANATH S**

Professor

Dept. of Mechanical Engineering



Chairman - DRPC



## ABSTRACT

Wrought magnesium alloys are lightest engineering material and it has quite special properties which lead to particular applications. In specific, their highest strength to weight ratio, good machinability and high damping capability makes magnesium alloys tremendously attractive in aerospace, electronics, marine and automobile industries. Indeed, Magnesium alloys have poor tensile strength, ductility and corrosion resistance properties associated with other engineering materials like aluminium alloys, steels and super alloys etc. Therefore, many researchers worked on equal channel angular pressing of magnesium alloys to improve the mechanical properties and corrosion resistance. In this work, the effect of channel angles on material properties were investigated during equal channel angular pressing of AZ80/91 magnesium alloy using processing route-R at 523K, 598K and 663K processing temperature. Channel angles of 90° and 110°, common corner angle of 30° have been considered for the study. It has been revealed that the channel angle has a significant influence on deformation homogeneity, microhardness, ultimate tensile strength, ductility and corrosion behaviour of AZ80/91 magnesium alloys. Specifically, AZ80/91 Mg alloys processed through 90° channel angle i.e die A is considered as optimal die parameter to improve above-said material properties. Investigation showing with reference to as-received AZ80 and AZ91 Mg alloy indicates 11 %, 14 % improvement of UTS and 69 %, 59 % enhancement in ductility after processing through 4P through die A (90°) at 598K respectively. Also, the corrosion rate reduces to 97 % and 99 % after processing the sample with 4P-ECAP die A (90°) at the same processing temperature for AZ80 and AZ91 Mg alloys respectively. This is mainly due to grain refinement and distribution of Mg<sub>17</sub>Al<sub>12</sub> secondary phase during ECAP. Further, this work investigates the effect of annealing and aging treatment on microstructure and corrosion behaviour of as-received and ECAPed AZ80/91 Magnesium alloys. Here, annealing at 523K, 623K, and 723K were accomplished, meanwhile samples were cooled in the furnace after 6 h and 12 h of diffusion annealing treatment. In this study, samples were characterized by using optical microscopy (OM) and scanning electron microscopy (SEM) and electrochemical corrosion behavior of annealed AZ80/91 Mg alloy has been

investigated. With this, an attempt has been made to enhance the corrosion resistance of the AZ80/91 Mg alloy by changing its microstructure and re-distribution of secondary phase during annealing and aging treatment. It was found that corrosion rates are minimum at higher annealing temperature and aging time because of uniform distribution of secondary  $\beta$ -phases in Mg matrix, evidently shown in the microstructure of the heat-treated AZ80/91 Mg alloy. As a result, the annealing treatment at 723K for 12 h aging is desirable to enhance the corrosion resistance. Further enhancement of as-received and ECAPed AZ80/91 Mg alloys were observed after High Velocity Oxy-Fuel (HVOF) coating of 316 stainless steel powder. Our results revealed that 316 stainless steel coating on ECAP-4P AZ80/91 Mg alloys were uniform and compact on substrate with a thickness of  $80\pm 5$   $\mu\text{m}$ . Furthermore, HVOF-coating process of 4P-ECAP significantly reduce corrosion rate at 3.5wt.% NaCl solution making it promising for industrial applications. The corrosion behaviour and effect of the ECAPed fine-grained magnesium alloy and coarse-grained as-received AZ80/91 Mg alloy was investigated in a 2.5wt.% NaCl, 3.5wt.% NaCl solution and Natural Sea Water (NSW) in order to explore the corrosion performance of ECAPed magnesium alloys in various environments. From, electrochemical corrosion experiments and surface morphology observations evidently shown that grain refinement exhibited improved corrosion resistance of the AZ80/91 alloy in all environments, also which shown a protective passive film on the surface to shield corrosion.

**Keywords:** *Equal Channel Angular Pressing, Magnesium Alloys, Microstructure, Grain Refinement, DRX, Mechanical Properties, Microhardness, Corrosion, Scanning Electron Microscope, X-ray Diffraction, Annealing, aging, High-velocity oxy-fuel coating, Natural Sea Water.*

## ACKNOWLEDGMENT

I express my deep sense of gratitude and indebtedness to my supervisor **Dr. Narendranath S**, Professor, Department of Mechanical engineering, National Institute of Technology Karnataka, Surathkal for providing precious guidance, inspiring discussions and constant supervision throughout the course of this work being carried out. His timely help, constructive criticism and conscientious efforts made it possible to present the work contained in this thesis.

I express my sincere thanks to **Dr. Prasad Krishna**, Professor and **Dr. K V Gangadharan**, Professor, Former HoD, Department of Mechanical engineering, National Institute of Technology Karnataka, Surathkal. I am grateful to **Dr. Shrikantha S Rao**, Professor and Head, Department of Mechanical engineering for providing me the necessary facilities in the department.

I gratefully acknowledge the support from the **Naval Research Board (NRB)**, Government of India, under the project reference number **NRB/4003/PG/366-2015**.

I do thank **Dr. Satheesh Kumar S S**, Scientist, Near Net Shape Group, Aeronautical Materials Division, Defence Metallurgical Research Lab, DRDO, Hyderabad for timely help and cooperation extended to me during completion of the research work.

I am grateful to the members of the Research Program Assessment Committee including **Dr. S. M. Murigendrappa**, Professor, Department of Mechanical Engineering, **Dr. Nagendrappa. H**, Assistant Professor, Department of Electrical and Electronics Engg., for their unbiased and critical evaluation during the progress of my research.

I express my sincere thanks to **Sri. Rajesh Chouta**, Chairman, **Dr. G.L Easwara Prasad**, Principal, **Dr. Diwakar Shetty**, Dean Academics, **Dr. Rajashekhar C R**, Vice Principal and HoD, Dept. of Mechanical Engineering. I am indebted to all **my colleagues** and **students** of Department of Mechanical Engineering, Mangalore Institute of Technology and Engineering, Moodbidri, Mangaluru for their timely help and cooperation extended to me during completion of Ph.D. work.

I express my sincere thanks to **Dr. Chandra Rao madane**, Academic Director and HoD, Mech., MITK-Kundapura.

I do thank **Dr. Sachin B**, Assistant Professor, Nitte Meenakshi Institute of Technology, Bangalore. **Dr. Charitha Rao**, Assistant Professor, Jain University, Bangalore. **Dr. Ravindra I Badiger**, Associate Professor, Dept. of Mech. Engg., YIT-Moodbidri, Mangalore.

I express my sincere thanks to my friends **Mr. Chethan K, Mr. Kumar Karthik, Mr. Girish L V, Mr. N.T.K Prasad, Mr. Vishwas C J, Mr. Manikanta swamy, Mr. Kiran Kumar B J, Mr. Shashidhara M, Mr. Ajay P D, Mr. Narayan Naik. Mr. Devendra Gowda etc.**

I do thank **Mr. Gopal D Gote**, Research Scholar, Dept. of Mech. Engg. IIT-Bombay, Mumbai., **Mr. Sandeep Sahu**, Research Scholar, Dept. of Materials Science and Engineering, IIT-Kanpur, Kanpur.

I am grateful to all my research colleagues of Department of Mechanical Engineering, **Mr. Mohanraj G T, Mr. Abhinaba Roy, Mr. Anjan B N, Mr. Ramesh S, Mr. Manjunath, Mr. Manoj I V, Mr. Prithiviraj Sekar, Mr. Kishan, Mr. Sreeniva K, Mr. Jaipal Reddy, Mr. Karthik, Mr. Madhukar, Mr. Mayur, Mr. Praveen J, Mr. Manjunath G K, Mr. Sudeep N S** and also the **Teaching and Non-teaching staff** members of the Department of Mechanical Engineering, NITK for their continuous help and support throughout the research work.

I express my sincere thanks to **Dr. M. Manjaiah**, Assistant Professor, NIT Warangal, **Dr. Muralidhar Avvari**, Assistant Professor, Bhair Dar University, Ethiopia, **Dr. Nithin**, Assistant Professor, Malnad College of Engineering, Hassan, **Dr. Gopi K R**, Assistant Professor, Malnad College of Engineering, **Dr. Priyaranjan Sharma**, Assistant Professor, JK Lakshmipat University, Rajasthan, **Dr. Hargovind Soni**, Post-Doctoral Fellow University of Johannesburg, **Dr. Gajanan anne**, Associate Professor, Shri Madhwa Vadiraja Institute of Technology, Udupi. **Dr. Mahesh D**, Professor, SCEM-Mangalore, **Dr. Sachinkumar Patil**, Associate Professor, Reva University-Bangaluru.

I do thank **Dr. Sathisha**, Professor and Head, Dept. of Mech. Engg., YIT-Moodbidri, Mangalore, **Mr. Sadashiva Bellubbi**, Assistant Professor, AEIT-Moodbidri, **Mr. Nandeesh M**, SSIT-Tumkur for their timely help and cooperation extended to me during composition of the thesis.

I express my sincere thanks to **Mr. Jaya Devadiga, Mr. C A Verghese, Mr. Pradeep, Mr. Aravind, Mrs Rashmi, Mr. Shailesh and Mr. Shashi**, Staff, NITK-Surathkal.



I am extremely grateful to my parents **Sri. Manjunath R Naik** and **Smt. Lalita M Naik** who have been a motivating force throughout my life. It is a pleasure to thank my brother **Mr. Sachin M Naik** and sister **Ms. Shwetha M Naik** for their support rendered during the study.

Finally, I wish to thank all those who have helped me directly or indirectly during various phases of this research work. I THANK YOU ALL.....!

**GAJANAN M NAIK**

# CONTENTS

<i>Declaration</i>	
<i>Certificate</i>	
<i>Acknowledgements</i>	
<i>Abstract</i>	
<i>Contents</i>	<i>i</i>
<i>List of Figures</i>	<i>vi</i>
<i>List of Tables</i>	<i>xv</i>
<i>List of Symbols and Abbreviations</i>	<i>xvi</i>
<b>CHAPTER-1 INTRODUCTION</b>	<b>1</b>
1.1 BACKGROUND	1
1.2 MAGNESIUM ALLOYS AND ITS APPLICATIONS	1
1.3 STRENGTHENING MECHANISMS	5
1.3.1 Introduction to sever plastic deformation	5
1.3.1.1 Equal Channel Angular Extrusion process	6
1.3.1.2 Factors affecting grain refinement in ECAP	9
1.4 INTRODUCTION TO CORROSION	9
1.4.1 Corrosion of magnesium alloys	10
1.4.2 Corrosion Thermodynamics	11
1.4.3 Corrosion Kinetics	12
1.5 INTRODUCTION TO ANNEALING AND AGING TREATMENT	13
1.6 COATING OF MAGNESIUM ALLOYS	13
1.6.1 Working principle of high velocity oxy fuel coating	14
1.7 THESIS ORGANIZATION	15
<b>CHAPTER-2 LITERATURE REVIEW</b>	<b>17</b>
2.1 INTRODUCTION	17
2.2 WROUGHT MAGNESIUM ALLOYS	17
2.3 STRENGTHENING MECHANISMS	19

2.3.1 Solid solution strengthening and alloying	19
2.3.2 Precipitation Strengthening	20
2.3.3 Grain boundary strengthening	20
2.4 OVERVIEW OF SEVERE PLASTIC DEFORMATION	21
2.4.1 Effect of microstructure on mechanical properties	21
2.4.2 Impact of microstructure on corrosion behaviour	22
2.5 EQUAL CHANNEL ANGULAR PRESSING OF MAGNESIUM ALLOYS	22
2.5.1 Result of die parameters in equal channel angular extrusion	22
2.5.2 Influence of processing temperature and routes on grain size during ECAP	24
2.5.3 Impact of grain size on mechanical properties	25
2.5.4 Observation from fracture study	27
2.5.5 Observation from XRD analysis	29
2.6 CORROSION BEHAVIOR OF MAGNESIUM ALLOYS	30
2.6.1 Effect of alloying elements on the corrosion behaviour of magnesium alloy	30
2.6.2 Effect of environment on corrosion behaviour of Mg alloys	35
2.7 CORROSION BEHAVIOUR OF ECAPED MAGNESIUM ALLOYS	36
2.7.1 Effect of grain refinement on corrosion behavior	36
2.7.2 Influence of annealing and aging treatment on corrosion behaviour	41
2.7.3 Corrosion morphology studies of ECAPed Mg alloys	42
2.8 PREVENTION OF ECAPed MAGNESIUM ALLOYS	42
2.8.1 Effect of coating on corrosion behaviour of ECAPed Mg alloys	42
2.9 CONCLUDING REMARKS	54
2.10 RESEARCH GAP FROM LITERATURE SURVEY	54
2.11 PROBLEM STATEMENT	54
2.12 OBJECTIVES OF THE RESEARCH WORK	55

<b>CHAPTER-3 EXPERIMENTAL WORK</b>	<b>57</b>
3.1 INTRODUCTION	57
3.2 WROUGHT AZ SERIES MAGNESIUM ALLOYS	57
3.3 EQUAL CHANNEL ANGULAR EXTRUSION	59
3.4 SELECTION OF PROCESSING TEMPERATURE	61
3.5 MICROSTRUCTURAL CHARACTERIZATION	63
3.5.1 Optical Microscope	63
3.5.2 Scanning Electron Microscopy	64
3.5.3 X-Ray Diffraction	64
3.6 MECHANICAL TESTING	65
3.6.1 Microhardness Test	65
3.6.2 Tensile Test	66
3.7 ELECTROCHEMICAL CORROSION TEST	67
3.8 ANNEALING AND AGING TREATMENT	69
3.9 HIGH VELOCITY OXY FUEL COATING	69
3.10 SUMMARY	72
<b>CHAPTER -4 EFFECT OF ECAE ON MICROSTRUCTURE</b>	<b>73</b>
<b>MECHANICAL PROPERTIES AND CORROSION</b>	
<b>BEHAVIOR OF AZ80/91 MAGNESIUM ALLOYS</b>	
4.1 INTRODUCTION	73
4.2 EFFECT OF ECAP DIE CHANNEL ANGLE ON AZ80/91 MAGNESIUM ALLOY	73
4.2.1 Microstructure Evolution of AZ80 Mg alloy	73
4.2.2 Microstructure Evolution of AZ91 Mg alloy	75
4.2.3 Variation of grain size with two different die after 2 and 4 ECAP passes for AZ Mg alloys	77
4.3 EFFECT OF ECAP AT DIFFERENT PROCESSING TEMPERATURE	79
4.3.1 Microstructure analysis on AZ80 Mg alloys	79

4.3.2	Microstructure analysis on AZ91 Mg alloys	83
4.3.3	Effect of ECAP processing temperature on grain size	88
4.4	X-RAY DIFFRACTION ANALYSIS	90
4.5	MECHANICAL BEHAVIOUR	91
4.5.1	Effect of die parameters and processing temperature on microhardness	92
4.5.2	Variation of tensile strength with two different die and processing temperature	94
4.6	FRACTOGRAPHY	97
4.6	CORROSION STUDY	100
4.7.1	Effect of ECAP die and processing temperature on corrosion rate	100
4.7.2	Effect of grain size and distribution of secondary phases on corrosion behavior	103
4.7	CORROSION MORPHOLOGY	105
4.8	SUMMARY	111
<b>CHAPTER-5 CORROSION BEHAVIOR OF ECAPED AZ80/91 MAGNESIUM ALLOYS AFTER ANNEALING TREATMENT, COATING AND IN DIFFERENT ENVIRONMENT</b>		<b>113</b>
5.1	INTRODUCTION	113
5.2	ANNEALING AND AGING TREATMENT ON MICROSTRUCTURE OF AS-RECEIVED AND ECAPED AZ80/91 MAGNESIUM ALLOYS	113
5.2.1	Microstructure evolution of as-received AZ80 Mg alloys	114
5.2.2	Microstructure evolution of ECAPed AZ80 Mg alloys	116
5.2.3	Microstructure evolution of as-received AZ91 Mg alloy after annealing and aging treatment	121
5.2.4	Microstructure evolution of ECAPed AZ91 Mg alloys	123
5.3	IMPACT OF ANNEALING AND AGING TREATMENT ON CORROSION RESISTANCE OF AS-RECEIVED AND ECAPED AZ80/91 MAGNESIUM ALLOYS	126

5.3.1 Corrosion behavior of as-received AZ80/91 Mg alloy after annealing Treatment	126
5.3.2 Corrosion morphologies as-received AZ80/91 Mg alloys	129
5.3.3 Influence of annealing and aging treatment on corrosion resistance of ECAPed AZ80/91 Mg alloys	132
5.3.4 Corrosion morphologies of ECAPed AZ80/91 Mg alloys	137
5.4 COATING OF AZ80/91 MAGNESIUM ALLOY	141
5.4.1 High-Velocity Oxygen Fuel coating on as-received and ECAPed AZ80/91 Mg Alloy	141
5.4.2 Surface morphology studies on coated AZ80/91 Mg alloys	141
5.4.3 Microhardness evolution	143
5.4.4 Corrosion behavior of AZ80/91 Mg alloys after HVOF coating	145
5.5 CORROSION BEHAVIOUR OF ECAPED AZ80/91 Mg ALLOYS IN DIFFERENT ENVIRONMENTS	149
5.5.1 Corrosion behavior of ECAPed AZ80/91 Mg alloys	149
5.5.2 Corrosion Morphology	152
5.6 SUMMARY	154
<b>CHAPTER-6 CONCLUSIONS AND SCOPE FOR FUTURE WORK</b>	<b>157</b>
6.1 CONCLUSION	155
6.2 CHALLENGES IN ECA EXTRUSION OF MAGNESIUM ALLOYS	159
6.3 SCOPE FOR FUTURE WORK	160
<b>REFERENCES</b>	<b>161</b>
<b>LIST OF RESEARCH PAPERS PUBLISHED</b>	
<b>BIO-DATA</b>	

## LIST OF FIGURES

<b>Figure No.</b>	<b>Description</b>	<b>Page No.</b>
Figure 1.1	Applications of magnesium alloys in a) Automobile (Dziubińska et al., 2016) b) Aircraft (Dziubińska et al., 2016) c) Biomedical: implants for orthopaedic application (Waizy et al., 2001) d) Marine field (Adapted from <a href="http://electricalfundablog.com">http://electricalfundablog.com</a> )	4
Figure 1.2	Schematic of equal channel angular extrusion. (Agwa et al. 2016)	7
Figure 1.3	Different processing routes of ECAE (Avvari et al. 2015)	8
Figure 1.4	Atmospheric corrosion of magnesium (Yun et al., 2009)	10
Figure 1.5	Polarization curve (Sukiman et al. 2012)	12
Figure 1.6	High-Velocity Oxy-Fuel (HVOF) process (Ann Gan et al., 2017)	14
Figure 2.1	a) Yield tensile strength vs % elongation (b) YTS vs degradation rate of the as- cast and wrought and SPD processed Mg alloys. (Zheng et al., 2014)	18
Figure 2.2	Various equivalent strain values for different channel angle and an outer arc of curvature (Furuno et al., 2004)	23
Figure 2.3	Stress-strain curves for as-cast, homogenized, and ECAP-processed samples (Gopi et al., 2016)	26
Figure 2.4	SEM-fractured images of tensile specimens of AZ61 alloy: (a) as received and (b) after four ECAP passes at 523 K (Muralidhar et al., 2016)	27
Figure 2.5	SEM images of fracture surfaces (a) as-cast, (b) 2P, (c) 4P samples (Gopi et al., 2016)	28
Figure 2.6	X-ray diffraction peaks of AZ91 Mg alloys a) As-received b) ECAP-4P at 533K. (Naik et al., 2019)	29

Figure 2.7	SEM micrographs of alloys immersed in 3.5 wt.% NaCl solution for 2 h: (a) AZ31; (b) AZ80 and (c) AZ91D (Pardo et al., 2008)	31
Figure 2.8	Representation of the electrochemical impact of alloying elements in magnesium alloy. (Esmaily et al. 2017)	32
Figure 2.9	Corrosion rate of 99.97% Mg and four high pressure die casting Mg-Al alloys (RH: 95%, CO <sub>2</sub> : 400 ppm :NaCl: 70 µg/cm <sup>2</sup> , time: 504 h). (Esmaily et al. 2016)	33
Figure 2.10	Corrosion morphology of alloy AM50 of 4°C, 672 h, with 400 ppm CO <sub>2</sub> (a) No NaCl, (b) 14 µg/cm <sup>2</sup> NaCl (c) 70 µg/cm <sup>2</sup> NaCl (Esmaily et al. 2016).	34
Figure 2.11	SEM images of the corroded alloy specimen after immersion in 3.5% NaCl. (a) The top view after 2 h. b) The transverse section after 2 h. (Pawar et al., 2017)	35
Figure 2.12	Pure Mg/as-cast and ECAPed alloys after immersion in 3.5 wt.% NaCl solution. a) OCP curves b) Polarization curves c) Nyquist plots of impedance spectra immersed for 6 h. d) Fitted Rt value curves in different immersion periods. (Song, et al. 2010)	38
Figure 2.13	Nyquist plots of Mg–2Gd–1Y–1Zn–0.2Zr samples with various ECAP passes in 3.5 wt %NaCl solution (Jiang et al. 2014)	39
Figure 3.1	Chemical compositions for wrought AZ80 and AZ91 Mg alloys	57
Figure 3.2	AZ80 Mg alloy a) Microstructure b) EDS results	58
Figure 3.3	AZ91 Mg alloy a) Microstructure b) EDS results	58
Figure 3.4	ECAP die having 90 <sup>0</sup> and 110 <sup>0</sup> channel angle and 30 <sup>0</sup> corner angle. (Naik et al. Copyrights: Diary Number: 14668/2018-CO/L., Reg. No: L-79923/2018)	59
Figure 3.5	Equal Channel Angular Extrusion experimental setup	61



Figure 3.6	a) Route-R b) ECAPed sample	61
Figure 3.7	ECAPed samples processed through different temperature	62
Figure 3.8	Optical Microscopy with BIOVIS material plus software	63
Figure 3.9	Scanning Electronic Microscopy equipped with EDS	64
Figure 3.10	X-ray diffraction operated at 20 mA and 30 kV with Cu- $\alpha$ radiation	65
Figure 3.11	Vickers Microhardness Setup	66
Figure 3.12	Tensile test specimen as per ASTM-E8	67
Figure 3.13	Shimadzu Tensile Tester	67
Figure 3.14	Electrochemical Corrosion Analyzer setup (Gill AC: Model No: 1845)	68
Figure 3.15	316 stainless steel powder a) SEM micrograph b) EDS result	70
Figure 3.16	Flow chart of research methodology	71
Figure 4.1	Optical images of (a) as-received b) Homogenized at 673K-24h	74
Figure 4.2	SEM images of (a) as-received b) Homogenized at 673K-24h	75
Figure 4.3	Optical images for Die A and die B after 2 and 4 ECAP passes	75
Figure 4.4	Optical images of (a) as-received b) Homogenized at 673K-24h	76
Figure 4.5	SEM images of (a) as-received b) Homogenized at 673K-24h	76
Figure 4.6	Optical images for Die A and die B after 2 and 4 ECAP passes	77
Figure 4.7	Variation of average grain size with two different die	78
Figure 4.8	Optical microstructure of AZ80 Mg alloys at ECAP processing temperature of 533K for different passes a) 1P b) 2P c) 3P and 4) 4P	79

Figure 4.9	SEM microstructure of AZ80 Mg alloys at ECAP processing temperature of 533K for different passes a) 2P and b) 4P	80
Figure 4.10	Optical microstructure of AZ80 Mg alloys at ECAP processing temperature of 598K for different passes a) 1P b) 2P c) 3P and 4) 4P	81
Figure 4.11	SEM microstructure of AZ80 Mg alloys at ECAP processing temperature of 598K for a) 2P and b) 4P	81
Figure 4.12	Distribution of secondary phase of AZ80 Mg alloys after ECAP-4P	82
Figure 4.13	Optical microstructure of AZ80 Mg alloys at ECAP processing temperature of 663K for different passes a) 1P b) 2P c) 3P and 4) 4P	83
Figure 4.14	SEM microstructure of AZ80 Mg alloys at ECAP processing temperature of 663K for different passes a) 2P and b) 4P	83
Figure 4.15	Optical microstructure of AZ91 Mg alloys at ECAP processing temperature of 533K for different passes a) 1P b) 2P c) 3P and 4) 4P	85
Figure 4.16	SEM microstructure of AZ91 Mg alloys at ECAP processing temperature of 533K for different passes a) 2P and b) 4P	86
Figure 4.17	Optical microstructure of AZ91 Mg alloys at ECAP processing temperature of 598K for different passes a) 1P b) 2P c) 3P and 4) 4P	89
Figure 4.18	SEM microstructure of AZ91 Mg alloys at ECAP processing temperature of 598K for a) 2P and b) 4P	87
Figure 4.19	Distribution of secondary phase of AZ91 Mg alloys after ECAP-4P	87

Figure 4.20	Optical microstructure of AZ91 Mg alloys at ECAP processing temperature of 663K for different passes a) 1P b) 2P c) 3P and 4) 4P	88
Figure 4.21	SEM microstructure of AZ91 Mg alloys at ECAP processing temperature of 663K for different passes a) 2P and b) 4P	88
Figure 4.22	Mean grain size variation for different ECAP passes at three different processing temperatures	89
Figure 4.23	XRD analysis on AZ80 Mg alloys a) as-received b) Homogenized at 673K-24h c) Die A: 2P at 598K d) Die A: 4P at 598K. XRD analysis on AZ91 Mg alloys e) as-received f) Homogenized at 673K-24h g) Die A: 2P at 598K h) Die A: 4P at 598K	91
Figure 4.24	Variation of microhardness for AZ Mg alloys after processing through two different dies	93
Figure 4.25	Variation of microhardness for different processing temperatures.	93
Figure 4.26	Variation of tensile strength for different ECAP die	95
Figure 4.27	Variation of Ultimate Tensile Strength for different processing temperature	95
Figure 4.28	Variation of % elongation for different processing temperature	96
Figure 4.29	Fractured surface of AZ80 Mg alloys a) As-received b) Homogenized at 673K-24h c) 4P-533K d) 4P-598K e) 4P-663K	99
Figure 4.30	Fractured surface of AZ91 Mg alloys a) As-received b) Homogenized at 673K-24h c) 4P-533K d) 4P-598K e) 4P-663K	100
Figure 4.31	Corrosion rate vs ECAP die	102

Figure 4.32	Corrosion rate vs the number of ECAP pass after processing through die A at three different temperatures	103
Figure 4.33	Polarization curves of Mg alloys processed through die A a) ECAPed AZ80 Mg alloys A b) ECAPed AZ91 Mg alloys	104
Figure 4.34	Corrosion morphology of AZ80 Mg alloys a) as-received b) Homogenized at 673K-24h c) 4P-533K d) 4P-598K e) 4P-663K f) XRD for corroded specimen of as-received	107
Figure 4.35	Corrosion morphology of AZ91 Mg alloys a) as-received b) Homogenized at 673K-24h c) 4P-533K d) 4P-598K e) 4P-663K f) EDX for corroded specimen of as-received	108
Figure 5.1	The microstructure of annealed AZ80 wrought Mg alloys at different temperature and aging time a) 523K-6h b) 523K-12h c) 623K-6h d) 623K-12h e) 723K-6h and f) 723K-12h	115
Figure 5.2	Effect of temperature on grain growth a) As-received b) 723K-6h and c) 723K-12h	116
Figure 5.3	SEM images of ECAP-2P AZ80 Mg alloy a) 523K-6h b) 523K-12h c) 623K-6h d) 623K-12h e) 723K-6h and f) 723K-12h.	118
Figure 5.4	SEM images of ECAP-4P AZ80 Mg alloy a) 523K-6h b) 523K-12h c) 623K-6h d) 623K-12h e) 723K-6h and f) 723K-12h.	119
Figure 5.5	Effect of temperature on grain growth (a) ECAP-4P (b) 723 K–6 h and (c) 723 K–12 h.	120
Figure 5.6	The microstructure of annealed as-received AZ80 Mg alloys at different temperature and aging time a) 523K-6h b) 523K-12h c) 623K-6h d) 623K-12h e) 723K-6h and f) 723K-12h.	121

Figure 5.7	Effect of temperature on grain growth a) As-received b) 723K-6h and c) 723K-12h	122
Figure 5.8	SEM images of ECAP-2P AZ80 Mg alloy a) 523K-6h b) 523K-12h c) 623K-6h d) 623K-12h e) 723K-6h and f) 723K-12h	124
Figure 5.9	SEM images of ECAP-4P AZ91 Mg alloy a) 523K-6h b) 523K-12h c) 623K-6h d) 623K-12h e) 723K-6h f) 723K-12h.	125
Figure 5.10	Effect of temperature on grain growth (a) ECAP-4P (b) 723 K–6 h and (c) 723 K–12 h	126
Figure 5.11	The polarization curves for heat treated AZ80 Mg alloys in 3.5wt.% NaCl	127
Figure 5.12	The polarization curves for heat-treated AZ91 Mg alloys in 3.5wt.% NaCl	128
Figure 5.13	The microstructure of corroded AZ80 wrought Mg alloys a) As-received b) annealed at 523K-12h. c) 623K-12h d) 723K-6 h e) 723K-12h and f) X-ray diffraction of as-received AZ80 alloy	129
Figure 5.14	The SEM images of corroded AZ91 wrought Mg alloys a) As-received b) annealed at 523K-12h. c) Annealed at 723K-12h and d) XRD peaks of AZ91 annealed at 523K-12h	131
Figure 5.15	The polarization curves for heat treated ECAP-2P AZ80 Mg alloys in 3.5wt.% NaCl	134
Figure 5.16	The polarization curves for heat treated ECAP-4P AZ80 Mg alloys in 3.5wt.% NaCl	134
Figure 5.17	The polarization curves for heat-treated ECAP-2P AZ91 Mg alloys in 3.5wt.% NaCl	135
Figure 5.18	The polarization curves for heat-treated ECAP-4P AZ91Mg alloys in 3.5wt.% NaCl	136

Figure 5.19	Variation of corrosion rate of AZ80/91 Mg alloys after heat treating at 723K-12h	136
Figure 5.20	Corrosion morphology a) ECAP-2P a1) 523K-12h a2) 723-12hr b) ECAP-4P b1) 523K-12h b2) 723K-12h c) EDS for a1 at position X and d) EDS for b1 at position Y.	138
Figure 5.21	Corrosion morphology a) ECAP-2P a1) 523K-12h a2) 723-12hr b) ECAP-4P b1) 523K-12h b2) 723K-12h	139
Figure 5.22	316 stainless steel powder a) SEM micrograph b) size distribution	142
Figure 5.23	SEM surface morphologies of HVOF-coating on the ECAPed AZ80 Mg alloy a) as-received + 316SS b) EDS of the sealed coating c) ECAP-4P +316SS and d) 316SS Coating thickness	142
Figure 5.24	SEM surface morphologies of HVOF-coating on the ECAPed AZ91 Mg alloy a) as-received + 316SS b) EDS of the sealed coating c) ECAP-4P +316SS and d) 316SS Coating thickness	143
Figure 5.25	Sub surface microhardness of 316 SS coated AZ80 Mg alloys	144
Figure 5.26	Sub surface microhardness of 316 SS coated AZ91 Mg alloys	144
Figure 5.27	Corrosion behavior of ECAPed AZ80 Mg alloy after HVOF-coating	146
Figure 5.28	Corrosion morphology of ECAP-4P AZ80 Mg alloys after HVOF with EDS	146
Figure 5.29	Corrosion behavior of ECAPed AZ80 Mg alloy after HVOF-coating	147
Figure 5.30	Corrosion morphology of ECAP-4P AZ91 Mg alloys after HVOF with EDS	147

Figure 5.31	Corrosion rates of ECAP-4P AZ80/91 Mg alloy before and after 316 SS coating	148
Figure 5.32	Potentiodynamic polarization curves for ECAPed AZ80-Mg alloys in a) 2.5wt.% NaCl b) 3.5wt.% NaCl and c) Natural Seawater	150
Figure 5.33	Potentiodynamic polarization curves for ECAPed AZ91-Mg alloys in a) 2.5wt.% NaCl b) 3.5wt.% NaCl and c) Natural Seawater	151
Figure 5.34	Corrosion morphologies of AZ80 Mg alloys ECAP processed at 4P a) 2.5wt.% NaCl b) 3.5wt.%NaCl c) NSW and d) NSW at higher magnification	152
Figure 5.35	Corrosion morphologies of AZ91 Mg alloys ECAP processed at 4P a) 2.5wt.% NaCl b) 3.5wt.%NaCl c) NSW and d) NSW at higher magnification	153
Figure 5.36	XRD for corroded ECAP-4P specimen a) AZ80: 2.5wt.% NaCl and b) AZ91: 2.5wt.% NaCl	153

## LIST OF TABLES

<b>Table No.</b>	<b>Description</b>	<b>Page No.</b>
Table 1.1	Properties of magnesium aluminium and iron (Pathak et al., 2012)	3
Table 2.1	Summary of corrosion behaviour of Magnesium alloys.	44
Table 2.2	Summary of the corrosion behavior of ECAPed Mg alloys.	47
Table 3.1	Material properties of as-received AZ Mg alloys	58
Table 3.2	Properties of hot die steel H13 (Koneshlou et al., 2011)	59
Table 3.3	Experimental conditions	62
Table 3.4	The process variables for the HVOF process	70
Table 4.1	Data Sheet of AZ80 Mg alloy processed with die A and die B	109
Table 4.2	Data Sheet of AZ91 Mg alloy processed with die A and die B	110
Table 5.1	Data Sheet of processed and unprocessed AZ80/91 Mg alloys after annealing and aging treatment	140
Table 5.2	Data Sheet of ECAPed AZ80/91 Mg alloy after HVOF coating	148
Table 5.3	Data Sheet of as-received and ECAPed AZ80/91 Mg alloy after testing in three different environments	154



## LIST OF SYMBOLS AND ABBREVIATIONS

AE	: Auxiliary Electrode
AM	: Aluminium-Manganese
ANOM	: Analysis of Mean
ANOVA	: Analysis of Variance
ARB	: Accumulative Roll Bonding
AZ	: Aluminium-Zinc
ASTM	: American Society for Testing and Materials
BCC	: Body Centered Cubic
BSE	: Backscattered Electron
CP	: Continuous Precipitation
CR	: Corrosion Rate
DRX	: Dynamic Recrystallization
DSR	: Differential Speed Rolling
DP	: Discontinuous Precipitation
$E_0$	: Equilibrium Electrode Potential
EBSD	: Electron Back-Scatter Diffraction
ECAP	: Equal Channel Angular Pressing
$E_{corr}$	: Corrosion Potential
ECAE	: Equal Channel Angular Extrusion
EDS	: Energy Dispersive X-ray Spectroscopy
EIS	: Electrochemical Impedance Spectroscopy
$F$	: Faradays Constant
FCC	: Face Centered Cubic
FE	: Finite Element
FEA	: Finite Element Analysis

GBS	: Grain Boundary Strengthening
GS	: Grain size
GTTC	: Government Tool Room and Training Centre
HAGB	: High Angle Grain Boundaries
HDS	: Hot Die Steel
HCP	: Hexagonal Closed Pack
HPT	: High Pressure Torsion
HVOF	: High Velocity Oxygen Fuel Coating
$I_{corr}$	: Corrosion Current Density
LAGB	: Low Angle Grain Boundaries
LP	: Linear Polarization
LPG	: Liquid Petroleum Gas
MAF	: Multi-Axial Forging
MAO	: Metal Arc Oxidation
MDF	: Multi-Directional Forging
MH	: Microhardness
NSW	: Natural Sea Water
OCP	: Open Circuit Potential
OM	: Optical Microscopy
P	: Pass
PD	: Potentiodynamic
PEO	: Plasma Electrolytic Oxidation
PS	: Precipitates Strengthening
PSI	: Pound per Square Inch
RE	: Rare Earth
REC	: Reciprocating Extrusion Compression

RCS	: Repetitive Corrugation and Straightening
$R_t$	: Charge Transfer Resistance
RT	: Room Temperature
SCE	: Saturated Calomel Electrode
SCFH	: Standard Cubic Feet per Hour
SEM	: Scanning Electron Microscopy
SPD	: Severe Plastic Deformation
SS	: Solid solution Strengthening
SS	: Stainless Steel
UFG	: Ultrafine grain
UTM	: Universal Testing Machine
UTS	: Ultimate Tensile Strength
WE	: Working Electrode
XRD	: X-ray Diffraction
YTS	: Yield Tensile Strength
ZK	: Zinc-Zirconium
$\phi$	: Channel Angle
$\psi$	: Corner Angle
$\gamma$	: Shear Strain
$\epsilon_{eq}$	: Equivalent Strain
$n$	: Number of Electrons

# CHAPTER 1

## INTRODUCTION

### 1.1 BACKGROUND

Wrought magnesium alloys are one of the most promising lightweight materials of special interests in structural applications due to their homogeneous microstructure and improved mechanical properties compared to as-cast Mg alloys (Zhongyu et al., 2013). Mg alloys are one of the most reactive metals that have poor corrosion resistance and low mechanical properties, which limits its applications in industries. Therefore enhancement of mechanical properties and corrosion resistance have led to greater interest in magnesium alloys because of its special applications (Noor et al., 2008; Miao et al., 2016; Tan et al., 2016; Bao et al., 2017). Presently much effort is required for preparation of magnesium alloys with a grain size lower than 1  $\mu\text{m}$ , i.e. ultrafine-grained (UFG) materials in order to improve the strength and corrosion resistance of Mg alloys, many researchers worked and finally developed a severe plastic deformation (SPD) process which greatly contributes towards grain refinement and distribution of secondary phases to enhance mechanical and corrosion properties (Shaeri et al., 2016). However, in SPD, ECAP is most developed and frequently used metalworking technique for significant materials hardening due to increasing dislocation density and considerable grain size reduction to sub-micro-level (Brunner et al., 2009). Finally, ultra-fine grain structure and uniformly distributed secondary phase particles increase re-passivation tendency, which exhibits the improved mechanical properties and corrosion resistance. Further, annealing treatment and consequently ageing as well as High-Velocity Oxygen Fuel-coating process on ECAPed Mg alloys significantly reduce corrosion rate at 3.5 wt.% NaCl solution making it promising for industrial applications.

### 1.2 MAGNESIUM ALLOYS AND ITS APPLICATIONS

Magnesium alloys were used since Sir Humphry Davy first produced pure Magnesium in 1808 (Živić et al., 2014). Mg is an alkaline earth metal (Group IIA) with hexagonal closed pack (HCP) crystal structure. Magnesium is the lightest metal among all

categories of metals. Magnesium alloys have excellent material properties like strength-to-weight ratio, good fatigue and impact strengths, and large thermal and electrical conductivities and excellent biocompatibility (Mezbahul-islam, et al., 2014). Its low density is one of the most promising property and a key material to increase fuel efficiency and to reduce environmental pollution. Indeed alloying elements not only revise the mechanical properties and also it shows the significant impact on corrosion behaviour because of alloying elements form secondary particles which are noble or active towards corrosion (Pardo et al., 2008). Therefore in order to enhance the mechanical and corrosion properties of Magnesium alloys, Al, Zn, Sn, Ca, Sc, Si and rare earth (RE) are usually selected as strengthening elements. The addition of alloying elements is to promote the strengthening of base metal and it also shows better corrosion resistance. RE addition improves the formability of wrought Mg alloys (Rossouw et al., 2016). There are 17 rare earth (RE) elements which are identified through literature (Esmaily, et al., 2017). Considering, Aluminum has a comparatively lower density and high solid solubility in magnesium, therefore firstly, Mg base metal combined with 2 to 10 % Al and slight addition of Zinc 0.5 to 3 %, manganese 0.1 to 0.4 % formed AZ alloys, AZ series magnesium alloys which are readily available. This poses good mechanical properties and corrosion resistance at a lower temperature but at elevated temperature mechanical properties of the materials reduces and material deterioration can be observed thus the inclusion of Rare Earth, Zinc, silver, thorium and zirconium content significantly improves the mechanical properties and corrosion resistance. Indeed the addition of zinc to AZ Mg alloys are limited to 1-3% because of its micro shrinkage characteristics, also above 3% of Zn accelerates corrosion and addition of zirconium acts as a strong grain refiner for magnesium. Li addition to Mg reduces the density by about  $1.35\text{g/cm}^3$  which is much lower than other Mg alloys like AZ31, AZ61, AZ80, ZK60 etc and also improves the ductility. Additionally, Mg alloys have major applications in automobile, aerospace and medical field (Dziubińska et al., 2016; Sahu et al., 2015; Rossi et al., 1998; Aghion et al., 2000; Kappes et al., 2013). However, inadequate research towards the application of Mg and its alloys in the marine field was observed. Rossi et al. (1998) investigated the use of Mg as a sacrificial anode for the protection of offshore steels and aluminium structures. Table 1.1 presents the properties comparison between wrought aluminium, magnesium and iron.

Table 1.1 Properties of magnesium aluminium and iron (Pathak et al., 2012)

Properties	Magnesium (Mg)	Aluminium (Al)	Iron (Fe)
Crystal Structure	HCP	FCC	BCC
Density at 20°C (g/cc)	1.74	2.70	7.86
	Al is ~2.9 x and Mg is ~4.5 x lighter than Fe		
Coefficient of thermal expansion 20-100 X 10 <sup>-6</sup> /°C	25.2	23.6	11.7
Elastic Modulus (10 <sup>6</sup> psi)	6.4	10	30
Melting Point (°C)	650	660	1536
Standard reduction potential (V vs. standard Hydrogen Electrode )	-2.37	-1.66	-0.447
	The higher reactivity of Mg and Al atmosphere than Fe Mg can act as a sacrificial anode		
Cost	Mg>Al>Fe		

Magnesium alloys must be used in applications where less mass and high specific strength are required. According to the specific modulus and high specific strength, magnesium alloys show better values than aluminium and many commercial steels. Which makes it more attractive towards industrial applications (Blawert et al., 2004; Kulekci 2008; Profile et al., 1994). Specifically, the automobile sector, aerospace, marine and electronics industries. Indeed, magnesium alloys are used in automotive vehicle parts such as front end structures, transmission case, cam cover, seat frames, header bow, steering wheel cores and instrumental panel etc. are shown in figure 1.1 (a). Some of the aerospace applications of magnesium alloy include aircraft service door inner panel, window frame, rudder pedal impeller blade and cockpit instrumental panel as shown in figure 1.1 (b). Also, Mg alloys are using it as implants for orthopaedic application and sacrificial anode in the marine field as shown in figure 1.1 (c) and (d) respectively. However, Magnesium alloys have become an attractive alloy in the development of strategic industries and cannot be substituted by any other alloy for typical applications due to its high specific strength and physical properties and easy machinability. But it has low mechanical strength, ductility and corrosion resistance properties. Therefore, current research work focuses on the strengthening of magnesium alloys specifically AZ Mg alloys.

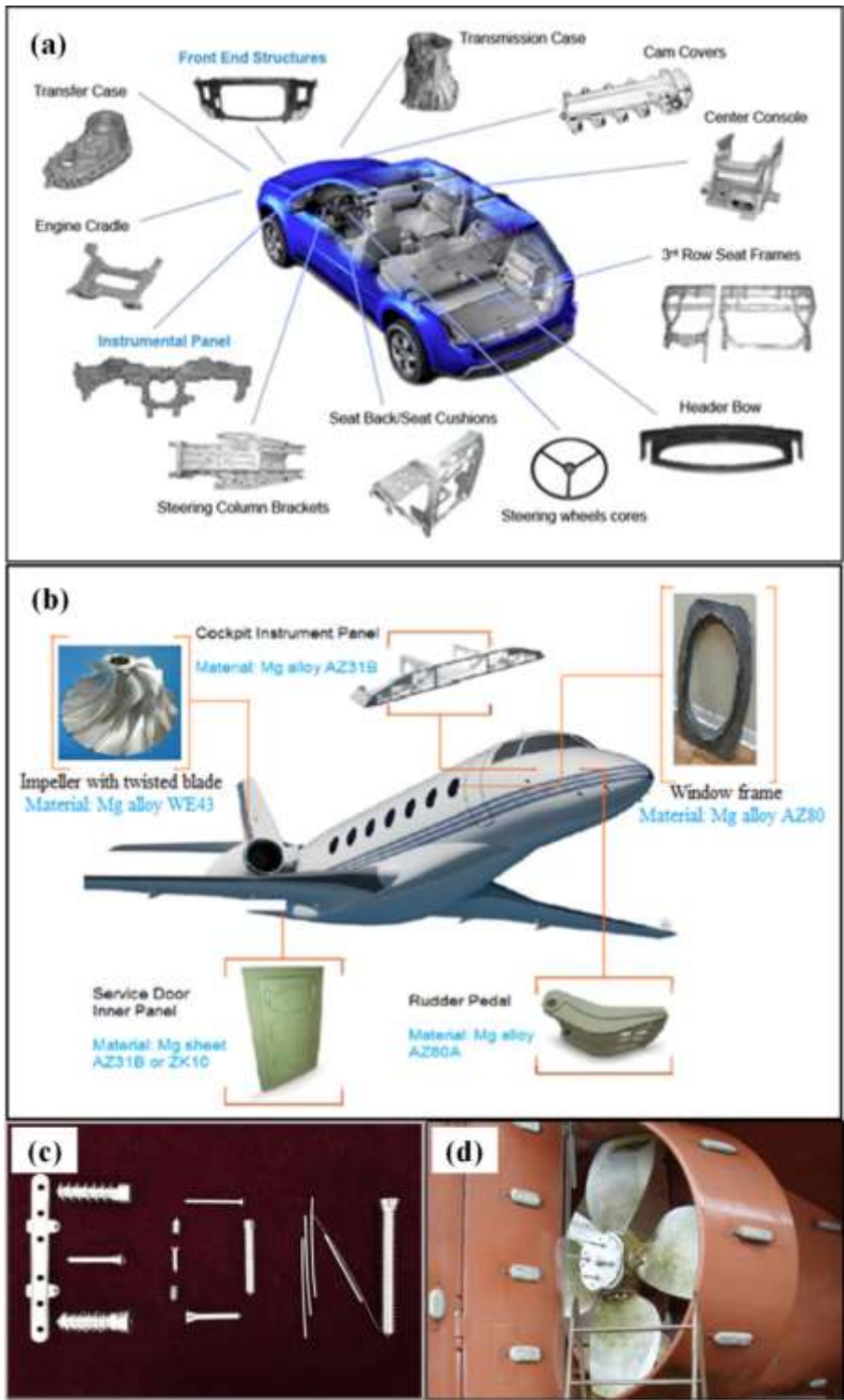


Figure 1.1 Applications of magnesium alloys in a) Automobile (Dziubińska et al., 2016) b) Aircraft (Dziubińska et al., 2016) c) Biomedical: implants for orthopaedic application (Waizy et al., 2001) and d) Marine field (Adapted from <http://electricalfundablog.com>)

### **1.3 STRENGTHENING MECHANISMS**

Magnesium and its alloys were first introduced as a structural material in 1909 (Luo et al., 1994). The most primitive commercial alloying elements were aluminium and zinc. Mg-Al-Zn castings were used widely, but they suffered from low mechanical strength and corrosion problems in wet environments. It is believed that the above material properties can be improved through strengthening mechanisms. The strengthening mechanisms of magnesium-based alloys are commonly described to four well-known mechanisms. (i) Precipitation strengthening: this involves strengthening of grains due to the formation of precipitates. (ii) Solution strengthening: this involves the strengthening of the alloys phases because of dissolved secondary phases. (iii) Grain refinement and sub grain strengthening: this strengthening mechanism occurs due to hindering of dislocation movement by the presence of grain and sub grain boundaries. (iv) Dislocation density strengthening: this strengthening of the magnesium-rich phase grains is attributed to obstructing of dislocation movements formed within the alloys due to prior plastic deformation (Ishikawa et al., 2005; Cheng et al., 2010). The grain refinement or grain boundary strengthening was found to be a promising method to improve material properties of magnesium alloys (Cheng et al., 2014; Ghader Faraji et al., 2012).

The most effective approach to improve both mechanical properties and corrosion resistance of magnesium is grain refinement and distribution of secondary phases through equal channel angular extrusion process. In addition, numerous studies stated that grain refinement induced by severe plastic deformation (SPD) is an effective method to improve both mechanical and corrosion properties of Magnesium alloys due to Hall-Petch strengthening and uniform distribution of precipitates, respectively (Mostaed et al., 2014; Qi et al., 2012).

#### **1.3.1 Introduction to Severe Plastic Deformation**

Severe plastic deformation (SPD) process which greatly contributes towards grain refinement to enhance mechanical properties of the metal which leads to super-elastic properties with respect to temperature (Shaeri et al., 2016). Various SPD processes such as Equal channel angular pressing (ECAP), High-pressure torsion (HPT),



Accumulative roll bonding (ARB), Reciprocating extrusion-compression (REC), Repetitive corrugation and straightening (RCS) are employed to modify the microstructure to improve the strength, ductility and hardness of the magnesium alloys (Verlinden et al., 2018; Estrin et al., 2013). However, in SPD, ECAP is most developed and frequently used metalworking technique for significant materials hardening due to increasing dislocation density and considerable grain size reduction to sub-micro level. Grain size reduction of metals or alloys increases the strength of the material by accumulating large strain into work-piece and without changing the shape of the material.

### 1.3.1.1 Equal Channel Angular Extrusion Process

Segal proposed this experimental technique in 1977 in Russia to improve the yield strength of materials through grain refinement (Zrnik, et al., 2008; Ghader Faraji et al., 2012). Figure 1.2 depicts, principle of ECAP and illustrates the schematic of equal channel angular press (ECAP) with its terminologies the die consisting of two equal channels intersecting at an channel angle ( $\phi$ ) and corner angle ( $\Psi$ ) the material is pressed under load P, which induces intense plastic strain via simple shear without equivalent change in the cross-sectional dimension of the workpiece, It has unique qualities compared to the other methods of grain refinement, which is to build up plastic strain in the material at shear region, by increasing the number of passes which leads to reduction of the grain size in the material and it is more flexible compared to other SPD techniques. Moreover, the strain distribution in the process depends on the friction uniformity, die channel and corner angle. Indeed the grain size of the polycrystalline materials generally plays a significant role, thus the strength of the all polycrystalline material depends on average grain size 'd'. The relationship between the yield strength and average grain size is clearly explained through Hall-Petch relation given in equation (1.1) explicitly materials yield strength is inversely proportional to the square root of the grain size (Avvari et al., 2015,).

$$\sigma_y = \sigma_0 + \frac{k_y}{\sqrt{d}} \quad (1.1)$$

Where  $\sigma_y$  is the yield strength,  $\sigma_0$  (MPa) is the friction stress for dislocation movement,  $k_y$  (MPa-mm<sup>1/2</sup>) is the strength coefficient for the normal stress and 'd' is the grain size.

For AZ31B magnesium alloys the friction stress  $\sigma_0$  ranges from 10 to 131MPa, the strength coefficient  $k_y$  ranges from 5.0 to 12MPa-mm<sup>1/2</sup> (Wang et al., 2014). The ECAP consists of two-channel intersects at a particular angle called channel angle ( $\phi$ ) and the subtended intersection point of the channel is called corner angle ( $\Psi$ ). Based on this geometry factor, the total strain developed in the ECAPed sample can be calculated and is given by the Eq. (1.2). The total accumulated strain ( $\epsilon_{eq}$ ) is  $N*\gamma$  given in Eq. (1.3), (Azushima et al., 2008). Also, it is reported that the lower channel and corner angle gives larger accumulative strain to get ultra-fine grains in the materials. Ultrafine microstructure with equiaxed grains which is separated by grain boundaries having high angles of misorientation can be accomplished most easily when imparting a very intense plastic strain with a value of channel angle ( $\phi$ ) is very close to 90°, from Eqn. (1.2) the strain imposed on a single pass through the die is very close to one (1).

$$\gamma = \frac{1}{\sqrt{3}} \left( 2 \cot \left( \frac{\phi + \Psi}{2} \right) + \Psi \operatorname{cosec} \left( \frac{\phi + \Psi}{2} \right) \right) \quad (1.2)$$

$$\epsilon_{eq} = \frac{N}{\sqrt{3}} \left( 2 \cot \left( \frac{\phi + \Psi}{2} \right) + \Psi \operatorname{cosec} \left( \frac{\phi + \Psi}{2} \right) \right) \quad (1.3)$$

$\gamma$  = shear strain

$\epsilon_{eq}$  equivalent strain

In equal channel angular extrusion, the metal is pressed through the die using a plunger with a specific die and corner angle  $\phi$  and  $\Psi$  respectively. The process has four basic processing routes in ECAP (Figure 1.3), such as Route A: here the samples are pressed without any rotations.

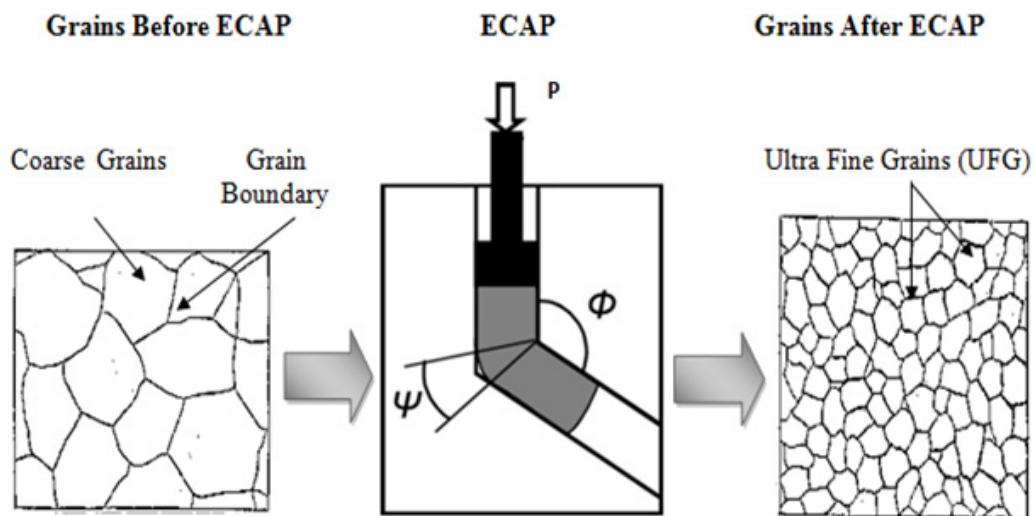


Figure 1.2 Schematic of equal channel angular extrusion. (Agwa et al., 2016)

Route  $B_A$ : the specimen is rotated by 90 degrees in a clockwise direction between consecutive passes. Route  $B_c$ : the specimen is rotated by 90 degrees in counter-clockwise direction between consecutive passes. Route  $C$ : The specimen is rotated by 180 degrees between the passes, there is a provision to rotate the work-piece between the successive pressing in order to activate the shear planes and direction. From the above-said routes, ultra-fine grains can be obtained. It was reported that the route  $B_c$  is most effective and route  $A$  is least effective in grain refinement. Also, the author summarized the effectiveness of ECAP processing routes that are in the order of route  $B_c >$  route  $C >$  routes  $A$  and  $B_A$  to facilitate the process. Muralidhar et al., (2015) introduced the new ECAP route Route-R on wrought AZ61 magnesium alloys at 483K for grain refinement. Here the specimen is inverted to the original position in each ECAP passes (Figure 1.3), subsequently; the average grain size of the AZ61 alloy is reduced from  $66\mu\text{m}$  to  $16\mu\text{m}$ ,  $14.1\mu\text{m}$  and  $10\mu\text{m}$  for Route  $A$ , route  $B_c$  and route  $R$  respectively. It is clear that route-R ECAP processing produces enhanced ultra-fine grains (UFG) compare to route  $B_c$ .

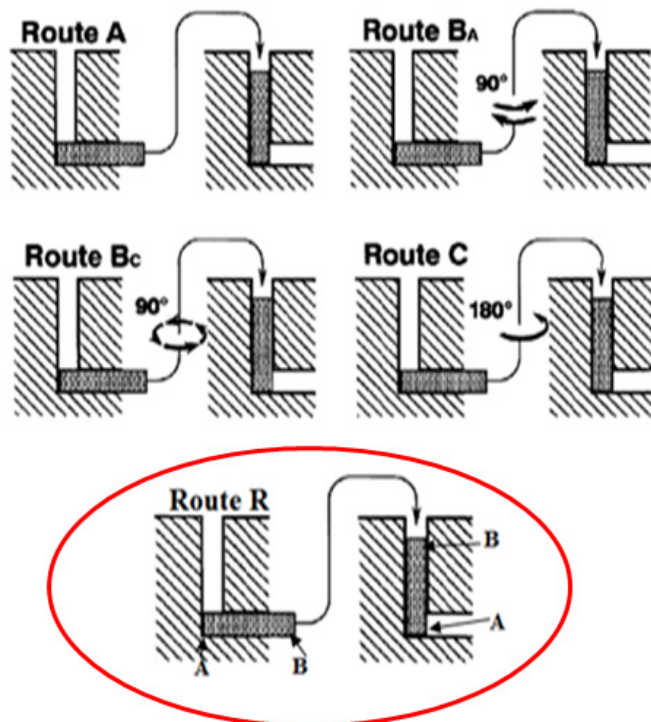


Figure 1.3 Different processing routes of ECAE (Avvari et al., 2015)

### 1.3.1.2 Factors affecting grain refinement in ECAP

Equal channel angular pressing is capable of refining the grain sizes of metallic materials to sub-micro-meter level. This section presents the effect of ECAP process parameters on grain refinement.

**i) Die geometry:** The accumulation of effective strain magnitude in a single passage through the ECAP die is inversely proportional to the  $\phi$  and  $\Psi$  channel angle and corner angles respectively. Also, it is most effective in grain refinement. (Avvari et al., 2018 and Djavanroodi et al., 2010)

**ii) Processing temperature:** ECAP processed at a lower temperature improves the mechanical properties. Accordingly, by increasing processing temperature, it increases the grain size and also this reduces the dislocation density (Kumar et al., 2015; Argade et al., 2012 and Zhu et al., 2000)

**iii) Processing routes:** There are five fundamental routes of ECAP, route Bc and route R are considered as optimum routes for getting UFG microstructure in the ECAPed samples (Avvari et al., 2015; Furukawa et al., 2001; Zhu et al., 2000)

**iv) Backpressure:** This improves the plastic strain in the material, prevents cracking when ECAP working at lower temperatures. This leads to enhanced grain refinement in the ECAPed sample and results in considerable improvement on mechanical properties (Kang et al., 2010 and Shen et al., 2016)

**v) Ram speed:** Increased ram speed can be employed to attain a homogeneous microstructure even at elevated temperatures. Typically the ram speed (mm/s) in the range of 1-20mm/s prepared. (Valiev et al., 2006 and Sabirov et al., 2010)

## 1.4 INTRODUCTION TO CORROSION

“Corrosion is the deterioration of a material due to a reaction with its environment”. Degradation implies deterioration of physical properties and the microstructure, mechanical properties and the physical appearance of the materials. This can be a weakening of the material due to a loss of cross-sectional area of the material. Materials

can be metals, polymers (plastics, rubbers, etc.), ceramics (concrete, brick, etc.) or composites and alloys. But more attention is given to corrosion of metals because metals are the most used type of structural materials and most of the corrosion of metals is electrochemical in nature. Further sections discuss the corrosion thermodynamics, kinetics and Mg corrosion (Edward et al., 2004; Froes et al., 1998).

#### 1.4.1 Corrosion of magnesium alloys

Corrosion is the deterioration of a material because of a reaction with its environment. During Mg corrosion, Mg dissolves as  $Mg^{2+}$  which reacts with water, generates hydrogen bubbles, creates hydroxyl groups and increases pH. Micro-bubbles that get larger and float in the air are generated from pitting or active corrosion sites. Dissolved divalent  $Mg^{2+}$  ions react with hydroxyl groups ( $OH^-$ ) and precipitate as Mg hydroxide ( $Mg(OH)_2$ ).

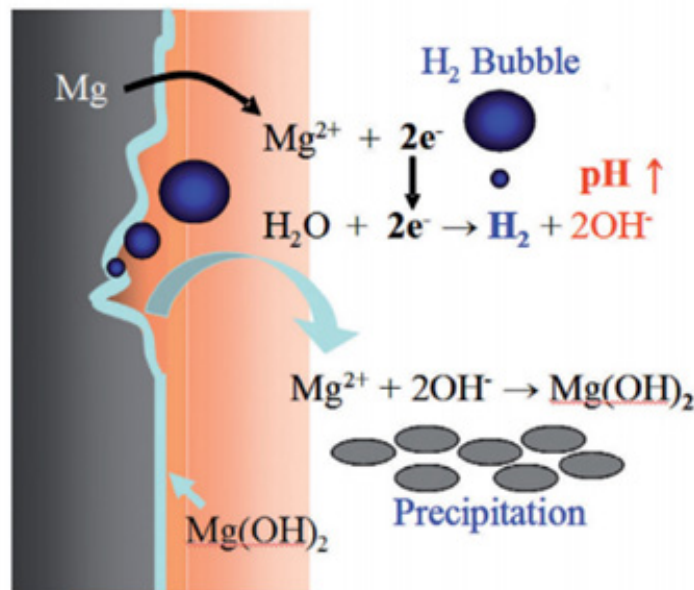
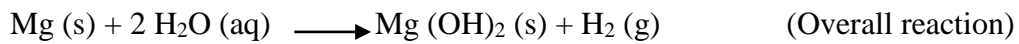


Figure 1.4 Atmospheric corrosion of magnesium (Yun et al., 2009)

Also, a passive interlayer of  $Mg(OH)_2$  or  $MgO$  is formed on the degradation surface. Magnesium and its alloys generally show a less corrosion resistance in aqueous Environment, this limit its use in marine applications (Edward et al., 2004 and Liu et al. 2009). In general, Mg failure fall into one of four categories: pitting corrosion, galvanic corrosion, stress corrosion cracking and Intergranular corrosion (Zeng et al.,

2006; Ghali et al., 2004; Sekar et al., 2019). However, Corrosion of magnesium in an aqueous environment takes place according to the following anodic and cathodic reactions leading to the formation of gaseous hydrogen and magnesium hydroxide. The magnesium hydroxide produced acts as passive film and provides protection to the bulk materials as shown in figure 1.4 (Yun et al., 2009). The electrochemical corrosion of Mg in water corresponds to the sum of the two half-cell reactions (Agarwal et al., 2016).



The reaction includes anodic dissolution of Mg according to:



The corresponding cathodic reaction is the evolution of hydrogen



Magnesium has a very less standard electrode potential with a value of  $-2.37 \text{ V}_{\text{SHE}}$  with respect to the hydrogen electrode potential taken as zero and at  $25^\circ\text{C}$  it is less noble than most metals (Li et al., 2010).

#### 1.4.2 Corrosion Thermodynamics

Metal corrosion occurs because due to all metals are unstable (high energy) and have a tendency to revert to their more stable (lower energy) states by combination with elements present in their environment (Song et al., 1999; Song et al., 2003). The possibility of this combination or reaction occurring can be linked thermodynamically to the free energy change for the reaction. The Gibbs free energy change ( $\Delta G$ ), therefore it can be used as a measure of the corrosion occurring. Values of free energy change can be obtained from the relationship given in Equation 1.4. Which indicates that the thermodynamic tendencies for corrosion can be discussed in terms of an electrochemical parameter ( $E$ ) called the electrode potential (González et al., 2012).

$$\Delta G = - nF\Delta E \quad (1.4)$$

Where:  $n$  is no of electrons passed;

$F$  = Faradays constant, 96500 coulombs/equivalent;

$\Delta E = E - E_0$ ; and  $E_0$  is the equilibrium electrode potential.

### 1.4.3 Corrosion Kinetics

Corrosion kinetics refers to the scientific measurement of the stability of chemical species present during corrosion for various substrate materials. Corrosion kinetics examine the polarization of reactants in terms of their cathodic and anodic tendencies. The use of polarization curves for the study of corrosion reactions can be traced back to the 1930s with the work of Wagner and Traud. However, the representation of the mixed potential behaviour is often associated with Professor Evans who has popularized this representation of corrosion polarization measurements (Figure 1.5) (Sukiman et al., 2012). These polarization diagrams can be quite useful for describing or explaining parallel corrosion processes.

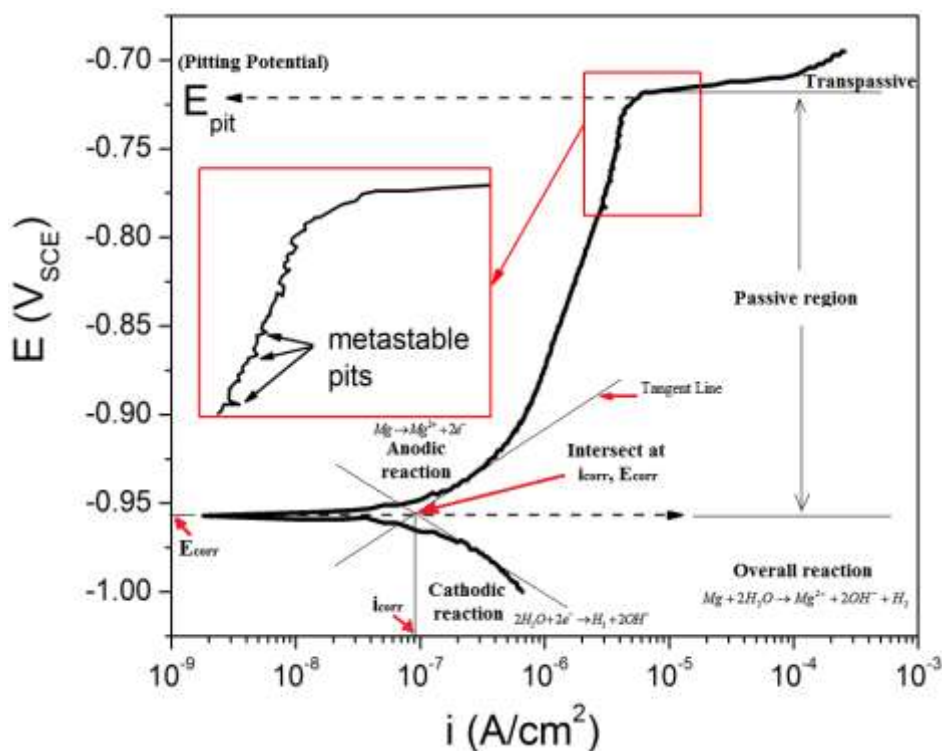


Figure 1.5 Polarization curve (Sukiman et al., 2012)

According to the mixed-potential theory underlying these diagrams, any electrochemical reaction can be algebraically divided into separate oxidation and reduction reactions with no net accumulation of electrical charge. Under these circumstances the net measurable current is zero and the corroding metal is charge

neutral, which is all electrons produced by the corrosion of a metal have to be consumed by one or more cathodic processes. While it is relatively easy to estimate the corrosion potential ( $E_{\text{corr}}$ ) from the sharp peak observed at  $-0.96 \text{ V}_{\text{SCE}}$ , when the current crosses zero (infinity on a log scale), the projected lines are required to find the intercept indicating where the cathodic and anodic currents actually cancel each other. The corrosion current density ( $I_{\text{corr}}$ ) can be obtained by dividing the anodic current by the surface area of the specimen. (Liu et al., 2009)

## **1.5 INTRODUCTION TO ANNEALING AND AGING TREATMENT**

Annealing is a heat treatment technique in which the Mg alloys is heated up to the recommended annealing temperature for a prescribed holding time followed by controlled cooling in order to change the properties of the magnesium alloys by altering the microstructure. The different types of annealing treatments with different objectives exist depending on the alloy system and prior processing methods. Diffusion annealing produces the most ductile and workable conditions for wrought Mg alloys (Xu et al., 2018 and Silva et al., 2014).

The microstructural modification to enhance the mechanical and corrosion behaviour of magnesium alloys is a well-established approach in the materials research (Li et al., 2017). Altering the microstructure of Mg alloy has also presented substantial effects on modifying different structure sensitive properties. During annealing and aging process, the material undergoes recovery, partial recrystallization, or full recrystallization and grain growth (Naik et al., 2019). Which effects on re-distribution and partial dissolution of secondary phases, results in improved formability and corrosion resistance.

## **1.6 COATING OF MAGNESIUM ALLOYS**

Magnesium and its alloys are capable materials for lightweight structures such as in aircraft, marine and in automobile industry due to their high specific strength. But, the use of magnesium alloys is limited by their low corrosion resistance. Surface modifications such as painting, electroplating, anodizing and conversion coatings have been used now to improve their surface properties (Sidhu et al., 2005; Poinern et al.,



2012). In addition to those conventional approaches, recent investigations have shown that the thermal spray method has enormous potential for the surface modification of magnesium alloys.

### 1.6.1 Working principle of high-velocity oxy fuel coating

The thermal spray technology offers a variety of techniques, among those techniques, the High-Velocity Oxy-Fuel (HVOF) spray process is of greater importance because it is possible to produce very dense coatings with outstanding corrosion and wear resistance (Oksa et al., 2011).

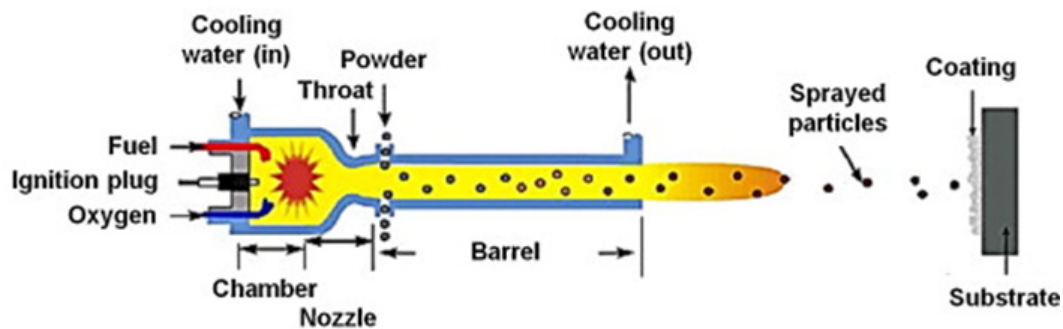


Figure 1.6 High-Velocity Oxy-Fuel (HVOF) process (Ann Gan et al., 2017)

In HVOF process (Fig. 1.6), the powder material is liquefied and propelled at a high velocity toward the surface with the use of oxygen and fuel gas mixtures. Propylene, propane, hydrogen, acetylene, methane, ethylene, kerosene, LPG, etc. are used as fuels. The HVOF process consists of a spray gun, powder-feed unit, flow-meter unit, and an air and gas supply unit. The amount of powder essential for deposition can be controlled by using the powder feed-rate meter. In the combustion chamber, the powder material enters the flame, where it converts molten or semi-molten state, depending on the melting temperature and the feed rate of the powder material. The flame temperature for the HVOF process is approximately 3000°C. The molten or semi-molten particles are then propelled out of the gun at very high velocities toward the substrate. Powder particles, typically within the range 10–63  $\mu\text{m}$ , attain velocities of 300–800 m/s at the substrate to be coated. The quality of the coatings significantly

depends on the velocity and temperature of the powder particles impinging upon the substrate surface (Mardali et al., 2018).

## **1.7 THESIS ORGANISATION**

The outline of the thesis has been divided into the following sections:

### **CHAPTER 1**

In this chapter, the background of magnesium alloys and severe plastic deformation process, the introduction of magnesium alloys and their applications have been described. The chapter also discusses the equal channel extrusion process, the corrosion behaviour of magnesium, corrosion rate measurement through corrosion kinetics and corrosion prevention by annealing treatment and high-velocity oxygen fuel coating.

### **CHAPTER 2**

This chapter presents a complete literature review relating to the works reported on the effect of microstructure on mechanical and corrosion properties of magnesium alloys after processing through equal channel angular press and also present recent developments in improvement of corrosion resistance through heat treatment. Finally coating have been studied and reported. In addition, the effect of different environment on corrosion resistance of magnesium alloys is also dealt with.

### **CHAPTER 3**

The chapter deals with the material selection, die fabrication, material preparation, experimental setup, procedure and methodology involved in the research work. This chapter also mentions the procedure involved in the measurement of grain size. Moreover, the details of the equipment used for material characterization and corrosion test have also been described in this chapter.

### **CHAPTER 4**

Investigation on the effects of die geometries on the material properties such as grain size, ultimate tensile strength, ductility and corrosion resistance of the ECAPed AZ80/91 magnesium alloys are presented in this chapter. Also, the effect of ECAP processing temperature on grain size was addressed through microstructure. Further,

the corrosion behaviour of AZ80/91 Mg alloys was evidently discussed with corrosion morphologies in this chapter.

## **CHAPTER 5**

The chapter deliberates with the annealing and aging treatment of as-received and ECAPed AZ80/91 magnesium alloys and its testing and characterization. In this chapter, the effect of various annealing temperature and aging time on corrosion resistance have been discussed through microstructure, polarization curves and corrosion morphologies. Further, High-velocity oxygen fuel coating is extended for the complete prevention of ECAPed AZ80/91 magnesium alloys. Also, deals with the corrosion behavior of as-received and ECAPed AZ80/91 magnesium alloys in different concentration of NaCl and marine environment.

## **CHAPTER 6**

Lastly this chapter deals with the conclusions of the investigations carried out through this research work. Further it also proposed future scope of research based on the present study.

## **CHAPTER 2**

### **LITERATURE REVIEW**

#### **2.1 INTRODUCTION**

This chapter presents the review of research work which is associated with the corrosion behaviour of equal channel angular pressed magnesium alloys. The effect of ECAP die angles and processing routes on grain size, impact of environment on corrosion performance of as-received and ECAPed Mg alloys. The surface morphology of corroded surface has been reported. Predominantly, the effect of grain refinement on mechanical and corrosion characteristics have been reviewed. Further, effect of annealing and aging treatment was reported and an overview of prevention of corrosion for improving the corrosion resistance of as-received and ECAPed magnesium alloy has been presented.

#### **2.2 WROUGHT MAGNESIUM ALLOYS**

Wrought magnesium alloys are of special interest as lightweight structural components as a result of their more homogeneous microstructures and improved mechanical properties compared to as-cast components. Letzig et al. (2007) have reported the effect of microstructure on the tensile/compression deformation behaviour of the AZ and ZK series alloys, from the investigation it was found that AZ80 wrought Mg alloys exhibited highest ultimate tensile strength (UTS) and yield strength (YS) followed by ZK30 and ZK60. With respect to the alloys used in this study, the commercial wrought magnesium alloy AZ80 is of special interest for die forging. Wrought magnesium alloys were first used in large quantities during the 1930s, for aircraft engines and armaments in the form of extruded, rolled, and forged alloys (Chris Davies and Barnett., 2004). Colleen (2005) reported Mg-Al based wrought alloys suitable for engineering applications because of their relative ease of extrusion and adequate mechanical properties. Mohd Ruzi H et al. (2009) reviewed the machinability of wrought Mg alloys from the report it was concluded that the machinability of wrought magnesium alloys can be improved by increasing the processing temperature. Moreover, wrought Mg alloys are poor corrosion resistance, poor creep resistance as well as fatigue failure but

these can be improved by various techniques of surface treatments, alloying additions and by achieving fine or ultra-fine grain structure. Zheng et al. (2014) Figure 2.1, depicts the mechanical strength and degradation rate of as-cast, wrought and SPD/ECAPed processed Mg-based alloys. The yield strength and % elongation of cast product is less compared to the wrought product, which is further increased by severe plastic deformation or ECAP technique. Furthermore, the cast Mg product is prone to corrosion, whereas wrought Mg alloys or SPD processed Mg alloys have shown resistance to corrosion. That is wrought Mg alloys exhibited high strength and lower corrosion rate when compared to cast alloys. Then, Agnew et al. (2004) have suggested that wrought Mg alloys most promising material and which has a significant impact on engineering applications and R&D research. Therefore, based on literature our research work focusing on wrought Mg alloys (AZ-series).

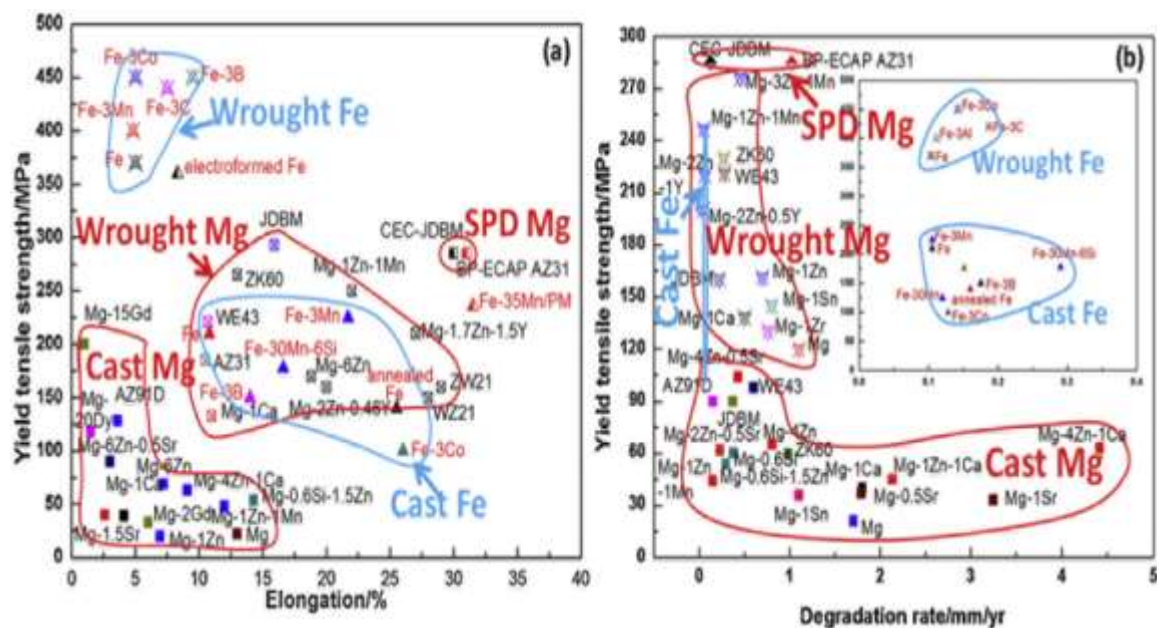


Figure 2.1 a) Yield tensile strength vs % elongation (b) YTS vs degradation rate of the as-cast and wrought and SPD processed Mg alloys. (Zheng et al., 2014)

Also, Poggiali et al. (2014) have discussed the evolution of the microstructure for commercial pure magnesium was processed by ECAP from the as-cast condition and also processed by rolling followed by ECAP. This work revealed that processing by rolling followed by ECAP is an effective route to obtain homogeneous grain

distribution with finer grain sizes and also improves the ductility. Here, strengthening of magnesium alloys were achieved by processing through rolling and by ECAP.

### **2.3 STRENGTHENING MECHANISMS**

In modern years, there is an increasing interest in the development of high strength magnesium-based alloys. The few studies indicated that the Mg-based alloys show higher tensile strength and elongations after implementing the strengthening mechanism. Basically, the strength of a magnesium alloy is dependent on how dislocations in its crystal can be easily propagated. These dislocations generate stress fields within the material depending on their character. Normally, the following strengthening mechanisms such as solid solution strengthening (SS), precipitates strengthening (PS) and grain boundary strengthening (GBS) are relevant in extruded and processed magnesium materials established at room temperature (Wu et al., 2014; Maruyama et al., 2016).

#### **2.3.1 Solid solution strengthening and alloying**

Solid-solution strengthening results from solutes hindering the glide of dislocations. Existing theories of strength depend on solute/dislocation interactions but do not consider dislocation core structures, which need an accurate treatment of chemical bonding (Bennett et al., 2010; Yasi et al., 2010). Here, we focus on strengthening of Mg, the lightest of all structural metals and a promising replacement for heavier steel and aluminium alloys. Joseph et al. (2010) developed the strengthening model and is validated with available experimental data for several solutes, including Al and Zn, considered the most common solutes in Mg. resulting, improvement in mechanical properties of magnesium alloy. Caceres and Rovera (2001) investigated the solid solution strengthening on the hardness and strength in the Mg alloys with aluminium content between 1 and 8 wt.%, as a result, the hardness increases and strength vary linearly with the aluminium content. Gao et al. (2009) studied the effect of rare-earth elements Gd and Y on the mechanical properties of Magnesium solid solutions mechanism. It was observed that hardness and strength increases with the increasing Gd content. Also, Luo et al. (2011) show that an addition of zinc  $\leq 2\%$  can significantly

improve the tensile strength of the Mg–0.2% Ce alloy. The results disclosed that Zn increased tensile strength through solid solution strengthening mechanism and the addition of Ce increased the ductility.

### **2.3.2 Precipitation Strengthening**

Precipitate particles are exploited for strengthening in many commercially available magnesium alloys. The precipitates that typically form in magnesium alloys take the form of rods or plates lying on particular crystallographic planes, with the precipitate morphology depending on the alloy system and heat treatment. It is identified that different precipitate types and thermal treatment lead to markedly different strengthening responses. Few studies in the literature are strengthened to the above statement. Specifically, Gao and Nie (2007) reported strengthening precipitation in an Mg–8 wt.% Zn alloy, aged isothermally at 200°C, observed the  $Mg_4Zn_7$  and  $MgZn_2$ . Robson et al. (2011) have been confirmed the effect of precipitation strengthening against mechanical data for alloy AZ91. As a result, ageing provides improved mechanical strength and ductility due to phase precipitation. Similarly, Zhao et al. (2014) studied the Microstructure evolution of the AZ80 magnesium alloy and precipitation behaviour of  $Mg_{17}Al_{12}$  phase in different heat treatment conditions. As a result, the dissolution of  $Mg_{17}Al_{12}$  phase and the grain coarsening was observed. During aging, discontinuous precipitates were preferentially started at the grain boundaries and then continuous precipitates appeared in the grain interiors. After solution and aging treatment, an improved combination of strength and elongation was obtained.

### **2.3.3 Grain boundary strengthening**

Magnesium alloys have an HCP crystal structure and there are only three independent slip systems on the basal plane, which is less than the five independent slip systems required for uniform deformation. This slip system makes the development of magnesium alloy, especially wrought magnesium alloys extremely limiting of its applications. To improve the mechanical properties and formability of wrought magnesium alloy, many studies have investigated the use of grain refinement or grain boundary strengthening through various plastic deformation processes (Avvari et al.,

2014). Shahzad et al. (2009) studied the effect of grain size on mechanical properties during extrusion of AZ80 Mg alloys, from the result it was reported that compared to the as-cast condition, the as-extruded alloys possess much finer grain size and consequently higher Yield Strength, Ultimate Tensile Strength and tensile elongation. Huang et al. (2009) have reported the as-rolled sheet exhibits a combination of high strength (TS: 329 MPa) and high ductility (elongation: 25%) when a heat-treatable AZ80 Mg alloy subjected to differential speed rolling (DSR) at a large thickness reduction per pass of 33%.

## **2.4 OVERVIEW OF SEVERE PLASTIC DEFORMATION**

The strengthening capability of the Magnesium alloy is strongly affected by severe plastic deformation. In recent years, high-pressure torsion (HPT), multi-axial forging (MAF) and equal channel angular pressing (ECAP) technique have been utilized for enhancing mechanical properties, corrosion resistance and formability of the Mg alloy by microstructure modifications. In addition, the ECAP has the potential to produce high strength and corrosion-resistant magnesium alloys.

### **2.4.1 Effect of microstructure on mechanical properties**

The review described here is aimed at understanding contribution of microstructure on mechanical properties after processing through various severe plastic deformation techniques. Here, Arpacay et al. (2008) examine the microstructure evolution and the hardness variations during HPT of AZ80 at room temperature. The grain structure becomes more homogeneous and finer with an increasing number of HPT revolutions. Initially, with minimum number of revolutions, the grain refinement occurs only locally in the vicinity of grain and twin boundaries. Pronounced grain refinement was observed in the specimen after 15 revolutions. Many grains in the nanometer range, i.e. having the size below 100 nm were found. The hardness of the HPT samples do not vary with an increasing number of revolutions. This can be explained by the relatively large indentation size covering many fine grains and by rapid strengthening of the sample so that maximum hardness is reached already after 1 revolution. Chen et al. (2012) studied the grain refinement in an as-cast AZ61 magnesium alloy processed by multi-axial



forging. The results show that the microstructure can be effectively refined with increasing equivalent strain during MAF. Also, this process produces a fine-grain AZ61 alloy with a grain size of 8  $\mu\text{m}$ . This fine-grained alloy has an excellent strength accompanied by reasonable good tensile ductility.

#### **2.4.2 Impact of microstructure on corrosion behaviour**

A literature on the effect of microstructural changes on the corrosion behavior of magnesium alloys have been reported in this section. Specifically, Zhang et al. (2017) described the microstructure and corrosion resistance of HPT-processed Mg-Zn-Ca alloy. The corrosion resistance of the HPT processed Mg alloy increased due to the uniform dense distribution of second phases after the process. Bahmani et al. (2019) investigated the microstructure evolution of the extruded ZAXM4211 Mg alloy. The grain size was significantly refined and uniform after MDF due to dynamic recrystallization, as a result, corrosion resistance of the MDFed alloy was remarkably improved. Gajanan et al. (2019) have reported the effect of grain refinement and its impact on corrosion resistance after the combined processes of multi-direction forging and equal channel angular pressing. This study outstandingly obtained a 94% reduction of corrosion rate for AZ80 Mg alloy after MDF-3 passes followed by an ECAP-2 passes (0.77mm/y) process compared to as-received Mg alloy.

### **2.5 EQUAL CHANNEL ANGULAR PRESSING OF MAGNESIUM ALLOYS**

#### **2.5.1 Result of die parameters in equal channel angular extrusion**

Many researchers worked on the effect of die parameters on deformation homogeneity, plastic stress and plastic strain through FE analysis. Djavanroodi and Ebrahimi (2010) investigated the effect of channel angle and friction coefficient on the deformation behaviour of aluminium alloy during ECAP through FE method. The analysis was carried out by considering the channel angle of 60°, 75°, 110°, 120° and constant corner angle 25° and also friction coefficients of 0.001 and 0.3. The study revealed that the amount of strain and distribution of strain increases with decreasing ECAP die channel angle and increases the coefficient of friction. Djavanroodi et al. (2012) simulated combinations of four die channel angles such as  $\phi = 60^\circ, 90^\circ, 105^\circ$  and  $120^\circ$  and two

corner angles  $\psi = 0^\circ, 15^\circ$  and pass numbers up to eight passes have been simulated by route A. Patil et al. (2015) investigated the effect of ECAP channel angle and inner and outer corner radii through 3D FE analysis. Obtained results in terms of peak pressure, strain and strain inhomogeneity were reported and analyzed using analysis of mean (ANOM). Main effects and interaction effects of all geometric parameters were computed by means of analysis of variance (ANOVA). From the simulation, it was noticed that the peak pressure is mainly influenced by channel angle ( $\phi$ ). Also from the study, it is revealed that to achieve the preferred strain the most important die parameters are channel angle ( $\phi$ ) and corner angle ( $\psi$ ). Along with this Park & Suh (2001), researcher simulates the effect of the corner angle on deformation behaviour in ECAP.

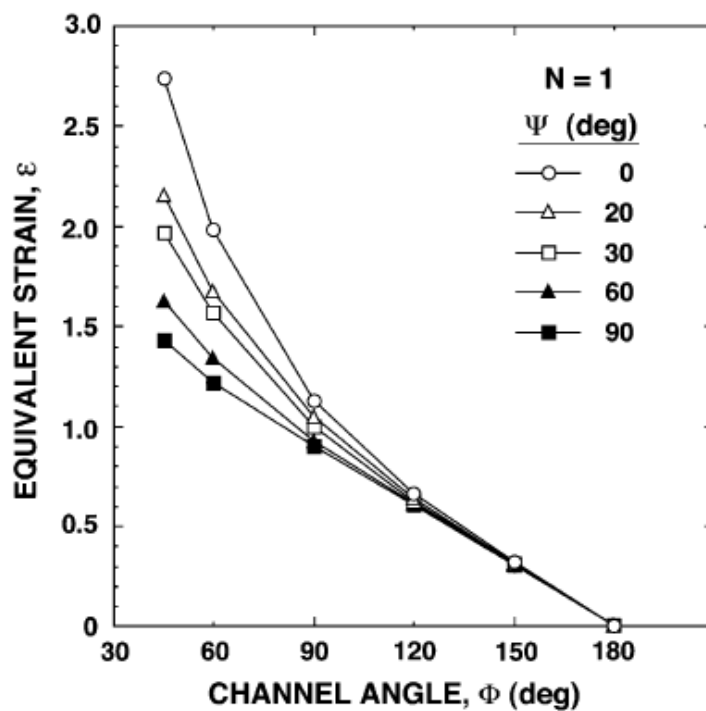


Figure 2.2 Various equivalent strain values for different channel angle and an outer arc of curvature (Furuno et al., 2004)

FE simulation revealed that a sharp corner die produces more uniform deformation than the round corner dies under frictionless condition. Thus, ECAP is presently being extensively examined because of its ability to produce fine-grained microstructures in metals. The effect of channel angle and its influence on deformation homogeneity and

strain distribution is significantly stated in the literature through finite element analysis (FEA). Ding et al. (2009) studied the effect of ECAP channel angle on the Grain Refinement of Magnesium from the study it was found that 90° channel angle exhibited lower grain size with respect to number of passes compare to die having channel angle 120°. Also, the study revealed that the fine grain structure and improved tensile strength can be obtained by using reduced ECAP processing temperature. Kočiško et al. (2014) investigated the influence of ECAP geometry on the effective strain distribution through FEM simulation by considering  $\phi = 90^\circ, 100^\circ, 110^\circ$  a  $120^\circ$ , outer corner angle ( $\psi$ ) and inner corner angle ( $r$ ) were being varied. The results from simulations have indicated that if the outer corner angle increases, mean effective strain decreases. After two ECAP passes (route C). Han et al. (2009) examine the effect of die geometry on the variations of normal and shear deformations with a deformation rate tensor. The study concludes that maximum shear deformation was activated in the region near the line of intersection of the two die channels in die with a lower curvature angle ( $\Psi < 48^\circ$ ). For different channel angle ( $\Phi$ ) and outer arc of curvature ( $\Psi$ ), the variation in equivalent strain is represented in figure 2.2. Reports of all theoretical simulations do not give sufficient details of its effect on mechanical properties and corrosion behaviour of the workpiece. The experimental study on the effect of channel angle is not yet reported, and therefore, our work aims to accomplish the research gap. In our present work, an attempt has been made to study the deformation behaviour of AZ80 Mg alloy by pressing the sample through two different channel angles ( $\phi$ ) 90° and 110° by treating corner angle ( $\psi$ ) 30° as constant in both cases. Further, a study of microstructure, mechanical properties and corrosion behaviour of AZ80 and AZ91 magnesium alloys after ECAP were reported and discussed in the results and discussion section.

### **2.5.2 Influence of processing temperature and routes on grain size during ECAP**

To improve mechanical properties several studies focused on grain refinement and processing routes during equal channel angular press. During the ECAP process, dynamic recrystallization easily occurs in many engineering materials including magnesium alloys. Arab and Akbarzadeh (2013) concluded that the average diameter of the grains is decreased by increasing the stress level or number of ECAP passes and fine grains can be obtained by processing below the recrystallization temperature of

magnesium alloys. Muralidhar Avvari et al. (2014) studied the microstructure evolution and mechanical properties of AZ80 Mg alloys. The average grain size was obtained of 7  $\mu\text{m}$ , 9.5  $\mu\text{m}$  and 11.2  $\mu\text{m}$  for the temperatures of 275°C, 300°C and 350°C respectively after 4 ECAP passes. The average grain size of the procured AZ80 alloy was 44.5  $\mu\text{m}$ . Lower processing temperature showed a significant effect on microstructure and mechanical properties of AZ80 alloy. Song-Jeng Huang et al. (2018) the effect of ECAP processing route on AZ61 magnesium alloys were investigated. The AZ61 alloy processed through Bc route with eight passes exhibited the smaller grain size, Avvari et al. (2014) introduced the new ECAP route called Route-R on wrought AZ61 magnesium alloys at 483K for grain refinement. Here the specimen is inverted to the original position in each ECAP passes, subsequently; the average grain size of the AZ61 alloy is reduced from 66 $\mu\text{m}$  to 16  $\mu\text{m}$ , 14.1  $\mu\text{m}$  and 10  $\mu\text{m}$  for Route A, route Bc and route R respectively and further the hardness of the material also increases in route R.

### **2.5.3 Impact of grain size on mechanical properties**

Recent studies have shown that grain refinement has major contribution to improve the mechanical properties of magnesium alloys. Few such studies were reviewed in this section. Here, Minárik et al. (2017) have reported microstructural evolution and mechanical properties of heat-treated and ECAPed Mg-4Y-3RE (WE43) by reducing ECAP processing temperature. The study achieved significant improvement in mechanical properties and obtained lower average grain size of ~ 340 nm after the eighth ECAP passes. Yuchun Yuan et al. (2013) worked to achieve an excellent combination of high strength and good ductility in the AZ91 Mg alloy. The approach involves equal channel angular pressing (ECAP) and subsequent aging. This approach is effective in accumulating dislocations and promoting the formation of large spherical precipitates during ECAP. The hierarchical grain refinement produced by the current approach extracted high strength and good ductility. Muralidhar et al. (2013) improved the mechanical properties of AZ31 Mg alloys after processing with ECAP owing to grain refinement. Yuchun et al. (2016) achieved high tensile strength and improved ductility in ZK60 Mg alloy by grain refinement and precipitate hardening through the use of annealing treatment and ECAP. Minárik et al. (2016) explored the grain refinement through ECAP for LAE442 Mg alloys. The as-cast and ECAPed

microstructure of average grain size of  $\sim 1$  mm and  $\sim 1.7$   $\mu\text{m}$  achieved respectively. Gopi et al. (2016) employed ECAP at below recrystallization temperature to prepare AM70 alloy with a mean grain size of  $1\mu\text{m}$ , and noticeable improvement in mechanical properties was observed. From that ECAP-2P samples exhibited highest strength and ductility compared to other samples, even though there was a decrease in UTS and ductility of 3 pass and 4 pass samples was observed as compared to as-cast and homogenized samples as shown in figure 2.3. Suh et al. (2016) studied on the enhancement of mechanical properties and reduced mechanical anisotropy of AZ31 Mg alloy sheet processed by ECAP study revealed that the grain size and texture change has a more dominant influence on the mechanical properties in AZ31 Mg sheet.

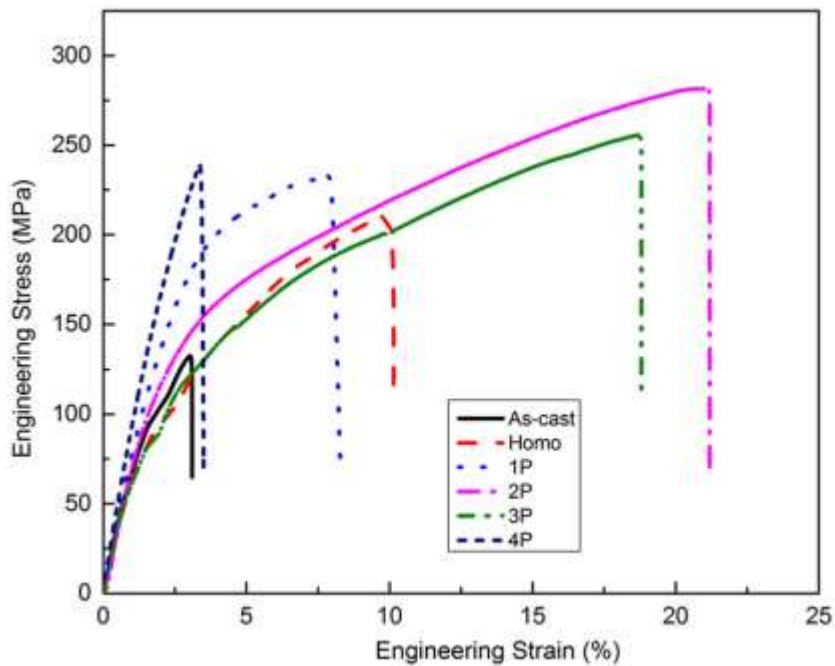


Fig. 2.3 Stress-strain curves for as-cast, homogenized, and ECAP-processed samples (Gopi et al., 2016)

Yuchun Yuan et al. (2016) have investigated the effect of heat treatment and deformation temperature on the mechanical properties of ECAP processed ZK60 magnesium alloy. The study reported high strength and good ductility by combining heat treatment with ECAP for ZK60 Mg alloy. Yoshifumi Ogushi et al. (2014) have studied the aging behaviour of equal channel angular processed AZ80 Mg alloys, their

study revealed the Microhardness and microstructure evolution showed that re-precipitation of the  $Mg_{17}Al_{12}$  phase appears during warm temperature in ECAP and aging in the AZ80 alloy at grain cores. This precipitation behaviour can potentially generate a significant contribution to the strength of the ultra-fine grains alloy.

#### 2.5.4 Observation from fracture study

Features observed on fractography of several tensile specimens. For as extruded condition at room temperature, cleavage facets and steps, as well as limited shallow dimples, are the predominant features observed on the fracture surfaces (Ding et al., 2010; Ehsan et al., 2015; Ehsan Mostaed et al., 2014; Xia Yu et al., 2015). The amount of observed dimples on the fracture surface of specimen increased steadily with the improved ductility. As the number of ECAP passes increases, particularly for 2P and 4P samples, the amount of plastic dimples observed on the fracture surface increased significantly and the observed dimples became deeper. With an increasing number of ECAP passes, the fracture surfaces were almost completely covered by ductile dimples and some tearing edges emerged (Ehsan Mostaed et al., 2014; Xia Yu et al., 2015). These features are believed to be a clear indication for an enhancement of plasticity after ECAP which was discussed and reported by Wang et al. (2016). Also, Muralidhar et al. (2016) discussed the fracture surface of ECAPed and as-received AZ61 Mg samples. From the study, it was observed that fractured surface of the as-received sample has few dimples of various sizes.

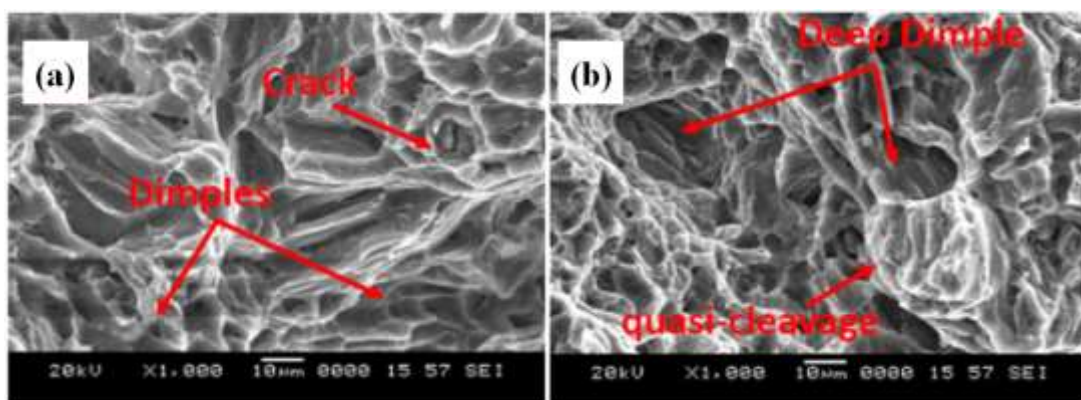


Figure 2.4 SEM-fractured images of tensile specimens of AZ61 alloy: (a) as received and (b) after four ECAP passes at 523 K (Muralidhar et al., 2016)

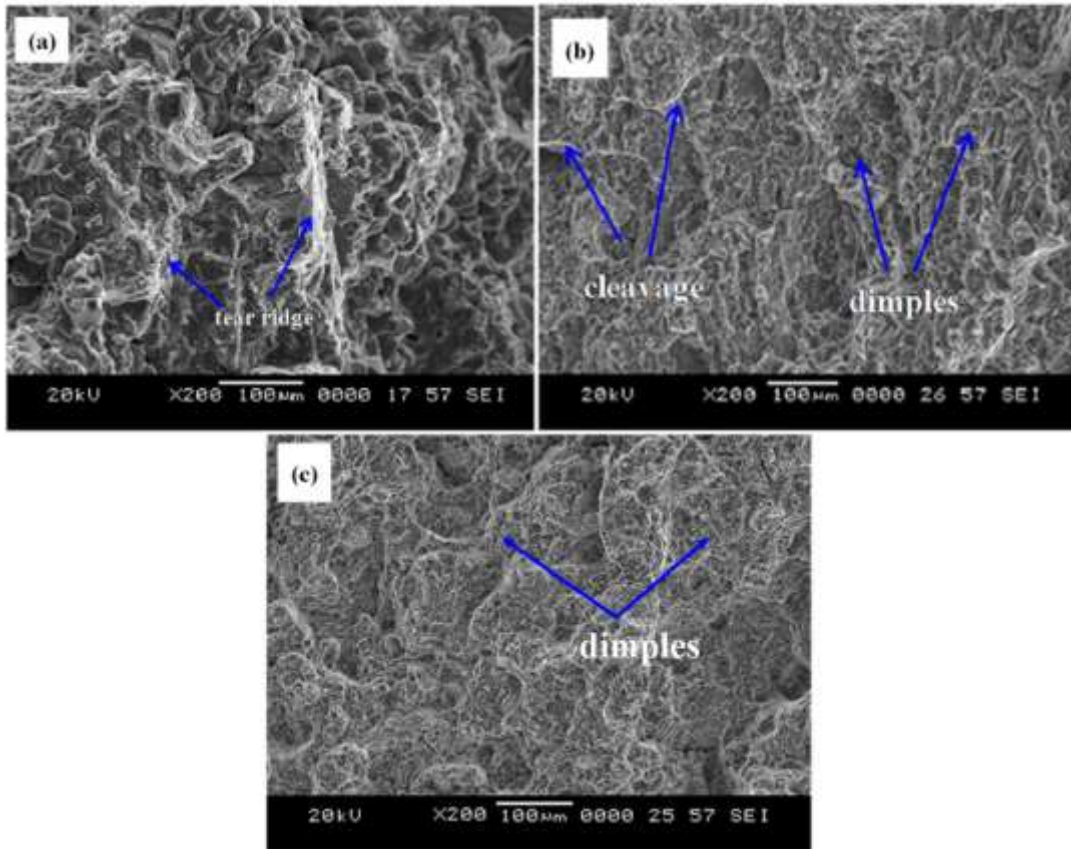


Figure 2.5 SEM images of fracture surfaces (a) as-cast, (b) 2P, (c) 4P samples (Gopi et al., 2016)

Correspondingly, shows that there are bright tearing ridges along the grain boundaries and few quasi cleavage fractures. Further, The AZ61 alloy specimen was deformed uniformly in the refined and equiaxed grain structure. This led to the higher tensile elongation observed for the ECAP-processed samples at 523 K, this is due to increased volume fraction of dimples. However, dimple sizes decreasing with increase in ECAP passes, which is attributed to grain refinement as well as strain hardening which was evidently shown by Muralidhar et al. (2016) presented in figure 2.4. Similarly, according to Gopi et al. (2016) the frequency of cleavage planes decreased as grain size reduced with higher number of ECAP passes and fewer cleavage planes were observed on the fracture surfaces for ECAP 4 pass AM70 sample. Initially, it looked like a mixed-mode of ductile and brittle fracture. After 2 passes, fracture surface with high fraction of fine and equiaxed dimples is observed as shown in figure 2.5.

### 2.5.5 Observation from XRD analysis

XRD is one of the experimental techniques used to determine unknown compounds and phases in a specimen. The following literature was used to explore the phases of magnesium samples through X-ray Diffraction. Naik et al. (2019) observed the x-ray diffraction patterns of AZ80 Mg alloy before and after ECAP processes. The XRD patterns of the as-received AZ80 Mg alloy and homogenized at 400 °C for 24 h and ECAPed AZ80 Mg alloys revealed two major peaks: one is for  $\alpha$ -Mg primary phase and another one for the  $\beta$ -Mg<sub>17</sub>Al<sub>12</sub> secondary phase. But in case of Mg-Al-Zn alloy has shown new peaks corresponding to the formation of the ternary phase and it appeared in 41.4°. Further, which is disappeared after homogenization treatment and ECAP process, this is due to diffusion annealing treatment and dynamic precipitation during the ECAP process respectively. Avvari et al. (2016) observed the XRD results of the AZ61 alloy after four passes at three different processing temperatures.

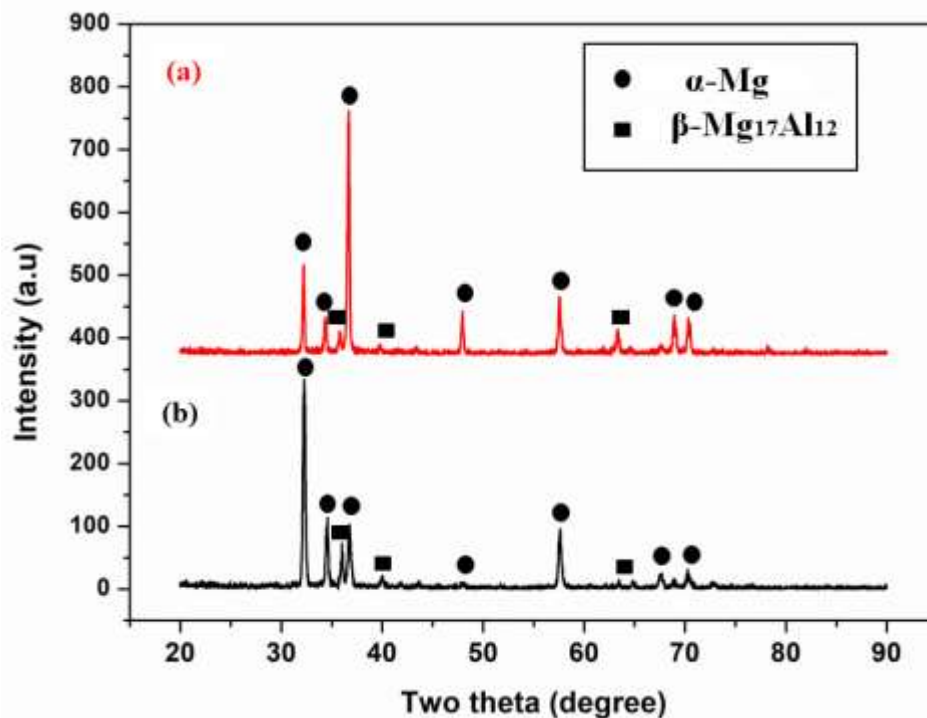


Figure 2.6. X-ray diffraction peaks of AZ91 Mg alloys a) As-received and b) ECAP-4P at 533K. (Naik et al., 2019)



The XRD results were compared with unprocessed specimens to understand the variation of intensity in the AZ61 alloy. There were no changes observed in the intensity of the peaks after ECAP processing at the temperature of 483 K. At a processing temperature of 523 K, and after four ECAP passes, the AZ61 specimens had lower intensities of the peaks when compared to as-received alloy. A similar observation was noticed by Gajanan et al. (2019) on AZ91 Mg alloy. Here, the peak intensity of ECAPed AZ91 Mg alloy was reduced when compared to as-received alloys as shown in figure 2.6, this is mainly due to induced plastic strain and grain refinement during ECAP. Gopi et al. (2016) shows the x-ray diffraction (XRD) patterns of as-cast and 4 pass ECAP-processed of AM70 samples. They reported decrease in intensity was observed for ECAP-4 pass samples. These changes are due to grain refinement occurring during ECAP processing.

## **2.6 CORROSION BEHAVIOR OF MAGNESIUM ALLOYS**

Corrosion susceptibility limits the use of Mg alloys in engineering applications, therefore it is essential to comprehend to improve the corrosion properties. The corrosion behaviour of Mg and its alloys depends on the medium which they are exposed and also it is strongly influenced by microstructure, alloying composition and secondary  $\beta$  phases. Hence, a detailed review of Mg corrosion behaviour was studied and reported in our work.

### **2.6.1 Effect of alloying elements on the corrosion behaviour of Magnesium alloy.**

In recent researches, it is found that in Mg-Al alloys solid solution  $Mg_{17}Al_{12}$  precipitates were found along the grain boundaries as a continuous phase or laminar structure. Which shows a passive behaviour over a wide pH range. Also, it is found that distribution of  $Mg_{17}Al_{12}$  improves the corrosion resistance of Mg-Al alloys. When unalloyed Mg gravimetric corrosion test of 3.5wt% NaCl was carried and it presented the highest mass loss about 196 mg/cm<sup>2</sup> after 16 h of immersion. On the other hand, addition of aluminium notably increases the corrosion resistance. Thus, 3 wt.% Al in AZ31 alloy reduced the mass loss up to 55.2 mg/cm<sup>2</sup> after 10 days of immersion.

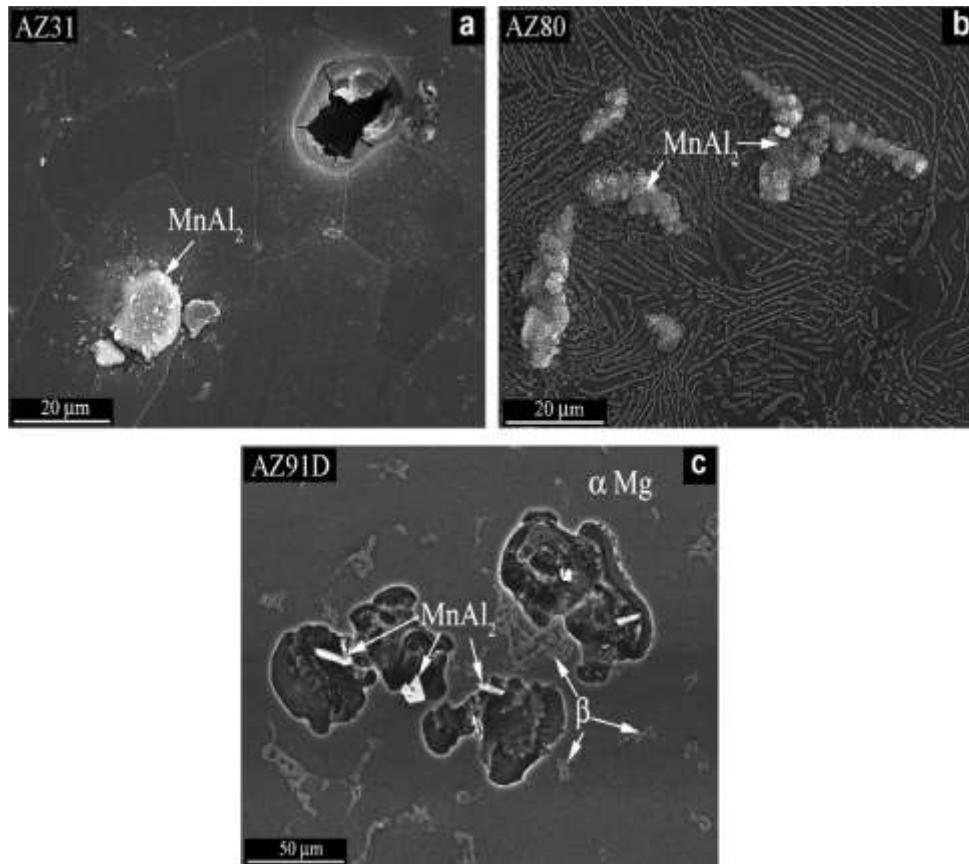


Figure 2.7. SEM micrographs of alloys immersed in 3.5 wt.% NaCl solution for 2 h: (a) AZ31; (b) AZ80 and (c) AZ91D (Pardo et al., 2008)

Nevertheless 8–9 wt.% Al in AZ80 and AZ91D alloys reduced the mass loss to 0.75 and 1.05 mg/cm<sup>2</sup> at the end of the test respectively. In early stages of corrosion for AZ31, AZ80 and AZ91D alloys when immersed in 3.5 wt.% NaCl revealed localized or pitting corrosion around MnAl<sub>2</sub> inclusions and  $\beta$ -phase interfaces due to a galvanic couple surrounded Mg matrix as shown in figure 2.7 (Pardo et al., 2008). Hamu et al. (2014) reported that grain size of the extruded Mg alloys are noticeably reduced by adding Ag to the Mg-6Zn and from the Potentiodynamic polarization (PD) measurements, linear polarization (LP) of DC polarization and Electrochemical impedance spectroscopy (EIS) tests revealed that the addition of Ag to the Mg-6Zn reduces the corrosion resistance (galvanic corrosion), this is due to the formation of micro-galvanic corrosion between  $\alpha$ -Mg and the precipitates of Mg–Ag (Mg<sub>54</sub>Ag<sub>17</sub>) of different electrochemical potentials. In another study, the addition of silicon to Mg-6Zn increased the corrosion resistance and they reported that the addition of silicon to Mg-

Zn-Mn improved the surface oxidation, but the addition of calcium to Mg-6Zn-5Si decreases the corrosion resistance. Addition of Si and Ca to Mg-6%Zn-1%Mn corrosion rate increases with increasing NaCl concentration due to the presence of aggressive chloride ion (Hamu et al., 2014).

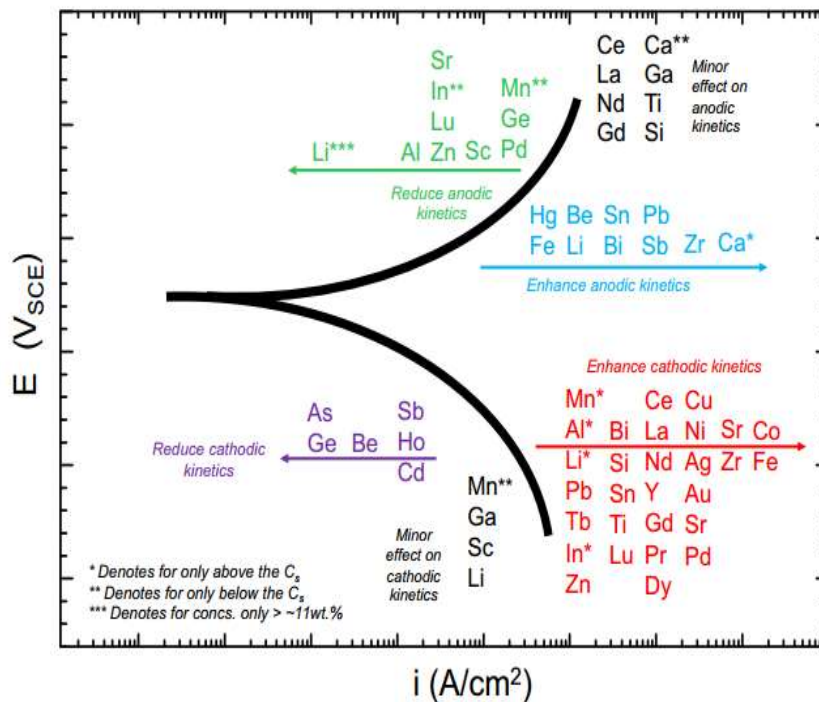


Figure 2.8 Representation of the electrochemical impact of alloying elements in magnesium alloy. (Esmaily et al., 2017)

Singh et al. (2015) compared the corrosion behaviour of Mg, AZ31 and AZ91 in 3.5% NaCl solution using electrochemical polarization and impedance measurements. From the study, it was observed that pure Mg has less corrosion rate compared to AZ91 and AZ31 alloys. Also, the AZ91 has less corrosion rate compared to AZ31 because of high aluminium contents. Since the majority of the magnesium alloys are produced by conventional casting process that results in casting defects, therefore, there is a strong reason to produce extruded Mg alloys. Researchers have attempted to develop an improved mechanical and corrosion-resistant extruded Mg-Zn and Mg-Zn-Ag alloy and the effect of Ag addition was investigated. The electrochemical impact of alloying elements is shown in Figure 2.8, which reveals that many alloying element additions

enhance the cathodic and anodic kinetics of the Mg alloys. Therefore during the development of new Mg alloys, the proper care should be taken for high purity Mg alloy, means percentage impurities such as Fe, Cu, Ni should be within the tolerance limit (Fe = 3.2%Mn max.; Ni = 50 ppm max.; and Cu = 400 ppm max.). This results in reduction of corrosion rates of Mg and its alloys.

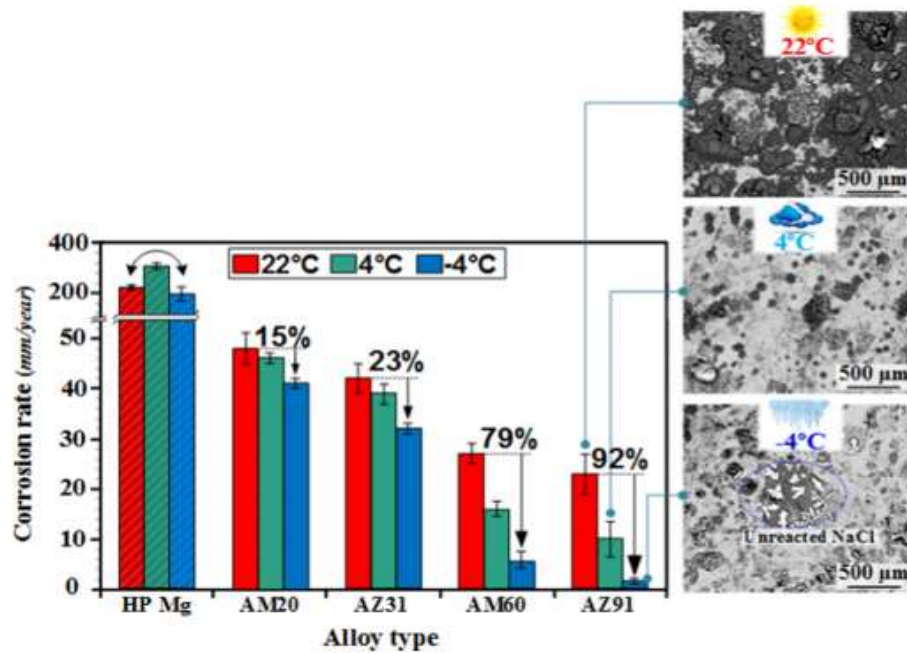


Figure 2.9 Corrosion rate of 99.97% Mg and four high pressure die casting Mg-Al alloys (RH: 95%, CO<sub>2</sub>: 400 ppm :NaCl: 70 μg/cm<sup>2</sup>, time: 504 h). (Esmaily et al., 2016)

Further Zn free AM60 Mg alloy has the lower tolerance limits of Fe, Ni, Cu this newly developed material shows higher corrosion resistance than AZ91C (Makar et al., 1993). And also, distribution of secondary β phase (Mg<sub>17</sub>Al<sub>12</sub>) also plays a significant role in the corrosion of Mg alloys (Guo et al., 2010). The electrochemical test confirmed that increase in Zinc (Zn) content from 2 to 6% in Mg-10Gd-xZn alloys, reduces the corrosion resistance due to presence of secondary phase at grain boundary. Which causes micro galvanic corrosion (Raman et al., 2004). Esmaily et al. (2016) have investigated the contribution of Al content in Mg alloys at three different temperatures. Which revealed that corrosion resistance of the alloys increased strongly with increasing Al %. The temperature effects on pure Mg have shown no clear correlation between the corrosion rate and temperature. In contrast, AM20 alloys exhibited, 15%

decrease in corrosion rate by lowering the exposure temperature from 22 to  $-4\text{ }^{\circ}\text{C}$ , and decrease in temperature resulted in 92% decrease of corrosion rate in AZ91D alloy, presented in Figure 2.9. Esmaily et al. (2016) strongly described the corrosive nature of NaCl in the presence of  $\text{CO}_2$  at  $-4\text{ }^{\circ}\text{C}$ . The corrosion evidence was identified with an increase of salt (NaCl) addition, detailed in the morphology of the corroded surface of AM50 as shown in figure 2.10. Pawar et al. (2017) observed microscopic filiform-like corrosion in AZ31 Mg sheets with 3.5% NaCl solution, as a result, localized pits were identified initially at the cathodic-intermetallic sites and the surrounding Mg matrix. After 2 h of immersion, it was observed the dendrite arms as shown in Figure. 2.11 (a).

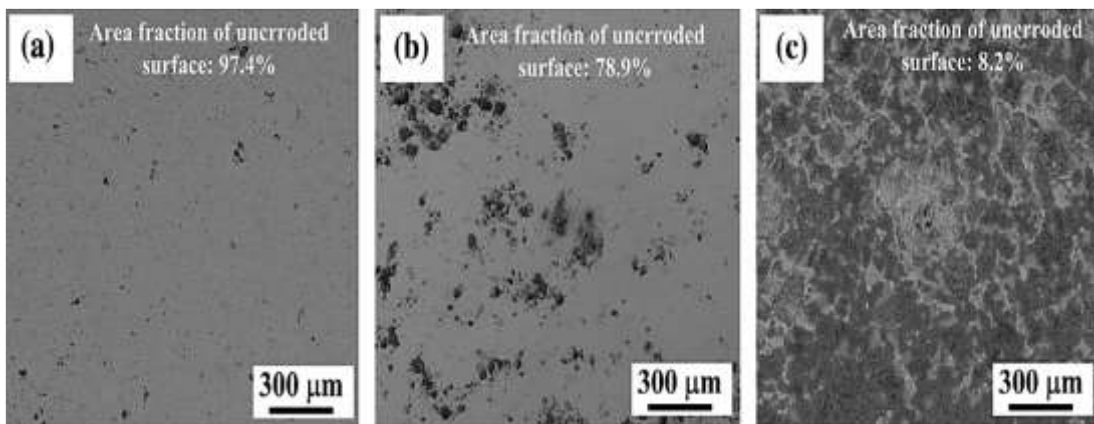


Figure 2.10 Corrosion morphology of alloy AM50 of  $4^{\circ}\text{C}$ , 672 h, with 400 ppm  $\text{CO}_2$  (a) No NaCl, (b)  $14\ \mu\text{g}/\text{cm}^2$  NaCl (c)  $70\ \mu\text{g}/\text{cm}^2$  NaCl (Esmaily et al., 2016).

The dendrite arms consist of Mg matrix preferentially corrode, this is anodic and highly prone to corrosion. Filiform-like corrosion reduced at the interdendritic, grain boundaries because these interdendritic and grain boundaries have quite high Aluminum (Al) and Zinc (Zn) contents compared to the dendrite arms concluded from the SEM and EDS study. This makes them relatively resistant to corrosion. Also author made an attempt to measure corrosion depth from the top surface. Type A and Type B grains showed a corrosion depth of  $\sim 35\ \mu\text{m}$  and  $\sim 55\ \mu\text{m}$  respectively shown in Figure 2.11 b). The study noticed that the corrosion depth varied significantly with immersion time (Pawar et al., 2017).

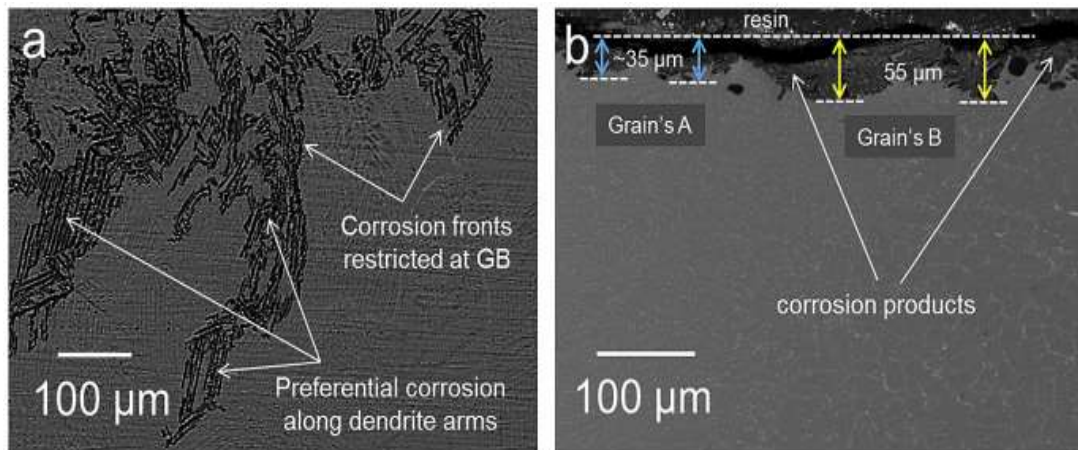


Figure 2.11 SEM images of the corroded alloy specimen after immersion in 3.5% NaCl. (a) The top view after 2 h. b) The transverse section after 2 h. (Pawar et al., 2017)

### 2.6.2 Effect of environment on corrosion behaviour of Mg alloys

Some of the researchers reported corrosion behaviour in the various environment of coarse-grained Mg-based alloys in literature. In order to understand the performance of magnesium alloy in aqueous media and to investigate the electrochemical properties of Mg alloys. Abbasi et al. (2017) studied the corrosion behaviour of pure magnesium and AZ31 magnesium alloy in electrolyte containing different concentrations of sodium chloride and pH. 3.5, 0.3 and 0.03 wt % of NaCl salt has been utilized in immersion. It was found that corrosion rate is higher and open-circuit potential was more negative at higher chloride ion concentration in each pH, and also the same trend is observed at lower pH for each chloride ion concentration in corrosion rate and open circuit potential. Indeed, solution pH value follows an inverse relationship with alloys corrosion rate in that solution and by increasing pH. Prondziono et al. (2010) examined the electrochemical corrosion of AZ31 alloy after casting and metal forming in NaCl solutions. These alloys tested in various concentrations of chlorine ions. The tests were carried out in 0.01, 0.2, 0.6, 1.0 and 2.0 M NaCl. The study revealed that corrosion resistance of AZ31 magnesium alloy decrease with increasing of chlorine ions concentration. Some more literature review on corrosion of Magnesium alloys has been summarized and presented in Table 2.1. However, to the best of the authors' knowledge the influence of different corrosion environment on the ECAPed Mg alloys have not been previously reported in the literature. In the current research work,

wrought AZ80 Mg alloys were used to comprehend the electrochemical corrosion behaviour of coarse-grained and fine-grained Mg alloys in different concentration of NaCl solution as well as in marine environment.

## **2.7 CORROSION BEHAVIOR OF ECAPed MAGNESIUM ALLOYS**

Few publications of corrosion behaviour of UFG structured Mg alloys have reported that grain refinement reduces the corrosion rate for AZ31, AZ91D, ZK60, AM70 and AE21 Mg alloy in NaCl solution (Song et al., 2010). Hence, the corrosion behaviour of equal channel angular processed magnesium alloy has been discussed in the following sections.

### **2.7.1 Effect of grain refinement on corrosion behavior.**

In material strengthening process of severe plastic deformation particularly ECAP can obtain the fine-grained Mg alloys. Due to a decrease in grain size and uniform distribution of secondary phase  $\beta$  particles leads to decrease of localized or pitting corrosion. ECAPed material has a higher corrosion resistance than conventional extrusion evidently discussed by Birbilis et al. (2010). Furthermore, twins which occur during casting or extrusion in microstructure decreases the corrosion resistance therefore for a new generation of alloys need to reduce the twins in the microstructure Gray et al. (2002). Finally with a limited percentage of impurities in alloys, modifying the microstructure through ECAP can develop new application-oriented Mg alloys with higher corrosion resistance than conventional Mg alloys. Accordingly corrosion results of ECAPed pure Mg alloys have discussed, Dan Song et al. (2010) refined the grain size of pure Mg of 800-1500 $\mu\text{m}$  to 50-100 $\mu\text{m}$  at 573K after first, fourth and sixth passes of ECAP. Subsequently, studied the effect on corrosion of ECAPed pure Mg through electrochemical corrosion analyzer with 3.5wt% NaCl solution. The open-circuit potential values were observed for 600s shown in Fig 2.12 (a), it is revealed that OCP of ECAPed pure Mg alloys takes less time to take top OCP value compare to un-ECAPed pure Mg alloys because of energetic crystalline defects which have more nucleation sites and comparatively it is much easier to form  $\text{Mg}(\text{OH})_2$  than the pure Mg.

Fig 2.12 (b) shows the potential versus current density polarization curve of the samples after stabilizing the OCP values. From the experimental results, it was cleared that the ECAPed pure Mg has less corrosion resistance than as-cast pure Mg. Furthermore, the author had studied the EIS test to understand the electrochemical characteristics during 6 h of immersion of ECAPed and un-ECAPed pure Mg. It is revealed that Nyquist plots of impedance spectra of as-cast and ECAPed pure Mg samples in 3.5wt% NaCl the diameters of capacitance arcs of ECAPed pure Mg are much smaller than the as-cast pure Mg as shown in Figure 2.12 (c). Therefore ECAPed pure Mg with more number of passes processed sample found smaller capacitance arcs it corresponds to decrease in corrosion resistance. Also the corrosion resistance of the samples with respect to immersion time of about 6 h shown with equivalent circuit in Figure 2.12 (d). From the graph it is understood that the pure Mg has higher corrosion resistance than the ECAPed samples. It is also found that the corrosion resistance of the samples decreased with increasing the immersion time. The poor resistance of the ECAPed samples is due to the defects like energetic grain or subgrain boundaries and dislocations present no protection which activates the drastic corrosion reaction. Therefore the ECAPed pure Mg is erodible than as-cast Mg. Hence consequent annealing at below recrystallization temperature is useful to improve corrosion resistance of ECAPed Mg, attributed to the decrease of crystalline defects or dislocations. ECAPed pure Mg can be anticipated to obtain better corrosion resistance than coarse-grained or as-cast Mg with its excellent mechanical properties. Unfortunately similar results of reduction in corrosion resistance of ECAPed ZK60 Mg alloys were observed in aqueous NaCl solution. The corrosion resistance of ultra-fine grained ECAPed ZE41A alloy increases in HCl aqueous solution but the same alloy has shown decreased corrosion resistance in NaOH aqueous solution Shen et al. (2012). Fortunately, some of the researchers have published the corrosion tendency of ECAPed Mg alloys in noble side; which offers important step toward corrosion study of Mg alloys after ECAP. The ECAPed Mg alloy with more number of passes attains higher electrochemical activity and the increased corrosion tendency, thus more easily forms oxidation product in various corrosive environment. This oxidation product with improved adhesion force can make ECAPed Mg alloy from SPD become more corrosion-resistant. Vratna et al. (2015) Studied the electrochemical corrosion behaviour of AZ31 magnesium alloy processed by extrusion and equal



channel angular pressing. As a result, material after extrusion offers more corrosion nucleation sites, but UFG microstructure causes that only smaller clusters of corrosion products fall off the surface.

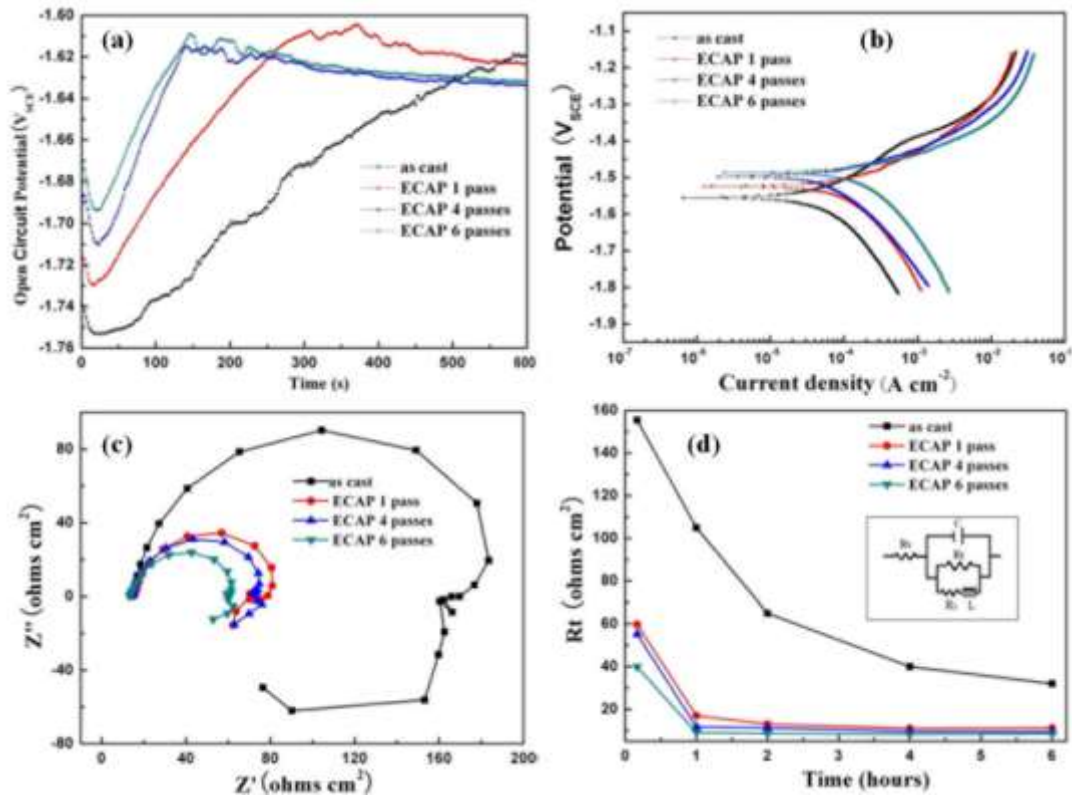


Figure 2.12. Pure Mg/as-cast and ECAPed alloys after immersion in 3.5 wt.% NaCl solution. a) OCP curves b) Polarization curves c) Nyquist plots of impedance spectra immersed for 6 h. d) Fitted  $R_t$  value curves in different immersion periods. (Song et al., 2010)

The easier and faster corrosion protective layer restoration on the surface of UFG material after ECAP leads to enhanced corrosion resistance. The study on corrosion behaviour of ECAPed AM 70 Mg alloys has shown better corrosion resistance properties, here ECAP 3<sup>rd</sup> pass sample charge transfer resistance ( $R_t$ ) values improved by ~5.28 and ~3.72 times in comparison to as-cast and homogenized specimens respectively. This is due to ultra-refined microstructure and the formation of  $\beta$  phases (Gopi et al., 2017). Similar observation was identified on AE42 Mg alloys after 8 ECAP passes due to more stable and thicker corrosion layer by Minárik et al. (2012). Fan et al. (2013) observed corrosion resistance of the fourth passed ECAPed Mg alloy was

higher than the as-cast alloys but the eighth pass ECAPed alloys have shown poor result on Mg-12Al-0.7Si alloy, this obtained result is rather contradictory to above discussions.

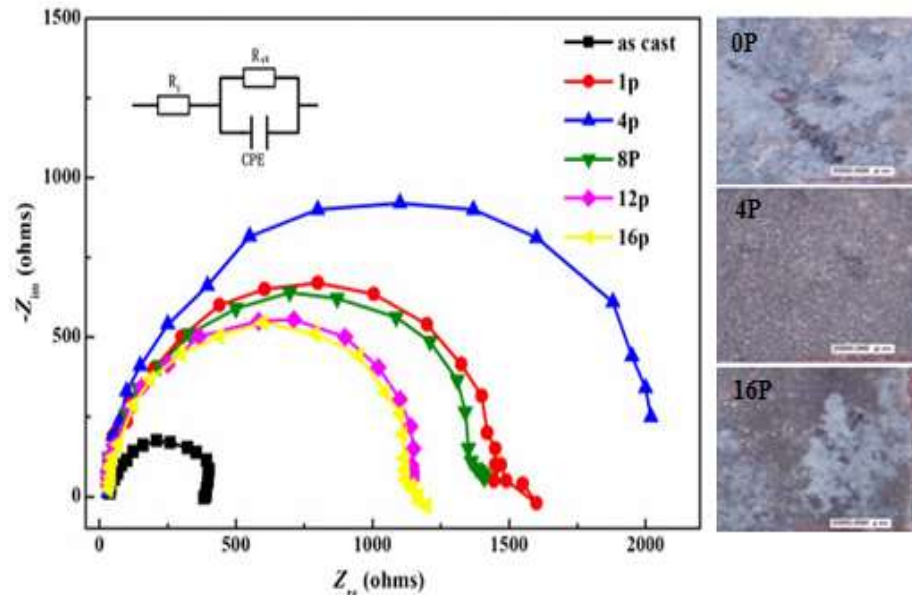


Figure 2.13 Nyquist plots of Mg-2Gd-1Y-1Zn-0.2Zr samples with various ECAP passes in 3.5 wt %NaCl solution (Jiang et al., 2014).

Jiang et al. (2014) also support the above conflicting situation, here author investigates the corrosion behaviour of ECAPed Mg-2Gd-1Y-1Zn-0.2Zr alloy with 3.5wt% NaCl solution and ECAP passes up to 12 passes. The study reveals, the corrosion rate of the ECAPed Magnesium alloy with fine-grained significantly decreased when it compared to the as-cast alloy. This means that grain refinement can inhibit micro-galvanic reactions and hindrance pitting corrosion. The ECAPed alloy with fourth pass showed lower corrosion current density and higher resistance to corrosion. But alloy processed twelfth pass shown lower corrosion resistance due to gradual loss of barrier effect of intergranular phases as shown in Figure 2.13. According to Hamu et al. (2009) fine grain size creates a number of grain boundaries which act as a corrosion barrier and also smaller grain size increases wettability and bioactivity of AZ31 Mg alloy. Hence the rapid bio-mineralization achieved in ECAPed samples helped to reduce the degradation of AZ31 Mg alloy. Gu et al. (2011) have checked the effect of back pressure in ECAP processing of AZ31 alloy on corrosion resistance. With or without

back pressure, ECAP extruded sample exhibited closer corrosion rate between them. The ECAP with backpressure appeared to be an efficient method to improve the mechanical property of Mg alloy without a considerable reduction in corrosion resistance. Zhang et al. (2013) worked on ZE41A, rare earth containing Mg alloys to study the charge transfer resistance after multi-pass of ECAP at 603K for 60 passes. This number of ECAP passes resulted the association of corrosion potential toward the noble direction. Which shows evidence of lower corrosion current density for ultra-fine ZE41A Magnesium alloy immersed in Hank's solution. The corrosion current density ( $i_{\text{corr}}$ ) of the ECAPed sample is minimum, results in low corrosion rate also from potentiodynamic polarization test obtained is  $8.1 \pm 1.1 \mu\text{A}/\text{cm}^2$  for ECAPed, which is lower than that of the as-cast ( $14.5 \pm 1.5 \mu\text{A}/\text{cm}^2$ ) (Junyi Zhang et al., 2016). Gopi et al. (2017) have studied corrosion properties of AM70 magnesium alloy processed by equal channel angular pressing. ECAP 4 pass sample showed decreased corrosion resistance due to increase in dislocation density with more ECAP passes which resulted in dislocations accumulation and consequently storing abundant internal energy like energetic grain boundaries which are more prone to corrosion. Mostaed et al. (2014) Ultra-fine grained ZK60 Mg alloy was obtained by multi-pass equal channel angular pressing at different temperatures of 250°C, 200°C and 150°C. Microstructural observations showed a significant grain refinement after ECAP, leading to an equiaxed and ultrafine grain (UFG) structure with an average grain size of 600nm. Open circuit potential, potentiodynamic and weight loss measurements in a phosphate buffer solution electrolyte revealed an improved corrosion resistance of UFG alloy compared to extruded material, stemming from a shift of corrosion regime from localized pitting in the as-received sample to a more uniform corrosion mode with reduced localized attack in ECAP processed alloy. In addition, internal stress at 4<sup>th</sup> pass of ECAPed ZK60 samples after aging is  $-1.52 \pm 0.23$  MPa (normal stress) and the stress in the 16<sup>th</sup> pass of ECAPed sample after aging was found  $-1.82 \pm 0.23$  MPa (normal stress). This result shows that the internal normal stress in the samples processed by equal channel angular press is compressive stress and also this proves the sample undergone more ECAP passes does accumulate larger compressive stress. The large compressive stress and secondary phases of the sample affect the corrosion resistance because which increases the activity of the Mg alloys likewise making it easier to corrode. Also, this study

demonstrates that aged samples have better corrosion resistance in comparison with the ECAP processed ZK60 alloys (Xin et al., 2015).

### **2.7.2 Influence of annealing and aging treatment on corrosion behaviour.**

The annealing and aging treatment play an effective role on improving the corrosion resistance of magnesium alloys. Recently, Yan et al. (2017) worked on ideal biodegradable implants of bone tissue engineering, here Mg-Zn alloys regarded as excellent biocompatibility materials based on its mechanical properties. But the corrosion resistance of Mg-xZn alloys was investigated by immersion and electrochemical tests in Ringer's solution, results revealed that by increasing Zn concentration increases the corrosion current, because micro-galvanic corrosion was caused by large-size intermetallic phases. Although solid solution treatment possibly reduces the intermetallic phase quantity. Remarkably, aging treatment could reduce the isolation of Zn and support the compactness and uniformity of corrosion product layer on the surface. This leads to the improvement of corrosion resistance. Additionally, have shown as-extruded Mg-6%Zn alloy (wt.%) aged for 72 h was harmless for biomedical applications. Further, Li et al. (2015) had discussed the significance of ECAP-aged Mg alloys, primarily author investigates the corrosion behaviour of ECAPed ZK60 Mg alloys by electrochemical test, ECAP processed with more number of passes shown higher current density ( $I_{corr}$ ) this shows alloy is susceptible to corrosion. Subsequently aged ECAPed Mg samples were examined, which reveals that ECAP aging can slightly improve the corrosion resistance of the Mg alloys and also enhance the performances due to stress relief and uniform dispersion of secondary particles. A similar investigation is also observed on AZ31 alloy. Here the aging of ECAPed AZ31 was carried at 220°C and 260°C prior to electrochemical corrosion test, the corrosion study showed that aging at 220°C has most favorable corrosion resistance compared to aging at 260°C and also investigation revealed that there is no significant effect of aging time (Shahar et al., 2017). The combination of thermo-mechanical treatment (ECAP), solid-solution strengthening, and precipitation strengthening of Mg alloys may lead to superior strengthening of Mg alloys. Therefore, the effort has been made to investigate the secondary phases and its effects on corrosion performance of AZ wrought Mg alloy after annealing and aging treatment.

### **2.7.3 Corrosion morphology studies of ECAPed Mg alloys**

Zhang et al. (2011) shown the typical corrosion morphologies of the as-cast and extruded magnesium alloys after 12 h immersion. The corroded surface of the as-cast alloy shown typical micro-galvanic corrosion features. The nature of corrosion of the extruded alloy seems to be remarkably different. Two kinds of corrosion morphologies were observed, the corroded surface area of the extruded Mg specimen exhibited both micro-galvanic corrosion morphology and pitting corrosion. Naik et al. (2019) observed that compared to as-received sample, the corrosion attack on ECAPed specimen is remarkably less. This indicates that decreasing the grain size of Mg alloy, the passivity of AZ91 alloy improves. Similar, Song et al. (2010) have observed the corrosion morphologies of as- received and ECAPed magnesium alloy. From the result it was concluded that ECAPed Mg alloys have thicker and more compact Mg(OH)<sub>2</sub> coating layer. Which act as a protective layer against corrosion.

## **2.8 PREVENTION OF ECAPed MAGNESIUM ALLOYS**

Every material is subject to corrosion with different corrosion rates in different environments. Corrosion can never be stopped but slowed down to technically acceptable rates. Therefore, corrosion protection deals with the finding of surface coating to prevent corrosion include a large set of attributes, such as corrosion resistance, environmental friendliness, cost and many more. The coating can be achieved through organic coating, inorganic coating and conversion coating. Accordingly for growing applications of Mg alloys, it is very important to study the prevention of corrosion of Mg and its alloys. There are some of the prevention techniques researchers used to prevent the corrosion of Mg alloys which are discussed in the following section.

### **2.8.1 Effect of coating on corrosion behaviour of ECAPed Mg alloys.**

Improvement of corrosion resistance of Mg alloys was reported after various coating for ECAPed Mg alloys in the literature. Recent studies by Ma, et al. (2008) reported that high-velocity oxygen fuel (HVOF) process gives the highest coating bond strength to the substrate and the highest coating density and thus has been proven to be more

preferable for making the metallic coatings. Further, Gnedenkov et al. (2015) have reported the conversion coating technique, Plasma Electrolytic Oxidation coating on magnesium alloys leads to improved wear and corrosion resistance. Jinghua Jiang et al. (2013) investigated the corrosion resistance of micro-arc oxidation coatings on coarse-grained and ultra-fine grained AZ91D Mg alloy. The effect of substrate microstructure on morphologies and corrosion resistance of the MAO coatings on AZ91D alloys were investigated by scanning electron microscopy observation, immersion tests and electrochemical impedance spectrum (EIS) measurements. In comparison, the MAO coating on the UFG Mg alloy has lower corrosion rate and larger oxide film resistance ( $R_f$ ). Three factors enhance corrosion resistance. The first is the MAO coating with uniform size and distribution of micro-pores due to homogenous micro-arc discharge. Secondly, the number of open holes decreases due to the finer  $\beta$ -phase after ECAP process. The last and most important one is the higher compactness and thickness of the coating on the UFG Mg alloy. This implies that the MAO coatings have great potential in surface protection of UFG Mg alloys. Pezzato et al. (2017) AZ91 magnesium alloy was treated with PEO process, worked with high current densities and short treatment times, using as electrolyte a base alkaline solution containing sodium hydroxide and sodium silicate. Then the porous surface of these samples was sealed with an aqueous solution containing lanthanum nitrate: this sealing process improved the corrosion resistance of PEO coated samples. Pardo et al. (2009) reported the thermal sprayed Al-coatings on AZ31, AZ80 and AZ91D Mg alloys in 3.5 wt.% NaCl solution by electrochemical and gravimetric measurements. The changes in the morphology and corrosion behaviour of the Al-coatings induced by a cold-pressing post-treatment were also examined. Which produced more compact Al-coatings with better bonding at the substrate/coating interface and higher corrosion resistance regardless of the nature of the magnesium alloy. However, the information on the corrosion behaviour of ECAPed Mg alloys after HVOF-coating is limited in the literature, mainly lacking for fine-grain Mg alloys. Therefore, in the current study, AZ magnesium alloy was selected and grain refinement was achieved by equal channel angular extrusion. Further, the effect of microstructural modification and HVOF-coating on corrosion behaviour was investigated and reported in the results and discussion section.

Table 2.1 Summary of corrosion behaviour of Magnesium alloys.

Reference	Mg-Based Alloys (x in wt%)	Corrosion					
		Media	Immersion Time (h)	Method /Test	Temp. & pH	Corrosion rate (mm/y)	Remark
Singh et al. (2015)	Mg	3.5 Wt% NaCl	3	Weight loss & Electrochemical	N/A	0.25	Weight loss measurement initially shows an increase in corrosion rate in order of Mg < AZ91 < AZ31 in 3.5% NaCl solution. After 3 h of immersion, the corrosion rate of AZ91 becomes much more than AZ31 alloy due to galvanic corrosion. Also from the Tafel plots, the corrosion resistance of the materials are given in order as AZ31 < AZ91 < Mg.
	AZ31					4.11	
	AZ91					1.16	
Hamu et al. (2006)	Mg–Zn–Ag	500 ml NaCl 3.5% saturated with Mg(OH) <sub>2</sub>	72	Immersion Test	N/A	N/A	Addition of silver (Ag) leads to grain refinement due to the formation of precipitates, increases hardness and reduces corrosion resistance.
Zhu et al. (2013)	AZ61+Mn+RE	3.5 Wt% NaCl	1-96	Electrochemical	Room temp. & 7 to 11	N/A	AZ61+Mn+RE have a significant effect on corrosion resistance.
	AZ61+Mn+RE	5 Wt% NaCl	72	Salt spray Test	N/A	N/A	
Jianghua et al. (2016)	AZ91	3.5 Wt% NaCl	150	Electrochemical	Room Temp. & N/A	0.77	Addition of Ti reduced the volume fraction of the β phases in AZ91. Also which shows corrosion resistance.
	AZ91+Ti					0.75	

Zhang et al. (2011)	Mg-5Y-7Gd-1Nd-0.5Zr	5 Wt% NaCl	2, 24, 60,108	Electrochemical	22±1°C N/A	N/A	Corrosion rates increases with immersion time
Xiaodong et al. (2017)	Mg-2Zn-0.5Ca-Y	Hank's Solution	120	Electrochemical	Room Temp. & N/A	$2.60 \times 10^{-7}$ g/h·mm <sup>2</sup>	The addition of more Y in the alloy leads to the formation of a second phase MgY. The second phase MgY can form many of corrosion micro-batteries, which accelerate the corrosion rate of the alloy.
			168			$2.78 \times 10^{-7}$ g/h mm <sup>2</sup>	
		3.5 wt% NaCl	N/A			N/A	
Bao et al. (2017)	AZ31B	Urban and Marine Environment	3 Years	Weight loss	Env. Temp & N/A	N/A	AZ91D Mg alloy had superior corrosion resistance properties
	AM60						
	AMX602						
	AZ91D						
Tong et al. (2016)	Mg-Zn-Ca-x(0,0.5,1)Ce/La	3.5 Wt% NaCl	1 to 7 days	Electrochemical	Room Temp. & N/A	0.82	Addition of Ce/La provides more fine secondary phase particles this makes more cathodic sites which accelerate the galvanic corrosion.
						3.12	
						1.73	
Zhao et al. (2016)	Mg-x(1,1,1,2,3)Sn-y(0.2, 0.5,1.5,0.5,0.5)Ca	1 L Hank's salt solution	250	Electrochemical	37°C & 7 to 10	0.31	The as-extruded Mg-1Sn-0.5Ca alloy has a homogenous microstructure, results in good mechanical properties and low corrosion rate, therefore this alloy might be potential for biomedical applications.
						0.27	
						0.40	
						0.30	
						0.31	
Zhao et al. (2017)	Mg-x(0.5,1,1.5,2.5)Sr	Hank's solution	500	Immersion & Electrochemical	37°C & N/A	0.29	As-extruded Mg-0.5Sr alloy had moderate mechanical properties and slow corrosion rate and good cytotoxicity
						0.33	
						0.40	
						0.52	



Yan et al. (2017)	Mg-x(6,14.5,25.3,40.3)Zn	Ringer's solution	96	Immersion & Electrochemical	37°C & N/A	0.72	Study revealed that by increasing Zinc (Zn) concentration reduced the corrosion potential but increased corrosion current.
						2.47	
						3.66	
						6.03	
Rajeshkumar et al. (2017)	Mg-x(2,4,6,8,4,4)Sb-x(0,0,0,0,2,4)Si	3.5 wt% NaCl solution	N/A	Electrochemical	Room Temp. & N/A	4.65	The electrochemical test reported that the corrosion resistance of Mg-Sb binary alloys reduced with an increase in Sb content. In contrast, Si additions improved the corrosion behavior of Mg-Sb-Si ternary alloys.
						5.70	
						7.21	
						9.08	
						5.20	
						4.06	
Wei et al. (2017)	AZ31	3.5 wt% NaCl solution	N/A	Electrochemical	Room Temp. & N/A	2.23	AZ91 magnesium alloys is resistant to corrosion
	AZ91					1.01	
	AZ111					1.33	
	AZ141					1.44	
Bakhsheshirad et al. (2016)	Mg-Zn-RE-x(0, 0.5, 1.5, 3, 6) Ca	0.9 wt% NaCl solution	168	Electrochemical	Room Temp. & 7 to 12.5	9.71	The quaternary Mg-Zn-RE-0.5Ca alloy acquires a lower corrosion current density ( $i_{cor}$ ) and higher charge transfer resistance ( $R_t$ ) compared to the ternary Mg-Zn-RE alloy.
						7.13	
						14.41	
						15.46	
						22.30	
Geng et al. (2016)	Mg-17Al-7Cu-3Zn-x(0,1,2,3)Gd	3 wt % potassium chloride (KCl) solution	0.5	Immersion & Electrochemical	25°C & N/A	11.01	The degradation rate of Mg-17Al-7Cu-3Zn-1Gd alloy reduced compared with the base alloy
						2.49	
						3.43	
						3.87	

Zhang et al. (2015)	Mg-x(1.7,2.8,3.8)Y-y(1.3,2.1,3)Zn-z(0.18,0.18,0.18)Zr	3.5 wt% NaCl solution	24	Electrochemical	25°C & N/A	0.60	As-extruded Mg-3.8Y-3Zn-0.18Zr alloy possess the maximum ultimate and yield strength of 420 MPa and 300 MPa, respectively, as well as it shown the best corrosion resistance
						0.55	
						0.51	
Hadzima, et al. (2008)	Mg-5Al-x(0,1,2,3,4)Zn	3.5 wt% NaCl solution	7	Electrochemical	Room Temp. & N/A	N/A	Mg-5Al alloys contain Zn shows lower corrosion and hydrogen evolution rate.

Table 2.2 Summary of the corrosion behavior of ECAPed Mg alloys.

Reference	Material	Equal Channel Angular Press (ECAP) of Mg alloys							Corrosion of ECAPed Mg alloy				
		$\Phi$ (deg)	$\Psi$ (deg)	Temp. (K)	Route	Speed (mm/min)	Number of pass	Grain size( $\mu\text{m}$ )	Media	Immersion Time (h)	Temp. (°C) & pH	Corrosion Rate (mm/y)	Remark
Song et al. (2010)	Pure Mg	90	N/A	573	N/A	30	6P	50-100	3.5 wt.% NaCl	6	Room Temp. & N/A	2.28	Pure Mg exhibits higher corrosion resistance than the ECAPed pure Mg.
Song et al. (2011)	AZ91D	90	N/A	523	C	60	1-12P	2-3	3.5 wt.% NaCl	48	Room Temp. & N/A	6.35	The corrosion rate increased with the increase of ECAP passes. The sample of 12 ECAP passes

													had average corrosion rate nearly 38 times larger than the as-cast alloy.
Minárik et al. (2013)	AE21 and AE42	90	0	453	Bc	50	8P	2-3	0.1 M NaCl solution	168	Room Temp. & 7	N/A	Corrosion resistance of AE21 was reduced after 8 passes of ECAP. But in AE42, observed that the corrosion resistance significantly higher.
Jiang et al. (2013)	AZ91D	90	0	523	C	30	16P	1-2	3.5wt.% NaCl solution	168	Room Temp. & 10-11	N/A	The Micro-arc oxidation (MAO) coating on the ECAPed AZ91D Mg alloy presents lower corrosion rate and the larger Rf value than that on the coarse-grained as-cast alloys.
Gopi et al. (2017)	AM70	110	20	548	Bc	60	4P	8	0.1 M wt% NaCl	N/A	Room Temp. & 7.5	N/A	Showed better corrosion resistance properties of ECAP at 3 pass sample and Rt values improved

													by ~ 5.28 and ~ 3.72 times in comparison to as-cast and homogenized samples
Minárik et al. (2012)	AE42	90	0	453-483	Bc	10 and 20	8P	8-10 & 3-4	0.1 M NaCl	168	Room Temp. & 7	N/A	The ECAPed AE42 Mg alloys showed substantially higher corrosion resistance.
Hoog et al. (2008)	Pure Mg	90	N/A	523	N/A	N/A	4P	2.35	0.1 M NaCl	N/A	Room Temp. & N/A	0.045	ECAP was shown to improve the corrosion and mechanical properties of pure Magnesium.
Fan et al. (2013)	Mg-12Al-0.7Si	90	20	573	Bc	1.5	2-8P	N/A	3.5% NaCl	0.055	Room Temp. & N/A	N/A	ECAP had a significant effect on corrosion for improving corrosion resistance of Mg-12Al-0.7Si magnesium alloy.
Taito Hosaka et al. (2017)	AZ31	120	60	423 & 573	Bc	240	8P	10-3	RPMI-1640	24	37 & 7.4	0.002	Immersion test results of AZ31 Magnesium alloy shows, Weight loss

													of ECAPed sample at 573K was smaller than the ECAPed sample at 473K.
Jiang et al. (2014)	Mg-2Gd-1Y-1Zn-0.2Zr	N/A	N/A	623	N/A	60	1-16P	N/A	3.5% NaCl	12	Room Temp. & N/A	N/A	Grain refinement through ECAP can inhibit general micro-galvanic reactions and hinder the pitting corrosion
Leiva et al. (2009)	ZK60	110	20	523	Bc	30	4P	0.7	phosphate buffer solution (PBS)	96	37 & 7.4	N/A	ECAP technique decreases the size of the second phase particles thus improving microstructure homogeneity, thereby decreasing the pitting corrosion effects.
Birbilis et al. (2010)	Pure Mg	90	N/A	523	Bc	N/A	8P	2.6	0.1M NaCl	N/A	N/A & <11	0.27	Smaller grain size had a lower current density
Xin et al. (2015)	ZK60	N/A	N/A	518	C	N/A	16P	N/A	3.5 wt.% NaCl	0.5	Room Temp. &	N/A	The corrosion behavior is improved after aging treatment.

											N/A		The improvement may be due to the reduction of stress and the better film Protection.
Hamu et al. (2009)	AZ31	90	N/A	623	Bc	350	4P	10-30	3.5 wt.% NaCl	N/A	Room Temp. & 10.5	N/A	Corrosion resistance after conventional Extrusion was higher than after the ECAP process.
Gu et al. (2011)	AZ31	N/A	N/A	573	N/A	24-30	4P	1.7	Hank's solution	480	37 ± 0.5 & N/A	0.73	ECAP with back pressure shows the improvement in mechanical properties without reducing the corrosion resistance.
Fan Zhang et al. (2013)	ZE41A	N/A	N/A	603	N/A	N/A	8,16,60P	2.5	250ml Hank's solution	1,96,192	Room Temp. & N/A	0.009	Observed decrement of corrosion current density for ultrafine-grained ZE41A Mg alloy immersed in Hank's solution.
Sunil et al. (2016)	AZ31	120	N/A	573	Bc	N/A	4P	1-5	saturate d simulate	72	Room Temp. &	0.22	ECAPed samples helped to reduce the

									d body fluid (SBF 5x)		N/A		degradation of AZ31 Mg alloy.
Zhang et al. (2016)	Mg-Gd-Nd-Zn-Zr	90	37	648	Bc	24	4P	2.5	simulated body fluid (SBF)	240	37 & N/A	0.36	The bio-corrosion resistance of ECAPed sample in simulated body fluid (SBF) was improved apparently.
Hadzima et al. (2018)	AZ80	90	N/A	623	Bc	N/A	8P	300-3	0.1M NaCl	0-96	22 & N/A	N/A	Enhanced electrochemical properties were found in the ultrafine-grained ECAP specimen as compared to its coarse-grained.
Vrátná et al. (2013)	AZ31	90	N/A	453	Bc	50	8P	1	0.1M NaCl	168	Room Temp. & N/A	1.32	After immersion time of 168 h the specimen after ECAP exhibits superior corrosion resistance to the specimen after extrusion.

Alvarez et al. (2010)	AZ31	90	N/A	523	N/A	6	1P	4.5	phosphate-buffer solution (PBS)	2,24,48	N/A	N/A	The best corrosion behavior corresponds to the AZ31 alloy with the finest grain size in PBS.
Xie et al. (2017)	AZ61	90	0	623,673	N/A	N/A	8,16P	10	Distilled water	N/A	N/A	N/A	The as-cast AZ61 Magnesium alloys with about 6% Aluminum content have a great tendency to stress corrosion cracking in distilled water and the ECAPed processing increased the susceptibility to SCC at room temperature.



## **2.9 CONCLUDING REMARKS**

Through this literature review, an attempt is made to record the earlier work reported the effect of ECAP on microstructure, mechanical properties and corrosion behaviour in magnesium alloys. Reviewed the effect of heat treatment and various coating on as-cast and ECAPed Mg alloys. Also, impact of various environment on magnesium and ECAPed Mg alloys. However, it was observed that very limited works have been published in these areas as discussed in literature review. Therefore, there is a scope to study the effect of die parameters on microstructure, mechanical properties and corrosion behaviour of wrought AZ Mg alloys. Further enhancement of corrosion resistance of ECAPed AZ Mg alloys through annealing treatment and HVOF coating. Furthermore, corrosion inhibition of ECAPed AZ Mg alloy studies carried out in different corrosion environment.

## **2.10 RESEARCH GAP FROM LITERATURE SURVEY**

Based on the data collected through the current literature. We have acknowledged the research gaps between what existing research yields to study the effect of corrosion behaviour after equal channel pressing of wrought Mg alloys. The study summed up in the four following aspects that are as follows.

- Effect of different ECAP die angles on microstructure, mechanical properties and corrosion behaviour for wrought AZ Mg alloys need to investigate.
- Need to explore the effect of grain size reduction and secondary phases on corrosion behaviour of wrought AZ Mg alloys after ECAP and Post-ECAP process.
- The analysis is required for different concentration of NaCl solution and natural seawater to observe the corrosion effect on ECAPed AZ-Mg alloys.
- Need to study the corrosion behaviour of ECAPed AZ-Mg alloys after High Velocity Oxy-Fuel coating technique.

## **2.11 PROBLEM STATEMENT**

Literature review reveals that, microstructure, mechanical and corrosion properties of various Mg alloys processed through ECAP. However, it is noticed that no works have been reported on effect of die channel angle on microstructure, mechanical and corrosion behaviour of wrought AZ80/91 Mg alloys at three different temperature through ECAE with processing route-*R*. It is also noticed that limited works have been reported on

enhancement of corrosion resistance through heat treatment and HVOF-316SS coating on ECAPed AZ80/91 Mg alloys. Therefore it was decided to carry out the ECAP of wrought AZ80/91 Mg alloy and subsequent characterization of the processed material through several techniques.

## **2.12 OBJECTIVES OF THE RESEARCH WORK**

Modern industrial applications with rapidly changing technology focus on light weight and high strength materials for processing wide variety of applications. Equal channel angular press of materials is one of the promising technique that could be develop a high strength and corrosion resistant material. In the recent year, researchers have effectively achieved grain refinement of various ferrous and non-ferrous alloys using ECAP in order to improve mechanical properties and corrosion behaviour of metals. However there is a wide scope to develop high strength and corrosion-resistant AZ Mg alloys using ECAP technique, as very limited work has been reported in this area. The present work utilizes the same principle introduced by Segal (1977) where an effort is made to analyse the effect of ECAP on microstructure, mechanical properties and corrosion behaviour of AZ Mg alloys. The current research work broadly aims to investigate the following objectives:

1. Perform experimental study to analyse the influence of equal channel angular extrusion die channel angles on the deformation homogeneity through processing route-R at three different temperatures.
2. Investigate the effect of microstructure on mechanical properties and corrosion behaviour of wrought AZ-Mg alloys subjected to equal channel angular extrusion technique.
3. Study the influence of annealing and aging treatment on the pitting corrosion resistance of coarse and fine-grained AZ Magnesium alloys.
4. Stainless steel coatings on the surface of ECAPed AZ Magnesium alloys using High-Velocity Oxygen-Fuel coating as a deposition technique to improve the corrosion performance.
5. Explore the effectiveness of corrosion inhibition of equal channel angular pressed AZ-Mg alloys in different concentration of NaCl solutions, as well as in the marine environment.

## CHAPTER 3

### EXPERIMENTAL WORK

#### 3.1 INTRODUCTION

This chapter summarizes the detail description of wrought AZ80/91 Magnesium alloys, its composition, properties, preparation of samples through Equal channel angular extrusion, characterization, mechanical and electrochemical corrosion testing. The experimental plan based on ECAP processing temperature and route-R. This chapter includes High Velocity Oxygen Fuel coating procedure, annealing and aging method of Mg alloys. Further, the chapter also explains the methodology adopted for measurement of grain size, microhardness, tensile strength and corrosion rate which is detailed in figure 3.16.

#### 3.2 WROUGHT AZ80/91 SERIES MAGNESIUM ALLOYS

Wrought AZ80 and AZ91 commercially available magnesium-based alloy, was selected as a work piece material because of its high strength and low cost when compared to other magnesium-based alloys. The Mg alloy was procured in the form of rod with dimensions 18mm diameter and 200 mm length, from Exclusive Magnesium Pvt. Limited, Hyderabad, India. The chemical composition of AZ Mg alloys, which has been verified by Energy-dispersive X-ray spectroscopy (EDS) analysis is presented in figure 3.1. Also, chemical composition presented along with the microstructure shown in figure 3.2 and 3.3. Further, material properties of as-received Mg alloys were measured and presented in table 3.1.

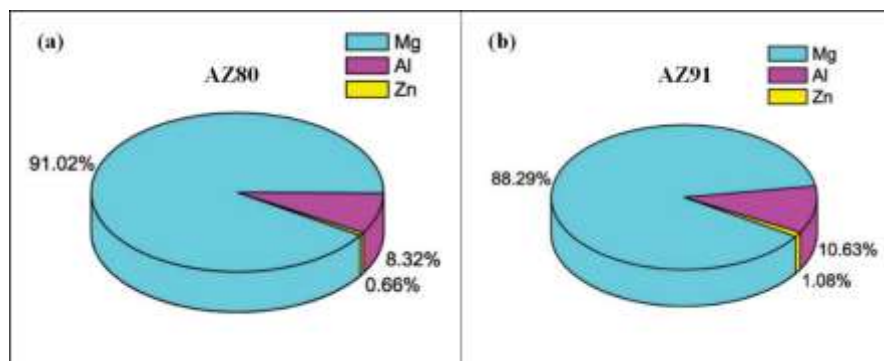


Figure 3.1 Chemical compositions for wrought AZ80 and AZ91 Mg alloys

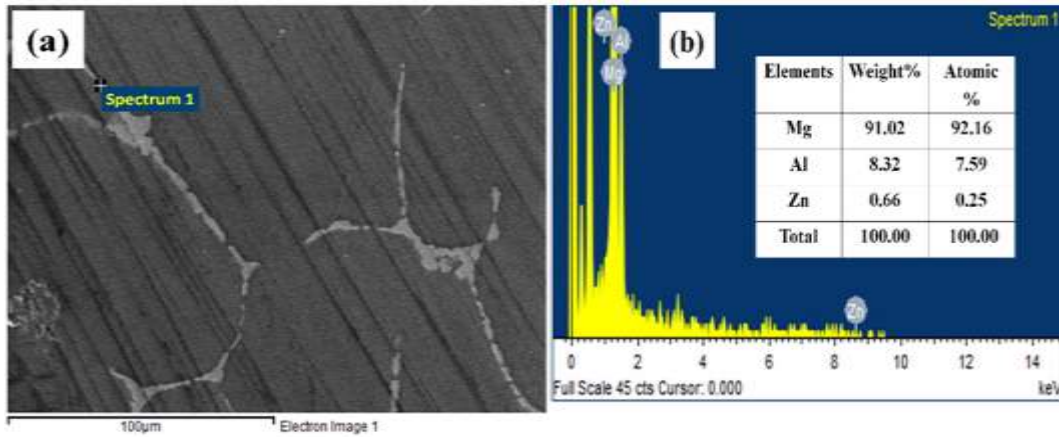


Figure 3.2 AZ80 Mg alloy a) Microstructure b) EDS results

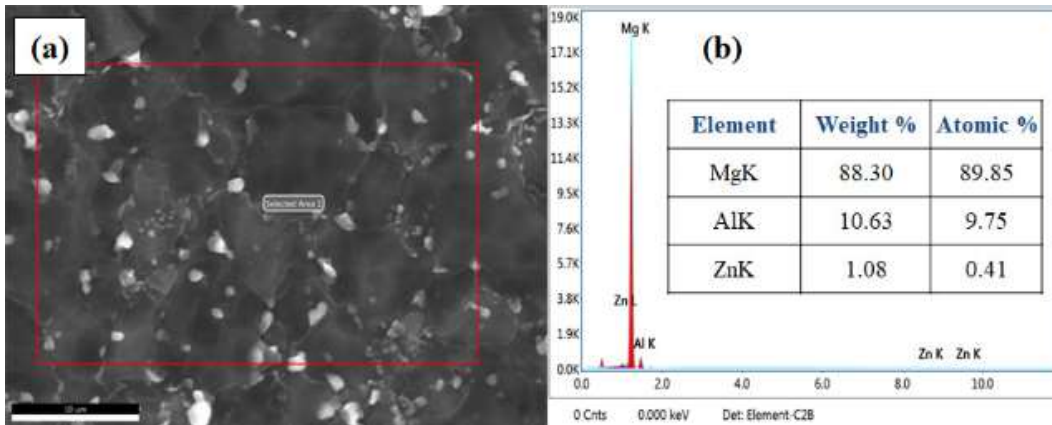


Figure 3.3 AZ91 Mg alloy a) Microstructure b) EDS results

Table 3.1 Material properties of as-received AZ80/91 Mg alloys

Materials	AZ80	AZ91
Properties		
Mean Grain Size ( $\mu\text{m}$ )	50.20	58.69
Microhardness (Hv)	64.58	68.52
Yield Strength (MPa)	329.13	308.68
Ultimate Tensile Strength (MPa)	401.15	372.74
Ductility (%)	6.64	7.84
Corrosion Potential- $E_{\text{corr}}$ (V)	-1.547	-1.539
Corrosion Current- $I_{\text{corr}}$ (mA)	0.297	0.263
Corrosion Rate (mm/y)	13.563	12.010

### 3.3 EQUAL CHANNEL ANGULAR EXTRUSION

Die-Material: Hot Die steel (HDS) was used for die making and properties of HDS material given in Table 3.2. The ECAE die design was done by using solid edge V.7 software and fabrication was carried out at Government Tool Room and Training Centre (GTTC) Baikampady, Mangalore, Karnataka, India. Figure 3.4 depicts the ECAE die having 90° and 110° channel angle and 30° corner angle.

Table.3.2 Properties of hot die steel H13 (Koneshlou et al., 2011)

Properties of Hot Die Steel	Density (g/cc)	Tensile strength (MPa)	Modulus of Elasticity (GPa)	Poisson's ratio	Melting Temperature (°C)
	7.8	1200-1590	215	0.27-0.3	1427

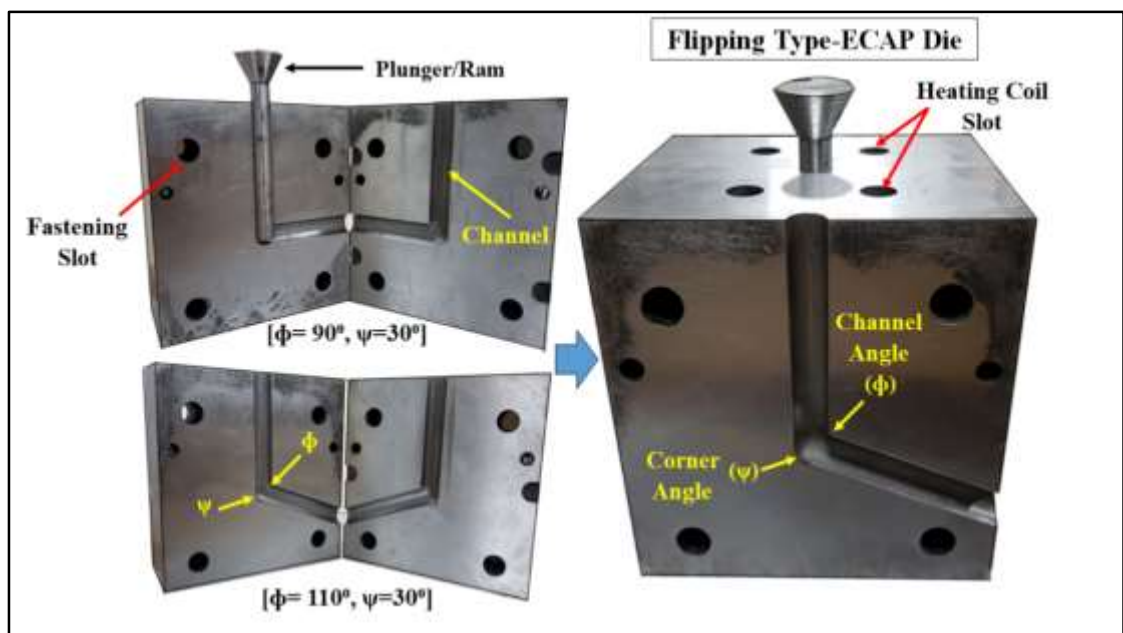


Figure 3.4 ECAE die having 90° and 110° channel angle and 30° corner angle. (Naik et al. Copyrights: Diary Number: 14668/2018-CO/L., Reg. No: L-79923/2018)

An equal channel angular extrusion thermo-mechanical apparatus is provided grain refinement to improve mechanical properties and corrosion resistance of magnesium alloys. ECAE is promising extrusion technique to achieve ultra-fine equiaxed grains

without changing the shape of workpiece. The extrusion die assembly having two angles such as channel angle ( $\phi$ ) and corner angle ( $\psi$ ) which decides the induced shear strain during ECAP. Current study focusses on effect of ECAE die angles on microstructure and mechanical properties of Mg alloys. According to the conditions die A has  $\phi= 90^\circ$ ,  $\psi = 30^\circ$ , the equivalent strain applied to the material at each pass was equal to 1.15. Calculated through equation 1.3, die B has  $\phi= 110^\circ$ ,  $\psi = 30^\circ$ , the equivalent strain applied to the material at each pass was equal to 0.9. (equation 1.3) Here corner angle ( $\psi$ ) kept constant to reduce the dead zone of material. On the other hand five basic routes available in literature. In the present study route *R* was considered to deform the material to achieve fine grain structure. Route *R*: specimen is inverted to the original position in each ECAP passes. The experimental setup of equal channel angular extrusion shown in Figure 3.5. During operation ECAP die (Fig.3.5) is placed on the base plate of UTM and plunger is aligned exactly to the centre of die where the specimen is placed inside the channel for pressing. Further, Die was homogeneously heated by 4 electrical resistance heaters, placed along the vertical channel. At the intersection of the channels, temperature was monitored throughout the process using thermocouples inserted in the die located near the intersection point. ECAP process was carried out at 533K, 598K and 663K three elevated temperatures. Firstly, the die is heated to the 533K and temperature is controlled by the temperature controller which is provided with the heating facility. The sample is placed in the die channel and needs to make sure that the temperature of the specimen also reached the 533K. A lubricant as Molybdenum disulphide ( $\text{MoS}_2$ ) was used to minimize the frictional effects between samples and die. After attaining the required temperature, the sample is pressed by applying a load at the rate of 1 mm/sec ram speed using plunger attached to the UTM for deformation of the specimen. The channels are intersected to impose the total strain on the material to get fine grain structure. This process is repeated by using route *R*, where the samples were inverted from its initial position between two successive passes as shown in figure 3.5. The processed samples after ECAP operation is shown in figure 3.6.

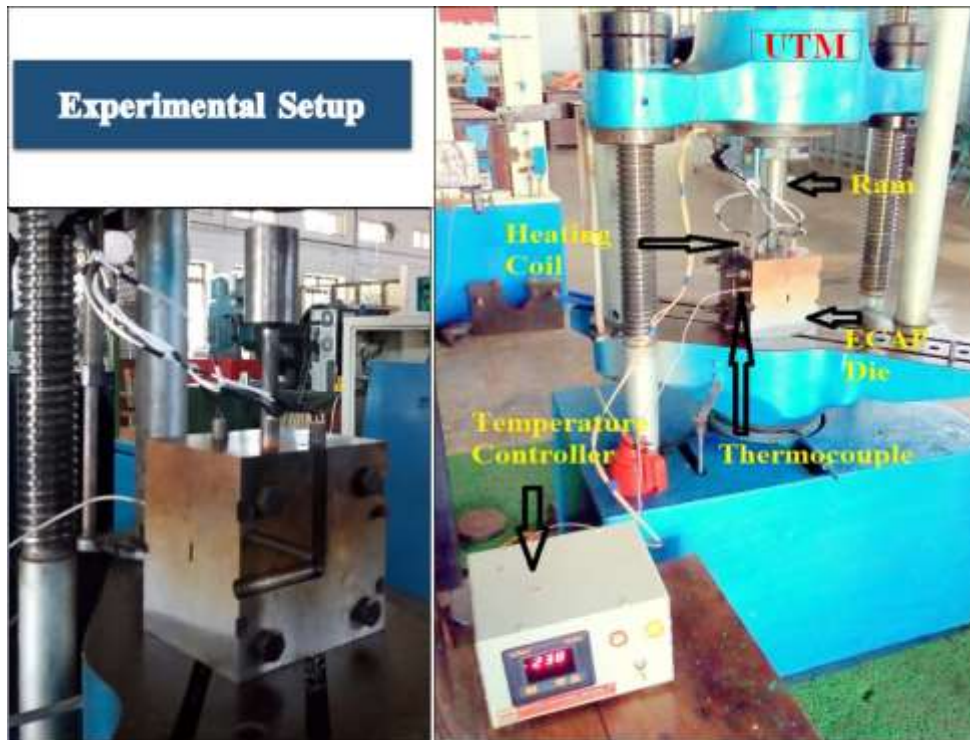


Figure 3.5 Equal Channel Angular Extrusion experimental setup

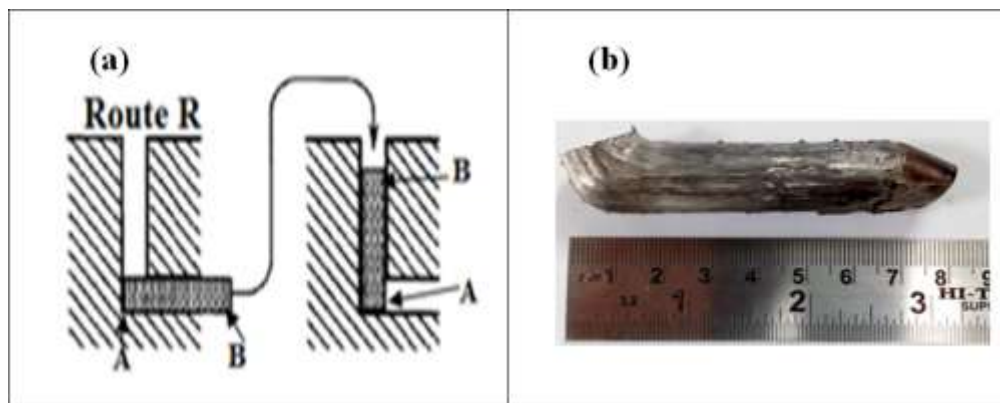


Figure 3.6 a) Route-R and b) ECAPed sample

### 3.4 SELECTION OF PROCESSING TEMPERATURE

ECAE process was carried out at 533K, 598K and 663K. Samples of 16 mm diameter and 80 mm in length were processed at temperatures varying from 65 °C (338K) to 260 °C (533K) and the samples are shown in figure 3.7. Sample processed at 60 °C temperature showed deeper surface cracks. However, at 130 °C (403K) and 195 °C (468K), deeper surface cracks were reduced as represented in figure 3.7. Further at 260

°C (533K) temperature processed a samples were showed with no surface cracks with a soaking time of 15 min and pressing speed of 1 mm/s as shown in figure 3.7. Therefore, 260 °C ( $0.4 \cdot T_m$ ) temperature was considered as initial temperature for processing the samples through ECAP process. It is difficult to deform magnesium at a lower temperature, due to hexagonal close-packed (HCP) structure with limited slip systems (Sun et al., 2007). Further, 0.5 times melting temperature of Mg alloys ( $T_m$ ) that is 325 °C (598K) and 0.6 times melting temperature of Mg alloys ( $T_m$ ) that is 390 °C (663K) were selected as processing temperature of equal channel angular extrusion process. Experimental conditions are summarized in table 3.3.

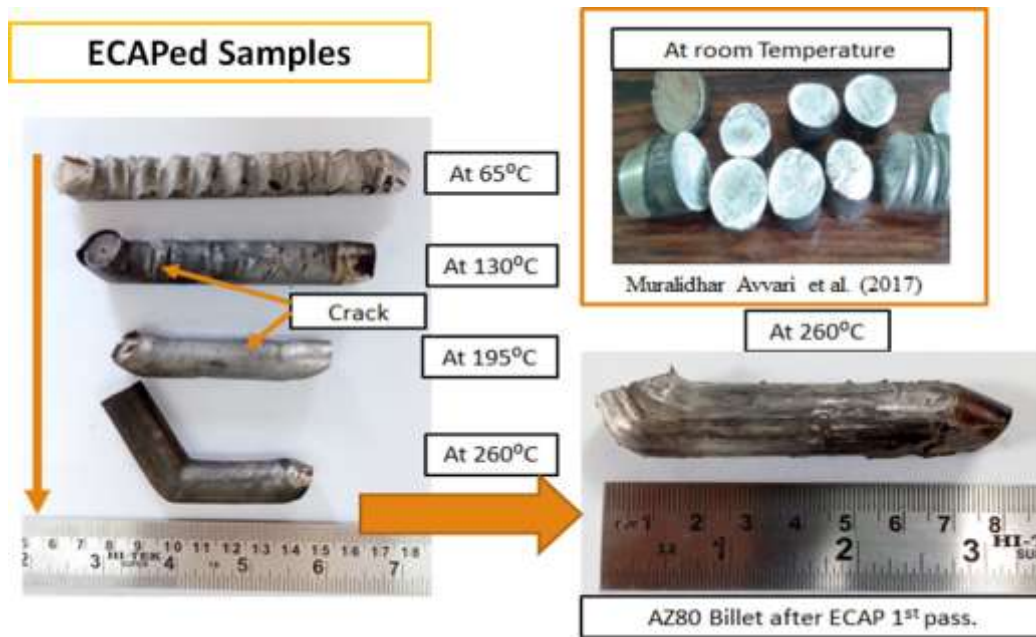


Fig 3.7 ECAPed samples processed through different temperature

Table 3.3 Experimental conditions

ECAP Die	Channel angle ( $\phi$ )	Corner angle ( $\psi$ )	Processing Route	Processing Temperature	Ram Speed	Material
A	90 °	30 °	R (reverse route)	533K, 598K, 663K	1mm/s	AZ80 and AZ91 Mg alloy
B	110 °					



### 3.5 MICROSTRUCTURAL CHARACTERIZATION

This section focuses on all characterization techniques of ECAPed magnesium alloys including all forms of microscopy and analysis especially microanalysis and surface analytical techniques. The methodology of microstructure analysis and phase identification are also discussed.

#### 3.5.1 Optical Microscope

Specimens for microstructure inspection were prepared by mechanical polishing with silicon carbide abrasive papers (grades of 400, 800, 1000, 1200, 1500, 2000) followed by cloth polishing using diamond paste and kerosene for obtaining mirror finish surface and finally cleaned with acetone. Further, Etching was carried on the polished surface for approximately 3 to 5 s, in a solution of 4.2g picric acid, 10ml acetic acid, 10 ml distilled water and 70ml ethanol for 3-5s (Naik et al., 2018). So that sample turns light brown in colour and washed with running distilled water and dried. Microstructures and elements distributions were observed and analysed using optical microscopy by image analyser facilitated BIOVIS material plus software, which is shown in figure 3.8 and average grain sizes were measured by linear intercepts method according to ASTM E-112. Same samples were observed under scanning electron microscope.



Figure 3.8 Optical Microscopy with BIOVIS material plus software

### 3.5.2 Scanning Electron Microscopy

Scanning electron microscope (SEM) equipped with energy dispersive spectroscopy (EDS) as shown in figure 3.9. Backscattered electron (BSE) detector coupled with the EDS allows for composition identification of materials. Scanning Electron Microscopy Model: JEOL JSM-6380LA from JEOL, USA, operated at 30kV; Magnification range-3,00,000 as shown in figure 3.9, which allows to study the microstructures and surface morphologies.



Figure 3.9 Scanning Electronic Microscopy equipped with EDS

### 3.5.3 X-Ray Diffraction

X-ray diffraction (XRD) is one of the primary techniques used for the characterisation of crystalline solids and determination of their structure or phases. XRD measurements are carried out in M/s Proto Manufacturing Ltd., CANADA make PROTO- iXRD MGR40 as shown in figure 3.10, wherein the analysis was carried out  $2\theta$ : angular range of  $20^\circ$  to  $90^\circ$  at a scanning speed of  $2^\circ/\text{min}$ . The XRD patterns obtained were analyzed with the help of PCPDFWIN software to identify the formation of primary, secondary and ternary phases.



Figure 3.10 X-ray diffraction operated at 20 mA and 30 kV with Cu- $\alpha$  radiation

### 3.6 MECHANICAL TESTING

The material strength measurements are obtained by standardized mechanical tests, which are described in this section. In this section not only covers details, principles, and practical aspects of the various tests, but also provides comprehensive reference to the standard procedures and sample geometries provided by the ASTM standards. As such, the section covers a methods used to measure materials strength behavior for a variety of engineering applications.

#### 3.6.1 Microhardness Test

Microhardness test is also performed on as-received heat-treated and some of the deformed or ECAPed samples. The measurements were carried out at a load of 100gm and dwell of 13 s the microhardness was calculated using the expression (Dieter and Bacon, 1986) given in Equation (3.1). Microhardness Model: MVH-S-AUTO from OMNI TECH, PUNE, INDIA. The experimental setup was shown in figure 3.11.

$$Hv = 1.854 \frac{F}{d^2} \quad (3.1)$$

Where,

$H_v$  = Vickers hardness of the sample,

$d$  = Mean of diagonals length of a squared pyramid and

$F$  = Applied load.

1.854 is the geometrical constant of the diamond pyramid.

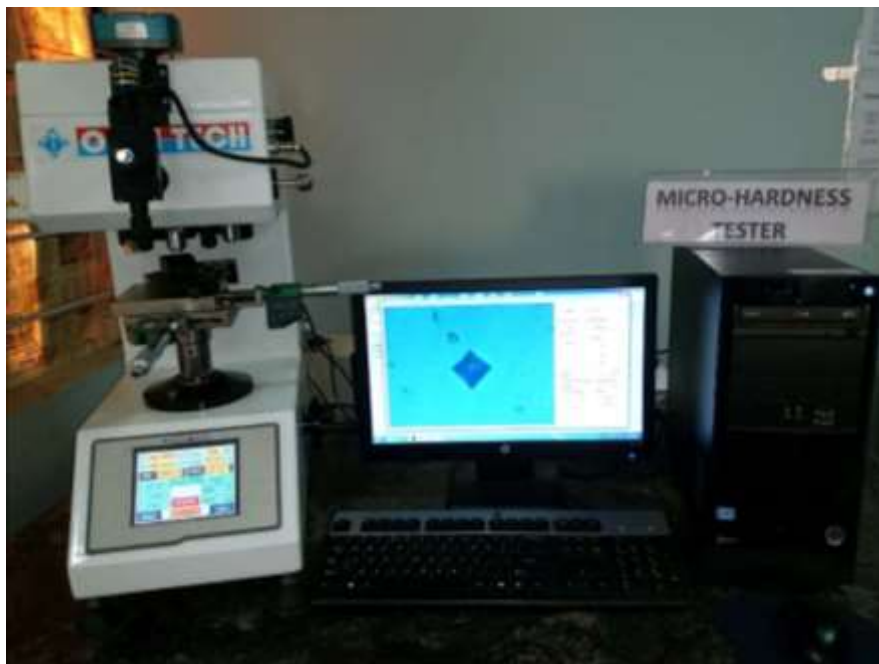


Figure 3.11 Vickers Microhardness Setup

### 3.6.2 Tensile Test

The tensile test is used to evaluate strength and ductility of as-received and equal channel angular extruded sample. Specimens were prepared according to the ASTM-E8 standard with 16 mm gauge length. A schematic tensile specimen has been illustrated in figure 3.12. The tensile properties of magnesium alloys were measured using UTM-Shimadzu AG-X plus™ equipped with 100 kN load cell and operated with a steady cross-head speed of 0.25 mm/min during all the tensile tests as shown in figure 3.13. Three samples were tested for each condition and uniaxial tensile testing was accomplished at room temperature and average reading was calculated and presented in the thesis.

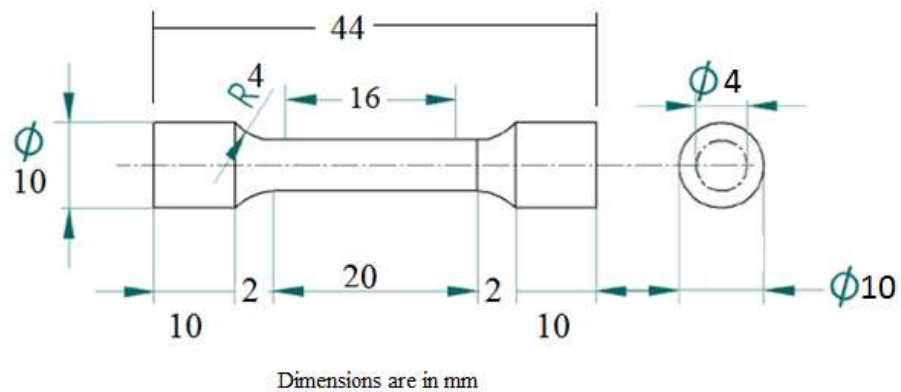


Figure 3.12 Tensile test specimen as per ASTM-E8



Figure 3.13 Shimadzu Tensile Tester

### 3.7 ELECTROCHEMICAL CORROSION TEST

Corrosion study of AZ wrought Mg alloys was investigated using electrochemical corrosion analyzer, model: Gill AC-1684 as shown in figure 3.14, supplied by Tech-science Pvt Limited, Pune (India). The potentiodynamic polarization tests were conducted in 3.5wt.% NaCl solution to estimate corrosion resistance or rate of corrosion of AZ wrought alloys. The auxiliary electrode (AE) was made of graphite (Gr) and the

reference electrode (RE) was made of a saturated calomel electrode (SCE). 1cm<sup>2</sup> area of working electrode (AZ80/91 alloys) was exposed to the 3.5wt.% NaCl solution. Prior to the electrochemical corrosion test, specimens were polished with 600, 800, 1000, 1200, 1500, 2000 grit emery papers and washed with ethanol. The specimens were kept in corrosion cell kit in NaCl solution for 20min to stabilize the open circuit potential (OCP). Further, the AC impedance test of starting frequency 10 kHz and ending frequency 10 MHz with a scan speed of 5mV/s and cyclic sweep experiments with -250 to +250mV was carried on electrochemical analyzer. Surface morphology of the corroded samples were examined by SEM. The corrosion product was removed using 200 g/L of chromic acid and 10 g/L of AgNO<sub>3</sub> solutions. The corrosion rate of the alloy was calculated by using equation (3.2) and (3.3).

$$CR (mpy) = \frac{0.129 * A * I_{corr}}{n\rho} \quad (3.2)$$

$$CR(mm/y) = 3.27X 10^{-3} \frac{i_{corr} X A}{\rho} \quad (3.3)$$

Where: CR is the corrosion rate in miles per year, A is the molar mass (for magnesium 24.3 g/mol),  $I_{corr}$  is the corrosion current density in  $\mu\text{A}/\text{cm}^2$ , n is the valance and  $\rho$  is the density (1.74 g/cm<sup>3</sup>). The obtained CR was converted into mm/year by considering 1 mils/year equal to 0.0254 mm/year.

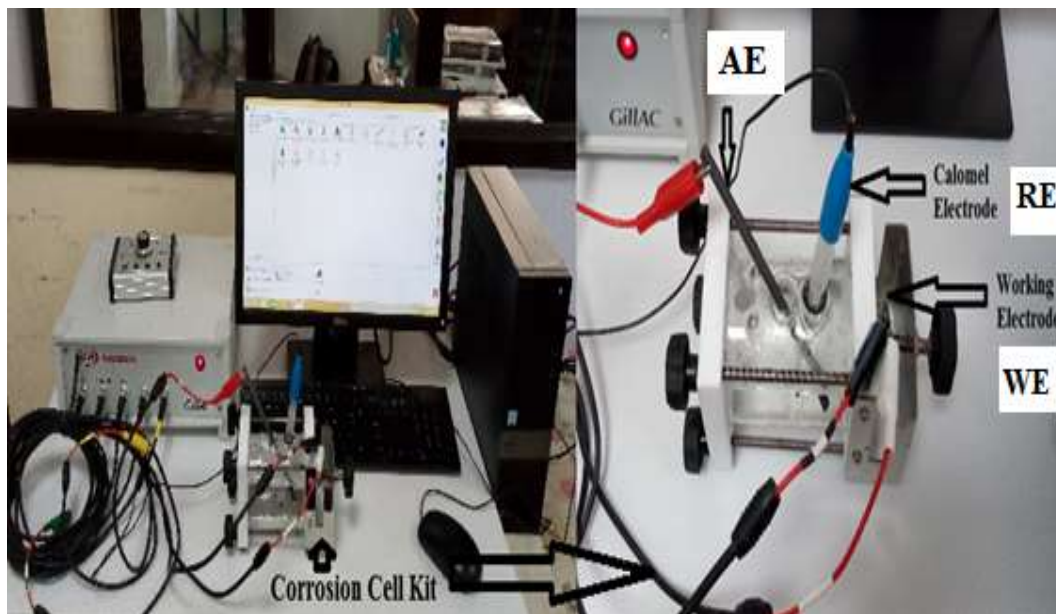


Figure 3.14 Electrochemical Corrosion Analyzer setup (Gill AC: Model No: 1845)

### **3.8 ANNEALING AND AGING TREATMENT**

The chemical composition of investigated AZ80/91 magnesium alloys was measured by EDS analysis which is presented in Figures 3.2 and 3.3. The as-received AZ80/91 Mg alloys are homogenized and extruded through ECAP. Then, examined the microstructure, mechanical properties and corrosion behaviour of Mg alloys. Further enhancement of corrosion resistance was planning to achieve by heat treatment. A short-term annealing treatment of as-received and ECAPed AZ80 and AZ91 alloys was conducted at three different temperatures of 523K, 623K and 723K for 6h and 12h with furnace cooling in order to modify their microstructural characteristics. The annealing treatment was carried out in Muffle furnace equipped with PID controller and maximum temperature range of 900 ° C/1000 ° C. Specimens for microstructure inspection were prepared by mechanical polishing and further etched in a solution of 4.2 g picric acid, 10 ml acetic acid, 10 ml distilled water and 70 ml ethanol for 3–5 s. Microstructures and elemental distributions were observed by Optical microscopy and Scanning Electron Microscopy. Further, cyclic sweep experiments with –250 mV to +250 mV was carried on the electrochemical corrosion analyser to estimate degradation rate of AZ Mg alloys before and after annealing and aging treatment.

### **3.9 HIGH-VELOCITY OXY-FUEL COATING**

Commercially available coating powder 316 stainless steel has been used in the present investigation to provide resistance against corrosion. Energy-dispersive spectroscopy (EDS) analysis of the coating powder confirms the presence of elements in the powder. The SEM image of 316 stainless steel powder of size  $21.6 \pm 1.6\mu\text{m}$  and compositions are shown in figure 3.15. A high-velocity oxy-fuel (HVOF) technique was used to deposit the coating on as-received and ECAPed AZ80/91 Mg materials in Spraymet Surface Technologies Pvt. Ltd, Bangalore, Karnataka, India. The process variables used for the HVOF process are presented in Table 3.4. A compressed air jet is used for cooling the test specimens during and after the coating process. Prior to powder coating deposition, the surface of Mg alloy was grit-blasted with  $\text{Al}_2\text{O}_3$  grit, which increases

the quality of coating adhesion by enhancing the surface roughness of the Mg specimens.

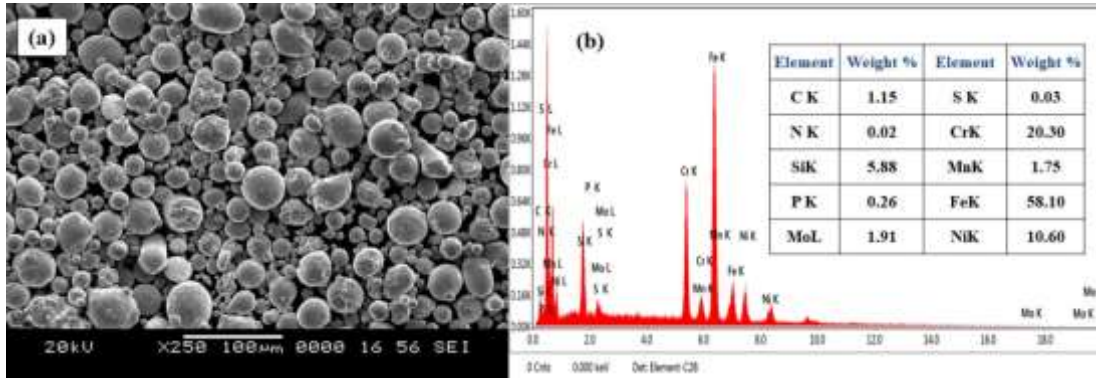


Fig 3.15. 316 stainless steel powder a) SEM micrograph b) EDS result

Table 3.4 The process variables for the HVOF process

Parameters	
Sample type (Substrate)	Magnesium alloy (AZ80 and AZ91)
Coating material	316 stainless steel powder
Coating thickness	80-100µm
Substrate Dimension	15 – 16 mm diameter and 3-5mm thick
Oxygen pressure	160-170 PSI
Oxygen flow rate	30-34 SCFH (SCFH-Standard Cubic Feet Per Hour)
Hydrogen Pressure	120-140 PSI (PSI-Pound per Square Inch)
Fuel flow rate	80-100 SCFH
Spraying distance	8'' - 10''



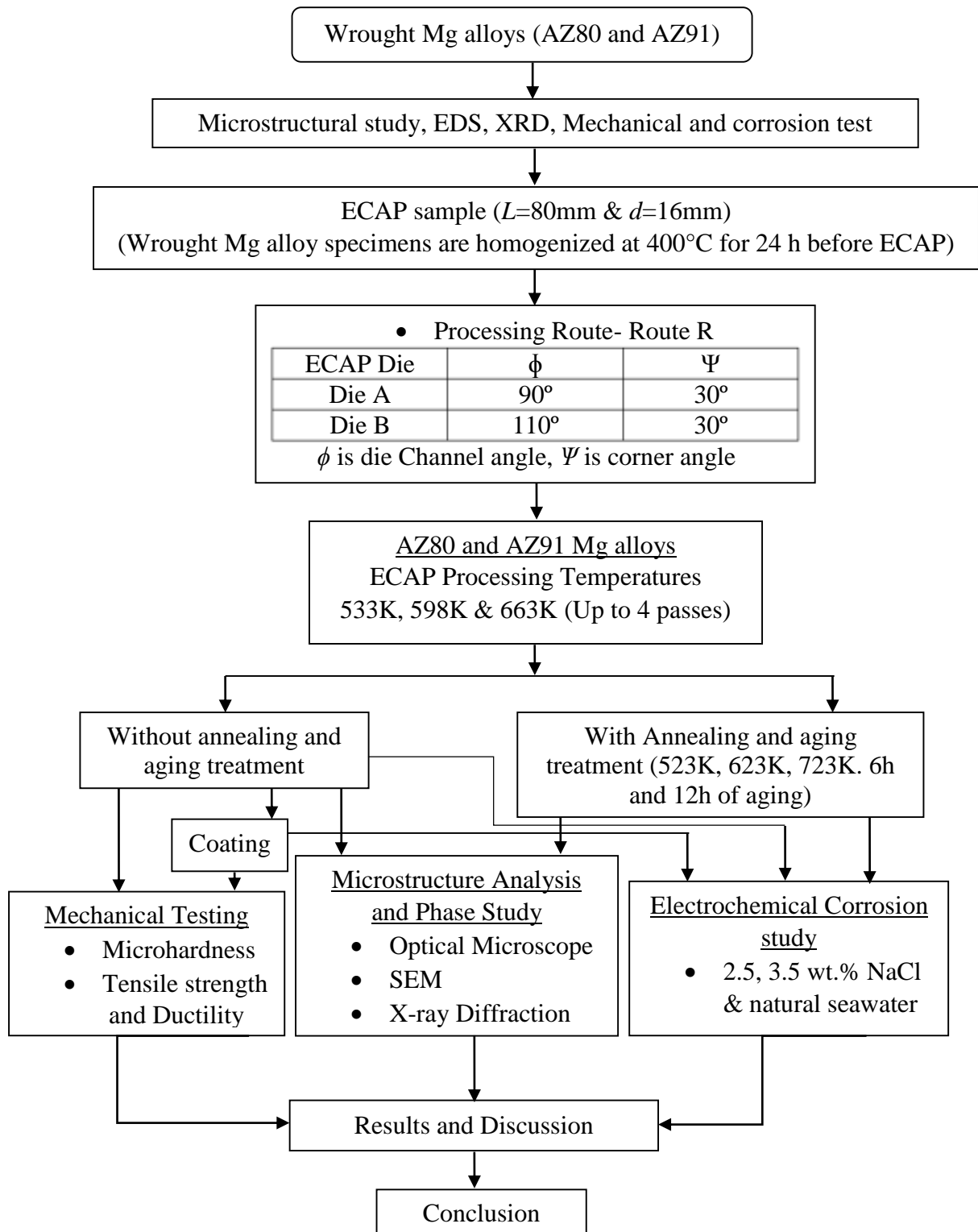


Figure 3.16. Flow chart of research methodology

### **3.10 SUMMARY**

The current chapter presents the plan of experimentation in detail with emphasizes on selection of materials for experimentation, procedure for severe plastic deformation through ECAP, preparation of specimens and subsequent characterization techniques adapted. In addition, details of the facilities employed for carrying out microstructural studies, XRD, tensile test, microhardness, corrosion test and annealing methods are also explained. Further, the selection of coating materials based on its corrosion resistance and high velocity oxygen fuel coating adapted in the present study for coating on as-received and ECAPed samples have been discussed.

## CHAPTER 4

# EFFECT OF ECAE ON MICROSTRUCTURE MECHANICAL PROPERTIES AND CORROSION BEHAVIOR OF AZ80/91 MAGNESIUM ALLOYS

### 4.1 INTRODUCTION

The ECAP process was planned with two equal channels: traversing at particular angles called the die channel angle ( $\phi$ ) and the corner angle ( $\psi$ ) subtended at the channels' intersection. In this work, effect of ECAP die channel angles and processing temperature on microstructures, mechanical properties and corrosion resistance of ECAPed AZ80/91 Mg alloys were investigated.

### 4.2 EFFECT OF ECAP DIE CHANNEL ANGLE ON AZ80/91 MAGNESIUM ALLOY

So far, many simulation studies have been executed to examine the impact of different die parameters on deformation homogeneity, strain rate, workflow etc. Although a number of researchers have been carried out on the efficiency of ECAP process routes and influences of various ECAP parameters on the strain behavior (Nagasekhar et al., 2005). There is limited work on study the effect of channel angle on grain size and other material properties through experimentally. In this chapter, the effect of ECAP channel angle on grain size, microhardness, tensile behaviour and corrosion rate for different passes were analyzed using working temperatures of 533K, 598K and 663K. Furthermore, die A was used for examining above said material properties since this die gives the best results.

#### 4.2.1 Microstructure Evolution of AZ80 Mg alloy

The optical and SEM microstructures of as-received, homogenized at 673K-24h sample and those after ECAP processed specimens are shown in Figures. 4.1, 4.2 and 4.3. The microstructure of the as-received AZ80 Mg alloy presents the  $\alpha$ -Mg and  $\beta$ -Mg<sub>17</sub>Al<sub>12</sub> secondary phases along the grain boundaries indicated in Figure 4.1 (a). After

homogenized at 673K for 24h secondary phases were partially dissolved along the grain boundaries as shown in figure 4.1 (b) this partial dissolution of secondary phases was achieved prior to ECAP and this sample is designated as 0P specimen. Figure 4.3 presents the optical images of the ECAPed AZ80 Mg alloy processed through two ECAP die of 2 and 4 passes at 598K processing temperature, in which the white and black contrast within the grains and along the grain boundaries represents  $\alpha$ -Mg primary phase and  $\beta$ -Mg<sub>17</sub>Al<sub>12</sub> secondary phases respectively. Also, the presence of  $\alpha$ -Mg and  $\beta$ -Mg<sub>17</sub>Al<sub>12</sub> phase in AZ80 alloys was confirmed through in accordance with the XRD analysis shown in Figure 4.23. The microstructure of the ECAPed Mg alloy showed significant grain refinement and bi-modal grains after ECAP of two passes for both die A and B, as shown in Figure 4.3. (a) and (c) these heterogeneous grains were typically obtained under the condition of lower deformation. When ECAP passes were gradually increased up to four passes bi-modal grain structure disappeared due to a large amount of induced plastic strain, as a result of the average grain size of ECAP-4P through die A was  $\sim 6.35 \mu\text{m}$  and the secondary phases are uniformly distributed throughout the material as shown in Figure 4.3 (b). Whereas ECAP-4P processed through die B exhibited slightly larger grains compared to die A, the obtained grain size is of about  $\sim 9.77 \mu\text{m}$ . Hence, the effectiveness of grain refinement can be enhanced based on a channel angle, particularly, material processed through  $90^\circ$  channel angle exhibited better grain refinement.

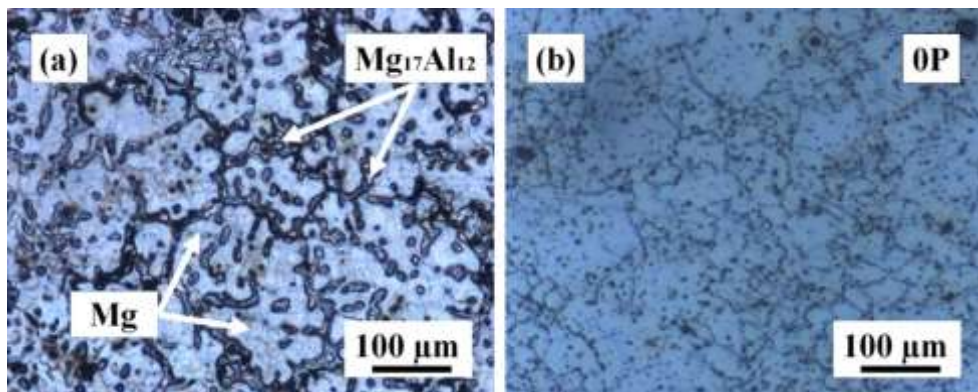


Figure 4.1 Optical images of (a) as-received (b) Homogenized at 673K-24h

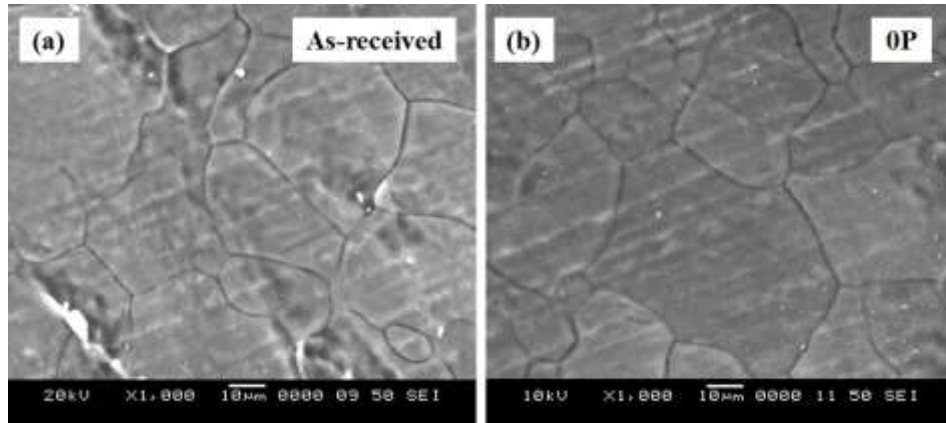


Figure 4.2 SEM images of (a) as-received b) Homogenized at 673K-24h

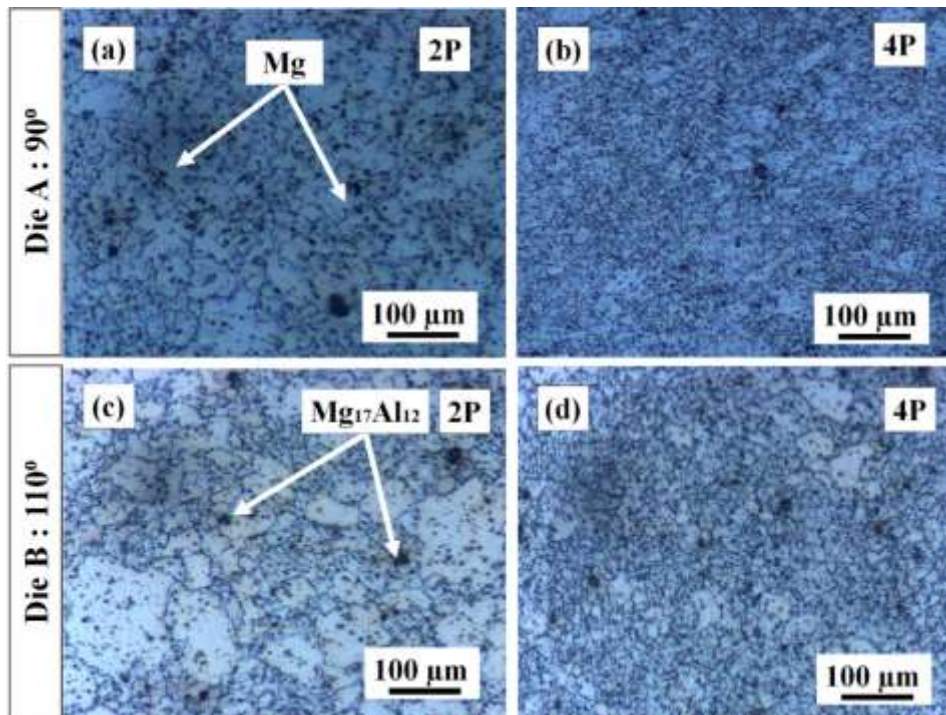


Figure 4.3 Optical images for Die A and die B after 2 and 4 ECAP passes

#### 4.2.2 Microstructure Evolution of AZ91 Mg alloy

Figs 4.4 and 4.5 show the microstructures of the as-received and homogenized AZ91 Mg alloy. The microstructure of the as-received AZ91 Mg alloy shows a coarse  $\alpha$ -Mg phase and  $\beta$ -Mg<sub>17</sub>Al<sub>12</sub> secondary phase along the grain boundaries which is confirmed through XRD analysis as shown in Figure 4.23. The mean grain size of as-received Mg alloy is  $\sim 58.69 \mu\text{m}$  as shown in figures 4.4 (a) and 4.5 (a), measured by linear intercept

method (ASTM E 112). From figures 4.4 (b) and 4.5 (b), it could be found that after homogenization treatment at 673K for 24h the slight increase of mean grain size of Mg alloy of  $\sim 59.82 \mu\text{m}$  was observed this is due to grain growth effect during homogenization process. Similar observations are made by Nikulin et al. (2012). After ECAP, the alloys microstructure are effectively refined by dynamic recrystallization process (DRX) (Orlov et al., 2009). From figure 4.6, it was observed that two-pass pressing through die A and die B exhibited bimodal grain structure and more fine grains appeared for the processing in the  $90^\circ$  die than the  $110^\circ$  die. The effectiveness of the grain refinement was observed after four passes of pressing in the  $90^\circ$  die as shown in figure 4.6 (b). Also, it is noticed that with the increase in the number of ECAP passes, the amount of fine grains is increased greatly.

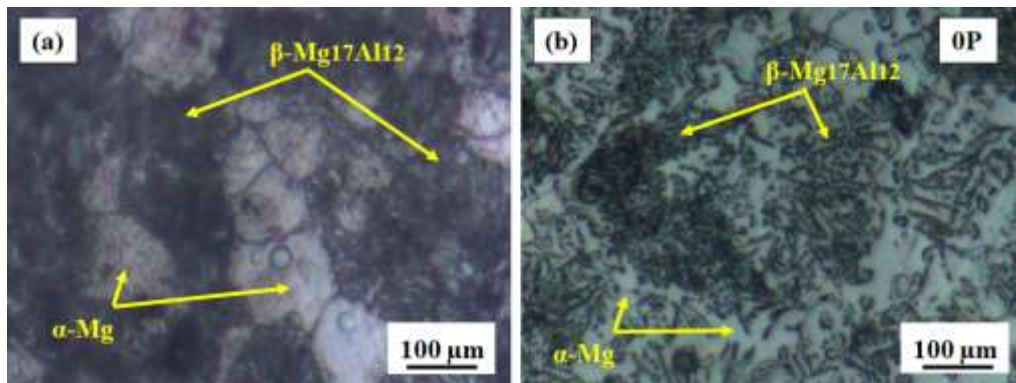


Figure 4.4 Optical images of (a) as-received b) Homogenized at 673K-24h

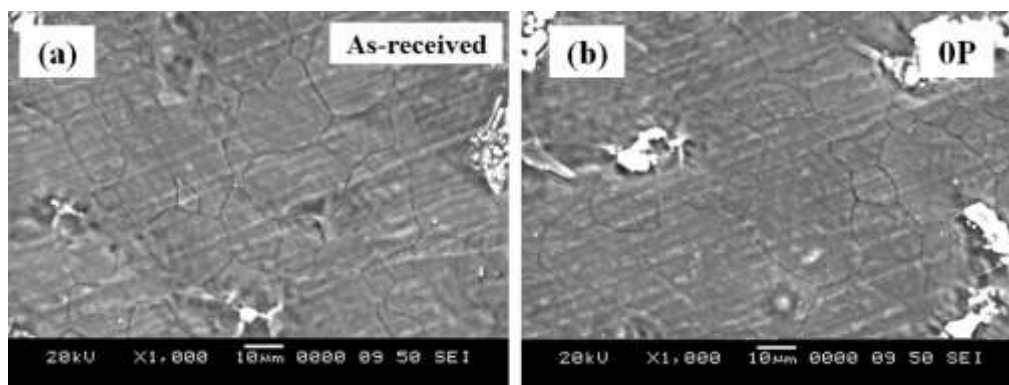


Figure 4.5 SEM images of (a) as-received b) Homogenized at 673K-24h

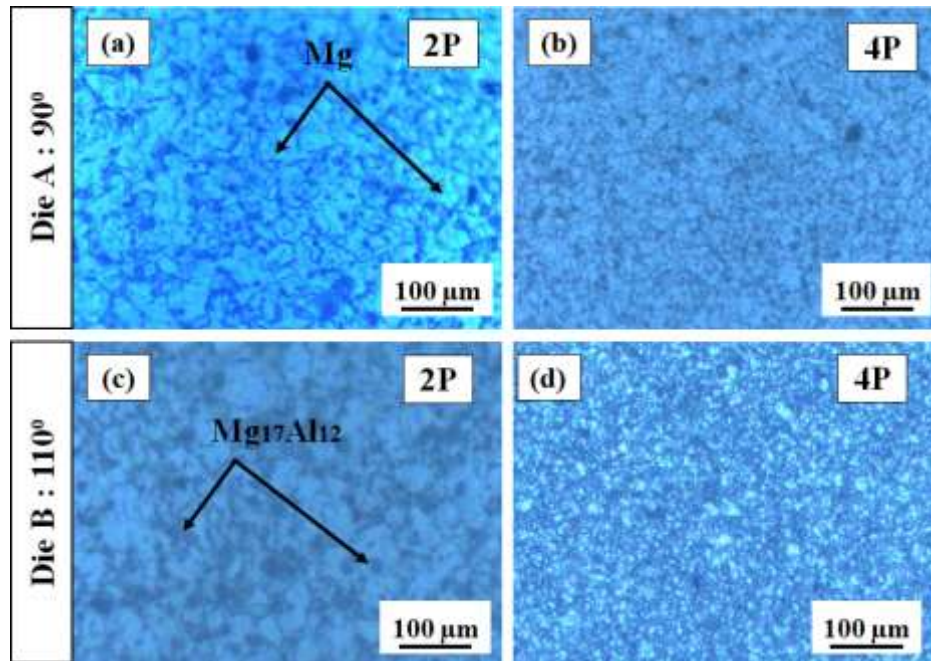


Figure 4.6 Optical images for Die A and die B after 2 and 4 ECAP passes

#### 4.2.3 Variation of grain size with two different die after 2 and 4 ECAP passes for AZ80/91 Mg alloys

Figure 4.7 displays the variation of average grain size of processed and unprocessed AZ80 and AZ91 Mg alloys of 2 and 4 ECAP passes through die A and die B. As it could be observed from figure 4.7 as-received and homogenized (0P) Mg alloy has moderately large grain size approximately  $\sim 50.20 \mu\text{m}$  and  $\sim 50.70 \mu\text{m}$  for AZ80 and  $58.69 \mu\text{m}$ ,  $59.82 \mu\text{m}$  for AZ91 alloy respectively. The increased average grain size of Mg alloy after homogenization treatment AZ80/91 Mg alloy at  $673\text{K}-24\text{h}$  is due to the phenomenon of grain growth effect (Naik et al., 2018). Further, it can be shown that after 2P and 4P ECAP volume fraction of grains increases compared to as-received and homogenized Mg alloy. Mean grain size of AZ80 Mg alloy after ECAP-2P and 4P were  $\sim 28.87 \mu\text{m}$  and  $\sim 6.35 \mu\text{m}$  respectively for die A. Similarly, the average grain size of same Mg alloy processed through die B is  $\sim 36.14 \mu\text{m}$  and  $\sim 9.77 \mu\text{m}$  for ECAP-2P and 4P respectively. Further, an average grain size of AZ91 Mg alloy after 2P and 4P of ECAP were  $\sim 30.86 \mu\text{m}$ ,  $\sim 7.58 \mu\text{m}$  for die A and  $\sim 36.14 \mu\text{m}$ ,  $\sim 9.7 \mu\text{m}$  for die B respectively. It is apparent that the obtained grain refinement is due to dynamic recrystallization process (DRX) during ECAP and they increase in a number of ECAP

passes which result in much smaller grain structure. However, from this it is noticed that the alloy processed with 90° die shows smaller grain sizes than 110° die for both alloy, this is due to accumulation of very large plastic strain while processing with a low angle die (Patil et al., 2015 and Figueiredo et al., 2010). The calculated equivalent plastic strain for 110° to be ~0.742 and ~1.015 for 90° indeed, the strain developed by 4P ECAP through 90° die is higher than that of 110° die. Therefore, large strain in the material exhibited more dislocation density lead to the formation of fine grains during this process. Therefore, undoubtedly it is evident that ECAP die angles significantly affect the deformation homogeneity and this influences the variation in microstructure (Agwa et al. 2016; Jin et al. 2009; Alaneme et al. 2019; Zhao et al. 2019).

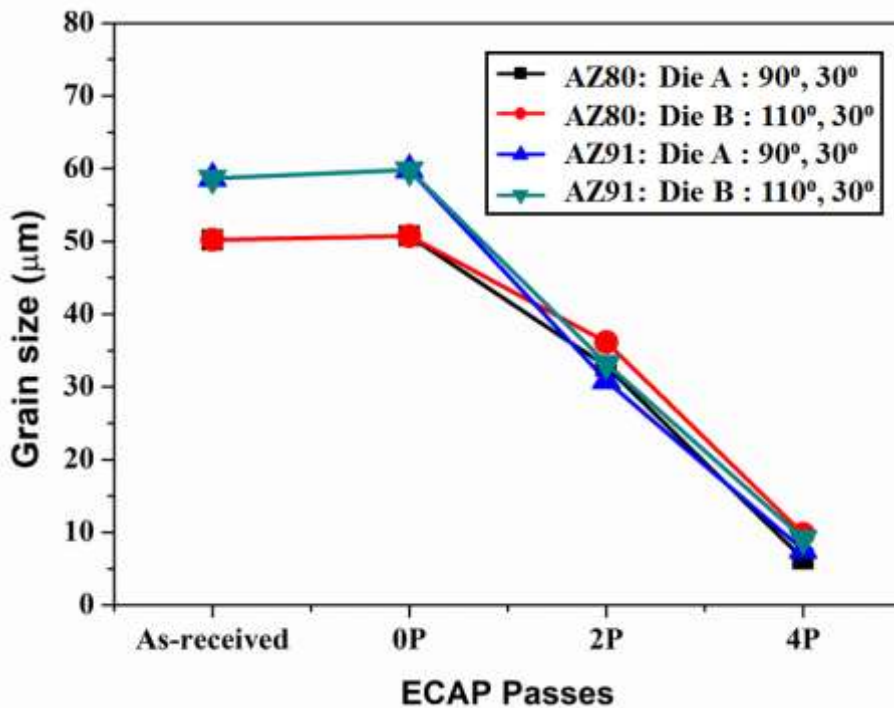


Figure 4.7 Variation of average grain size with two different die

Also, the microstructural change contributes towards improved mechanical properties and corrosion resistance. Finally, in general, AZ Mg alloy processed through die A and die B showed the same trend of decreasing grain size from the homogenized condition. By extruding in the die A, the mean grain size of AZ80 and AZ91 Mg alloy decreased by 35 % and 22% when compared with material processed through die B (Patil et al., 2015; Figueiredo et al., 2010). Also, from the result, it was observed that AZ80 Mg



alloy processed through die A at 598 K exhibited fine grain structure of about  $\sim 6.35$   $\mu\text{m}$  after four ECAP passes, which is lower when compared to ECAPed AZ91 Mg alloy processed at same processing temperature.

### 4.3 EFFECT OF ECAP AT DIFFERENT PROCESSING TEMPERATURE

ECAP processing through die A was carried out at three elevated temperatures 533K, 598K and 663 K at a strain rate of 1mm/s using a conventional flipping type ECAP die described earlier in experimental work. In this section, microstructure evolution in connection with grain refinement, distribution of secondary phases and grain growth effect were discussed evidently for AZ Mg alloys.

#### 4.3.1 Microstructure analysis on AZ80 Mg alloys

Figures 4.8-4.14 depicts the microstructure evolution of ECAPed AZ80 Mg alloys after processing through die A at 533K, 598K and 663K respectively. Figure 4.8 shows the microstructure evolution of AZ80 Mg alloy after ECAP for 1 to 4 passes.

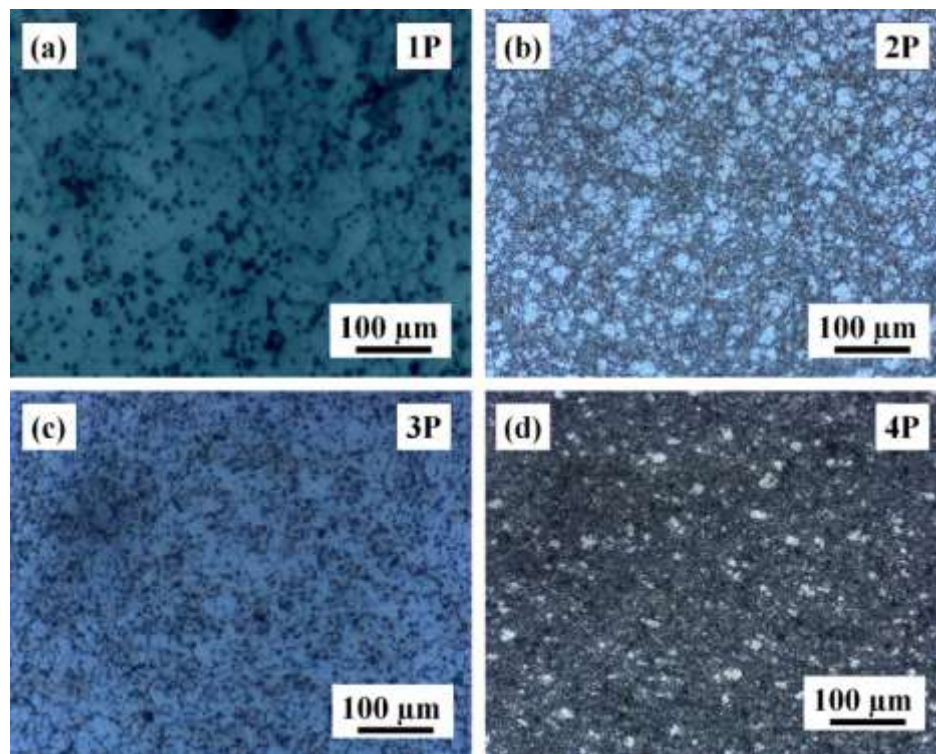


Figure 4.8 Optical microstructure of AZ80 Mg alloys at ECAP processing temperature of 533K for different passes a) 1P b) 2P c) 3P and 4) 4P

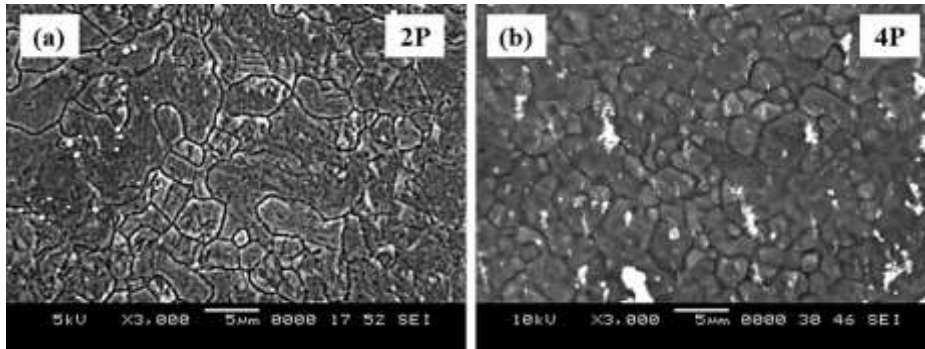


Figure 4.9 SEM microstructure of AZ80 Mg alloys at ECAP processing temperature of 533K for different passes a) 2P and b) 4P

The microstructure reveals a significant modification in grain size and grain homogeneity with the increase of ECAP passes. After ECAP of one pass, (Figure. 4.8 (a)), compared with the as-received and homogenized samples, the grain size has shown a noticeable refinement. The microstructure achieves a substantial reduction in grain size after ECAP-4P. Here, Maximum of coarse grains disappear and the average grain size decreases to  $\sim 5.12 \mu\text{m}$ . Therefore, the effectiveness of the ECAP process in grain refinement at higher passes is reduced and more uniform. A similar observation was made through SEM analysis as shown in figure 4.9. But, distribution of secondary phases was non-uniform, this is due to Mg alloy processed at below solubility temperature of  $\text{Mg}_{17}\text{Al}_{12}$  phases of the alloy which results in non-uniform distribution of secondary phases (Jun Qiao et al., 2013). The significant change observed in microstructure after ECAP processing at 598K shown in Figure 4.10. Certainly, more homogenous and uniform distribution of secondary phases were observed. This suggests that recrystallization has occurred during the ECAP process due to the accumulation of high plastic strain and recrystallization temperature. Therefore, after ECAP for 4 passes (Figure 4.10 (d)), the microstructures have homogenous grains. However, the homogeneity of microstructure increases gradually with the increase of ECAP passes. Also, the SEM micrographs confirm the same as shown in figure 4.11. In general, the distribution of secondary phases was controlled by the amount of deformation and ECAP pressing temperature. In the microstructure of as-received Mg alloy, there existed some brittle eutectic phases around the grains as shown in Figures 4.1 (a), but Figure 4.12 presents the uniform distribution of the secondary phase ( $\beta$ -

Mg<sub>17</sub>Al<sub>12</sub>) inside the grains of the ECAP-4P specimen processed at 598K. From this, it is evident that secondary phase particles distributed in the  $\alpha$ -Mg matrix as the ECAP passes progressed.

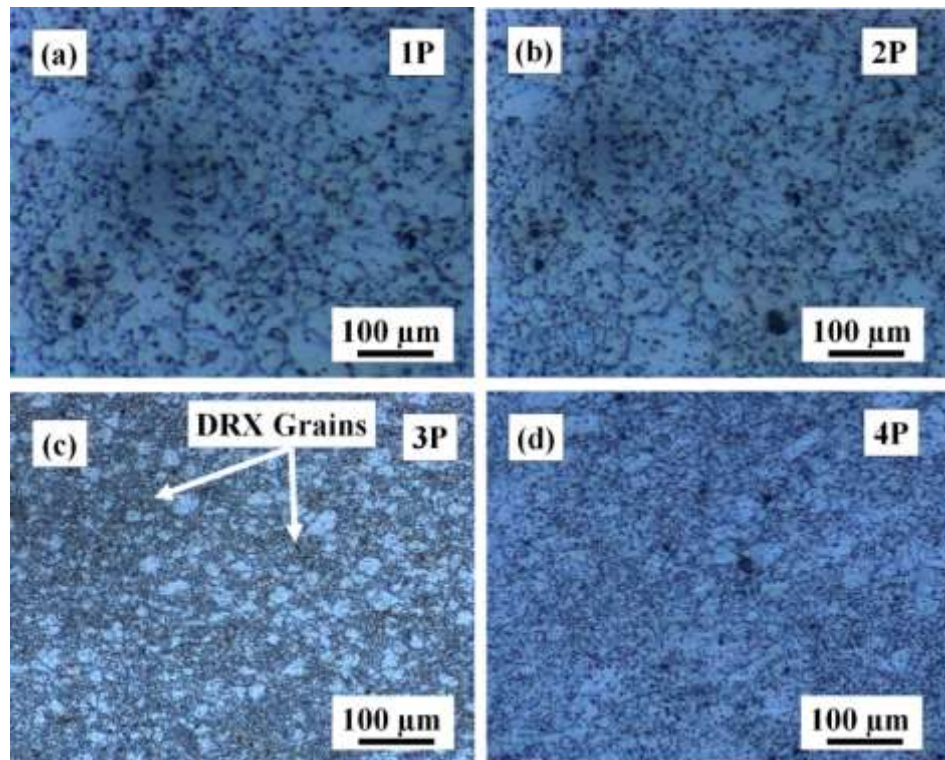


Figure 4.10 Optical microstructure of AZ80 Mg alloys at ECAP processing temperature of 598K for different passes a) 1P b) 2P c) 3P and 4) 4P

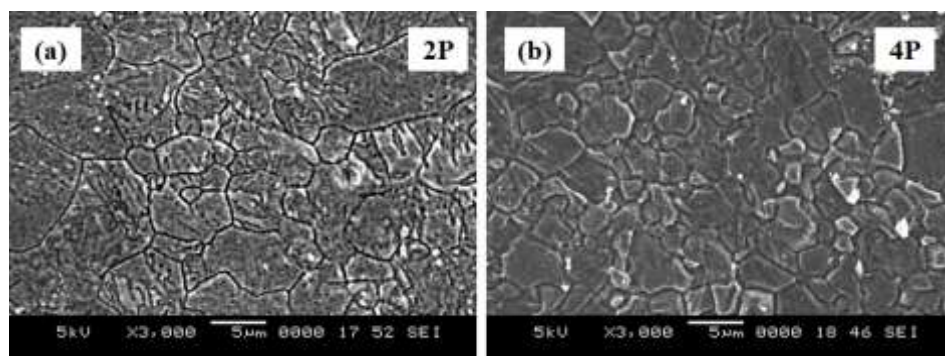


Figure 4.11 SEM microstructure of AZ80 Mg alloys at ECAP processing temperature of 598K for a) 2P and b) 4P

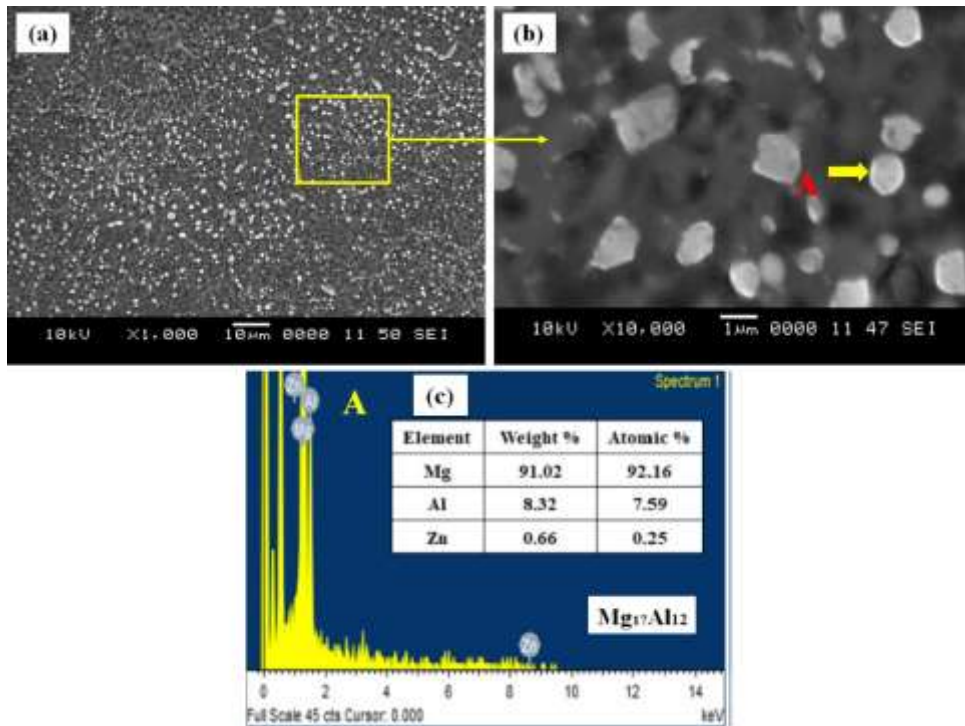


Figure 4.12 Distribution of secondary phase of AZ80 Mg alloys after ECAP-4P

Therefore, The ECAP processing not only caused grain refinement but also induced the precipitation of brittle secondary phases into fine particles, as shown in Figure 4.12 with EDS result. However, when ECAP accomplished at the higher processing temperature of 663K, with an increasing number of ECAP passes, presence of fine precipitates of secondary phases vanished fully except for the slight amount of partially dissolved fine eutectics as shown in Figure 4.13. The amount of brittle eutectic phases and its precipitates increased due to the higher processing temperature during ECAP because precipitation of secondary phases depends on solubility temperature of Mg<sub>17</sub>Al<sub>12</sub> phases (Jun Qiao et al., 2013). In contrast, AZ80 Mg alloys processed at 663K exhibited coarse grain even at higher ECAP passes the obtained mean grain size for 2P and 4P are ~37.26 μm, ~10.54 μm respectively. Also, grain growth during ECAP processing at 663K was noticed through SEM microstructure as shown in figure 4.14

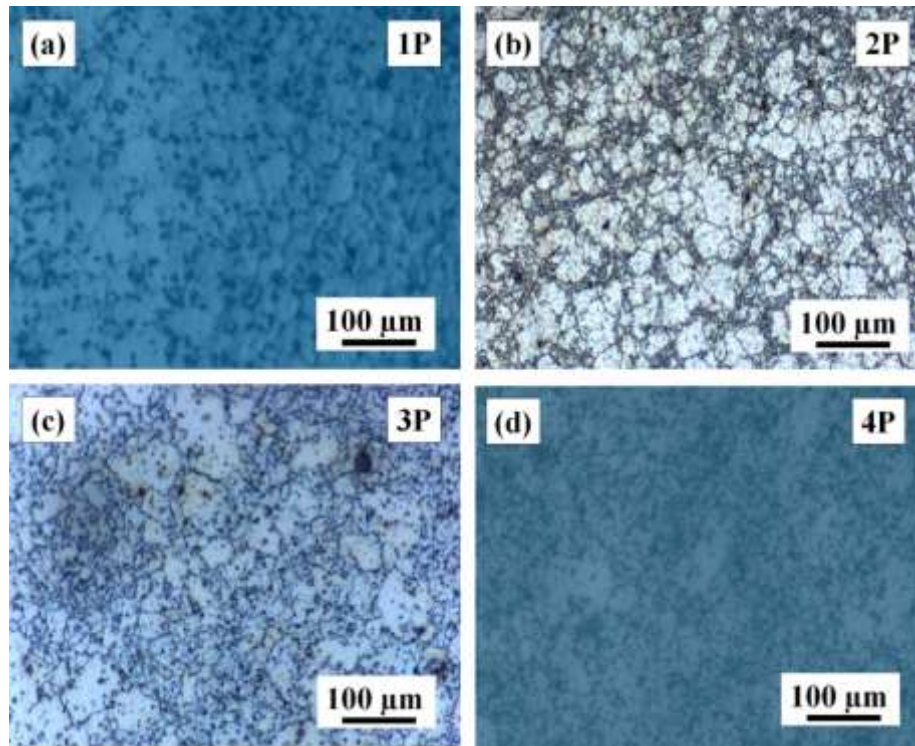


Figure 4.13 Optical microstructure of AZ80 Mg alloys at ECAP processing temperature of 663K for different passes a) 1P b) 2P c) 3P and 4) 4P

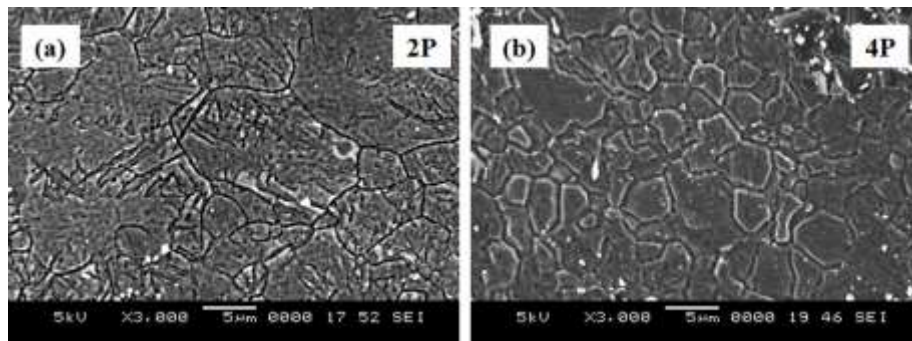


Figure 4.14 SEM microstructure of AZ80 Mg alloys at ECAP processing temperature of 663K for different passes a) 2P and b) 4P

### 4.3.2 Microstructure analysis on AZ91 Mg alloys

Optical photographs of the ECAP (a) one-passed; (b) two-passed; (c) three-passed and (d) four passed AZ91 alloys at 533K are presented in Figure. 4.15 and figure 4.16 presents the SEM images of ECAP-2P and 4P samples. After the second pass, grains of the initial microstructure were split into a bimodal distribution of coarse grains of

~30.52  $\mu\text{m}$ . The microstructure became more uniform and homogeneous by successive breaking-up of coarse grains with ECAP passes. The reasonably more homogeneous and equiaxed microstructure was obtained after four ECAP passes, it is believed that dynamic recrystallization occurs during ECAP. However, this does not occur the growth of new grains at recrystallization temperature. This is because the portion of fine grains in the ECAPed microstructure gradually increases with ECAP passes as shown in Figures 4.17 and 4.18. It is noted that the grains of the ECAPed AZ91 alloy at 598K is not fine as those of the ECAPed Mg alloys processed at 533K, this is mainly due to the difference in ECAP processing temperature similar observation was made by Kim et al. (2003) and Avvari et al. (2016). The grain size reduction is possibly associated with the gradual transformation of sub-grain-boundaries from low to high angles with pass number by absorbing dislocations generated during ECAP. As high angle grain boundaries (HAGBs) are prone to chemical attack due to their high grain boundary energies, their presence is easy to be uncovered by chemical etching. The ECAPed microstructure turns into the homogenous microstructure fully composed of fine grains with high angle boundaries and uniform distribution of secondary phases at 598K. Firstly, the grain refinement causes the density of grain boundary increase, which increases the hindrance for dislocation movement contributes to the improved mechanical properties of as-received AZ91 alloy. Secondly, grain refinement and continuous distribution of secondary phases during ECAP contribute towards improved mechanical strength and corrosion resistance respectively. Also, the distribution of  $\text{Mg}_{17}\text{Al}_{12}$  secondary phase after ECAP-4P was shown in figure 4.19 through SEM images with EDS result. Further, From Figures 4.20 and 4.21 it was observed that microstructure was commonly inhomogeneous and there were coarse grains. The initial grain size of ~58.69  $\mu\text{m}$  was reduced to the mean size of ~43.96  $\mu\text{m}$ , ~11.85  $\mu\text{m}$  after two and four ECAP passes at 663 K respectively, as shown in figure 4.20 (b) and (d). After 4 passes, the microstructural consistency improved compared to the 2-pass AZ91 Mg alloy processed at the same processing temperature. But, achieved grain size is much higher than the AZ91 Mg alloys processed at 533K and 598K. Grain refinement is observed at all the ECAE passes, it is believed that dynamic recrystallization (DRX) occurred during ECAE (Agwa et al., 2016 and Jin et al., 2009), whereas obtained coarse grain at 663K is mainly due to grain growth effect at higher temperature (Upadhyay

et al., 2018). However, the increase of ECAP passes a significant reduction in the bimodal microstructure of grain refinement were recorded. A Similar observation was made on Mg alloys by Roberto et al. (2015). From the results presented above, the effect of increasing ECAP processing temperature on the microstructure evolution during ECAP process of AZ Mg alloy can be concluded as: (a) the grain size increases, (b) the grains becomes more equiaxed, (c) the HABs significantly decreases and (d) the secondary phase distribution rate accelerates. Increasing mean grain size by increasing ECAP processing temperature is reliable with data stated for other materials extruded by ECAP (Avarri et al., 2018). Also, above results have good agreement with the reports by Song et al. (2016).

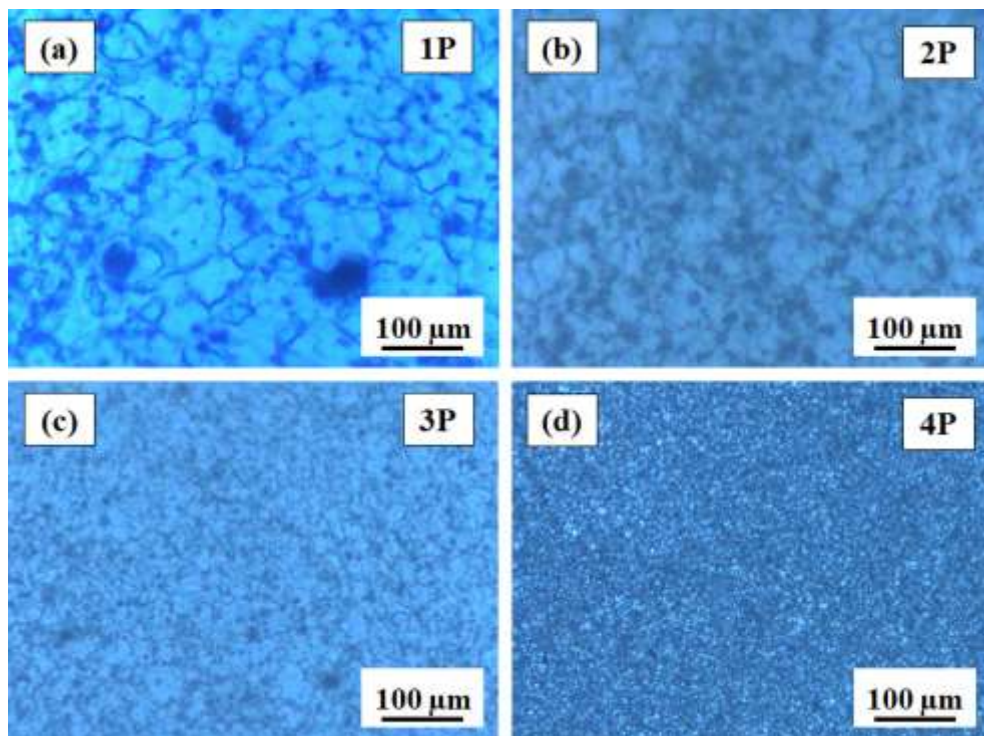


Figure 4.15 Optical microstructure of AZ91 Mg alloys at ECAP processing temperature of 533K for different passes a) 1P b) 2P c) 3P and 4) 4P

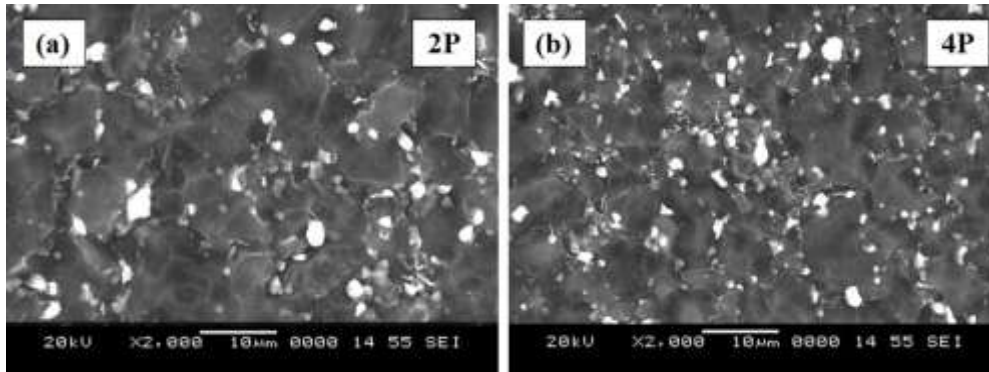


Figure 4.16 SEM microstructure of AZ91 Mg alloys at ECAP processing temperature of 533K for different passes a) 2P and b) 4P

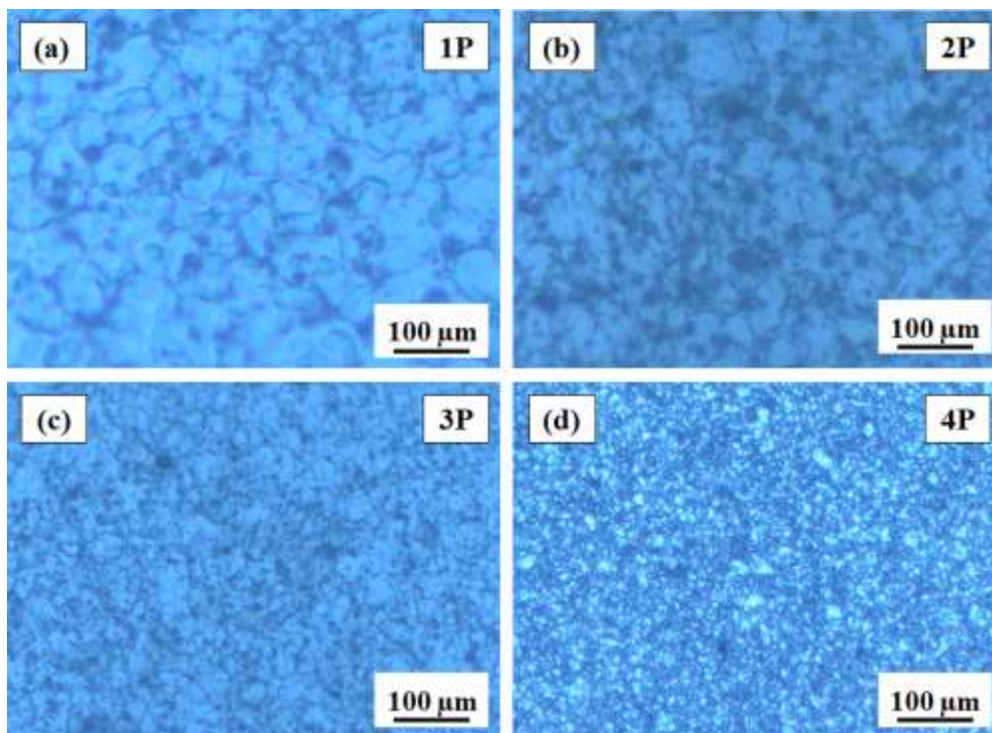


Figure 4.17 Optical microstructure of AZ91 Mg alloys at ECAP processing temperature of 598K for different passes a) 1P b) 2P c) 3P and d) 4P



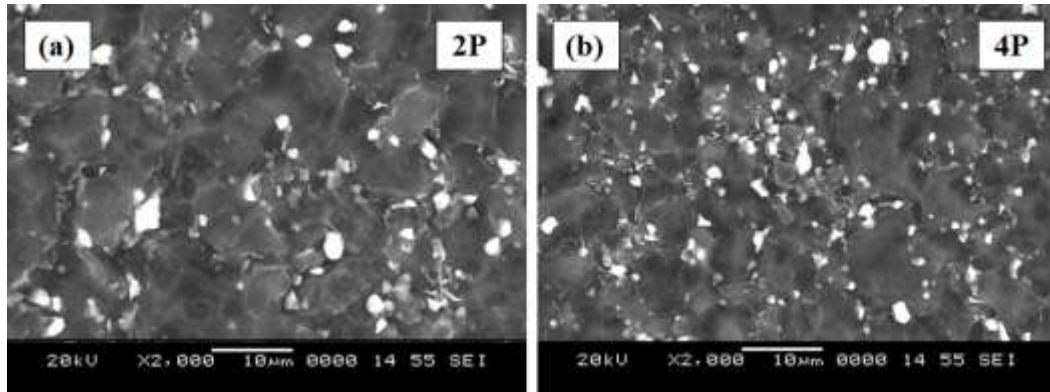


Figure 4.18 SEM microstructure of AZ91 Mg alloys at ECAP processing temperature of 598K for a) 2P and b) 4P

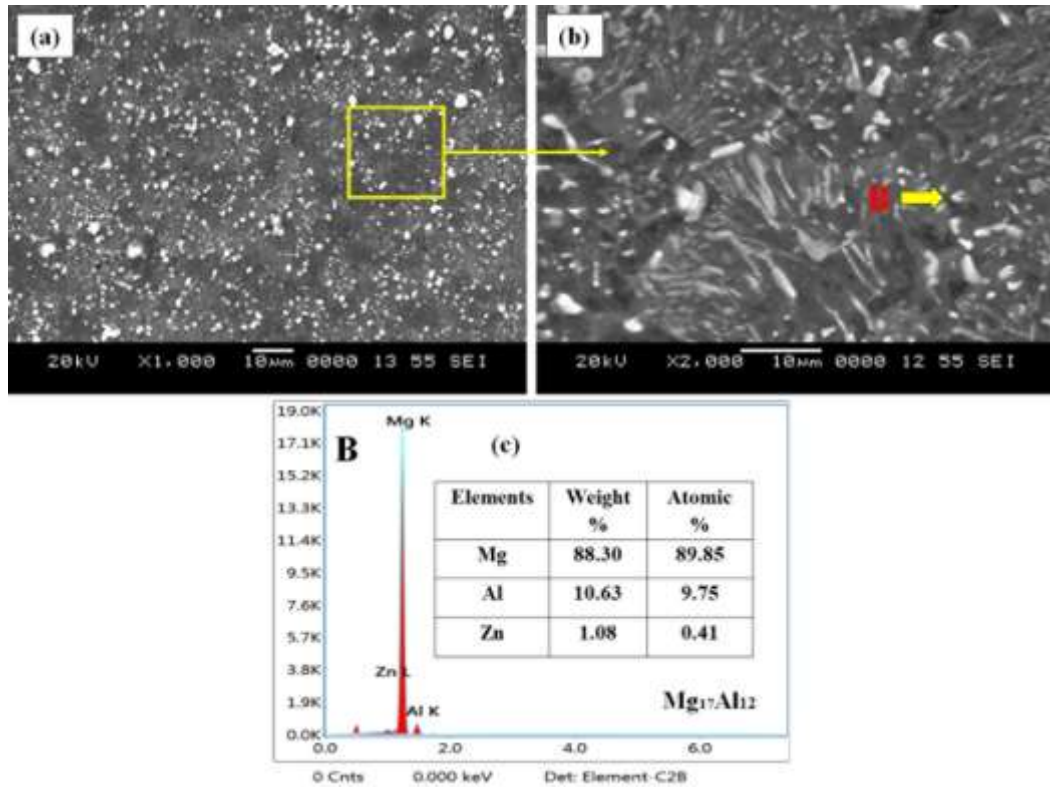


Figure 4.19 Distribution of secondary phase of AZ91 Mg alloys after ECAP-4P

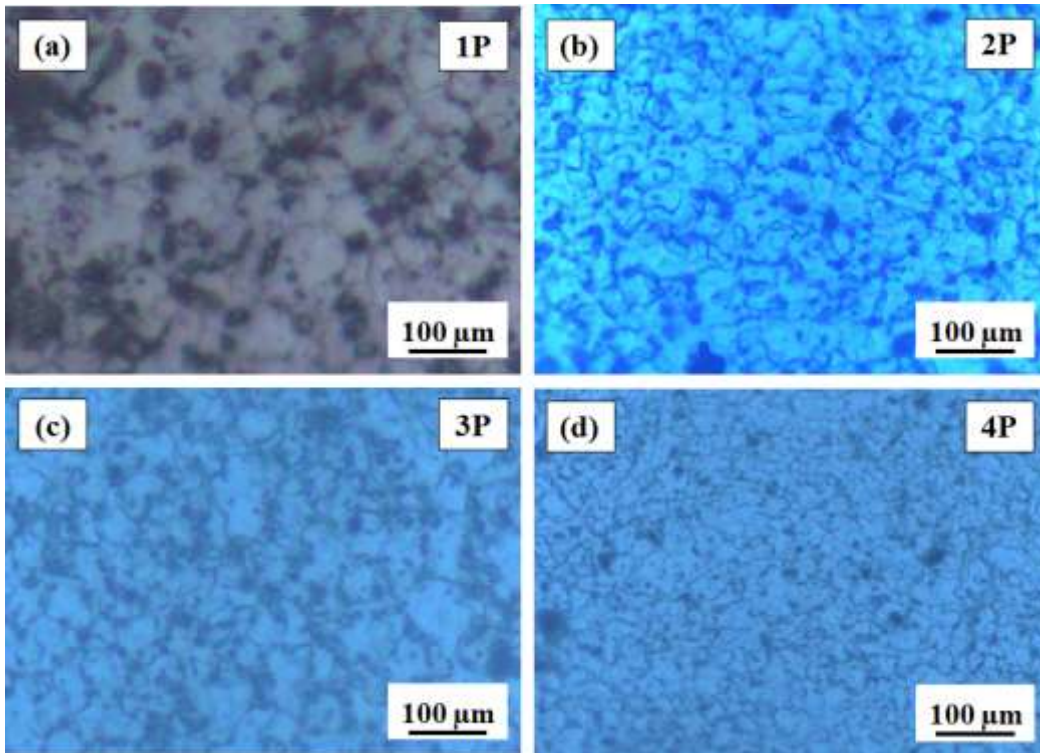


Figure 4.20 Optical microstructure of AZ91 Mg alloys at ECAP processing temperature of 663K for different passes a) 1P b) 2P c) 3P and d) 4P

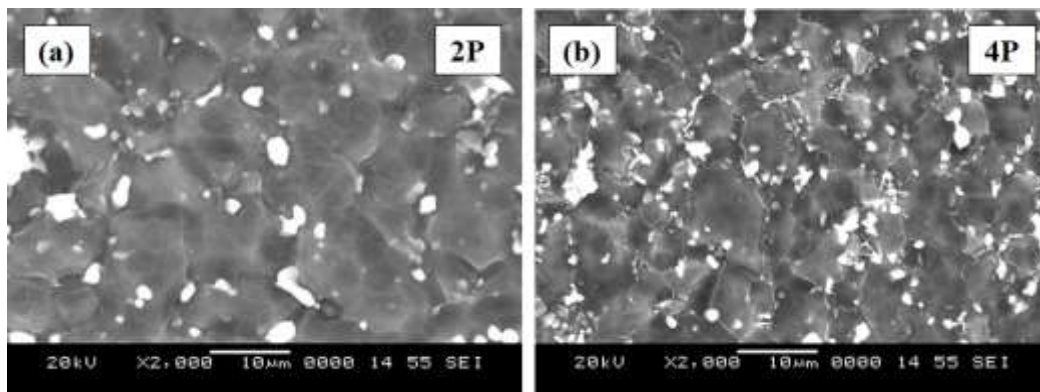


Figure 4.21 SEM microstructure of AZ91 Mg alloys at ECAP processing temperature of 663K for different passes a) 2P and b) 4P

#### 4.3.3 Effect of ECAP processing temperature on grain size

The previous section presents the optical images of ECAPed AZ80/91 alloys at 533K, 598K and 663K. U discussed the mechanism of grain refinement in magnesium alloys processed by ECAP. It was concluded that grain refinement is caused by dynamic

recrystallization (DRX). However, in this section, the impact of processing temperature on grain size was discussed. Figure 4.22 shows the variations of average grain size of ECAPed and un-ECAPed AZ80/91 Mg alloys with the increasing number of ECAP passes at 533K, 598K and 663K. Further, grain refinement was observed up to 4 ECAP passes, resulting in a fine and homogeneous microstructure consisting of equiaxed grains as shown in Figure 4.8-4.21. In contrast at 533K, 598K processing temperatures showed the fully refined homogeneous microstructure even after 2 and 4 Passes. After 4 passes a grain growth was observed and the microstructure remain almost unchanged during further processing at 663K. As a result, the microstructure of sample processed at 663K is coarser than that of the sample processed at 533K and 598K for both AZ Mg alloys. This is mainly attributed due to grain growth effect at higher processing temperature.

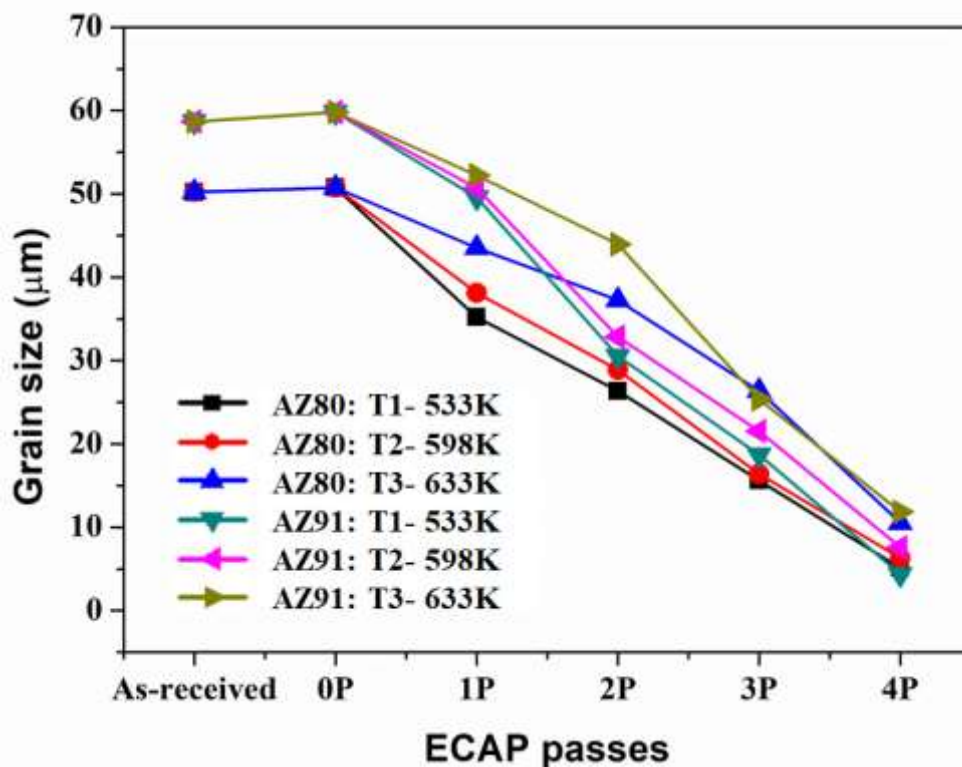


Figure 4.22 Mean grain size variation for different ECAP passes at three different processing temperatures

Figure 4.22 display typical grain size variation for Mg samples pressed at 533K (~0.4T<sub>m</sub>), 598K (~0.5T<sub>m</sub>) and 633K (~0.6T<sub>m</sub>) with corresponding average grain

sizes of  $\sim 5.12 \mu\text{m}$ ,  $\sim 6.35 \mu\text{m}$  and  $\sim 10.54 \mu\text{m}$  respectively after four ECAP pass for AZ80 Mg alloy. Similarly, the corresponding mean grain size of  $\sim 4.36 \mu\text{m}$ ,  $\sim 7.58 \mu\text{m}$  and  $\sim 11.85 \mu\text{m}$  respectively after four ECAP passes for AZ91 Mg alloy. The grains in the as-received alloy were significantly refined and the mean grain size decreased with reducing ECAP processing temperatures, reaching coarse to fine (i.e.  $<5 \mu\text{m}$ ) at 533K with AZ91 Mg alloy. The grain size distribution in the sample processed at three different temperature based on OM and SEM analysis is shown in Figures. 4.8-4.21. This formation of the fine grains related to dynamic recrystallization (DRX) which can take place in Mg at all processing temperature with large plastic deformation and more importantly, grain growth effect was observed at higher processing temperature that is 663K (Upadhayay et al., 2018).

#### 4.4 X-RAY DIFFRACTION ANALYSIS

The X-ray diffraction patterns of AZ Mg alloy before and after ECAP processes as shown in Figure 4.23. The XRD patterns of the as-received, homogenized at 673K and ECAPed AZ Mg alloys revealed two sets of peaks, one for the  $\alpha$ -Mg primary phase and another one for the  $\beta$ -Mg<sub>17</sub>Al<sub>12</sub> secondary phase. But as-received alloy of AZ80 has shown new peaks corresponding to the formation of the ternary phase appeared at  $41.4^\circ$  as shown in Figure 4.23 (a) which is disappeared after homogenization treatment and ECAP depicts in Figure 4.23 (b)-(d) due to diffusion annealing treatment and dynamic precipitation during the ECAP process. Further, Figure 4.23 (c) and (d) presents the XRD patterns for ECAPed AZ80 Mg alloys for 2P and 4P processed with die A at processing temperature 598K. It was observed that the peak intensities were increased after 4P ECAP when compared to the ECAP-2P sample. This is due to an increased volume fraction of secondary phases and more homogeneous microstructure. But 2P ECAP processed sample presented lower peak intensity this is mainly due to non-homogeneity in the microstructure and crystal defects. Furthermore, Figure 4.23 (e)-(h) shows the XRD spectra of AZ91 Mg alloy e) as-received f) the homogenized at 673K for 24 h g) the two-passed AZ91 Mg alloy ECAPed with die A at 598K and h) the four-passed AZ91 Mg alloy ECAPed with die A at 598K. Regardless of the number of ECAP pass, the as-received and processed samples contained  $\alpha$ -Mg and  $\beta$ -Mg<sub>17</sub>Al<sub>12</sub> phase. The intensity of the peak in the ECAP processed specimens at 598K is lower

than that of the as-received specimen. Also, it can be seen that there exists great difference on the magnitude of peak intensity of ECAP processed specimen at 598K for two and four passes this is mainly due to induced plastic strain during ECAP similar results has been observed by Avvari et al. 2016.

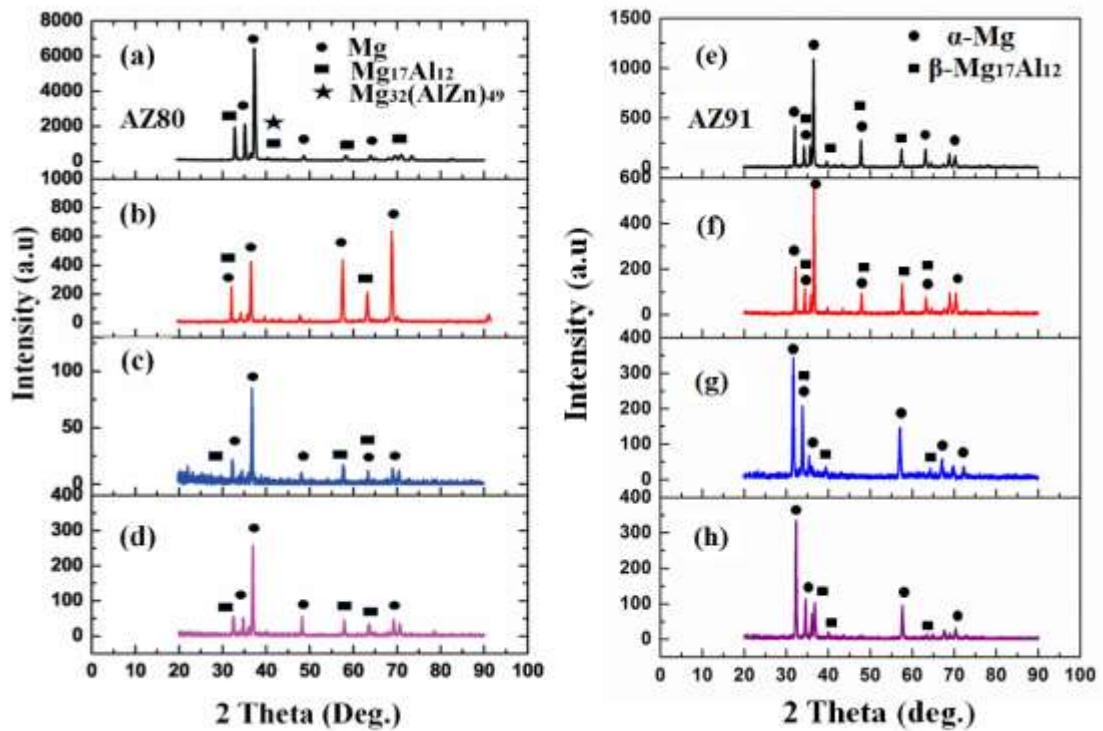


Figure 4.23 XRD analysis on AZ80 Mg alloys a) as-received b) Homogenized at 673K-24h c) Die A: 2P at 598K d) Die A: 4P at 598K. XRD analysis on AZ91 Mg alloys e) as-received f) Homogenized at 673K-24h g) Die A: 2P at 598K and h) Die A: 4P at 598K

#### 4.5 MECHANICAL BEHAVIOUR

This section explains the effect of ECAP die channel angle and processing temperature on mechanical properties of as-received and ECAPed AZ80/91 Mg alloys. Also, presents the fractography study on fractured surfaces of as-received and ECAPed AZ80/91 Mg alloys.

#### 4.5.1 Effect of die parameters and processing temperature on microhardness

Figure 4.24 shows the impact of channel angle on microhardness during ECAP of AZ80/91 Mg alloys. From the results, it was observed that AZ80/91 Mg alloy processed through lower channel angle of 90° (die A) exhibited enhanced microhardness when compared to material processed through die B at 598K after 4 Passes of ECAP. The improved microhardness is mainly due to the accumulation of large plastic strain while processing at 90° channel angle and obtained more equiaxed microstructure. Hence, die A which has 90° channel angle is considered as an optimal die parameter in order to get the highest microhardness for both AZ80/91 Mg alloys. Also, from Fig. 4.24 it was established that there is a significant increase in microhardness after a four pass of ECAP in AZ91 Mg alloy after processing using a die A compared to AZ80 Mg alloy processed through the same die and this is anticipated from measurements of the effective refinement of grain size. Furthermore, a variation of microhardness at three different temperature through die A for AZ80/91 Mg alloys were discussed.

Figure 4.25 demonstrates the effect of ECAP processing temperature on the microhardness of the AZ80/91 Mg alloys subjected to ECAP process at three different processing temperature. From literature, ECAP caused an increase of microhardness with an increase of ECAP passes. In the present work, it can be seen from Figure 4.25 increase of ECAP passes caused an increment in microhardness of the AZ80/91 Mg alloys. However, specifically for AZ80 Mg alloys by increasing ECAP processing temperature from 533K to 598K, the microhardness of the specimen decreases about 4.5 % after 4P-ECAP, while increasing ECAP temperature from 533K to 663K decreases the microhardness considerably, this decrease is about 9 % after ECAP-4P. Also, for AZ91 Mg alloys by increasing ECAP processing temperature from 533K to 598K, the microhardness of the specimen decreases about 3% after 4P-ECAP, while increasing ECAP temperature from 533K to 663K decreases the microhardness considerably, this decrease is about 8.6 % after ECAP-4P. Also, maximum microhardness of Alloy processed after 4 ECAP passes showed 90.32 Hv at 533K, which is 25 % higher than that of as-received AZ91 alloy. The increased microhardness mainly results from the sum of the effects of grain refinement and  $\beta$ -Mg<sub>17</sub>Al<sub>12</sub> phase

fragmentation, partial dissolution and distribution (Naik et al., 2019), which is evidently shown through microstructure discussed in the previous section.

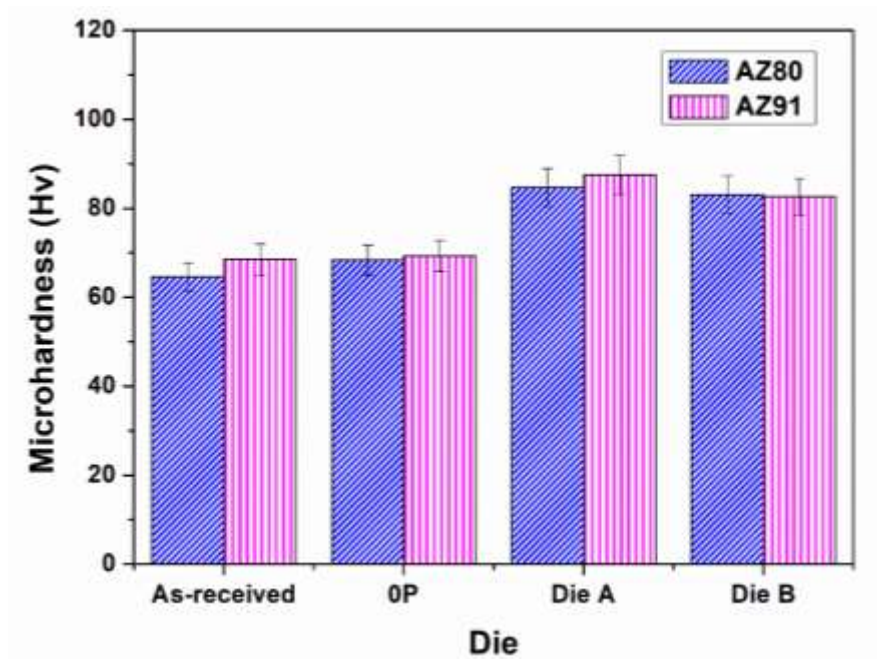


Figure 4.24 Variation of microhadness for AZ80/91 Mg alloys after processing through two different dies

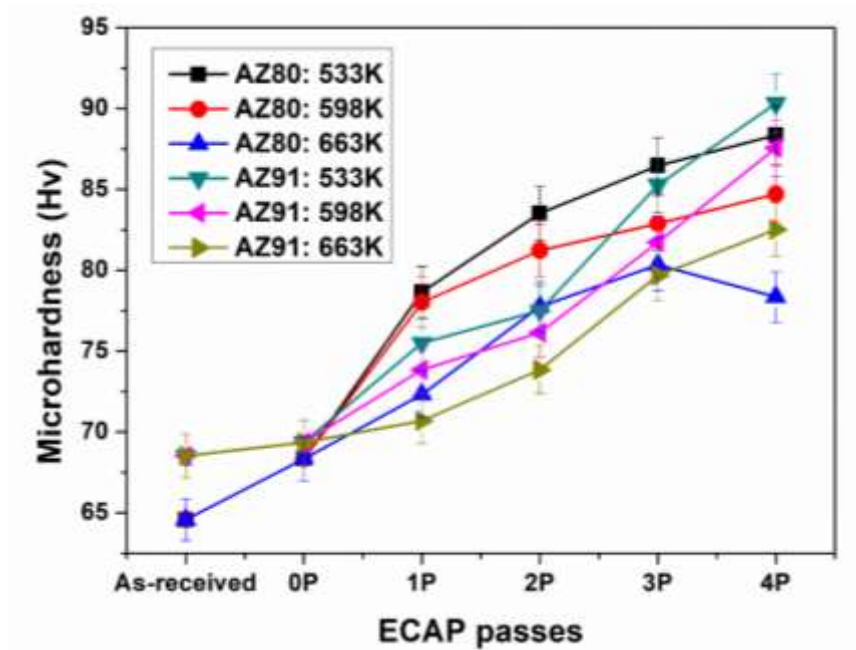


Figure 4.25 Variation of microhardness for different processing temperatures.

Further, the significant decrease of microhardness at higher processing temperature this is mainly due to thermal softening effect at a higher temperature. Similar observation is made on AZ61 Mg alloy by Avvari et al. (2016) and AZ80 Mg alloys by Naik et al. (2019). Therefore, the significant outcome is that the influence of ECAP passes on the microhardness increment decreases with increasing ECAP temperature from 533K to 663K for both materials. Also, it is observed that AZ91 alloy processed at 533K through ECAP showed higher microhardness compared to AZ80 Mg alloy.

#### **4.5.2 Variation of tensile strength with two different die and processing temperature**

The engineering stress-strain curves of un-ECAPed and ECAPed AZ80/91 Mg alloys at two different dies are shown in Figure. 4.26. Information regarding ultimate tensile strength (UTS) and ductility of the un-processed and the processed AZ80/91 Mg alloys for various temperature were also presented in figures 4.27 and 4.28 respectively. The stress-strain curves show that ultimate tensile strength and ductility of ECAP-4P processed AZ80 specimens at 598K are about 489.17MPa, and 19.03%, respectively for die A, Along with this, the same material processed through die B 4P-ECAP exhibited UTS and %elongation is 451.01MPa and 11.76% respectively, which are higher than that of as-received and homogenized specimen of AZ80 Mg alloys. Similarly, the AZ91 Mg alloy processed through die A has greatly improved ultimate tensile strength and ductility. Particularly, as-received AZ91 alloys have 372.74 MPa and 7.84 % of UTS and ductility respectively, which is further enhanced to 432.81 MPa and 19.13% after processing through die A for 4 passes and 410.35 MPa and 13.22 % of ultimate tensile strength and ductility was observed after processing through die B for 4 passes. From this result, it was found that compared with the ECAPed AZ91 Mg alloys processed with die A, the AZ80 Mg alloy processed through die A exhibited enhanced tensile properties compared to die B. This is due to an induced large amount of plastic strain during ECAP. Further, Figures 4.27 and 4.28 shows the mechanical properties of AZ Mg alloys before and after ECAP processing with die A up-to 4 ECAP passes at 533K, 598K and 663K. The ECAP processing temperature is a significant factor that affects the mechanical properties of the AZ80/91 Mg alloys after ECAP. AZ80 Mg alloys processed at 533K, the strength increased significantly. For instance,



the ultimate tensile strength (UTS) and ductility increased to 470.98 MPa and 16.36 %, respectively, after four ECAP passes about 15 % and 60 % higher than the sample before ECAP.

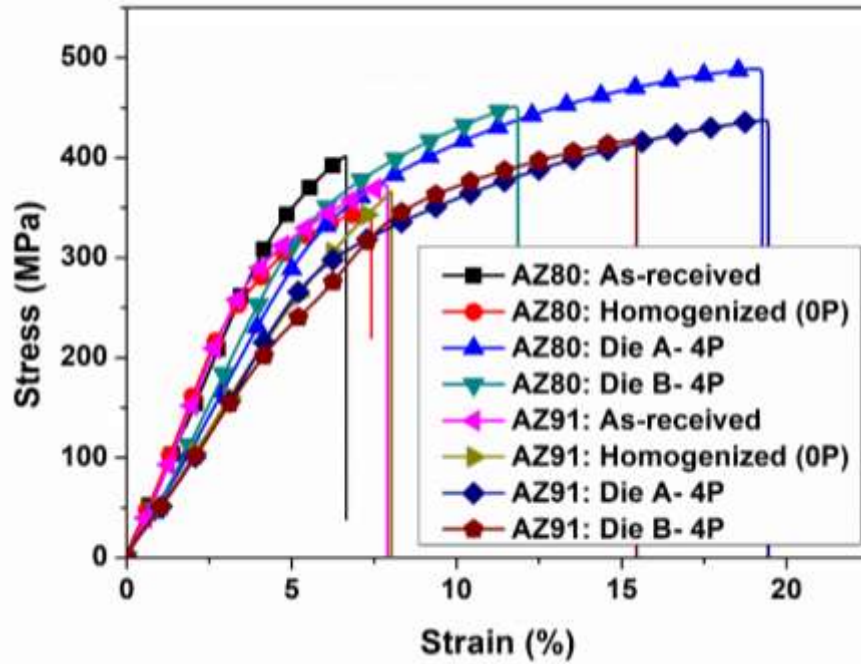


Figure 4.26 Variation of tensile strength for different ECAP die

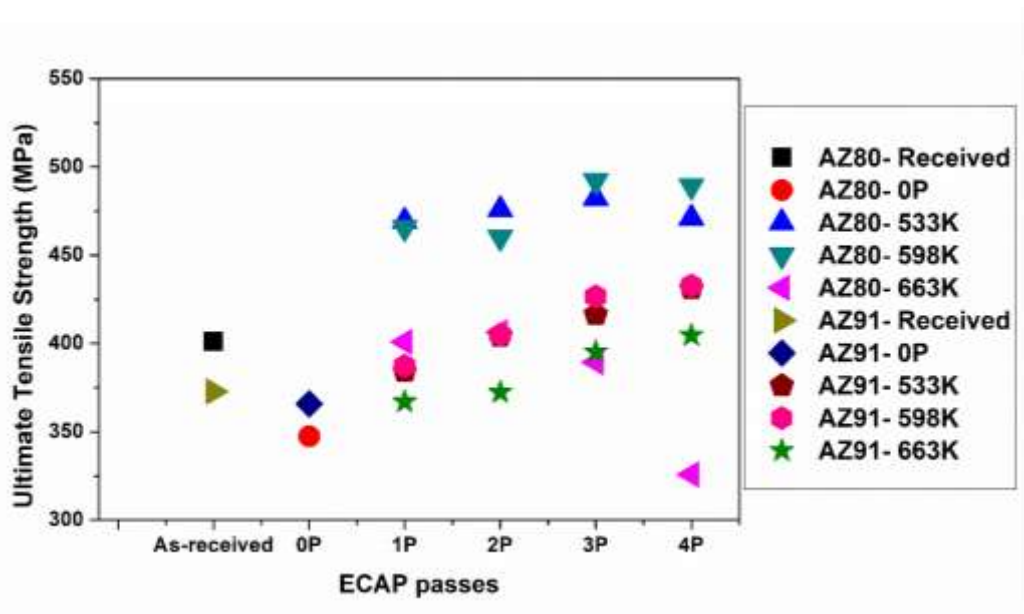


Figure 4.27 Variation of Ultimate Tensile Strength for different processing temperature

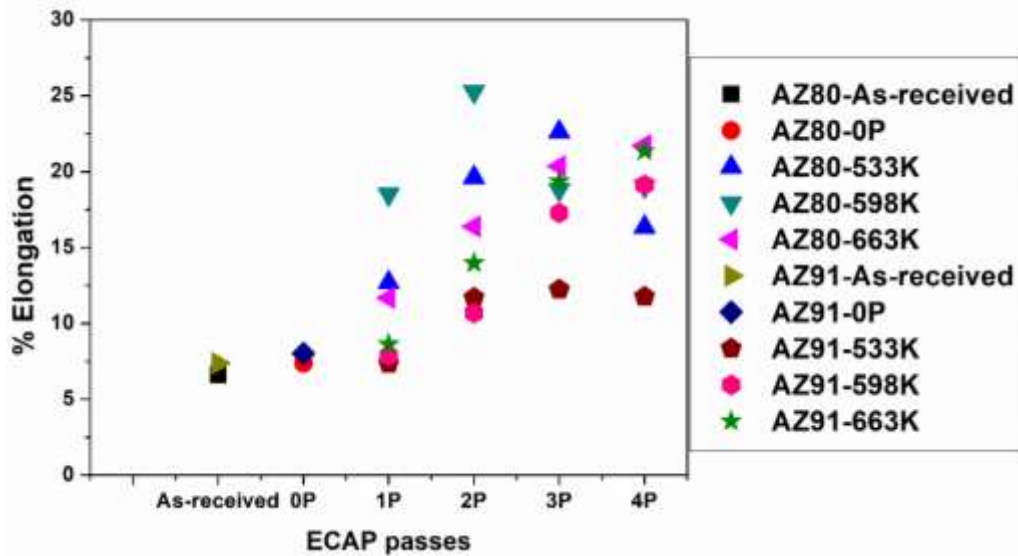


Figure 4.28 Variation of % elongation for different processing temperature

At 663K, the UTS and ductility were 498.10 MPa and 19.03 %, respectively after four ECAP passes, which is lower than the values at 533K and 598K. By contrast, a clearly visible decreasing trend in strength was observed in the sample that underwent ECAP at 663K. However, the elongation of the samples for all the passes ECAP increased with the increase in temperature, as shown in Figure 4.28. Apparently, the ultimate tensile strength (UTS) and % elongation were improved after ECAE processing compared with the as-received alloy. However, simultaneous growth in both tensile strength and % elongation with an increasing number of ECAP passes were observed, this enhancement is mainly due to grain refinement (Shaeri et al., 2016; Chiu et al., 2018; Shahzad et al., 2009). In addition, AZ91 Mg alloy after ECAP 2P and 4P achieved higher ductility and ultimate tensile strength respectively. It is reported that after 4P of ECAE at 598K the percentage increase of UTS and elongation is 14 % and 59 % respectively. Also, further decrease of UTS and ductility was observed by increasing the ECAP processing temperature which is shown in figures 4.27 and 4.28 evidently this is mainly due to thermal softening and grain growth effect. Similarly, Xia et al. (2008) observed the continuous improvement in hardness, tensile strength and ductility of the AZ31 Mg alloy during ECAP. Along with this the continuous improvement of tensile strength and ductility was observed during ECAP for both AZ Mg alloys. As a

comparison, the data plot for % elongation for three different processing temperature up to 4 ECAP passes as shown in Figures 4.27 and 4.28. From Figures 4.27 and 4.28, it was disclosed that after ECAE, UTS and % elongation increased noticeably. This result would be affected by the refinement of grain size.

#### **4.6 FRACTOGRAPHY**

Figures 4.29 and 4.30 shows the in-situ SEM morphology of fractured surfaces of AZ80 and AZ91 Mg alloy after a tensile test for both processed and unprocessed samples. The fractured surface provides an understanding of deformation regimes in the tested sample, the nature of fracture and changes in grain refinement. Also, which contributes extensive evidence for the effect of grain refinement on the strength and ductility of ECAPed samples due to processing temperature and ECAP passes. In addition, the sample failure is due to slip mechanism such as void nucleation, void growth and coalescence are observed in the analysis (Upadhayay et al., 2018; Avvari et al., 2014; Gopi et al., 2016). Figure 4.29 (a) showed the fractured surface of the as-received AZ80 specimen. The fractured surface morphology reveals the presence of few dimples with non-homogenous grains distribution. Also, Figure 4.29 (a) shows that there are tearing ridges along the grain boundaries and brittle transgranular fracture, this contributes to poor mechanical properties. From, Figure 4.29 (b) it can be seen that homogenized Mg alloy showed dimples are moderately shallow compared to as-received fractured surface due to the slight improvement in ductility during homogenization treatment at 673K for 24h similar observation was made by Wang et al. (2016). Figure 4.29 (c) (d) and (e) represents the fractured surfaces of Mg alloy processed through ECAP-4P with die A at 533K, 598K and 663K respectively. During the tensile test intergranular cracks are initiated at the outer edge of the sample, these initiated cracks convert into transgranular cracks which propagate through the sample till they reach the intergranular sites on the other side. At the interface of the intergranular and transgranular zone, from slip bands initiates coalescence of voids leads to voids growth, cracks and sample fracture. A similar observation was reported by Upadhayay et al. (2018) during their study. Figure 4.29 (c) exhibited fewer dimples compared with Figure 4.29 (d) due to the fine grain structure of alloy during 4P-ECAP which results in higher tensile strength with reduced plasticity. This specifies that the crack growth

is decelerated upon contact with large grain boundaries in the sample. Further, Figure 4.29 (e) illustrates the fractured surface of ECAP 4P processed AZ80 Mg alloys through 90° die. Here, a similar observation was made on fractured features of Mg alloy processed at 533K and 598K but volume fraction of dimples formed in the 4P-90° die at 663K processed samples are more when compared with the 533K and 598K processed sample. This reveals the proof for improved plasticity of AZ80 Mg alloys processed at higher temperature. This is due to softening and coarsening of grains at elevated temperatures which weakens the grain boundaries this contribute towards improved ductility. Recently, Yuchun Yuan et al. (2016) experimented to study the effect of deformation temperature on the mechanical properties of ECAP Processed ZK60 Magnesium Alloy. Here, authors observed notable decrease in the yield strength and ultimate tensile strength, while the ductility was improved. Further, from Figure 4.29 (c) – (e) the complex fine dimples were observed on fractured surfaces of ECAPed samples this is maybe due to the decohesion of  $Mg_{17}Al_{12}$  secondary precipitates during a tensile test. Furthermore, Figure 4.30 (a)-(e) shows the SEM images of fracture morphologies of tensile specimens of as-received, homogenized alloys prior to ECAP and of AZ91 Mg alloys processed by four passes of ECAP with three processing temperatures. In Figure 4.30, the fracture morphology of the as-received and homogenized sample is characterized by the existence of cleavages over the entire surface indicating the brittle failure (Fig. 4.30 a and b). In the fracture surface of ECAPed samples Fig. 4.30 (c) – (e), the dimples exist with smaller in sizes. However, a small number of larger dimples can be observed on the fractured surface. In addition, the cleavage fractures are also observed in some area of the fracture surfaces. It is clear from Figure 4.29 and 4.30 that the small size dimples have a more regular shape, where the initial voids might initiate at grain boundary as the strain concentrator. This indicates that the dislocation induced by severe plastic deformation of ECAP piled up at the grain boundary. Furthermore, the smaller size of dimples in ECAPed samples indicating the grain refinement occurred due to ECAP processing.

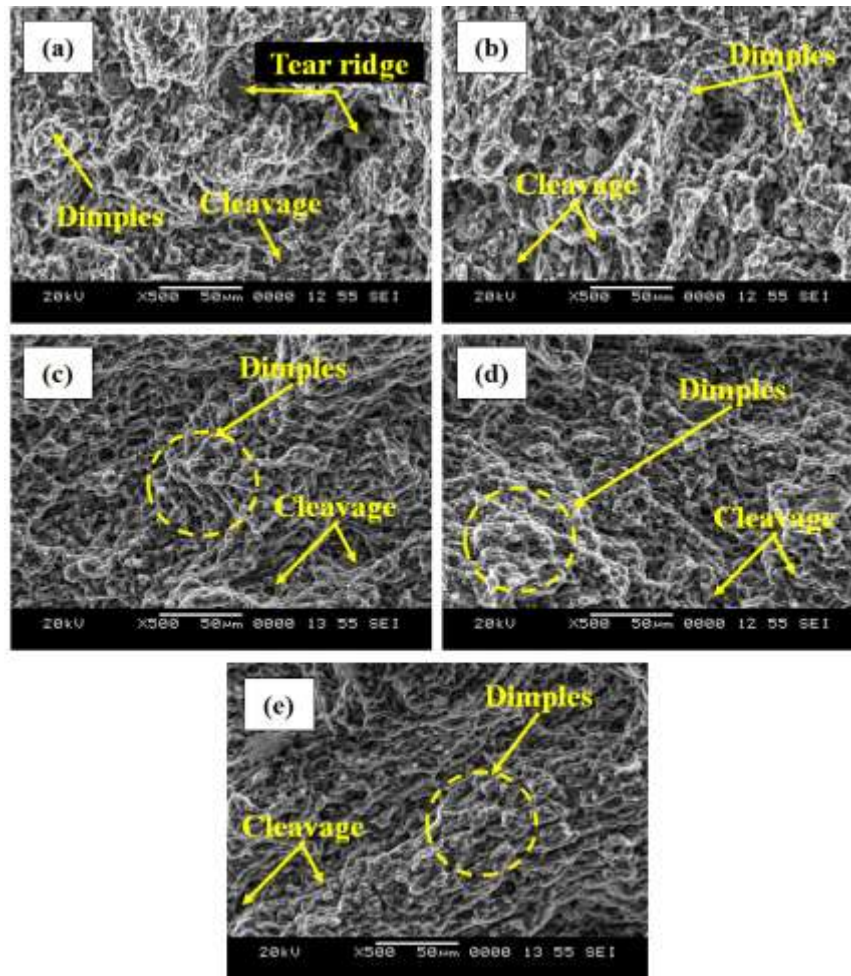


Figure 4.29 Fractured surface of AZ80 Mg alloys a) As-received b) Homogenized at 673K-24h c) 4P-533K d) 4P-598K and e) 4P-663K

Moreover, the fracture mode changed from a brittle fracture to a ductile fracture, and a large number of dimples appeared on the tensile fracture surface. However, Mg alloy processed at 533K of ECAP results in smallest dimples size when compared to other sample processed at 598K and 663K. This is consistent with the relatively highest tensile strength of ECAPed samples at 533K compared to that of other processing temperature. In over-all, surface observation of fractured samples revealed that void formation, coalescence and decohesion of secondary phase was dominant which leads to quasi-cleavage fractures (Avvari et al. 2016).

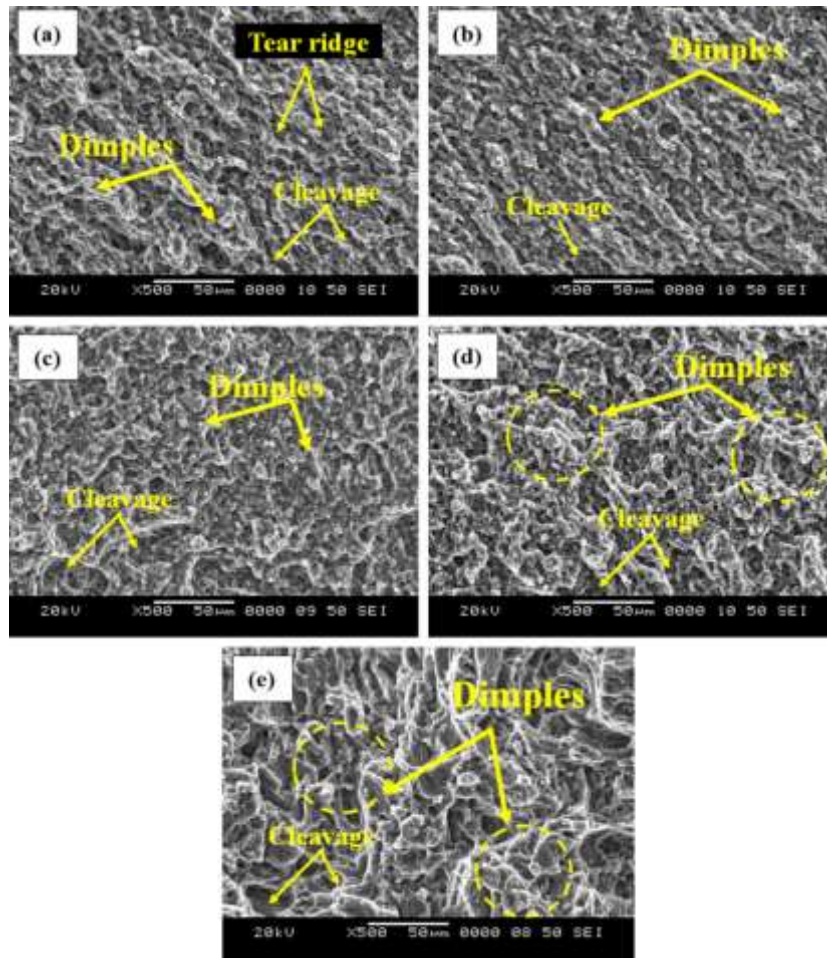


Figure 4.30 Fractured surface of AZ91 Mg alloys a) As-received b) Homogenized at 673K-24h c) 4P-533K d) 4P-598K and e) 4P-663K

## 4.7 CORROSION STUDY

This section illustrates the effect of ECAP die channel angle and processing temperature on corrosion behaviour of as-received and ECAPed AZ80/91 Mg alloys. Also, presents the morphology study on corroded surfaces of as-received and ECAPed AZ80/91 Mg alloys.

### 4.7.1 Effect of ECAP die and processing temperature on corrosion rate

The corrosion results of AZ80/91 Mg alloy processed through die A and die B at 598K after 4-ECAP passes including as-received and homogenized samples were shown in Figure 4.31. From figure 4.31, it was observed that the channel angle of ECAP significantly influences the grain refinement and distribution of secondary phases

which contribute towards corrosion resistance. ECAP processing through die A at 598K leads to lower corrosion rate after 4 passes of ECAP compared to die B under the same conditions for both AZ80/91 Mg alloys. This is mainly due to the lower dislocation density at recrystallization temperature (Gopi et al., 2015). Therefore the reduction of the grain size and the increase of the distribution of secondary phases can cause an improved corrosion resistance. In other words, the column chart shows the variation of corrosion rates of Mg alloys before and after ECAP process for both AZ Mg alloys. The corrosion potential ( $E_{\text{corr}}$ ), corrosion current ( $I_{\text{corr}}$ ), and corrosion rate (mm/year) obtained by using the potentiodynamic polarization curves are presented in Table 4.2 and 4.3. The more ECAP passes are related to the nobler corrosion potentials and the lower current density. The Mg alloy processed through die A and die B after four ECAP passes results that the ECAPed Mg processed through die A has nobler  $E_{\text{corr}}$  and  $I_{\text{corr}}$  values, leads to more corrosion resistance than the specimen extruded through die B, as-received and homogenized. Specifically, AZ91 Mg alloy processed through ECAP after 4 passes exhibited improved corrosion resistance than the ECAPed AZ80 Mg alloys this mainly due to elemental composition of AZ91 Mg alloy.

The results of the corrosion rates of AZ80 and AZ91 Mg alloys processed through ECAP for temperatures of 533K, 598K and 663K are shown in Figure 4.32 and presented in table 4.2 and 4.3. The corrosion rates are consistent with the corresponding microstructures at three different temperatures where the finer grain size and more uniform distribution of secondary phases lead to lower corrosion rates. Also, corrosion resistance was increased with respect to the number of ECAP passes. But, AZ80 Mg alloy processed at 533K showed reduced corrosion rate up-to 3-ECAP passes after 3P corrosion rate increased with the number of ECAP passes this is due to increased dislocation densities during processing at below recrystallization temperature. The processing of AZ80/91 Mg alloys at recrystallization temperature and above shows almost the same trend between 1 to 4 passes while measuring the corrosion rate. A corrosion rate drop in the ECAPed AZ80/91 Mg alloy was observed at 598K and 663 K compared to the AZ80/91 Mg alloy processed at 533K, thereby indicating a non-uniform distribution of secondary phases. The occurrence of secondary phases distribution leads to a lower corrosion rate after ECAP shown in Figure 4.32. At 598K

and 663 K, the corrosion rate show similar variations after 4 Passes of ECAP. From figure 4.32 it was observed that increasing the ECAP passes exhibited a clear shift in the corrosion rate to the lower corrosion rate, as compared with the as-received condition. The progressive decrease in the corrosion rate of the ECAPed samples is attributed to the modification of microstructure after ECAP processing (Argade et al., 2012; Atrens et al., 2013).

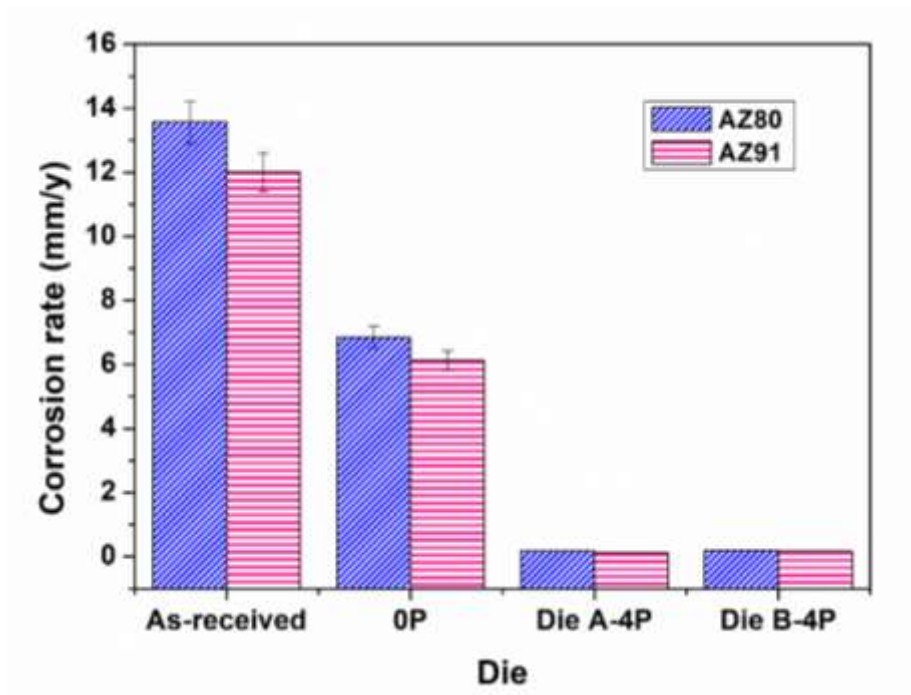


Figure 4.31 Corrosion rate vs ECAP die

Also, from figure 4.32, it was noticed that AZ80/91 Mg alloys processed through ECAP at higher processing temperature exhibited a lower corrosion rate when compared to the other two temperatures. This is mainly due to the reduction in the cathodic sites of the ECAPed samples after processing at a higher temperature can be considered as a result of the decrease in the size of secondary phase in the matrix. These phases act as cathodic sites as compared with the magnesium matrix. The anode/cathode ratio is more in the vicinity of the fine dispersed secondary phases than that in the sample processed at lower processing temperatures. Therefore, in the ECAPed sample processed at higher processing temperature, the secondary phases increased or distributed the



anode/cathode ratio in the magnesium matrix and consequently decreased the cathodic reaction leads to less corrosion rate. (Gobara et al., 2015; Chen et al., 2014).

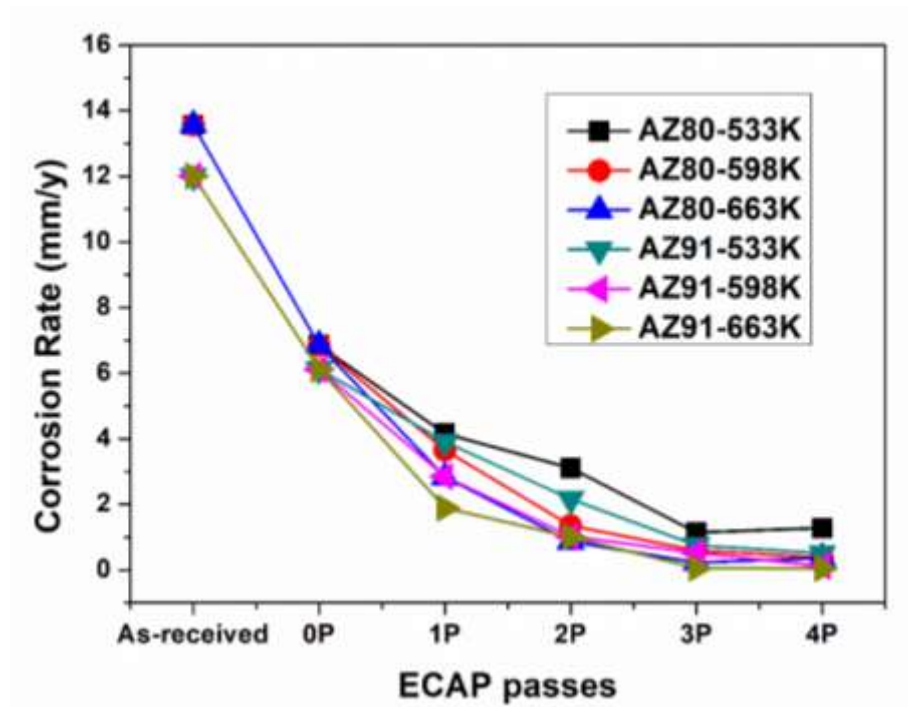


Figure 4.32 Corrosion rate vs the number of ECAP pass after processing through die A at three different temperatures

#### 4.7.2 Effect of grain size and distribution of secondary phases on corrosion behavior.

Figure 4.33 depicts the polarization plots for AZ80 and AZ91 Mg alloys processed with die A at 598K and measured  $E_{corr}$  and  $I_{corr}$  values are presented in Table 4.2. From Figure. 4.33 it was observed that the anodic branches of the unprocessed and processed AZ80 specimen showing the continuous active dissolution of the metal this indicate that AZ80 Mg alloy exhibit poor passivity (Gobara et al., 2015; Kakiuchi et al., 2015). Although,  $E_{corr}$  values of ECAP processed AZ80 Mg alloys are significantly shifted to the less negative potentials and highly reduced the magnitude of  $I_{corr}$  after 2 passes presented in table 4.2. A similar observation was made by Argade et al. (2012).

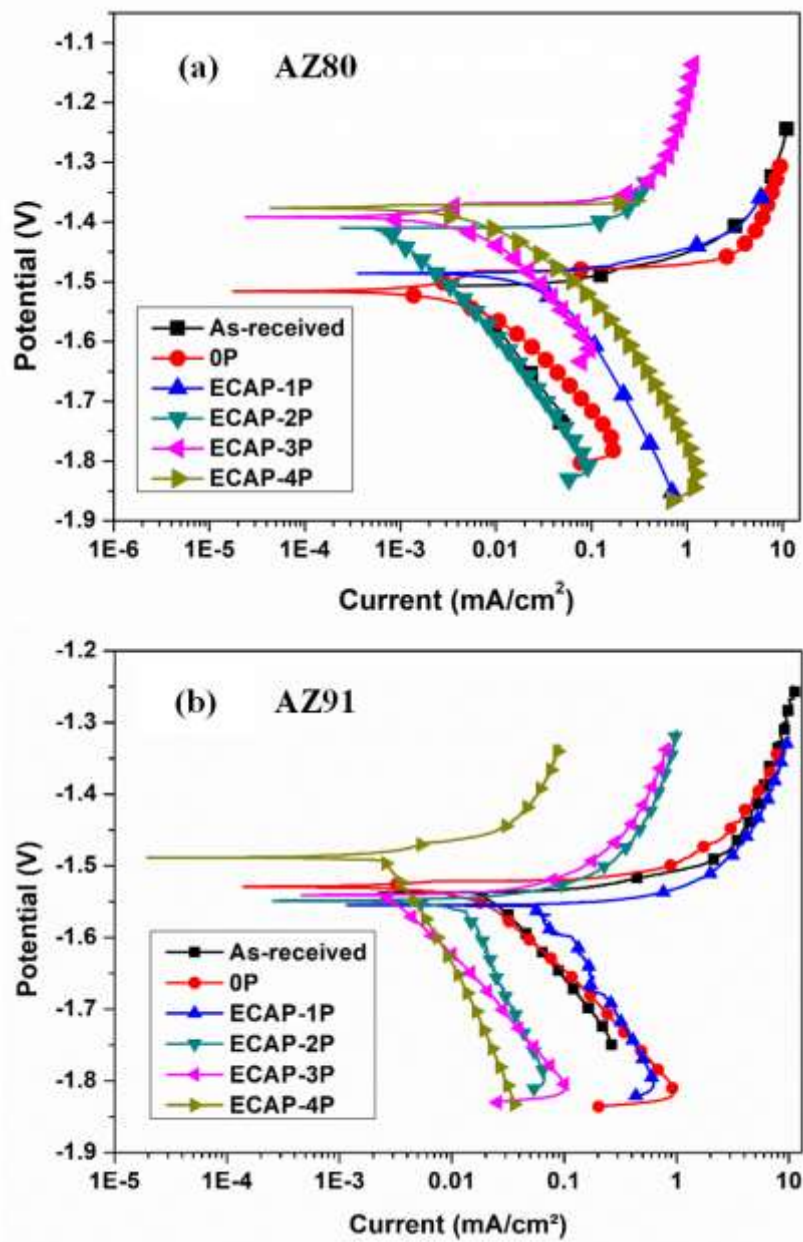


Figure 4.33 Polarization curves of Mg alloys processed through die A a) ECAPed AZ80 Mg alloys A and b) ECAPed AZ91 Mg alloys

Further, the polarization plot of the 4P ECAPed with 90° die exhibits a corrosion potential of -1.375 V<sub>SCE</sub> this is higher than corrosion potential of other ECAP passes. This indicates that AZ80 Mg alloy processed with 90° die sample has higher pitting corrosion resistance. Moreover, polarization results specify that the ECAPed AZ80 Mg processed with 90° die has nobler E<sub>corr</sub> values. Further, the potentiodynamic polarization curves of as-received and ECAPed AZ91 Mg specimens in 3.5wt.% NaCl

was also shown in Figure. 4.33. The experimental results revealed that the  $E_{\text{corr}}$ , corrosion potential of 4P-ECAPed AZ91 Mg alloys was  $-1.453V_{\text{SCE}}$ , which was less negative compared with the as-received alloy and other ECAP passes (Fig. 4.33). This phenomenon specifies that the cathodic reaction was more difficult in fine-grained Mg alloys compared to the coarse grain alloy. Therefore, with the ECAP, the corrosion potential ( $E_{\text{corr}}$ ) shifted to  $-1.536 V_{\text{SCE}}$  and  $-1.453 V_{\text{SCE}}$  after two and four ECAP passes which are considerably nobler in comparison with the as-received alloy ( $-1.540 V_{\text{SCE}}$ ). However, the corrosion potential increases with the grain refinement after ECAE in the alloy. Also, the corrosion current density ( $I_{\text{corr}}$ ) of 2P and 4P ECAPed AZ91 Mg alloy was  $0.0173 \text{ mA/cm}^2$  and  $0.0053 \text{ mA/cm}^2$  respectively, which is lesser than that of as-received AZ91 Mg alloy ( $0.0263 \text{ mA/cm}^2$ ). The obtained results revealed that the ECAPed Mg sample after 4 passes has nobler corrosion potential and lower current density when compared with as-received and ECAPed-2P. Therefore, ECAE increased the corrosion resistance of Mg alloy this is due to grain refinement and distribution of secondary phases. Which is evidently shown in OM and SEM microstructure in figure 4.19. Similarly, Shahar et al. (2017) explored that the grain refinement and secondary phase distribution through ECAP improves the corrosion resistance of Mg alloys.

#### **4.8 CORROSION MORPHOLOGY**

The corrosion morphologies of as-received and as-processed specimens of AZ80 and AZ91 Mg alloys immersed in 3.5wt.% NaCl solution observed through scanning electron microscopy and is shown in Figures 4.34 and 4.45. From Figure.4.34 (a) and (b), Figure.4.35 (a) and (b), it was observed the adequate amount of corrosion attack on the surface of the as-received and homogenized AZ80 and AZ91 Mg alloys after potentiodynamic polarization test. The ECAP performed samples of Mg alloys after the corrosion test exhibited comparatively less localized pits on the surface of ECAPed AZ80/91 Mg alloys have shown in Figure 4.34 (c)-(e) and 4.35 (c)-(e). This obtained result showed that pitting corrosion resistance of ECAPed Mg alloys are significantly improved through grain refinement and this is due to distribution of secondary phases (Lunder et al., 1994 and Singh et al., 2015). Also, from figures 4.34 (e) and 4.35 (e), it is observed that AZ80/91 Mg alloy processed at 663K exhibited improved pitting corrosion resistance. Remarkably, AZ80/91 Mg alloy processed at the higher

temperature (663K) revealed that decreased corrosion attack when compared with the Mg alloy processed at 533K and 598K shown in Figures 4.34, 4.35. From the study, the less corrosion attack of the AZ80/91 Mg alloy was stated due to better distribution of Mg<sub>17</sub>Al<sub>12</sub> secondary phases at higher processing temperature (663K). The process also proved that the Mg alloy processed through 90° ECAP die had higher corrosion pitting resistance in the chloride solution (table 4.2 and 4.3). It is worth to declare that this appeared improved for AZ80/91 Mg alloy was due to the grain refinement, distribution of secondary phases and formation of magnesium hydroxides formed on their surfaces. Which evidently proved through microstructure and X-ray diffraction analysis shown in Figures 4.34 (f) and 4.35 (f) for AZ80 and AZ91 Mg alloys respectively. The existence of such metal oxide partially protects the Mg surface from further dissolutions under this circumstance the breakdown of the film and the consequential nucleation and growth of a pit become more difficult. Moreover, the higher  $E_{\text{corr}}$  value for ECAPed Mg alloys at higher passes revealed that the surface of Mg alloys was more passivated against corrosion this is due to slow dissolution rate of fine grains structure (Wenming et al., 2017; Lunder et al., 1994). Finally, from the results, it was concluded that the severe corrosion attack was observed on as-received AZ80 and AZ91 Mg alloys and further continuous reduction in corrosion attack was observed for ECAPed samples. Further, corrosion attacks were minimal when AZ80/91 Mg alloys processed at 663K, specifically, ECAPed AZ91 Mg alloys processed at 663K undergo less corrosion attack due to uniform distribution of secondary phases and elemental composition of AZ91 Mg alloy. Similar kind of results and trends was reported by many authors in their studies (Ambat et al. 2000, Zeng et al. 2006, Yunchang et al. 2010 and Cheng et al. 2009).

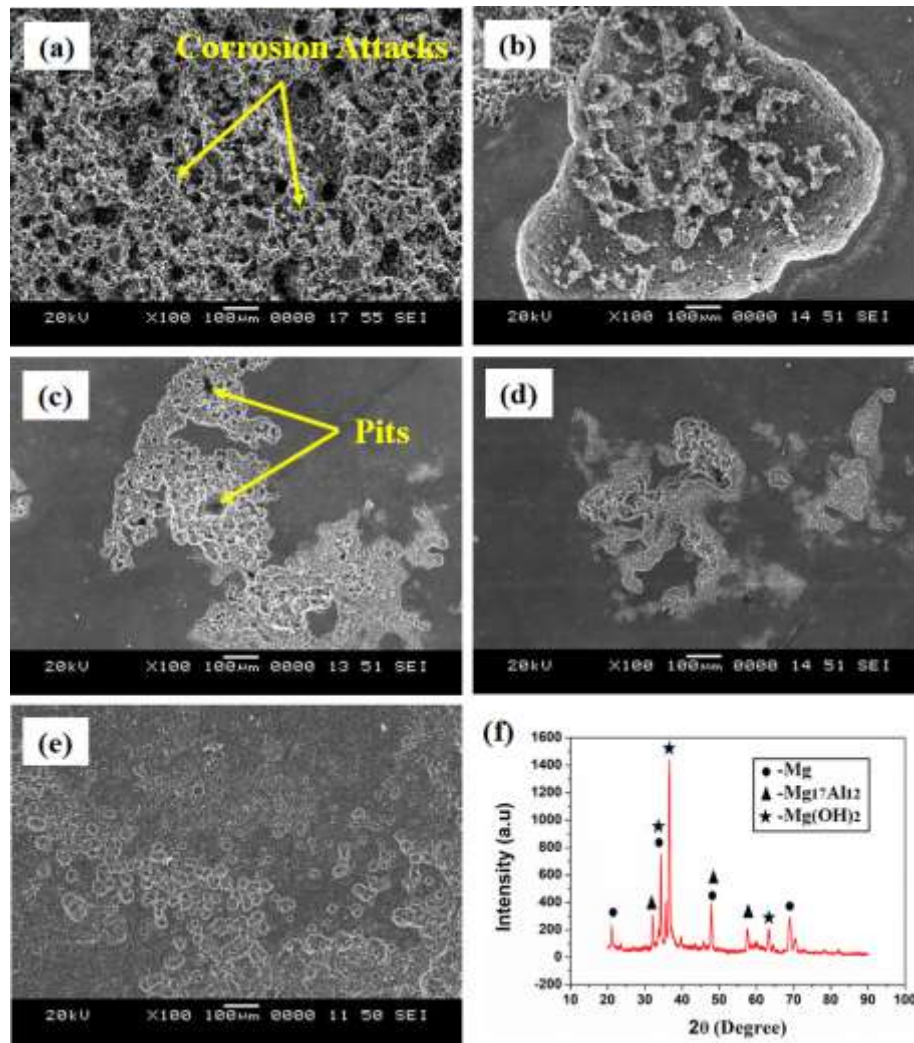


Figure 4.34 Corrosion morphology of AZ80 Mg alloys a) as-received b) Homogenized at 673K-24h c) 4P-533K d) 4P-598K e) 4P-663K and f) XRD for corroded specimen of as-received

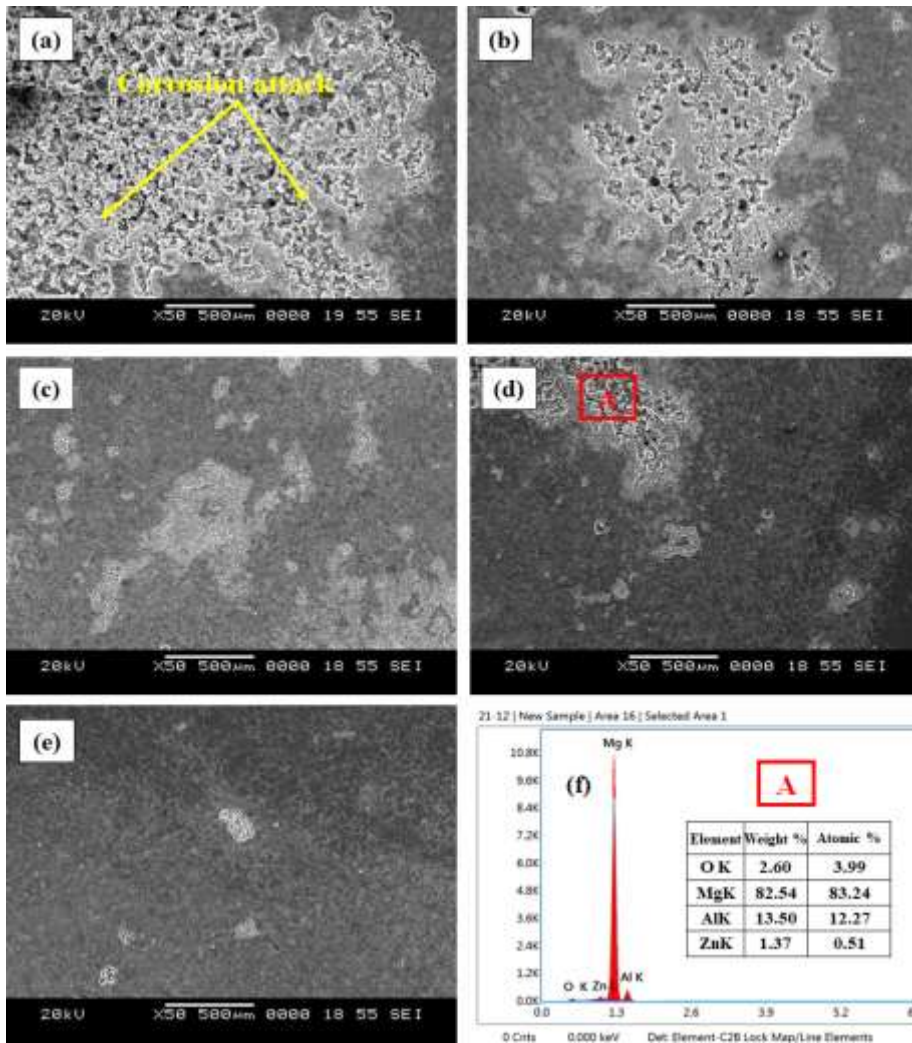


Figure 4.35 Corrosion morphology of AZ91 Mg alloys a) as-received b) Homogenized at 673K-24h c) 4P-533K d) 4P-598K e) 4P-663K and f) EDX for corroded specimen of as-received

Table 4.1 Data Sheet of AZ80 Mg alloy processed with die A and die B

AZ80 Mg alloy processed through Route-R																	
Temp	ECAE Passes	Die A (90° die angle)								Die B (110° die angle)							
		GS (μm)	UTS (MPa)	%E (%)	E (MPa)	MH (Hv)	E <sub>corr</sub> (V)	I <sub>corr</sub> (mA/cm <sup>2</sup> )	CR (mm/y)	GS (μm)	UTS (MPa)	%E (%)	E (MPa)	MH (Hv)	E <sub>corr</sub> (V)	I <sub>corr</sub> (mA/cm <sup>2</sup> )	CR (mm/y)
R.T	As-R	50.20	401.19	6.61	8438.3	64.58	-1.547	0.297	13.563	50.20	401.19	6.61	8438.3	64.58	-1.547	0.297	13.563
673K	0P	50.75	347.43	7.37	7620.1	68.34	-1.480	0.15	6.850	50.75	347.43	7.37	7620.1	68.34	-1.480	0.15	6.850
533K	1P	35.22	469.30	12.69	6269.3	78.65	-1.421	0.091	4.156	39.47	376.23	10.63	6278.3	72.60	-1.536	0.095	4.338
	2P	26.34	475.89	19.63	6458.9	83.53	-1.411	0.068	3.105	34.58	487.80	15.33	6128.3	82.37	-1.523	0.087	3.973
	3P	15.62	482.36	22.63	6425.8	86.47	-1.401	0.025	1.142	18.22	461.37	11.46	6236.5	83.45	-1.510	0.036	1.644
	4P	5.12	470.98	16.36	5896.3	88.36	-1.413	0.028	1.279	8.65	394.11	12.03	6128.6	85.12	-1.569	0.042	1.918
598K	1P	38.11	465.49	18.51	5592.5	78.02	-1.514	0.08	3.653	43.48	362.37	15.74	6533.5	70.68	-1.527	0.047	2.146
	2P	28.87	460.09	25.27	5402.8	81.22	-1.451	0.0295	1.347	36.14	472.28	27.63	4801.7	81.63	-1.501	0.031	1.416
	3P	16.41	492.08	18.82	4491.4	82.88	-1.430	0.013	0.594	20.42	437.51	19.29	5412.1	80.53	-1.523	0.018	0.822
	4P	6.35	489.17	19.03	5412.1	84.71	-1.412	0.0084	0.384	9.77	451.01	11.76	6647.9	83.14	-1.520	0.009	0.411
663K	1P	43.52	400.95	12.69	5236.9	72.32	-1.475	0.062	2.831	40.33	340.45	13.69	5136.7	70.66	-1.512	0.081	3.699
	2P	37.26	406.38	16.38	5124.2	76.75	-1.423	0.019	0.868	38.62	403.10	19.31	5236.4	72.68	-1.501	0.031	1.416
	3P	26.38	389.41	20.36	5632.2	80.34	-1.416	0.005	0.228	22.15	368.21	16.98	5031.6	73.42	-1.468	0.007	0.320
	4P	10.54	325.85	23.74	4987.5	78.36	-1.411	0.008	0.365	11.68	293.82	11.57	4836.7	78.63	-1.421	0.0091	0.416

Table 4.2 Data Sheet of AZ91 Mg alloy processed with die A and die B

AZ91 Mg alloy processed through Route-R																	
Temp	ECAE Passes	Die A (90° die angle)								Die B (110° die angle)							
		GS (μm)	UTS (MPa)	%E (%)	E (MPa)	MH (Hv)	E <sub>corr</sub> (V)	I <sub>corr</sub> (mA/cm <sup>2</sup> )	CR (mm/y)	GS (μm)	UTS (MPa)	%E (%)	E (MPa)	MH (Hv)	E <sub>corr</sub> (V)	I <sub>corr</sub> (mA/cm <sup>2</sup> )	CR (mm/y)
R.T	As-R	58.69	372.74	7.84	7237.2	68.52	-1.539	0.263	12.010	58.69	372.74	7.84	7237.2	68.52	-1.539	0.263	12.010
673K	0P	59.82	365.96	8.02	7121.6	69.35	-1.523	0.134	6.122	59.82	365.96	8.02	7121.6	69.35	-1.523	0.134	6.122
533K	1P	49.56	384.23	7.36	6689.8	75.50	-1.520	0.0855	3.905	50.63	375.32	8.21	6487.3	73.49	-1.511	0.0952	4.348
	2P	30.52	404.27	11.69	6388.2	77.50	-1.536	0.0473	2.160	32.47	403.68	15.3	6428.9	76.28	-1.530	0.0612	2.795
	3P	18.69	416.35	12.23	6628.1	85.28	-1.501	0.0165	0.754	20.12	409.98	19.36	6534.6	82.11	-1.521	0.021	0.959
	4P	4.36	451.01	11.76	6086.2	90.32	-1.495	0.0113	0.516	5.28	425.37	21.15	6235.3	88.36	-1.502	0.0233	1.064
598K	1P	50.68	387.36	7.86	5932.5	73.85	-1.523	0.0624	2.850	52.45	382.98	9.28	5836.8	71.87	-1.512	0.1245	5.686
	2P	30.86	392.12	10.68	6417.3	76.14	-1.448	0.0224	1.023	33.24	400.64	11.69	5778.2	74.08	-1.531	0.0617	2.818
	3P	21.54	416.69	14.28	5487.1	81.74	-1.421	0.0114	0.521	22.63	405.42	10.32	5873.8	80.17	-1.524	0.0154	0.703
	4P	7.58	432.81	19.13	5585.9	87.57	-1.418	0.0026	0.119	9.14	410.35	13.22	5423.5	82.61	-1.526	0.0036	0.164
663K	1P	52.23	366.96	8.63	5587.3	70.69	-1.511	0.0414	1.891	53.68	378.39	9.34	5368.2	69.58	-1.526	0.061	2.786
	2P	43.96	372.3	13.98	5512.7	73.85	-1.491	0.0221	1.009	44.15	386.23	13.68	5428.3	70.35	-1.538	0.0201	0.918
	3P	25.36	395.17	19.36	5287.3	79.68	-1.481	0.00135	0.062	27.19	396.47	16.78	5235.7	74.89	-1.523	0.00142	0.065
	4P	11.85	404.62	21.36	4796.6	82.53	-1.461	0.00111	0.051	12.48	401.28	14.36	4589.3	79.55	-1.522	0.00125	0.057



## 4.9 SUMMARY

AZ80 Mg alloy processed through both die A and die B at three different temperatures such as 533K, 598K and 663K were discussed in this chapter. Indeed, Mg alloy processed through die A has significantly shown fine grains than die B. Since the grain size and distribution of secondary phases are major factor in determining the strength and corrosion resistance of the material respectively, therefore die A is considered as optimal to achieve fine grain structure in our work. As a result the fine grains obtained through die A exhibited improved mechanical and corrosion resistance evidently discussed in the earlier sections. The AZ Mg alloy processed at 533K, 598K and 663 K. At 533K and 598 K, no grain growth occurs during ECAP processing but it is noticed at 663K. The grain refinement appears to result from a fragmentation of the larger grains by twinning due to the severe shear deformation. Specifically, the formation of a large population of small recrystallized grains at the original grain boundaries and the fragmentation of the secondary phases which serves enhanced mechanical and corrosion behavior of Mg alloys. The maximum strength is achieved for the temperatures of 533K and 598 K, minimum corrosion rate was achieved at 663K. These results confirm the advantage of processing the AZ80 and AZ91 alloy at a relatively lower temperature and higher temperature. Thus, processing at recrystallization temperature 598K avoids the problem of grain growth, produce more homogeneous grain structure and enhanced corrosion resistance without compromising mechanical characteristics. Therefore, further investigation were carried out for AZ Mg alloys processed through die A at 598K.

Also, based on the experimental results and discussion, the following conclusions were drawn.

- Increase in ECAP passes lead to homogeneous microstructure due to dynamic recrystallization which occurred during ECAP process. The secondary  $\beta$ -Mg<sub>17</sub>Al<sub>12</sub> phase was reduced and uniformly distributed throughout the extruded material. Here, the effectiveness of ECAP with die A in grain refining of AZ80/91 Mg alloys was quite significant because of imposing large plastic strain of ~4.06 after four ECAP passes.

- The average grain size of AZ80 and AZ91 Mg alloy was found to be reduced to 5.12  $\mu\text{m}$  and 4.36  $\mu\text{m}$  respectively after processing through die A at 533K.
- According to the microstructural observations, Optical microstructural studies establish that increasing ECAE processing temperature leads to an increase in the grain size due to grain growth effect.
- Microhardness, ultimate tensile strength and ductility for both AZ80 and AZ91 Mg alloy has been enhanced by refining grain size with increasing number of passes. Ultimate tensile strength of the AZ91 Mg alloy decreased when compared to AZ80 Mg alloy after ECAP this is due to the presence of the secondary  $\beta\text{-Mg}_{17}\text{Al}_{12}$  phase. Also, SEM fractured surfaces in all the three temperatures of ECAP-4P samples reveals dimples which shows the ductile brittle fracture.
- Mechanical properties such as ultimate tensile strength, ductility and microhardness of the AZ80/91 Mg alloy is directly proportional to the ECAE passes but it has an inverse effect on ECAE processing temperature.
- Potentiodynamic polarization test showed reduced corrosion current density ( $I_{\text{corr}}$ ) which indicates higher corrosion resistance for the ECAP processed samples due to the presence of equiaxed fine grain microstructure and homogeneously distributed secondary particles ( $\text{Mg}_{17}\text{Al}_{12}$ ).
- Polarization results showed that passive behavior of ECAPed AZ80/91 Mg sample enhances compared to as-received AZ80/91 Mg alloy owing to the grain refinement and distribution of secondary phase. An AZ80/91 Mg alloys processed with die A ( $90^\circ$ ) showed higher pitting corrosion resistance compared to die B ( $110^\circ$ ), by showing less negative pitting potential during 4P-ECAP. Also, the obtained polarization data have good agreement with the corrosion surface morphology.
- The electrochemical corrosion of AZ80/91 Mg alloys exhibited better corrosion resistance after ECAP at higher processing temperature of 663K compared to lower processing temperature 533K, this revealed a 71 % and 90 % improved corrosion resistance for AZ80 and AZ91 Mg alloy respectively.

## **CHAPTER 5**

### **CORROSION BEHAVIOR OF ECAPED AZ80/91 MAGNESIUM ALLOYS AFTER ANNEALING TREATMENT, COATING AND IN DIFFERENT ENVIRONMENT**

#### **5.1 INTRODUCTION**

In our previous chapter, we showed the positive impact of ECAP processing on the corrosion behaviour of the AZ80 and AZ91 magnesium alloy. It was observed that in the fine grain AZ80/91 Mg alloys after ECAP, the stability of the corrosion layer improved with decreasing grain size and uniform distribution of secondary phases. Therefore, overall corrosion resistance of the ECAPed AZ80/91 Mg alloys was enhanced. In case further enhancement of corrosion resistance which is effectively improved by annealing and aging treatment without significant grain growth. The objective of this chapter is to investigate corrosion resistance of the as-received and ECAP-2P, 4P samples of AZ80/91 magnesium alloy after annealing at the temperature range from 523K, 623K and 723K for 6h and 12h aging temperature to correlate corrosion resistance with microstructure of the AZ80/91 Mg alloys under study. On the other hand, High-Velocity Oxygen Fuel (HVOF) coating technique was used to improve the corrosion resistance of as-received and ECAPed AZ80/91 magnesium alloys. Further, the effectiveness of a corrosion resistance of ECAPed AZ80/91 magnesium alloys were studied in 2.5wt.% NaCl, 3.5wt.% NaCl solution and natural seawater. Which are detailed in the following sections.

#### **5.2 ANNEALING AND AGING TREATMENT ON MICROSTRUCTURE OF AS-RECEIVED AND ECAPED AZ80/91 MAGNESIUM ALLOYS**

The effect of annealing and aging treatment on microstructure of as-received and ECAPed AZ80 and AZ91 Magnesium alloy was reported in this section. Annealing at 523K, 623K, and 723K was accomplished, and the samples were cooled in the furnace after 6 h and 12 h of holding. Microstructure of AZ80 and AZ91 alloy has been observed under microscopy and the results were reported. Here, an attempt has been

made to enhance the corrosion resistance of the AZ80/91 Mg alloys by changing its microstructure with the help of annealing and aging treatment.

### 5.2.1 Microstructure evolution of as-received AZ80 Mg alloys

Figure. 5.1 (a)-(f) shows the micrograph of the as-received AZ80 Mg alloy annealed at 523K, 623K, 723K for 6 h and 12h. Where significant precipitation of secondary phases in Mg matrix and a narrow eutectic is revealed and clearly presents the presence of  $\alpha$ -Mg matrix and  $\beta$ -Mg<sub>17</sub>Al<sub>12</sub> secondary phases. Annealing treatment leads to a reduction in the area fraction of  $\beta$ -Mg<sub>17</sub>Al<sub>12</sub> phases compare to an as-received alloy which assists to improve the corrosion resistance. Figure 5.1 (a) (b) (c) and (d) shows the SEM images of the annealed AZ80 alloy of 523K-6h, 523K-12h, 623K-6h and 623K-12h respectively. Eutectic  $\beta$ -Mg<sub>17</sub>Al<sub>12</sub> phases and discontinuous  $\beta$ -Mg<sub>17</sub>Al<sub>12</sub> phases are revealed and distributed at the grain boundaries, which was shown in the form of the network at the grain boundaries and eutectic phases were observed in the specimen with aging, the dendrite structure and the secondary phases within the grains distributed completely during aging from 6h to 12h. Figure 5.1(e) and (f) presented the continuous precipitation (CP) and discontinuous precipitation (DP) of phases during annealing treatment at 723K-6h and 12h respectively. Moreover, the AZ80 Mg alloys under different annealing treatment conditions microstructure revealed a very fine uniform distribution of secondary phases at higher annealing temperature when compared to sample treated at the lower annealing temperature. As the holding time extends to 6 h and 12h the secondary phase precipitates resulting in an increase of precipitation density of secondary phases. This increase in precipitation density contributes towards an increase in corrosion resistance. Figure 5.2 revealed the effect of holding time on grain size during annealing treatment. Here, clearly observed that grain size increases with the increase of holding time at isothermal condition (723K). The original grain size of as-received AZ80 Mg alloy is 50.20 $\mu$ m revealed in figure 5.2 (a) and after homogenization at 723K-6h and 723K-12h leads to increase of grain size 53.02 $\mu$ m and 55.06 $\mu$ m respectively as presented in figure 5.2 (b) and (c). Wang et al. (2017) also reported that the average grain size of the alloy is a function of annealing time and temperature for AZ80 magnesium alloy under isothermal condition. Which means that temperature and aging time during homogenization treatment is substantial for uniform

distribution of secondary phases in the microstructure of Mg alloys. Specifically, higher aging time (12h) gives a better distribution of secondary phases compared to lower aging time (6h) at all annealing temperature. Therefore treatment at higher aging time is significant in order to modify the microstructure of Mg alloys. Zhao et al. (2014) also observed that the solution treatment and aging at higher temperature microstructures revealed both continuous and discontinuous precipitation on Mg matrix.

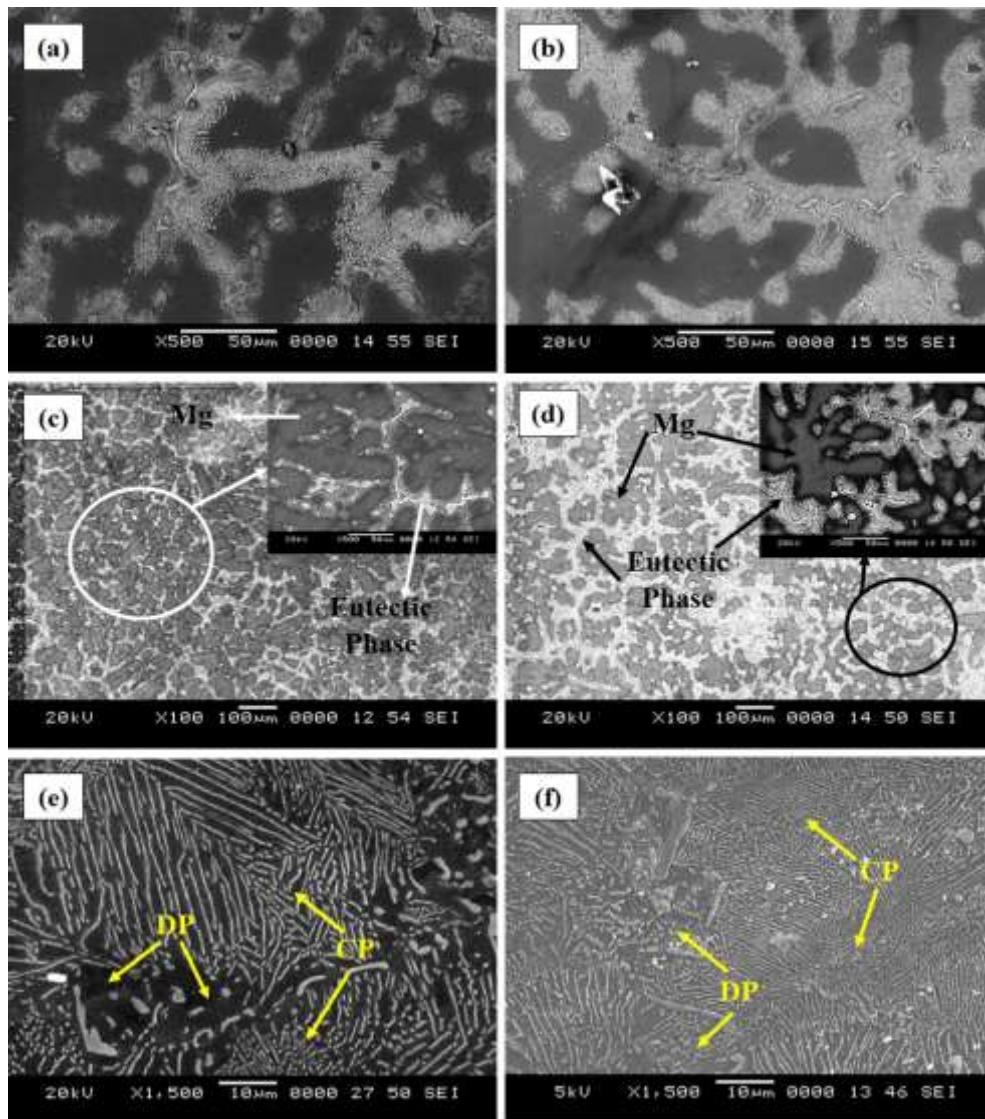


Figure 5.1 The microstructure of annealed AZ80 wrought Mg alloys at different temperature and aging time a) 523K-6h b) 523K-12h c) 623K-6h d) 623K-12h e) 723K-6h and f) 723K-12h.

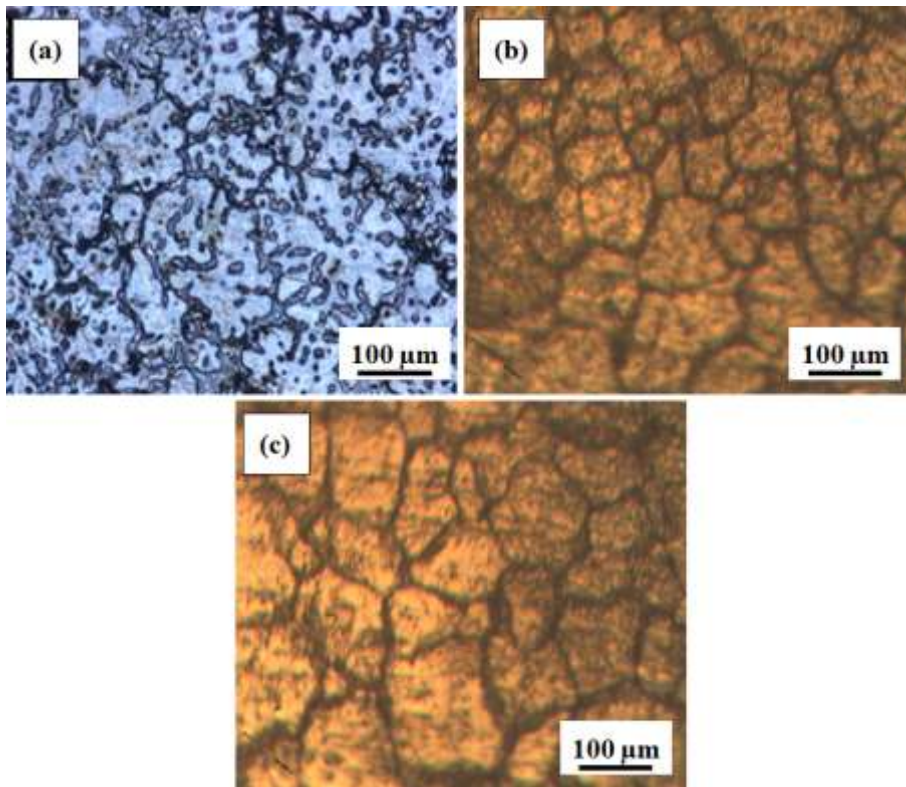


Figure 5.2 Effect of temperature on grain growth a) As-received b) 723K-6h and c) 723K-12h

The precipitation of the eutectic  $\beta$ -Mg<sub>17</sub>Al<sub>12</sub> phase substantially increases the corrosion resistance of the AZ80 Mg alloys. On the other hand oxidation of the alloy was observed with the increase of temperature and holding time, which was noticed at 723K and 12h of holding. Similar observation also made on Mg-5.8 Zn-0.5 Zr-1.0 Yb Alloy by Lu Li et al. (2017).

### 5.2.2 Microstructure evolution of ECAPed AZ80 Mg alloys

The annealing and aging treatment on the microstructure of the as-received AZ80 Mg alloy was investigated in previous section. Predominantly, in this section effect of annealing and ageing treatment on the microstructure of fine-grained AZ80 Mg alloys were discussed because the segregation of Mg<sub>17</sub>Al<sub>12</sub> phases hinders the corrosion resistance due to the galvanic corrosion in as-received form (Esmaily et al., 2017). Hence it is essential to distribute the presence of secondary phases in Mg alloy. The OM images in Fig. 4.10 (b) and (d) show the distributions of  $\beta$ -secondary phase

particles in the AZ80 Mg alloy processed by ECAP-2P and 4P at 598K respectively. Further aging for 6 h and 12h at 523K, 623K and 723 K were carried out for ECAPed 2P and 4P samples of AZ80 Mg alloys. Also, the redistribution of  $\beta$ -secondary phases after annealing and aging treatment in ECAPed 2P and 4P samples of Mg alloys were observed and reported in Figures 5.3 and 5.4 for 523K, 623K and 723K annealing temperatures and holding of 6h, 12h aging time. Figure 5.3 presents the SEM micrographs of heat-treated AZ80 Mg alloys after ECAP-2P, it is readily observed from reported images that there are eutectic precipitates of  $\beta$ -Mg<sub>17</sub>Al<sub>12</sub> distributed along the grain boundaries and within the grains when alloy heat-treated at 523K-6h shown in Figure 5.3 (a). Continued heat treatment at 523K-12h leads to a reduction in the volume fraction of eutectic phases as shown in Figure 5.3 (b), a similar observation was made on ECAP-2P AZ80 Mg alloy after heat treating at 623K-6h and 12h aging as shown in 5.3 (c) and (d) respectively. Further annealing at 723K-6h treatment for 2P-ECAPed AZ80 Mg alloy revealed discontinuous precipitation of  $\beta$ -Mg<sub>17</sub>Al<sub>12</sub> eutectic secondary phases and distributed at the grain boundaries which was appeared in the form of the network shown in Figure 5.3 (e). While ageing from 6h to 12h at 723K the  $\beta$ -Mg<sub>17</sub>Al<sub>12</sub> phases distributed more uniformly in the Mg matrix depicts in Figure 5.3 (f) which signifies secondary phase in AZ80 Mg alloy marginally decreases by increasing the aging time the similar observation was made on Mg-8%Sn alloy by Poddar et al. (2017). The  $\beta$ -Mg<sub>17</sub>Al<sub>12</sub> eutectic phases at the grain boundaries are dissolved and precipitated due to the low solubility temperature of 673K (Qiao et al., 2013; Xu et al., 2018). This continuous precipitation of secondary phases contributes to enhancing corrosion resistance of ECAPed AZ80 Mg alloys. The continuous precipitation (CP) and discontinuous precipitation (DP) of secondary phases during annealing treatment at 723 K– 6 h and 12 h respectively evidently shown in figure 5.3 (e) and (f). Precipitation of secondary phases of fine-grained Mg alloy after hot rolling process and age hardening was observed by Ning et al. (2016). AZ80 Mg alloy processing through 4P-ECAP passes exhibited uniform and more homogenous distribution of secondary phases shown in Figure 5.4 (d) and further annealing and ageing treatment on 4P-ECAPed AZ80 Mg alloy were carried out and reported in Figure 5.4. When AZ80 Mg alloy treated at 523K-6h, the discontinuous precipitation of eutectic  $\beta$ -Mg<sub>17</sub>Al<sub>12</sub> phases was observed in the form of dendritic as shown in Figure 5.4 (a), additional aging for 12h

presents the uniform distribution of eutectic phases revealed in Figure 5.4 (b). Further, annealing at 623K-6h and 12h have also shown partial distribution of secondary phases on microstructure as shown in figure 5.4 (c) and (d). Furthermore, annealing at 723K-6h, 723K-12h yield distribution of secondary phases in the AZ80 Mg matrix was noticed and presented in figure 5.4 (e) and (f) respectively. Hence, from the experimental results, it was confirmed that aging at higher annealing temperatures significantly improves the redistribution of the secondary phase yields a high area fraction of fine secondary phase precipitates in the AZ80 Mg matrix.

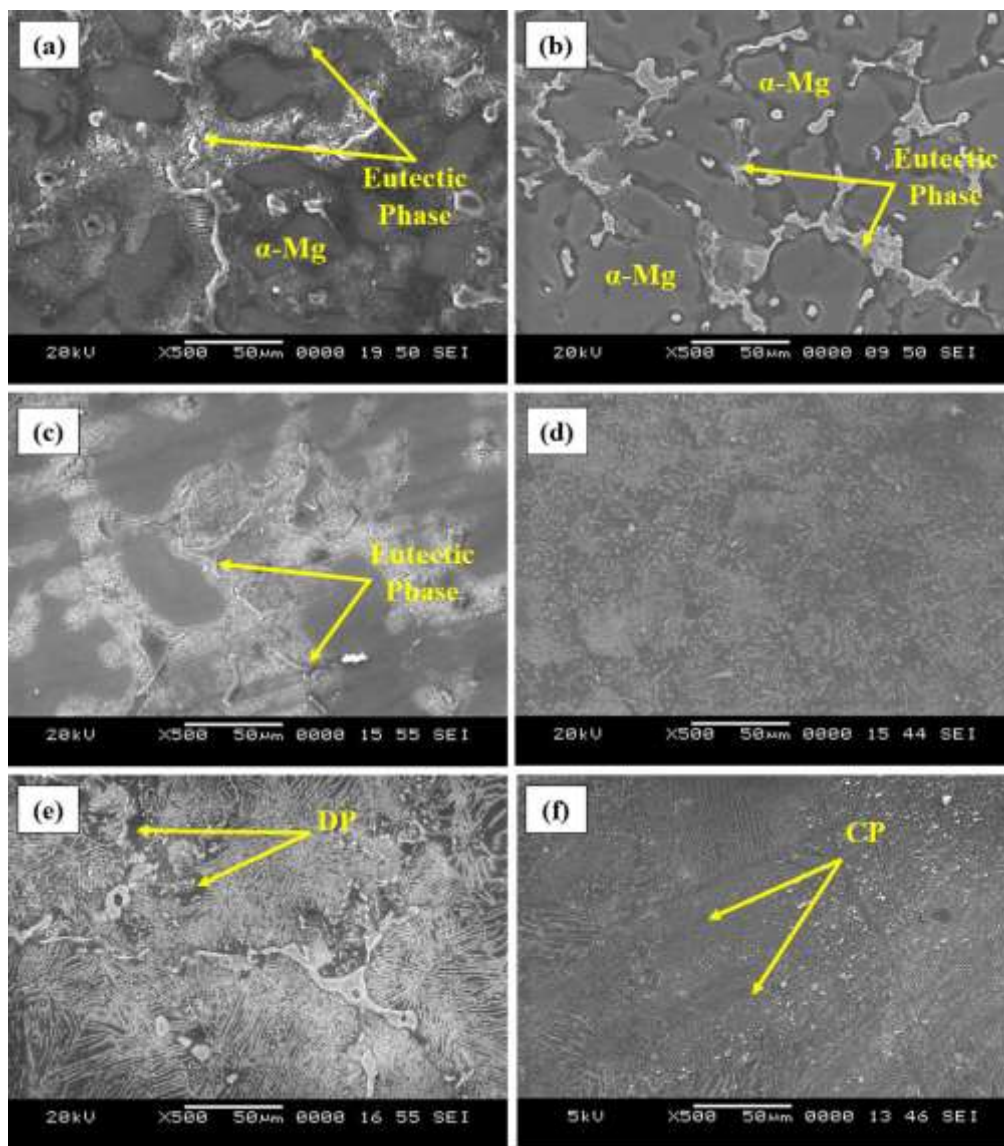


Figure 5.3 SEM images of ECAP-2P AZ80 Mg alloy a) 523K-6h b) 523K-12h c) 623K-6h d) 623K-12h e) 723K-6h and f) 723K-12h.



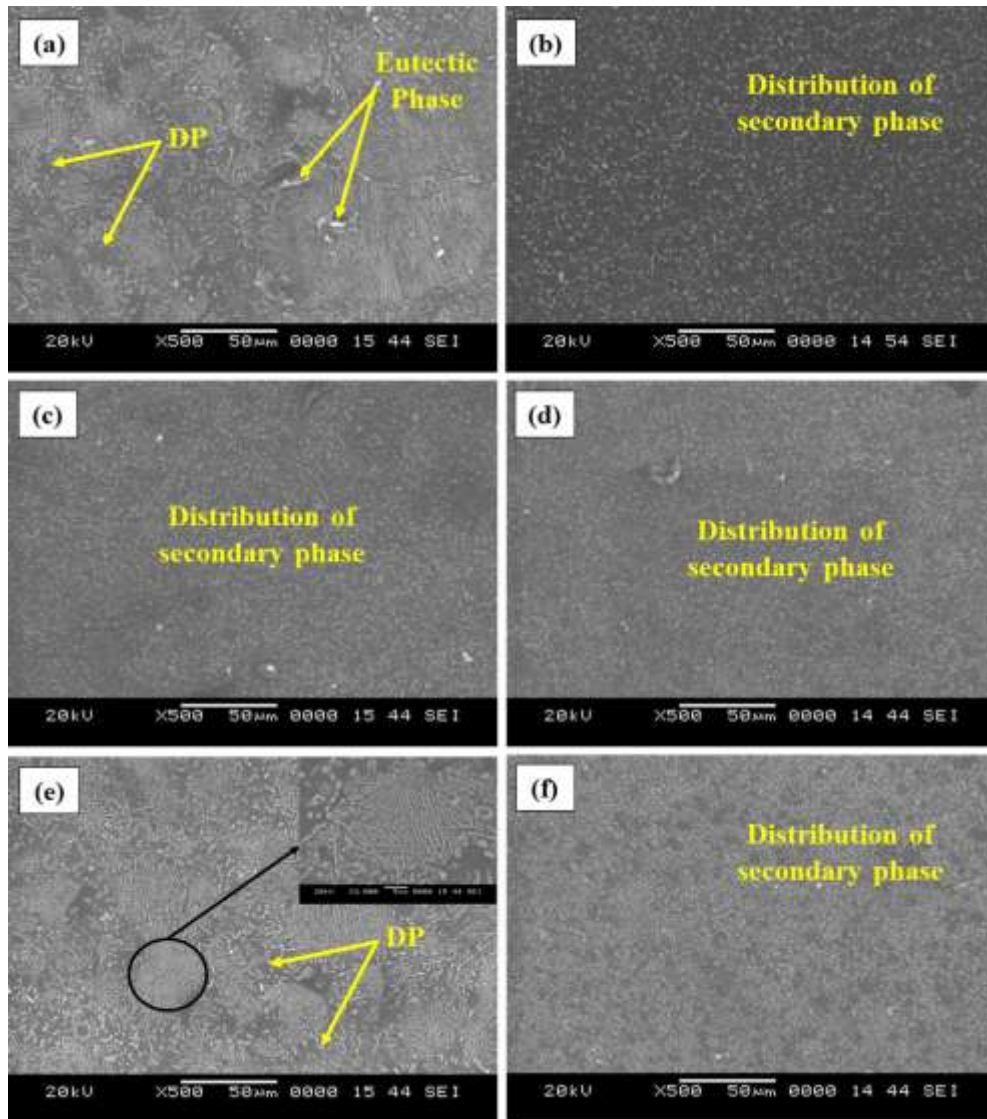


Figure 5.4 SEM images of ECAP-4P AZ80 Mg alloy a) 523K-6h b) 523K-12h c) 623K-6h d) 623K-12h e) 723K-6h and f) 723K-12h.

Moreover, Figures 5.3 and 5.4 demonstrates that redistribution of secondary phase particles is capable of inhibiting corrosion rate during the heat treatments which is evidently discussed in the upcoming sections. Also, from the literature the improvement of corrosion resistance after heat treatment of Mg alloys was observed by Liu et al. (2010) and Bakhsheshi et al. (2015). In addition, an evaluation of the mean grain size of ECAP-4P and after annealing at 723K for 6 h, 12h discloses small deviations in grain size due to the grain growth effect (Doiphode et al., 2015), which is clearly shown through SEM micrographs displayed in Figure 5.5. Figure 5.5 (a) presents the SEM

microstructure of the 4P-ECAPed Mg alloy has fine grains of  $\sim 6.35 \mu\text{m}$ . Further, annealing at 723K-6h a slight increase in grain size of about  $\sim 7.98 \mu\text{m}$  was observed from Figure 5.5 (b). Furthermore, coarsening of average grain size is  $\sim 10.63 \mu\text{m}$  was observed when 4P-ECAPed Mg alloy annealed at 723K-12h, which reveals the phenomenon of grain coarsening in ECAPed Mg alloy at higher annealing temperature with respect to aging time. Consequently, during thermo-mechanical, annealing and aging treatment leads to dissolution, redistribution of secondary phases with continuous precipitation of the dendrite and diffusion of alloying elements (Zhu et al., 2010). The optimum parameter of 723 K-12 h is selected to achieve a more uniform distribution of secondary phases for ECAPed AZ80 Mg alloys in order to improve corrosion resistance.

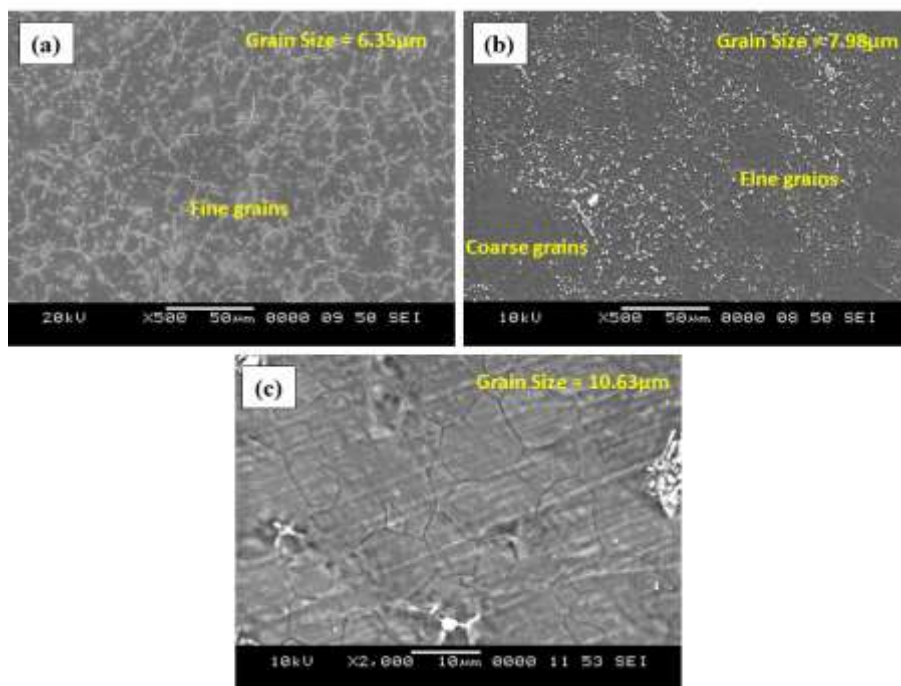


Figure 5.5. Effect of temperature on grain growth (a) ECAP-4P (b) 723 K–6 h and (c) 723 K–12 h.

### 5.2.3 Microstructure evolution of as-received AZ91 Mg alloy after annealing and aging treatment

The microstructures of the as-received AZ91 Mg alloy annealed at 523K, 623K and 723K temperatures for 6h and 12h are shown in Figure 5.6. Where significant

precipitation of secondary phases in Mg matrix and a narrow eutectic is revealed and clearly presents the presence of  $\alpha$ -Mg matrix and  $\beta$ -Mg<sub>17</sub>Al<sub>12</sub> secondary phases.

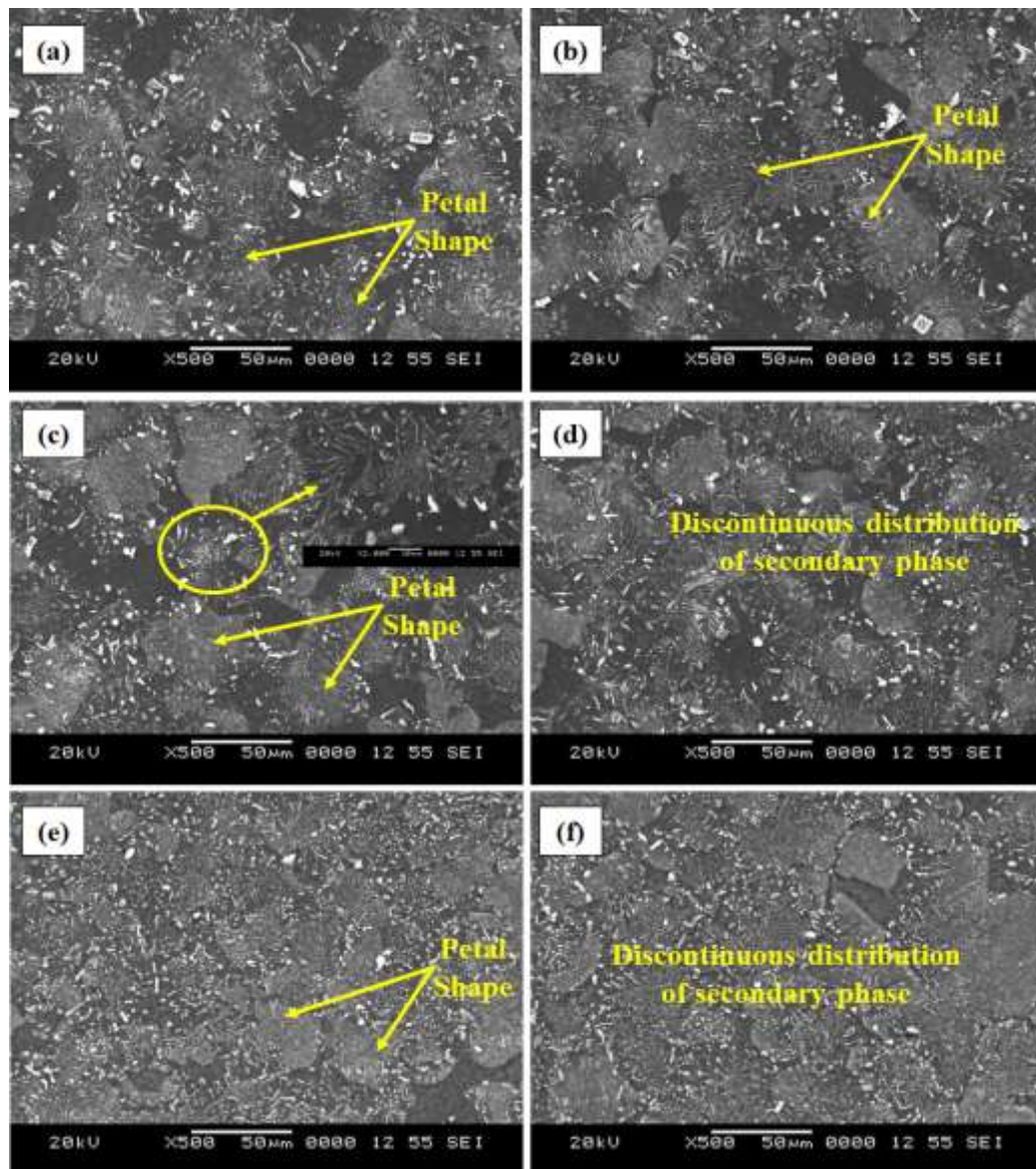


Figure 5.6 The microstructure of annealed as-received AZ80 Mg alloys at different temperature and aging time a) 523K-6h b) 523K-12h c) 623K-6h d) 623K-12h e) 723K-6h and f) 723K-12h.

Annealing treatment leads to an increase in the area fraction of  $\beta$ -Mg<sub>17</sub>Al<sub>12</sub> phases compared to as-received alloy, which contributes to improving the corrosion resistance. Figure 5.6 (a) to (f) shows the SEM image of the annealed AZ91 alloy of 523K-6h, 523K-12h, 623K-6h, 623K-12h, 723K-6h and 723K-12h respectively.

Eutectic  $\beta$ -Mg<sub>17</sub>Al<sub>12</sub> phases and discontinuous  $\beta$ -Mg<sub>17</sub>Al<sub>12</sub> phases are revealed and distributed at the grain boundaries, which was shown in the form of the petal-shaped and eutectic phases were observed in the specimen with aging time. Moreover, the AZ91 Mg alloys under different annealing treatment conditions microstructure revealed a fine uniform distribution of secondary phases at 723K, when compared to sample treated at 523K and 623K annealing temperature. As the holding time extends to 6 h to 12h the secondary phase precipitates resulting in an increase of precipitation density of secondary phases was observed for all conditions.

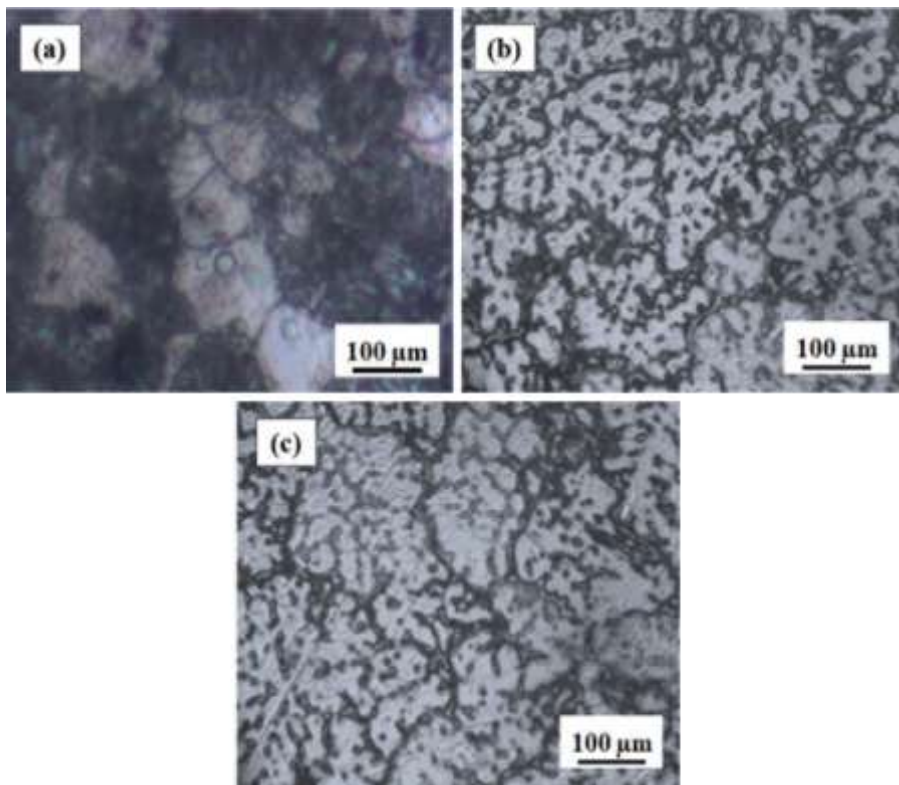


Figure 5.7 Effect of temperature on grain growth a) As-received b) 723K-6h and c) 723K-12h

This phenomenon contributes to an increase in corrosion resistance (Zhao et al., 2014). Further, an evaluation of the average grain size of as-received AZ91 Mg alloy after annealing at 723K for 6 h, 12h reveals deviations in average grain size due to the grain growth effect (Doiphode et al., 2015; Hono et al., 2010), which was shown through OM images as shown in Figure 5.7. Figure 5.7 (a) shows the microstructure of the AZ91 Mg alloy has a grain size of  $\sim 58.69 \mu\text{m}$ . Further, annealing at 723K-6h a slight increase

in average grain size of about  $\sim 60.12 \mu\text{m}$  was observed (Figure 5.7 (b)). Furthermore, average grain size is  $\sim 60.92 \mu\text{m}$  was observed when AZ91 Mg alloy annealed at 723K-12h, which discloses the phenomenon of grain coarsening in as-received AZ91 Mg alloy at higher annealing temperature with respect to aging time.

#### **5.2.4 Microstructure evolution of ECAPed AZ91 Mg alloys**

The microstructures of the ECAP-2 pass and ECAP-4 pass AZ91 Mg alloy heat-treated at 523K, 623K and 723K temperatures for 6h and 12h are shown in Figure 5.8 and Fig.5.9 respectively. Compared to the microstructures of heat-treated as-received alloy (Figure 5.8), the distribution of secondary phases of the alloy processed with ECAP grows continuously for all the aging temperatures and aging time. This is mainly due to primarily achieved phase distribution through ECAP, the differences between secondary phase distribution before and after ECAP can be seen in figures 4.4, 4.17 and 4.18. Certainly, as-received AZ91 Mg alloy rich in secondary phase which is segregated at the grain boundaries whereas ECAPed AZ91 Mg alloys showed uniform distribution of secondary phases compared to as-received alloys. Similarly, many authors observed the fine distribution of secondary phases after ECAP processes such as Shahar et al. (2017) and Chun et al. (2018). Further, re-distribution of secondary phases was achieved through heat-treating the ECAPed AZ91 Mg alloys are shown in Figures 5.8 and 5.9. The microstructures of the AZ91 Mg alloy after heat treatment of ECAP-2P samples at 523K, 623K and 723K for 6h and 12h were shown in Figure 5.8 (a)-(f). From the figure it was observed some petal-shaped phases appear on ECAP-2P sample when heat treated at 523K and 623K for 6h and 12h. Further, ECAP-2P samples heat treated at 723K for 6h and 12h, ECAP-4P samples heat treated at 523K, 623K and 723K for 6h and 12h, the residual phase in AZ91 Mg matrix is reduced and more dot-shaped particles exist in the Mg matrix, this continuous distribution of secondary phase were marked on the SEM images as shown in figure 5.8 (e), (f) and 5.9 (a)-(f). This continuous distribution of secondary phase explains why the ECAPed AZ91 Mg alloy heat-treated at 723K possesses higher corrosion resistance. Furthermore, compared with the AZ91 Mg alloy treated at 523K, 623K and 723K for 6 h, the distribution of  $\text{Mg}_{17}\text{Al}_{12}$  secondary phase at 523K, 623K and 723K for 12 h is obviously higher the percentage and fine distribution of secondary phase was increased. A similar

observation was reported by Yongdong et al. (2011) on Mg-Nd-Gd-Zn-Zr. Along with this, it is clearly observed that grain size increases with the increase of aging time at the isothermal condition of temperature 723K. The mean grain size of ECAP-4P AZ91 Mg alloy is  $\sim 7.58 \mu\text{m}$  revealed in figure 5.10 (a) and after annealing at 723K-6h and 723K-12h leads to increase of grain size  $8.06\mu\text{m}$  and  $8.98 \mu\text{m}$  respectively as presented in figure 5.10 (b) and (c). Further, the influence of annealing and aging treatment on corrosion resistance of as-received and ECAPed AZ80/91 Mg alloys were evidently discussed in the following sections.

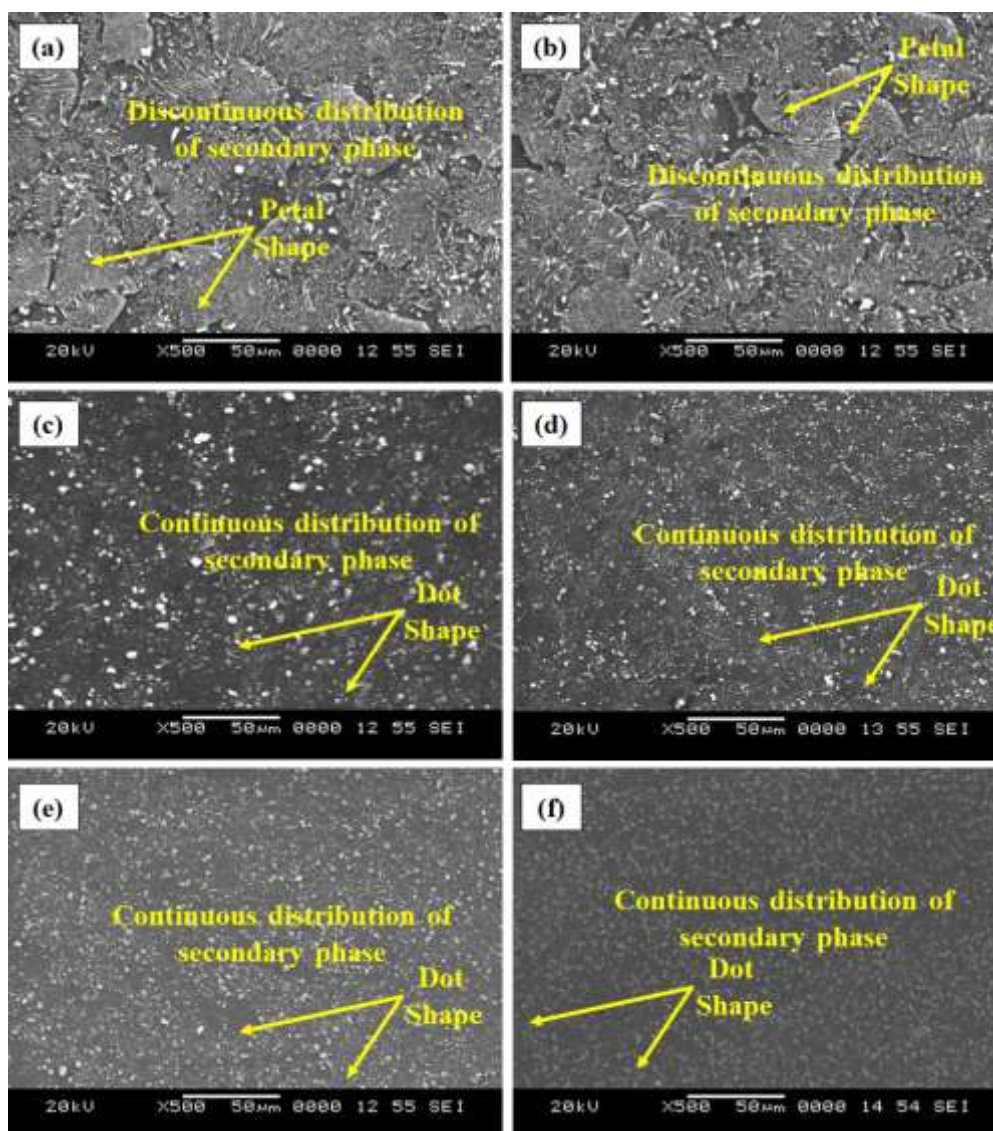


Figure 5.8. SEM images of ECAP-2P AZ80 Mg alloy a) 523K-6h b) 523K-12h c) 623K-6h d) 623K-12h e) 723K-6h and f) 723K-12h.

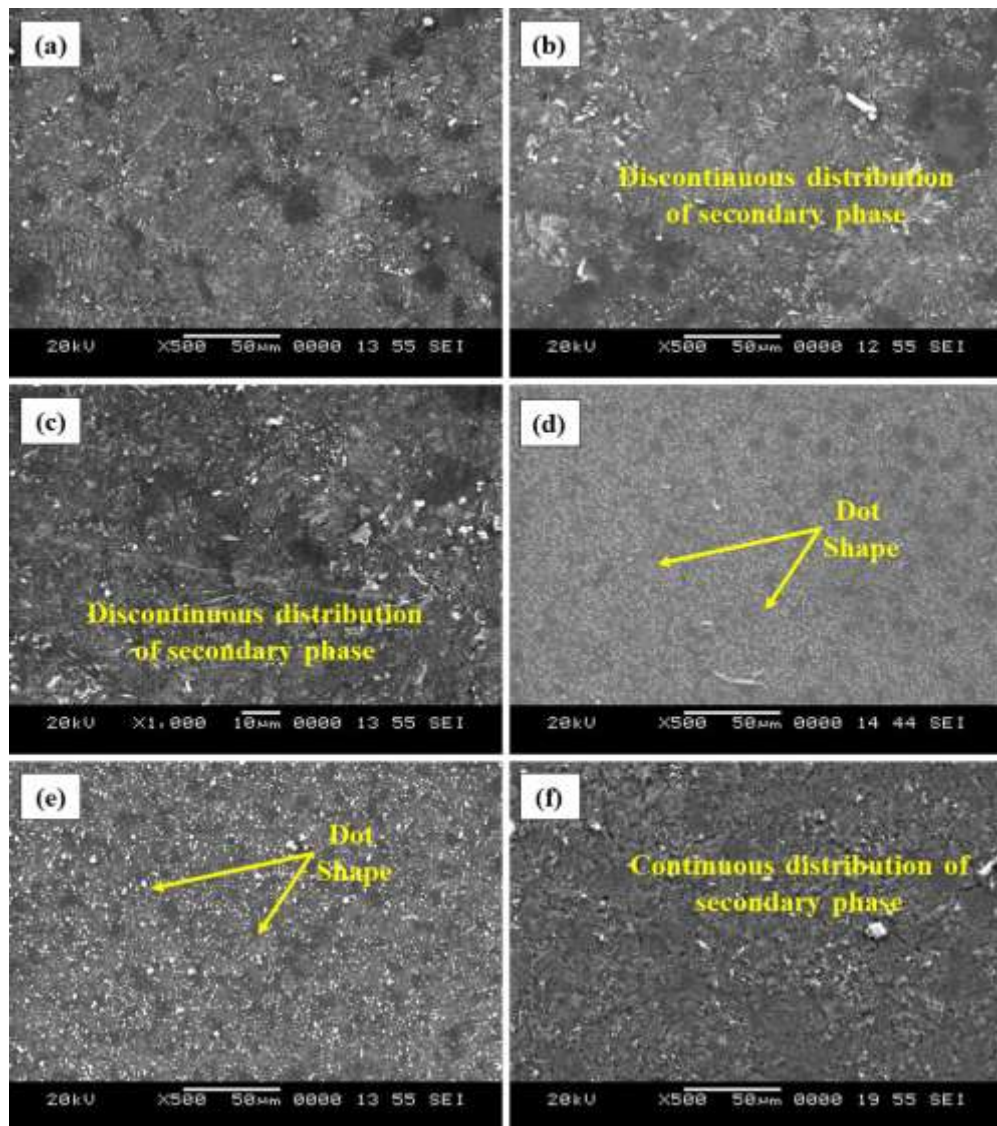


Figure 5.9 SEM images of ECAP-4P AZ91 Mg alloy a) 523K-6h b) 523K-12h c) 623K-6h d) 623K-12h e) 723K-6h f) 723K-12h.

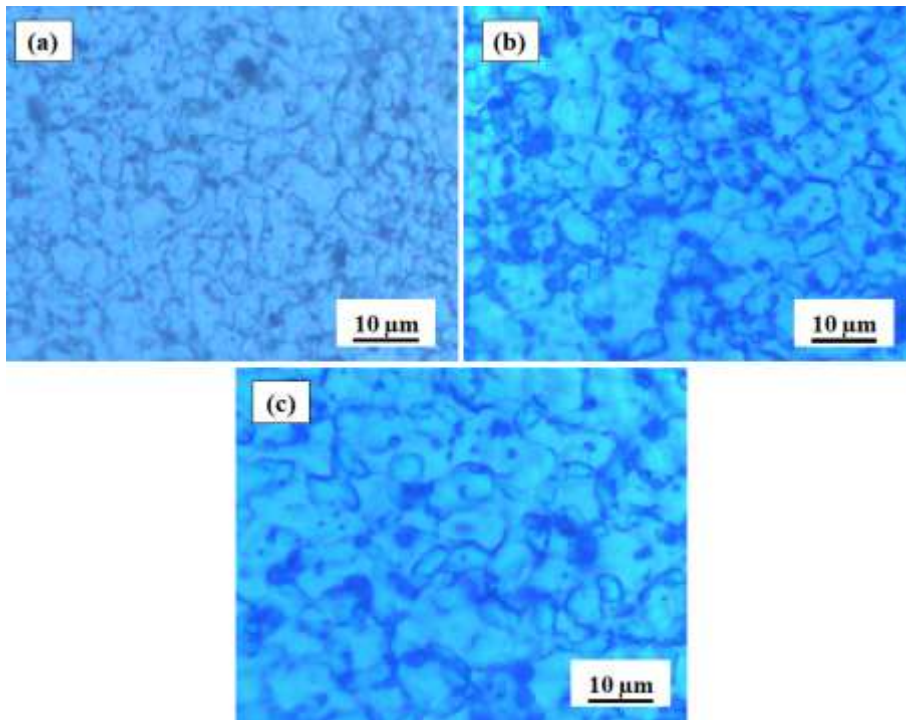


Figure 5.10 Effect of temperature on grain growth (a) ECAP-4P (b) 723 K–6 h and (c) 723 K–12 h.

### 5.3 IMPACT OF ANNEALING AND AGING TREATMENT ON CORROSION RESISTANCE OF AS-RECEIVED AND ECAPED AZ80/91 MAGNESIUM ALLOYS.

Annealing and aging treatment were conducted at 523K, 623K and 723K for 6h and 12h. Through comparison of microstructure, corrosion properties of heat-treated as-received and ECAP passed samples were discussed in this section. Further, the effect of annealing temperature and aging mechanism on corrosion properties of AZ Mg alloy was analyzed and reported.

#### 5.3.1 Corrosion behavior of as-received AZ80/91 Mg alloy after annealing treatment

Figure 5.11 shows the potentiodynamic polarization curves of the as-received and the annealed AZ80 Mg alloys at 523K, 623K and 723K after 6h and 12h of aging. Here, the curve tends to move forward and shifted to the positive amplitude of corrosion potential ( $E_{corr}$ ) for AZ80 alloy at 523K, 623K, and 723K of 6h and 12h of aging with



respect to the as-received alloy. It is apparent that the corrosion potential after annealing treatment moved forward compare to as-received alloy except alloy treated at 523K-12h aging treatment. The Mg alloy heat-treated at 723K-6h gives the more homogeneous distribution of secondary phases results in less induced cathodic sites. Therefore, potentiodynamic curves moved left compared with as-received and other heat-treated Mg alloys, a similar observation was made on Mg-3Zn by Liu et al. (2010). Further, the corrosion resistance of the cathode moved forward at 623K and 723K, which indicates that the corrosion resistance of the Mg alloy was improved after annealing treatment for a lower aging time. Hence higher the annealing temperature and lower the aging time, better the corrosion resistance. But sample heat-treated at 723K-12h exhibited poor corrosion resistance because of normal and anomalous grain growth at the higher aging time leading to lower passivity. Also, the impact of temperature and aging time on grain growth evidently shown in Figure 5.2.

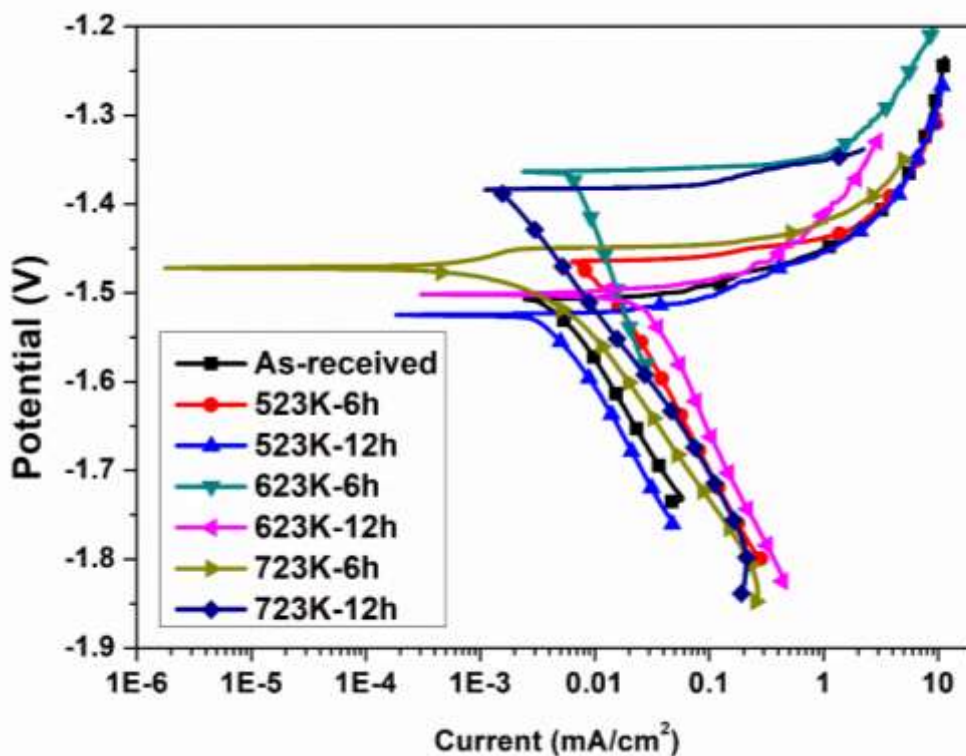


Figure 5.11 The polarization curves for heat treated AZ80 Mg alloys in 3.5wt.% NaCl

Results observed from the current study have good agreement with the results reported by Song et al. (2004) here. Authors noticed that corrosion rate of the die-cast

AZ91 increases with extended aging treatment and also Zengin et al. (2017) observation have a good agreement with obtained results. The electrochemical corrosion potential ( $E_{\text{corr}}$ ), current density ( $I_{\text{corr}}$ ) and corrosion rate for as-received annealed and aged AZ80 alloys was calculated using equation (3.3) and presented in table 5.1 for all cathodic polarization curves. The corrosion results revealed that annealing treatment hinders the corrosion rate except 623K-12h treated AZ80 Mg alloy. Meanwhile, alloy treated at 723K-6h presents the lowest corrosion rate due to distribution of secondary phases during annealing and aging treatment. Figure 5.12 shows the potentiodynamic polarization curves of the as-received and the annealed AZ91 alloy after 6h and 12h of aging at 523K, 623K and 723K. Here, the curve tends to move forward and shifted to the positive amplitude of corrosion potential ( $E_{\text{corr}}$ ) for AZ91 alloy at 523K, 623K, and 723K of 6h and 12h of aging with respect to the as-received alloy.

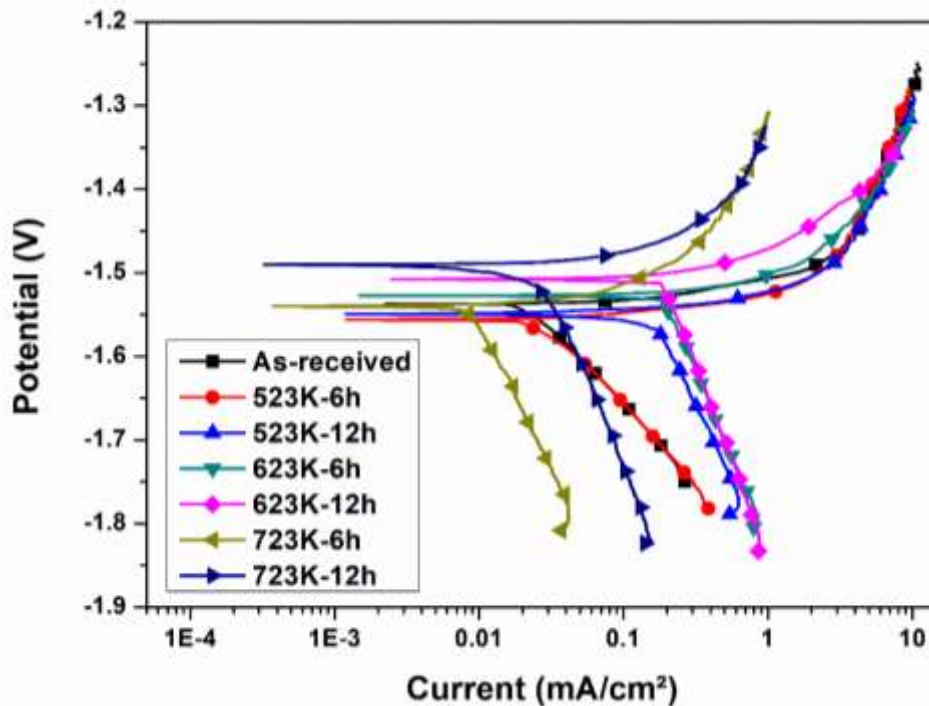


Figure 5.12 The polarization curves for heat-treated AZ91 Mg alloys in 3.5wt.% NaCl

It is apparent that the corrosion potential after annealing treatment moved forward compare to as-received alloy except alloy treated at 523K-6h and 523K-12h aging treatment. The Mg alloy heat treated at 723K-12h gives the more homogeneous distribution of secondary phases results in less induced cathodic sites. Therefore,

potentiodynamic curves moved left compared with as-received and other heat treated Mg alloys, a similar observation was made on Mg-3Zn by Xian-bin et al. (2010). Huseyin et al. (2017) observation have a good match with obtained results. The electrochemical corrosion potential ( $E_{\text{corr}}$ ), current density ( $I_{\text{corr}}$ ) and corrosion rate for as-received, annealed and aged wrought AZ91 alloys was calculated using equation (3.3) and presented in table 5.1 for all cathodic polarization curves (Zhao et al. 2014). The table 5.1 presents the corrosion rates of as-received, heat treated AZ80 and AZ91 Mg alloys. From the result, it was observed that the heat treated AZ80 Mg alloy exhibited higher corrosion rate than that of the heat treated AZ91 Mg alloy in 3.5wt.% NaCl solution. Therefore, annealed AZ91 Mg alloys are less susceptible to corrosion this is mainly due distribution of secondary phases during annealing and aging treatment, which was typically shown in figure 5.19.

### 5.3.2 Corrosion morphologies as-received AZ80/91 Mg alloys

Figure 5.13 shows the corrosion morphology of wrought AZ80 magnesium alloys in 3.5wt.% NaCl solution for as-received and after annealing treatment at 523K-12h, 623K-12h and 723K-6h and 12h.

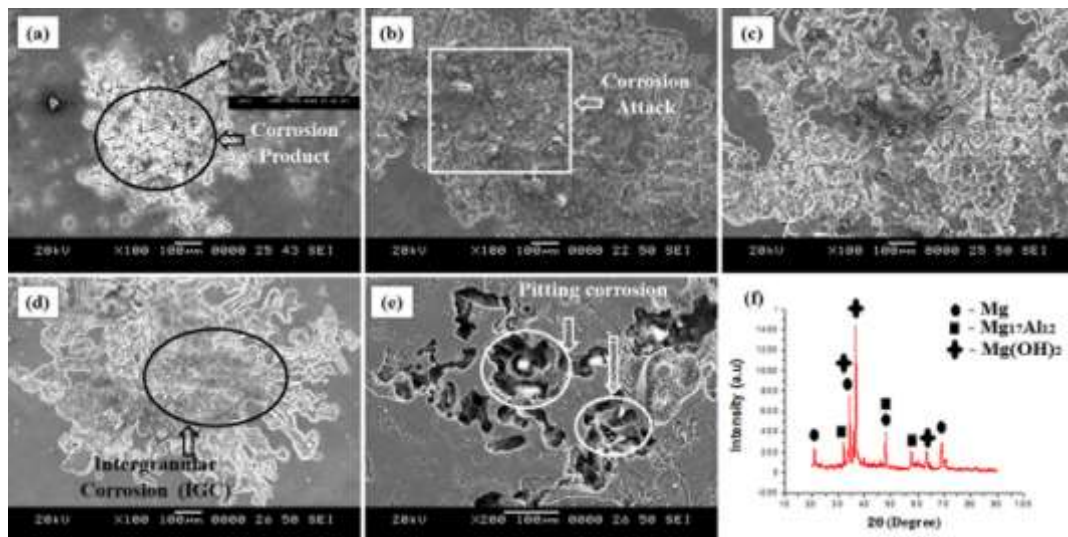


Figure 5.13 The microstructure of corroded AZ80 wrought Mg alloys a) As-received b) annealed at 523K-12h. c) 623K-12h d) 723K-6 h e) 723K-12h and f) X-ray diffraction of as-received AZ80 alloy.

During corrosion morphology study, a thin film of white corrosion products was removed from the surface to observe the corrosion attack on the AZ80 Mg alloy surfaces. The corroded surface of with and without corrosion product has shown in figure 5.13 (a). The morphology of AZ80 Mg alloy annealed at the 523K-12h aging have shown abundant uniform corrosion attack over the surface of the alloy presented in figure 5.13 (b). Figure 5.13 (c) and (d) depicts the intergranular and pitting corrosion morphology of alloys annealed at 623K-12h and 723K-6h, respectively. This was observed in the vicinity of grain boundaries. But  $\beta$ -secondary phases cannot be seen in the corrosion morphology, this confirms that the  $\beta$ -secondary phases are fully dissolved and distributed in the  $\alpha$ -Mg matrix due to annealing and aging treatment. The annealed sample exhibited a less corrosion attack compared to the as-received AZ80 alloy. But when AZ80 Mg alloy annealed at a higher temperature of 723K and 12h of aging alloy suffered severe pitting corrosion compared to the material treated at 723K-6h shown in figure 5.13 (d) and (e). Morphology data is also evident from the polarization resistance data. Figure 5.13 (f) the XRD spectra of corroded as-received AZ80 Mg alloys composed of Mg,  $Mg_{17}Al_{12}$  phases and also revealed the presence of  $Mg(OH)_2$ . Therefore, the formation of the hydroxides of Mg protective layer at their surface increases the corrosion resistance (Singh et al., 2015). Figure 5.14 shows the corrosion morphologies of wrought AZ91 magnesium alloys in 3.5wt.% NaCl solution for as-received and after annealing treatment at 523K-12h, 623K-12h and 723K-12h. During corrosion morphology study, a thin film of white corrosion products was removed to observe the corrosion attack on the as-received AZ91 Mg alloy surface. The corroded surface of without corrosion product has shown in figure 5.14 (a). The morphology of Mg alloy annealed at the 523K-12h, 723K-12h aging of AZ91 specimen have shown abundant uniform corrosion attack over the surface of the alloy presented in figures 5.14 (b) and (c) depicts the pitting corrosion morphology of alloys, respectively. Comparatively, specimen annealed at 723K-12h have shown less corrosion attack on the surface due to uniform distribution of secondary phases. Also, figure 5.14 (d) XRD peaks of specimen heat-treated at 523K-12h confirm that the corrosion product is  $Mg(OH)_2$ . The corrosion morphology has been shown good agreement with those obtained in polarization curves results, which are presented in Table 5.1.

Compared with annealed and aged AZ80 alloy, the surface morphologies of annealed and aged AZ91 alloy did not change much after polarization test, as seen in Figure 5.13 and 5.14. Similar to heat-treated AZ80 Mg alloy, a more compact layer of corrosion products were observed on the heat-treated AZ91 alloy sample in the 3.5wt.% NaCl solution as shown in Figure 5.14. After removing the corrosion products, small isolated pits were found on the samples, while more pits that spread laterally could be observed on the heat-treated AZ80 Mg alloy samples. Particularly, as-received AZ80 Mg alloy heat-treated at 723K-12h shown in figure 5.13(e). There are no such deep pits on the as-received AZ91 Mg alloy heat-treated at 723K-12h sample.

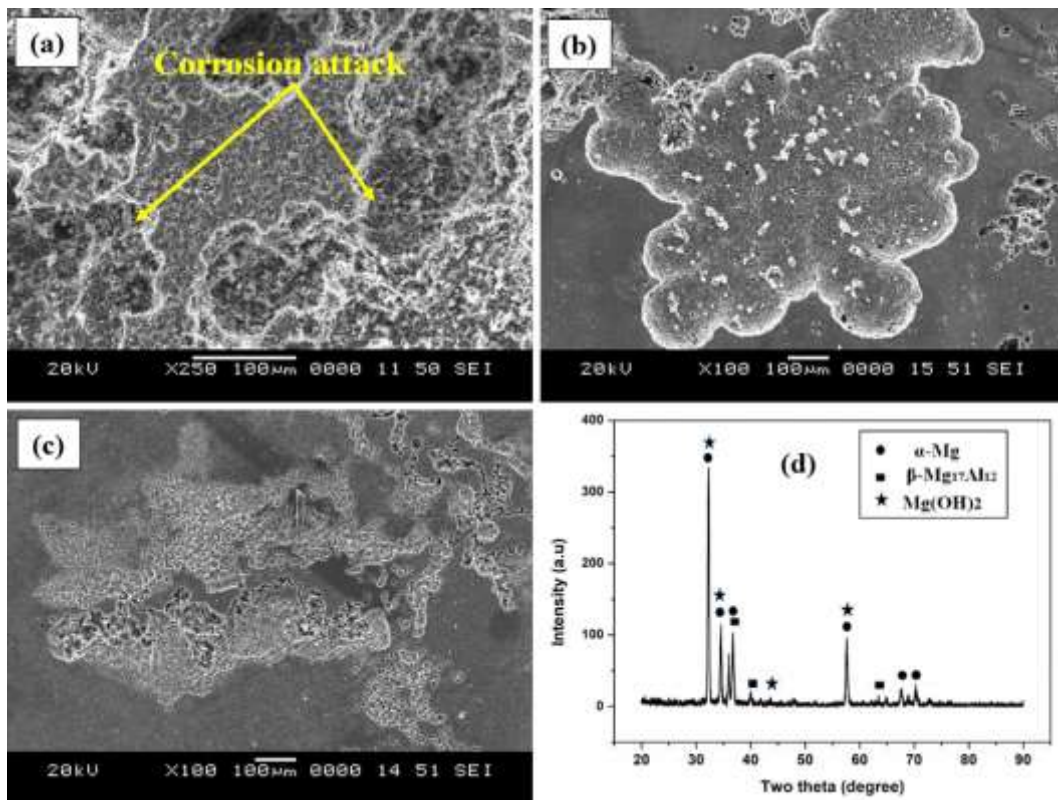


Figure 5.14. The SEM images of corroded AZ91 wrought Mg alloys a) As-received b) annealed at 523K-12h. c) Annealed at 723K-12h and d) XRD peaks of AZ91 annealed at 523K-12h

### 5.3.3 Influence of annealing and aging treatment on corrosion resistance of ECAPed AZ80/91 Mg alloys

The polarization curves of the 2 pass and 4 pass ECAP-processed, annealed and aged samples of AZ80 Mg alloys depicts in Figures. 5.15 and 5.16. Indeed, the corrosion behaviour of as-received AZ80 Mg alloy during annealing and ageing treatment was addressed in the previous section. In this section, the effect of annealing and ageing treatment on fine-grained AZ Mg alloys were discussed. The comparison of Figures. 5.15 with 5.16 illustrates that the curves of the heat-treated specimens of ECAP-2P and 4P shifted to the nobler side significantly. It indicates lower corrosion current density ( $I_{\text{corr}}$ ) and higher corrosion potential ( $E_{\text{corr}}$ ) this means material exhibited better corrosion resistance (Zhang et al., 2016). The  $E_{\text{corr}}$  and  $I_{\text{corr}}$  values of the with and without heat-treated ECAP-processed AZ80 Mg alloy samples can be obtained from the potentiodynamic polarization curves by Tafel extrapolating method (Shi et al., 2017). The potentiodynamic corrosion potential ( $E_{\text{corr}}$ ), current density ( $I_{\text{corr}}$ ) and corrosion rate for ECAPed and heat-treated ECAPed AZ80 alloys was calculated by equation (3.3) and presented in table 5.1 for all polarization curves. Here, the curves of heat-treated ECAPed AZ80 Mg alloy at 523 K, 623 K, and 723 K for 6 h and 12 h of ageing with respect to the ECAP-2P and ECAP-4P were shown in Figures 5.15 and 5.16 respectively. The ECAPed AZ80 Mg alloy annealing at 723K–12 h contributes improved corrosion resistance due to reduced cathode sites of ECAPed AZ80 Mg alloy, this can be achieved through the combined processes of ECAP, annealing and aging treatment. It can be observed that the corrosion potential ( $E_{\text{corr}}$ ) increased to -1.410 V from -1.553  $V_{\text{SCE}}$  for ECAP-2P and  $E_{\text{corr}}$  is increased to -1.408  $V_{\text{SCE}}$  from -1.494  $V_{\text{SCE}}$  for ECAP-4P after annealing and ageing treatment, this signifies improved pitting corrosion resistance of ECAPed Mg alloys. The main reason is due to distribution of secondary phases in the  $\alpha$ -Mg matrix which moved corrosion potential to nobler side. Also, the obtained grain refinement and homogeneous distribution of eutectic phases through ECAP and further redistribution of  $\beta$ -secondary phase results in improved passive stability and pitting corrosion resistance this is evidently proved through potentiodynamic test results and corrosion morphology studies. Therefore, potentiodynamic curves of ECAPed Mg alloy treated 723K-12h moved left compared

with ECAPed and other heat-treated Mg alloys. Thus, it was seen that the corrosion current density ( $I_{\text{corr}}$ ) has attained lower values that are  $0.0059 \text{ mA}\cdot\text{cm}^{-2}$  for ECAP-2P and  $0.0011 \text{ mA}\cdot\text{cm}^{-2}$  for ECAP-4P. Similar observations was made on ZK60 Mg alloys after ECAP and solution treatment by Xian et al. (2015). Hence, larger annealing temperature and ageing time supports the corrosion resistance due to improved passivity after ECAP and redistribution of secondary phases during annealing and ageing treatment. Also, it is noted from Table 5.1 that annealing and ageing treatment hinders the corrosion rate for all heat treated ECAPed AZ80 Mg alloys. Meanwhile, Mg alloy treated at 723 K–12 h presents the lowest corrosion rate for both ECAP-2P and ECAP-4P samples. Whereas, ECAPed Mg alloys treated at a lower temperature, such as 523K and 623K exhibited poor corrosion resistance than the alloy treated at 723K this is mainly due to the partial distribution of secondary phases in the Mg matrix. Further, increase in ageing time yields improved pitting corrosion resistance of ECAPed Mg alloy this is evidently shown through polarization curves of ECAP-2P (Figure 5.15) and ECAP-4P (Figure 5.16). Results obtained in the present study have good agreement with the results stated by Huiyan et al. (2018) and Xian et al (2015). On the other hand, it can be concluded that the corrosion resistance of AZ80 Mg alloys mostly increases with the increase of ECAP passes, annealing temperature and ageing time. Gopi et al. (2018) obtained reduced corrosion current density ( $I_{\text{corr}}$ ) for 3P-ECAP processed AM90 Mg samples due to grain refinement. The  $I_{\text{corr}}$  values of heat-treated and aged samples are nearly lower than those of only ECAP-processed AZ80 Mg alloy, especially the 4P-ECAP and the annealing at 723K and ageing for 12h implies better pitting corrosion resistance than ECAP-2P annealed at 723K-12h this is due to fine grains and distribution of secondary phases achieved by ECAP. Potentiodynamic polarization curves of annealed ECAPed AZ91 samples at 523K, 623K, and 723K for 6h and 12h are shown in Figures 5.17 and 5.18 and the electrochemical factors such as  $E_{\text{corr}}$  and  $I_{\text{corr}}$  resulting from Tafel extrapolation method. Results revealed that annealed ECAP-2P and 4P sample after annealing at 723K-12 showed the lowest  $I_{\text{corr}}$  ( $0.0110 \text{ mA}/\text{cm}^2$ ,  $0.0011 \text{ mA}/\text{cm}^2$ ) compared to ECAP-2P and ECAP-4P samples, indicating low corrosion affinity and corrosion rate.

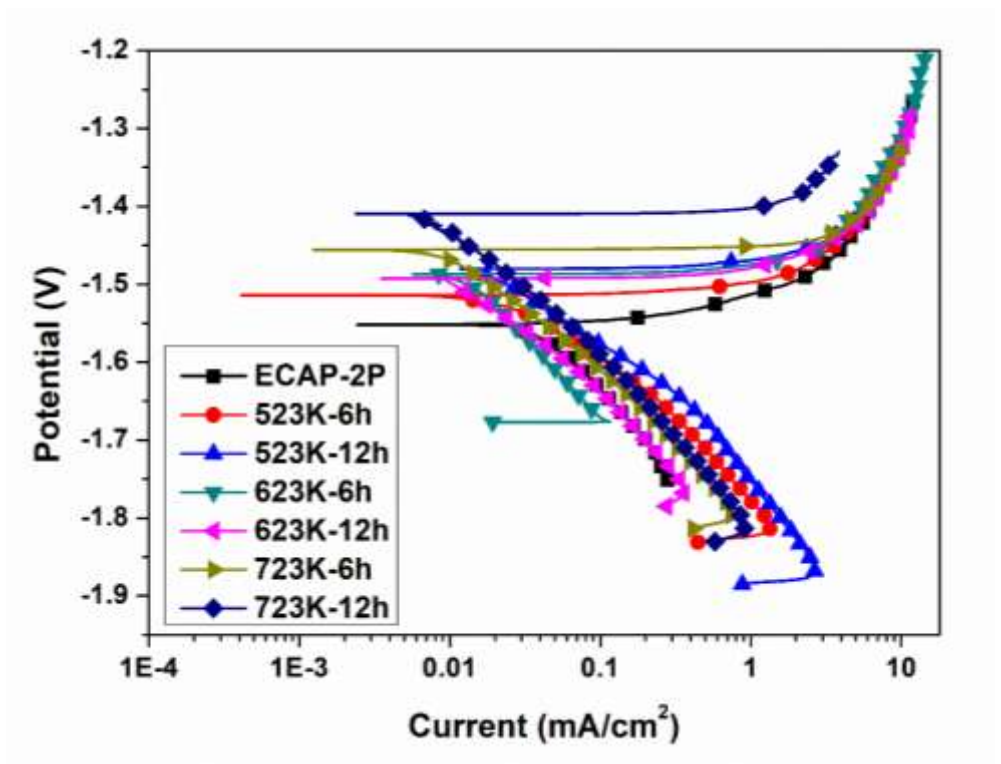


Figure 5.15 The polarization curves for heat treated ECAP-2P AZ80 Mg alloys in 3.5wt.% NaCl

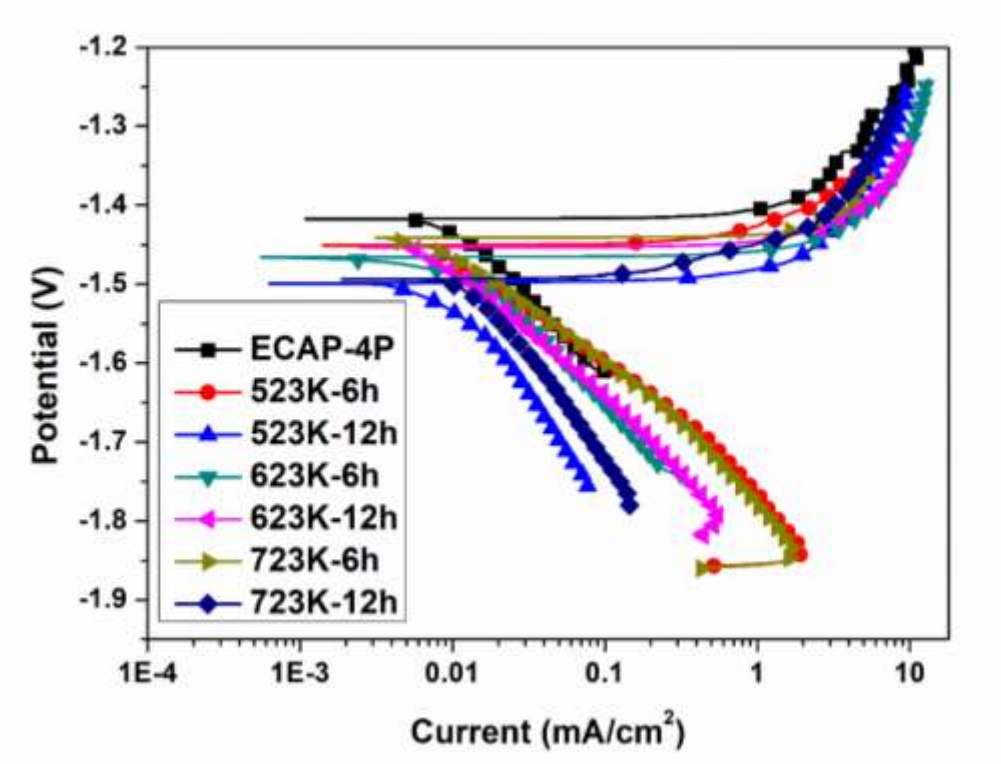


Figure 5.16 The polarization curves for heat treated ECAP-4P AZ80 Mg alloys in 3.5wt.% NaCl



Moreover, between all annealed samples, 523K-6h, 523K-12h, 623K-6h, 623K-12h, 723K-h and 723K-12h for ECAP-4P shown the smaller  $E_{corr}$  -1.488  $V_{SCE}$ , -1.500  $V_{SCE}$ , -1.512  $V_{SCE}$ , -1.489  $V_{SCE}$ , -1.408  $V_{SCE}$ , -1.402  $V_{SCE}$  and -1.400  $V_{SCE}$  respectively. Which is less than the annealed ECAP-2P Mg alloy, but it is confirming that continuous shift in the corrosion potential towards nobler side resulting in enhanced corrosion resistance owing to the annealing treatment. Tański et al. (2016) reported that compared to the bare Al-Mg sample, annealed alloy revealed much higher corrosion resistance. Furthermore, Naik et al. (2019) showed that AZ80 Mg alloy heat-treated at 723K revealed better corrosion resistance than as-received alloy. It might be due to uniform distribution of the secondary phase after annealing treatment. However, the corrosion current density could be arranged as ECAP-4P>523K-6h> 523K-12h>623K-6h> 623K-12h>723K-6h>723K-12h. When ECAPed-4P sample was aged at 523K for 6 h,  $Mg_{17}Al_{12}$  phases formed in the  $\alpha$ -Mg matrix and along the grain boundaries, resulting in the reduction of corrosion rate.

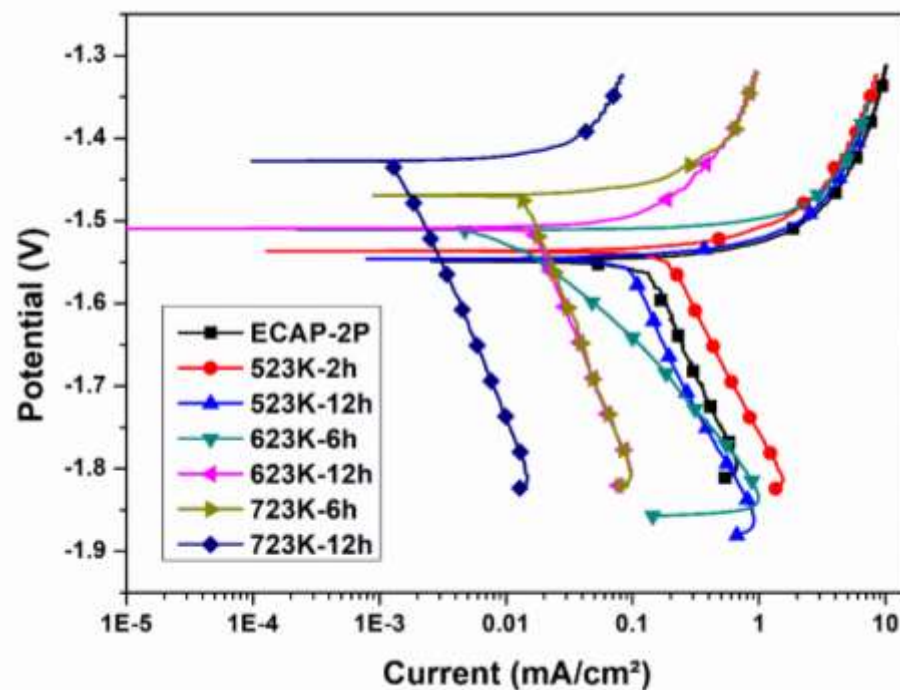


Figure 5.17 The polarization curves for heat-treated ECAP-2P AZ91 Mg alloys in 3.5wt.% NaCl

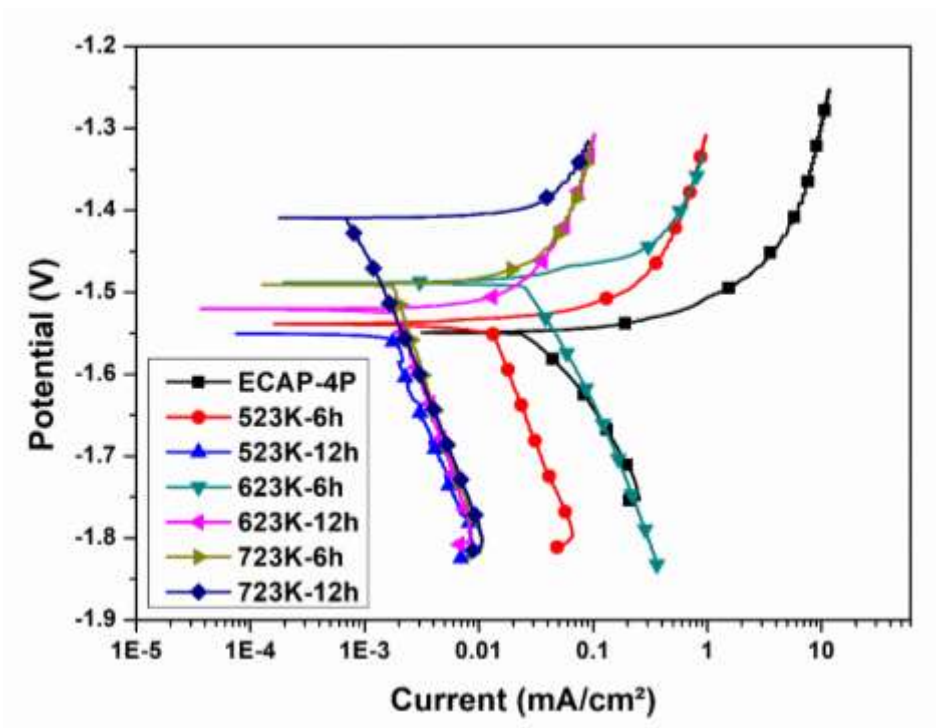


Figure 5.18 The polarization curves for heat-treated ECAP-4P AZ91Mg alloys in 3.5wt.% NaCl

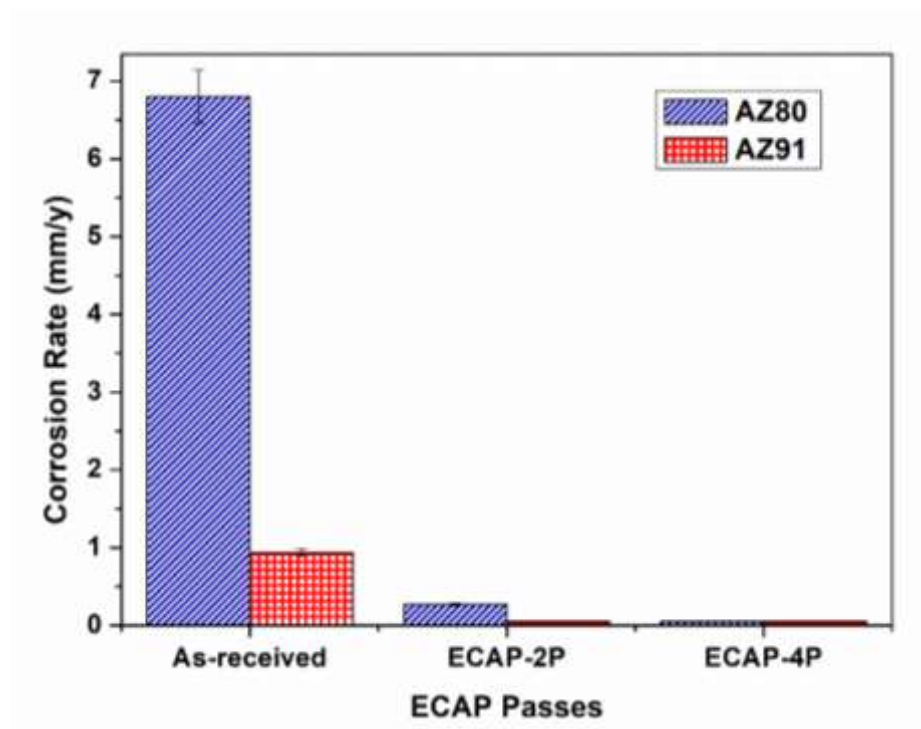


Figure 5.19 Variation of corrosion rate of AZ80/91 Mg alloys after heat treating at 723K-12h

When the aging time increased from 6 h to 12 h, the precipitated phases were distributed uniformly to form a corrosion barrier, so the corrosion rate decreased to some extent. The amount of distribution of  $Mg_{17}Al_{12}$  phases became more after the 723K-6h and 12 h heat treatment, which reduces the cathodic sites as a result, improved corrosion resistance was observed and confirmed in the literature by Gopi et al. (2016). Figures 5.15 to 5.18 demonstrates the anodic and cathodic polarisation curves of all the ECAPed followed by annealed and aged AZ80 and AZ91 Mg alloys. The corrosion behaviour of all the materials altered significantly under these conditions. Comparatively, ECAP-2P and ECAP-4P followed by heat-treated AZ91 have shown improved corrosion resistance than the ECAP-2P and ECAP-4P followed by heat-treated AZ80 samples, specifically at 723K for 12h treatment was shown in figure 5.19.

#### **5.3.4 Corrosion morphologies of ECAPed AZ80/91 Mg alloys**

Figure 5.20 displays the SEM corrosion morphologies of the ECAPed and heat-treated sample after being tested in 3.5wt.% NaCl solution through potentiodynamic polarization. It is established that the surface of the heat-treated ECAPed samples is less corroded when compared to the ECAPed samples without heat treatment. The energy dispersive X-ray (EDX) result shows that the main corrosion product is  $Mg(OH)_2$ . It can be observed that the corroded surface consists of corrosion pits which are shown in Figure 5.20 (a2). Also, it can be observed that 4P-ECAP sample heat-treated at 723K-12h exhibited less corrosion attack compared to 2P-ECAPed sample heat-treated at 723K-12h. Whereas, ECAP-2P and 4P samples heat-treated at 523K-12h and without heat treatment yields severe corrosion attack with deeper corrosion pits shown in Figure 5.20. The reason for the above mechanisms was confirmed from the microstructural characterizations of ECAPed and heat-treated ECAPed AZ80 Mg alloys. The significant difference between them was an effective grain refinement and distribution of secondary phases. In general, the  $\beta$ -secondary phases have positive potential than the  $\alpha$ -Mg matrix, secondary phases may act as cathode sites and the Mg matrix act as an anode, resulting in the formation of galvanic corrosion (Lunder et al., 1989 and Jia et al., 2015). Meanwhile, ECAP followed by annealing and ageing treatment on AZ80 Mg alloy, all the secondary phase particles were dissolved and redistributed in the Mg matrix which reduces the cathode sites and undergoes less local

reaction, so that Mg sample surface experiences uniform corrosion, causing a lower corrosion rate. Further, from the previous study homogenization treatment on as-revived AZ80 Mg alloy revealed severe intergranular and pitting corrosion at the vicinity of grain boundaries (Naik et al., 2018). The intergranular corrosion was completely nullified and minimum corrosion pits were observed during annealing and ageing treatment on ECAPed AZ80 Mg alloys. Figure 5.21 shows the corrosion morphologies of heat-treated ECAP-2P and 4P AZ91 Mg alloy samples after being tested in 3.5wt.% NaCl solution through electrochemical polarization test. From observation, complete reduction of corrosion attack on heat-treated samples of ECAP-2P and 4P when compared to without heat-treated ECAPed samples shown in figure 5.21.

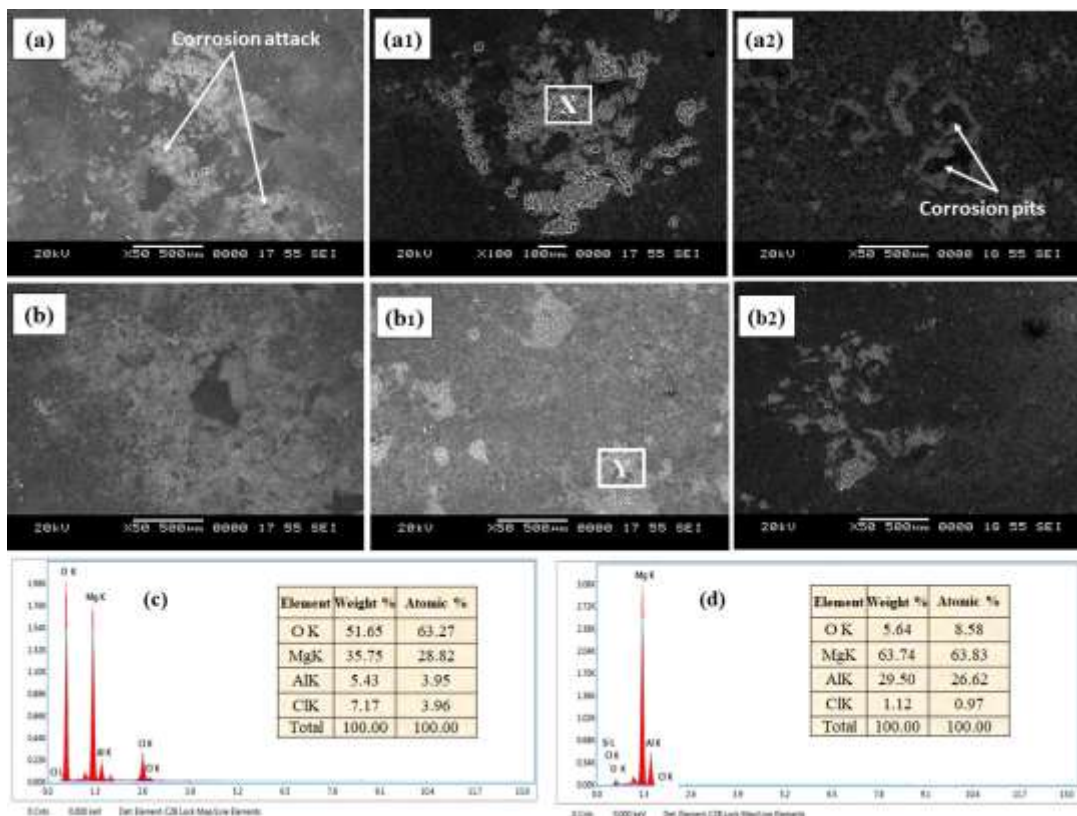


Figure 5.20 Corrosion morphology a) ECAP-2P a1) 523K-12h a2) 723-12hr b) ECAP-4P b1) 523K-12h b2) 723K-12h c) EDS for a1 at position X and d) EDS for b1 at position Y.

Also, it can be observed that AZ91 4P-ECAP sample heat-treated at 723K-12h exhibited less corrosion attack compared to 2P-ECAPed sample heat-treated at 723K-

12h as shown in figures 5.21 (a2) and (b2). The reason for such result was confirmed from the microstructural characterizations of ECAPed and heat-treated ECAPed AZ91 Mg alloys. This is due to grain refinement and majorly redistribution of secondary phases after ECAP and followed by heat treatment. For both AZ80/91 Mg alloy, the corrosion morphology study has been shown a good agreement with those obtained from potentiodynamic polarization results. Also, the corrosion morphologies study discloses that the corrosion attack on heat-treated AZ91 is less when compared to heat-treated AZ80 Mg alloys.

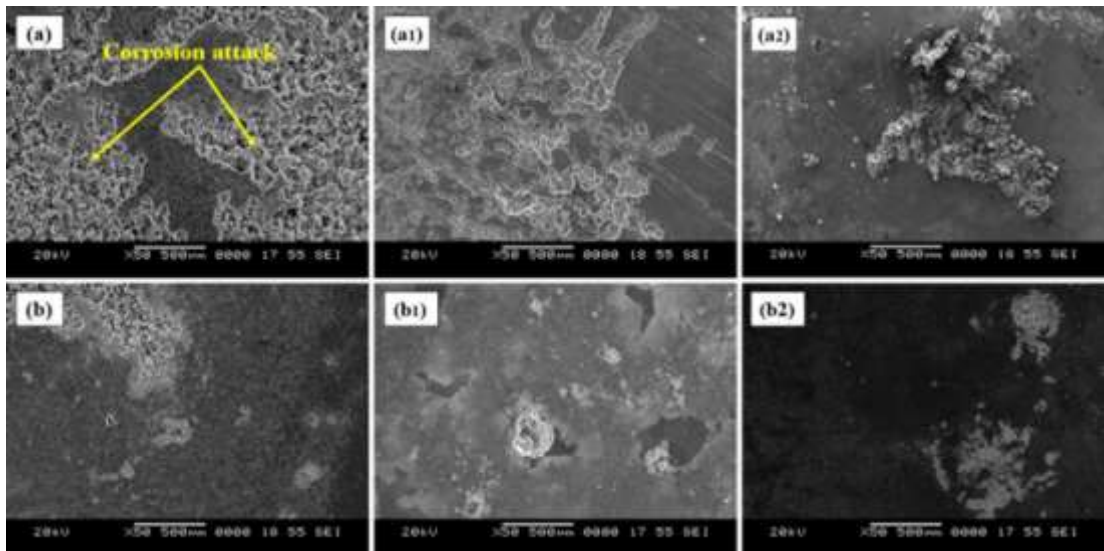


Figure 5.21 Corrosion morphology a) ECAP-2P a1) 523K-12h a2) 723-12hr b) ECAP-4P b1) 523K-12h b2) 723K-12h

Table 5.1 Data Sheet of processed and unprocessed AZ80/91 Mg alloys after annealing and aging treatment

Annealing Temperature	Annealing Time (h)	As-received			ECAP-2P			ECAP-4P		
		$E_{corr}$ (V <sub>SCE</sub> )	$I_{corr}$ (mA/cm <sup>2</sup> )	CR (mm/y)	$E_{corr}$ (V <sub>SCE</sub> )	$I_{corr}$ (mA/cm <sup>2</sup> )	CR (mm/y)	$E_{corr}$ (V <sub>SCE</sub> )	$I_{corr}$ (mA/cm <sup>2</sup> )	CR (mm/y)
AZ80 Magnesium alloys										
Room Temp.	0h	-1.507	0.2972	13.572	-1.553	0.0295	1.347	-1.494	0.0084	0.384
523K	6	-1.464	0.7004	31.985	-1.515	0.0160	0.731	-1.490	0.0038	0.174
	12	-1.524	0.2585	11.805	-1.483	0.0155	0.708	-1.464	0.0035	0.160
623K	6	-1.364	0.5561	25.396	-1.487	0.0105	0.480	-1.451	0.0033	0.151
	12	-1.502	1.4540	66.400	-1.470	0.0094	0.429	-1.450	0.0031	0.142
723K	6	-1.473	0.0412	1.881	-1.454	0.0067	0.306	-1.442	0.0022	0.100
	12	-1.383	0.1489	6.800	-1.410	0.0059	0.269	-1.408	0.0011	0.050
AZ91 Magnesium alloy										
Room Temp.	0	-1.539	0.2630	12.010	-1.548	0.0224	1.023	-1.488	0.0026	0.119
523K	6	-1.555	0.2610	11.919	-1.536	0.0128	0.585	-1.500	0.0028	0.128
	12	-1.548	0.1620	7.398	-1.510	0.0127	0.580	-1.512	0.0027	0.123
623K	6	-1.527	0.1200	5.480	-1.544	0.0129	0.589	-1.489	0.0021	0.096
	12	-1.507	0.0215	0.982	-1.510	0.00122	0.056	-1.408	0.0013	0.059
723K	6	-1.501	0.0235	1.073	-1.468	0.00120	0.055	-1.402	0.0012	0.055
	12	-1.489	0.0205	0.936	-1.428	0.00110	0.050	-1.400	0.0011	0.050

## **5.4 COATING OF AZ80/91 MAGNESIUM ALLOY**

This section studies the impact of 316 SS coating on corrosion behavior of as-received, ECAP-2P and 4P samples by high velocity oxygen fuel coating. The goal of this study is to validate the use of this technique as anticorrosion coatings for ECAPed AZ80/91 Mg alloys.

### **5.4.1 High-Velocity Oxygen Fuel coating on as-received and ECAPed AZ80/91 Mg alloy**

The use of AZ80/91 Mg alloys is restricted by their poor corrosion behaviour. Recent investigations have exposed a great potential of thermal spray methods for the surface modification of Mg alloys, one such process is High-Velocity Oxy-Fuel (HVOF) flame spray process achieved very dense coatings with favorable corrosion behaviour in comparison to other thermal spray processes, hence our study focused on HVOF coating (Oksa et al., 2011, Parco et al. 2006). In this section, as-received and ECAPed AZ80 and AZ91 Mg alloy were coated using the HVOF spraying process and 316 stainless steel powder of size  $21.6 \pm 1.6 \mu\text{m}$  was used as a coating material. Further, the coatings were characterized through microhardness and corrosion behaviour on AZ80 and AZ91 Mg substrates. The detailed discussion of HVOF coating on ECAPed Mg alloy is presented in the following sections.

### **5.4.2 Surface morphology studies on coated AZ80/91 Mg alloys**

The coated material was 316 Stainless Steel powder with spheroidal shape as shown in Figure 5.22. The average powder size measured was  $21.6 \pm 1.6 \mu\text{m}$ . Figures 5.23 and 5.24 shows SEM micrographs of an as-sprayed HVOF 316 SS coating and their cross-sections were shown for ECAPed AZ80 and AZ91 Mg alloys. The elemental distribution of 316 SS coatings was characterized by EDS analysis and shown in figures 5.23 (b) and 5.24 (b). The surface of the 316 SS coated AZ80 and AZ91 exhibits more compact and uniform coating. The average thickness was about  $80 \pm 5 \mu\text{m}$  that formed the base layer after depositing 316 SS shown in figures 5.23 (d) and 5.24 (d). 316 SS powder was homogeneously deposited on the surface of the as-received, ECAPed AZ80

and AZ91 Mg alloy substrates. No sub surface cracks formation or voids between coating and substrate interface were observed.

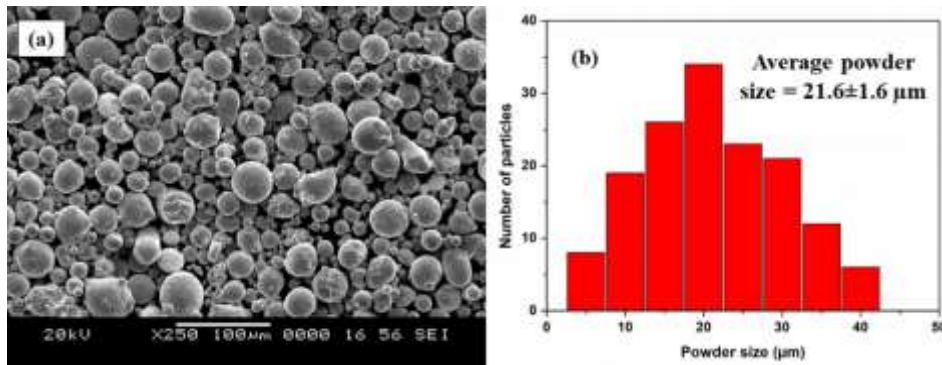


Figure 5.22 316 stainless steel powder a) SEM micrograph b) size distribution

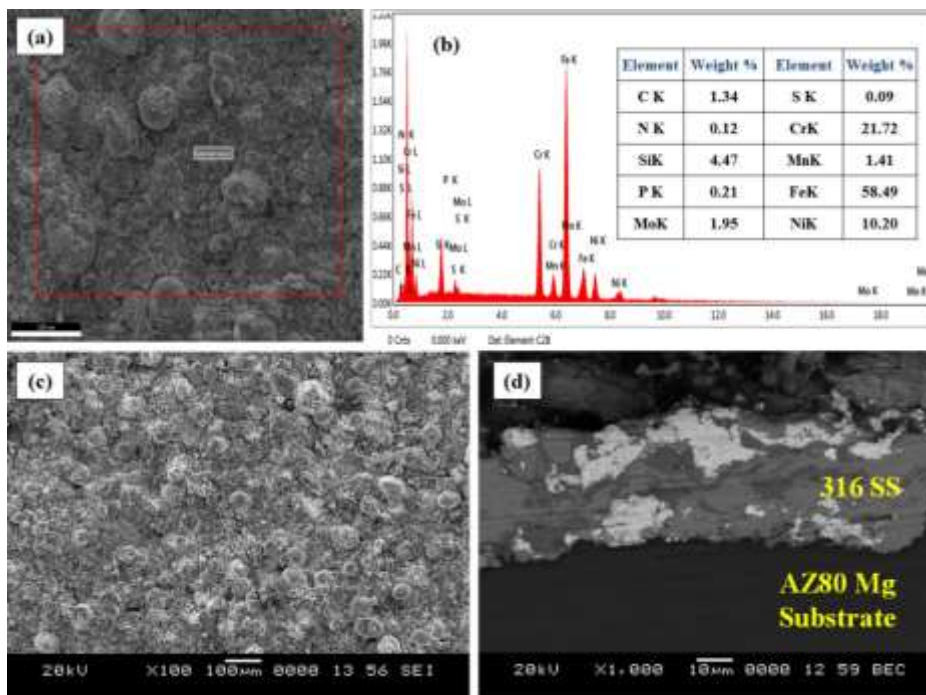


Figure 5.23 SEM surface morphologies of HVOF-coating on the ECAPed AZ80 Mg alloy a) as-received + 316SS b) EDS of the sealed coating c) ECAP-4P + 316SS and d) 316SS Coating thickness



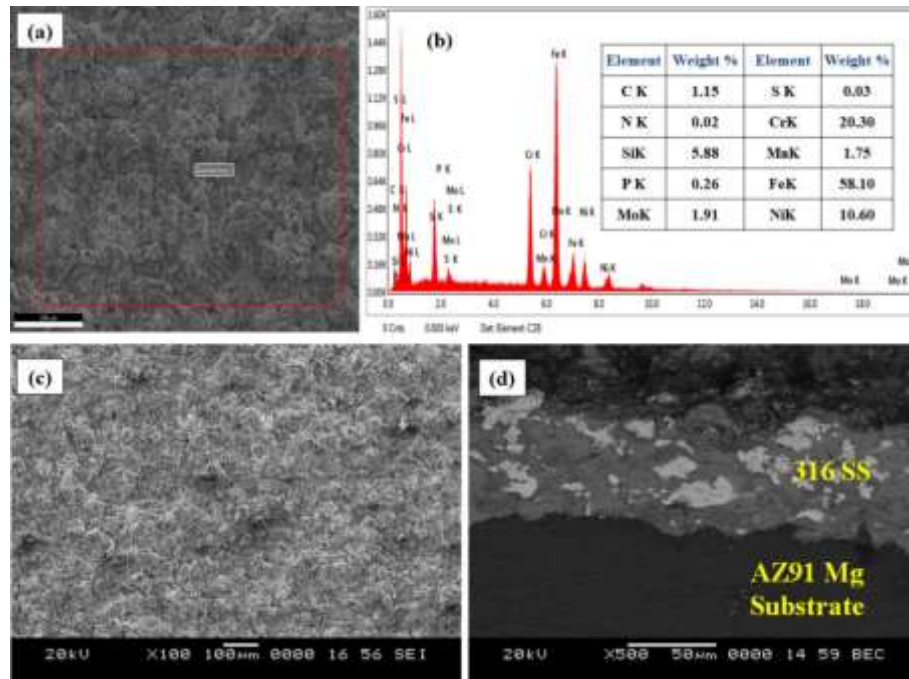


Figure 5.24. SEM surface morphologies of HVOF-coating on the ECAPed AZ91 Mg alloy a) as-received + 316SS b) EDS of the sealed coating c) ECAP-4P +316SS and d) 316SS Coating thickness

### 5.4.3 Microhardness evolution

Figure 5.25 and 5.26 shows the microhardness distribution along the depth in the cross section of the HVOF-316SS layer deposited over as-received and ECAPed AZ80 and AZ91 Mg alloys respectively. It can be observed that ECAPed samples with 316 SS coating results showed significant improvement in microhardness as compared to that of as-received AZ80/91 magnesium alloy coated with 316 SS. The average microhardness of the SS coated on as-received, ECAP-2P and 4P is 402 HV. Also, the interface of as-received and ECAPed AZ80/91 Mg alloys with 316 SS coating have shown slightly higher microhardness compared to 316 SS. Particularly, interface microhardness for 4P-ECAP AZ80 with 316 SS coating is 417.8 HV and 4P-ECAP AZ91 with 316 SS coating is 418.8 HV as shown in figures 5.25 and 5.26 respectively. Similar observations are made by García-Rodríguez et al. (2016) on un-ECAPed ZE41 Mg alloy. It is clear that the HVOF coatings typically exposed a microhardness gradient across the coating thickness with maximum hardness close to the interface and the lowest hardness at the substrate.

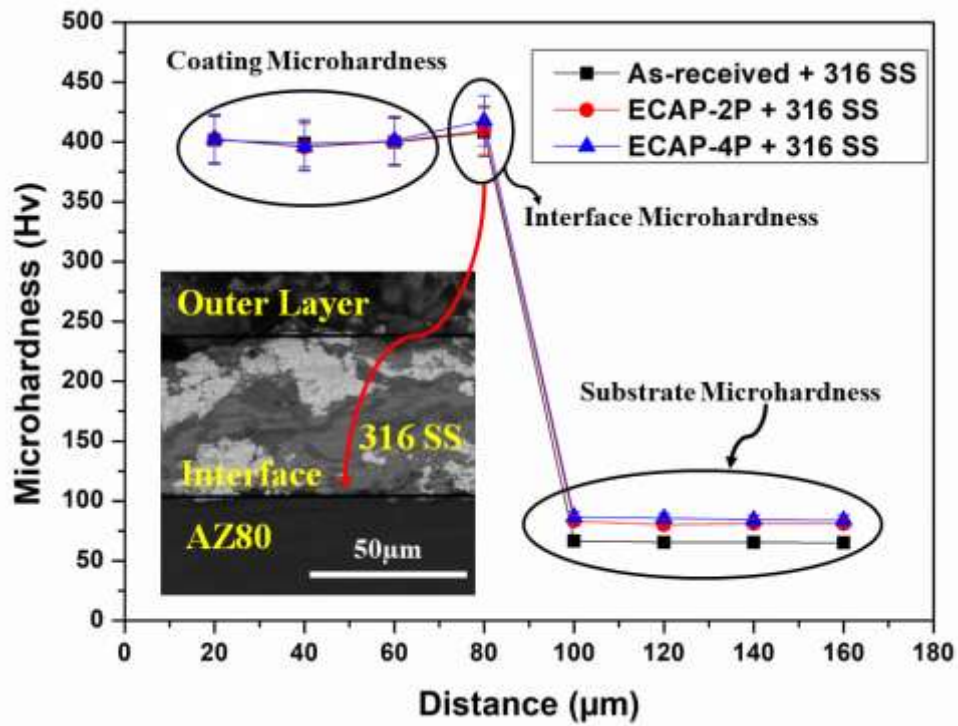


Figure 5.25 Sub surface microhardness of 316 SS coated AZ80 Mg alloys

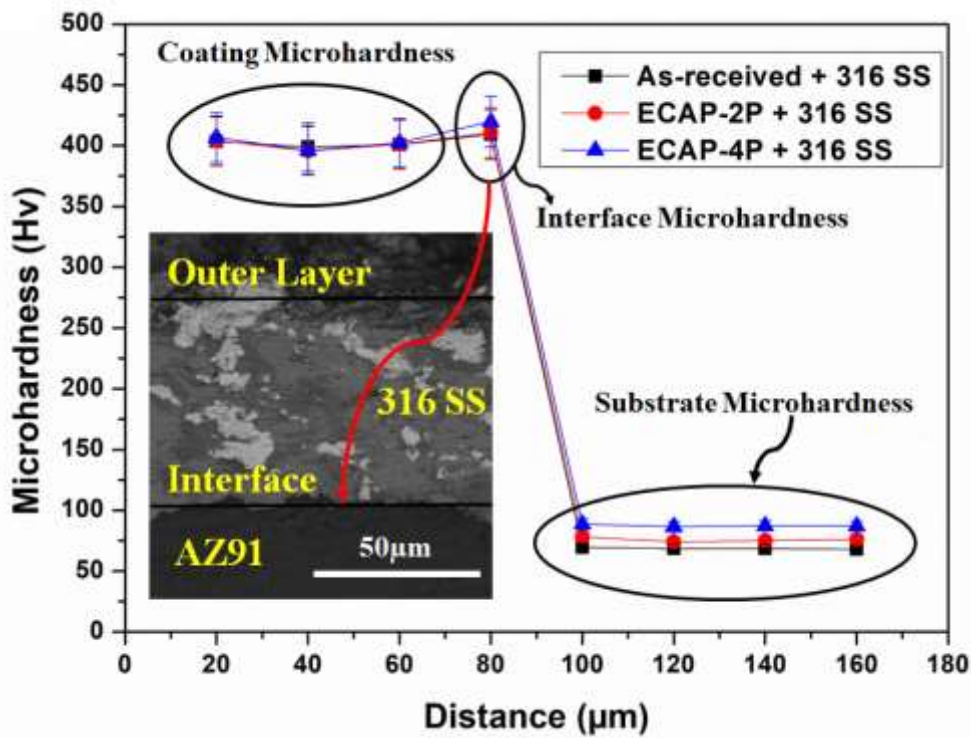


Figure 5.26 Sub surface microhardness of 316 SS coated AZ91 Mg alloys

The improvement of microhardness at the interface is attributed to the more uniform microstructure and finer grain size with less defect. From Figures 5.25 and 5.26 it is interesting to find that the microhardness of 316 SS layer on as-received Mg alloy has larger fluctuation than that of ECAPed material with 316 SS layer, this variation in microhardness proved in another perception that the microstructure of the ECAPed material with 316 SS coating becomes more uniform and dense (Sundararajan and Krishna 2003; Ma et al., 2008). Also, from the observation it was noticed that ECAPed AZ91 Mg alloy has consistently harder coatings than those of ECAPed AZ80 Mg alloys. The variations in microhardness with HVOF coating of 316 SS on ECAPed AZ80/91 Mg alloy were accompanied by changes in microstructure namely grain refinement and the precipitation of secondary phase and more denser coating which is evidently shown in figure 5.23 and 5.24 .

#### **5.4.4 Corrosion behavior of AZ80/91 Mg alloys after HVOF coating**

Anodic–cathodic potentiodynamic polarization curves of the as-received and ECAPed AZ80 and AZ91 Mg alloys after 316 SS coating in 3.5 wt. % NaCl aqueous solution are shown in Figures 5.27 and 5.29 respectively, where intersection of anodic and cathodic curves showing the corrosion potential ( $E_{\text{corr}}$ ) of 316 SS coated on as-received and ECAPed AZ80/91 magnesium alloy and of as-received AZ80/91 Mg alloy were also plotted for comparison. The open circuit corrosion potential of as-received AZ80 and AZ91 Mg specimen is  $-1.547 V_{\text{SCE}}$ ,  $-1.539 V_{\text{SCE}}$  was very close to that of the ECAPed AZ80 and AZ91 magnesium alloy, presenting that the substrate has low corrosion protection. This is established by the current density value obtained for as-received AZ80 and ECAP-2 and 4 passes, the measured current density was  $0.297 \text{ mA/cm}^2$ ,  $0.0295 \text{ mA/cm}^2$ ,  $0.0084 \text{ mA/cm}^2$  respectively. Similarly, for as-received AZ91 and ECAP-2P and 4P samples measures current density of  $0.263 \text{ mA/cm}^2$ ,  $0.0224 \text{ mA/cm}^2$ ,  $0.0026 \text{ mA/cm}^2$  respectively presented in table 5.2. Further, corrosion potential ( $E_{\text{corr}}$ ) for AZ80: As-received/316 SS, 2P-ECAP/316 SS and 4-P-ECAP/316 SS coatings were  $-1.211 V_{\text{SCE}}$ ,  $-1.206 V_{\text{SCE}}$  and  $-1.203 V_{\text{SCE}}$  respectively are comparable to that of the 316 SS bulk material ( $-1.2 V_{\text{SCE}}$ ). These three coatings also showed the lowest corrosion current densities,  $0.000184 \text{ mA/cm}^2$ ,  $0.000116 \text{ mA/cm}^2$  and  $0.000108 \text{ mA/cm}^2$  respectively (Fig. 5.27), evidence of their effectiveness as

corrosion protective coatings for magnesium alloys at higher ECAP passes. Which are smaller than the value obtained for the uncoated as-received AZ80 magnesium alloy ( $0.297 \text{ mA/cm}^2$ ) this is mainly due to the higher corrosion resistance performance of 316 SS and compact and dense coating, which is evidently discussed the previous section. Similar observation was made on AZ91 Mg alloys after 316 SS coating, here current densities,  $0.000136 \text{ } \mu\text{A/cm}^2$ ,  $0.00012 \text{ } \mu\text{A/cm}^2$  and  $0.00009 \text{ } \mu\text{A/cm}^2$ , for As-received AZ91/316 SS, 2P-ECAP/316 SS and 4P-ECAP/316 SS respectively (Fig. 5.29).

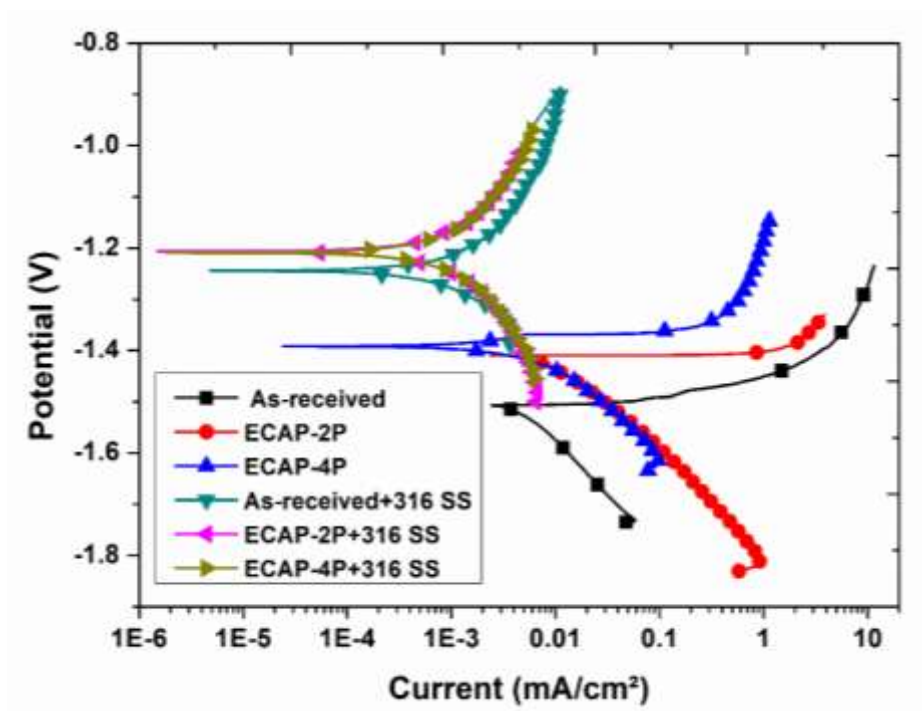


Figure 5.27 Corrosion behavior of ECAPed AZ80 Mg alloy after HVOF-coating

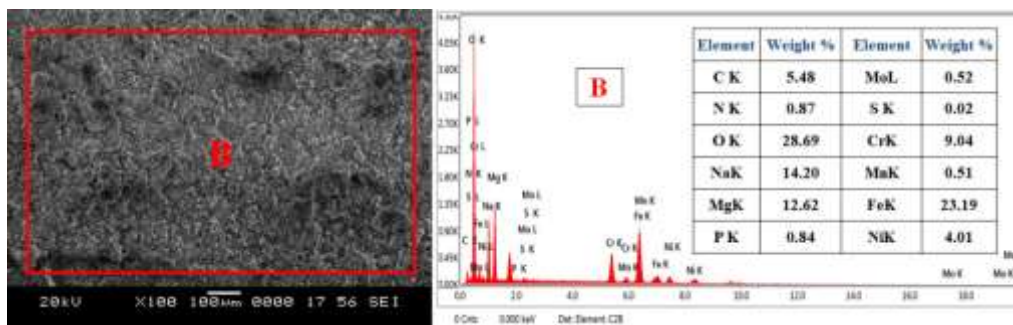


Figure 5.28 Corrosion morphology of ECAP-4P AZ80 Mg alloys after HVOF with EDS

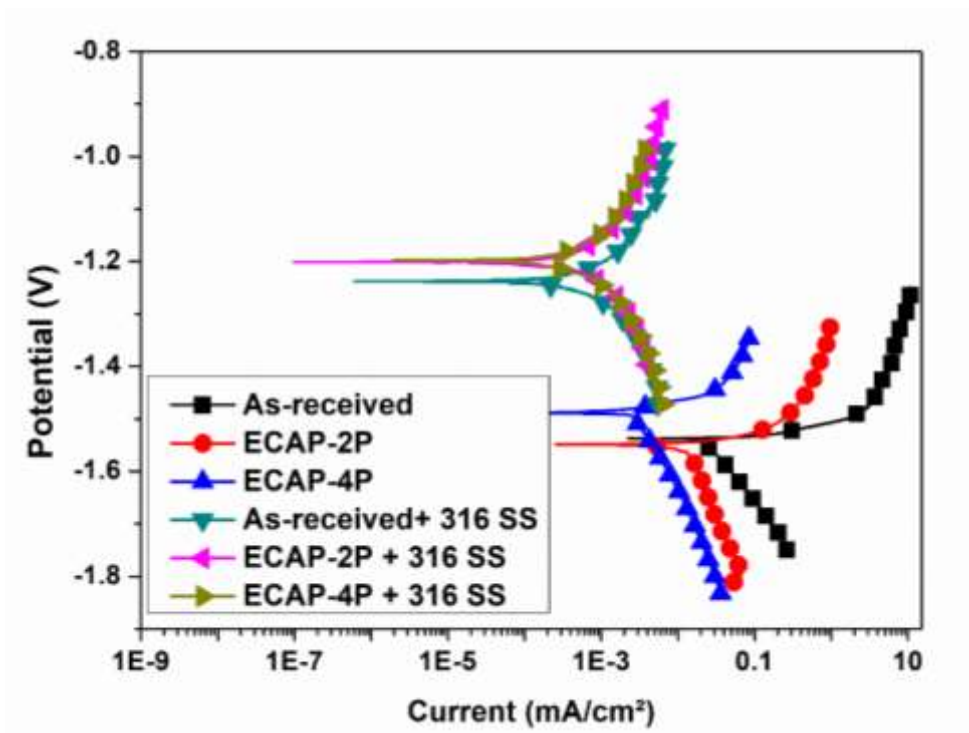


Figure 5.29 Corrosion behavior of ECAPed AZ91 Mg alloy after HVOF-coating

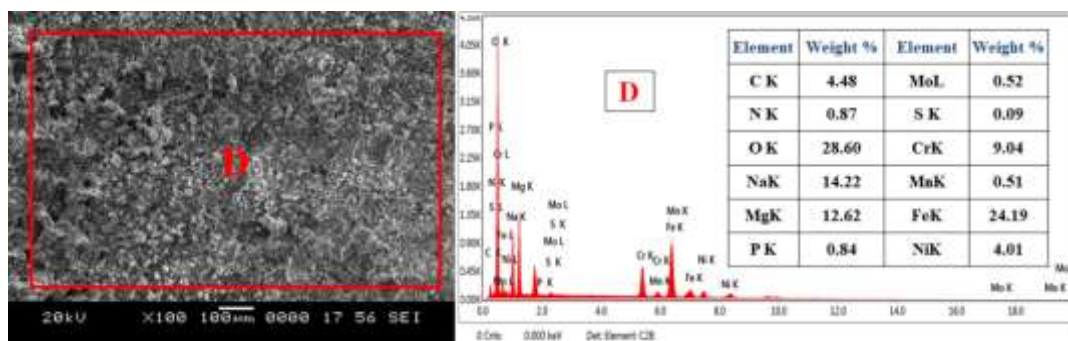


Figure 5.30 Corrosion morphology of ECAP-4P AZ91 Mg alloys after HVOF with EDS

Further, based on the polarization data of coated specimen, it can be concluded that ECAP-4P AZ91 Mg alloys has higher corrosion resistance than the ECAP-4P sample of AZ80 Mg alloy. After electrochemical polarization test, corroded specimen was taken to observe the surface morphologies of the coating by using SEM shown in figures 5.28 and 5.30, noticed the zones where pitting corrosion has occurred. It is revealed that corrosion attack are observed around the defects such as pores and cracks, and this displays that corrosion originated from these spots. Finally, figure 5.31 shows

the variation of corrosion rates of AZ80/91 Mg alloy after ECAP-4P and ECAP-4P followed by 316SS coating. From figure 5.31, it was observed that ECAP-4P sample significantly improved corrosion resistance after 316 SS coating, this is due to coated 316 SS is highly corrosion resistant material when compared to substrate.

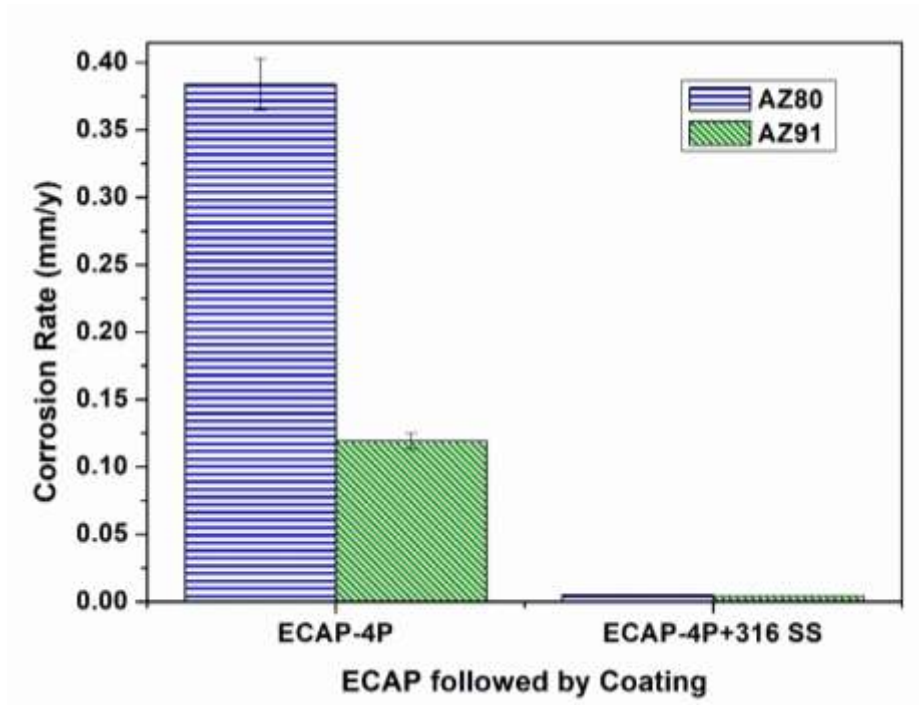


Figure 5.31 Corrosion rates of ECAP-4P AZ80/91 Mg alloy before and after 316 SS coating

Table 5.2 Data Sheet of ECAPed AZ80/91 Mg alloy after HVOF coating

Sample	AZ80			AZ91		
	$E_{corr}$ (V <sub>SCE</sub> )	$I_{corr}$ (mA/cm <sup>2</sup> )	CR (mm/y)	$E_{corr}$ (V <sub>SCE</sub> )	$I_{corr}$ (mA/cm <sup>2</sup> )	CR (mm/y)
As-received	-1.547	0.297	13.563	-1.539	0.263	12.010
ECAP-2P	-1.451	0.0295	1.347	-1.448	0.0224	1.023
ECAP-4P	-1.412	0.0084	0.384	-1.418	0.0026	0.119
AS-received +316SS	-1.211	0.000184	0.008	-1.237	0.000136	0.006
ECAP-2P+316SS	-1.205	0.000116	0.005	-1.201	0.00009	0.004
ECAP-4P+316SS	-1.203	0.000108	0.005	-1.195	0.00009	0.004

## **5.5 CORROSION BEHAVIOUR OF ECAPED AZ80/91 MAGNESIUM ALLOYS IN DIFFERENT ENVIRONMENTS**

In this section, AZ80/91 Mg alloys were used to comprehend the electrochemical corrosion behaviour of coarse-grained and fine-grained Mg alloys in different concentration of NaCl solution as well as in the marine environment. The inadequate studies of the corrosion response of ECAPed AZ80 and AZ91 Mg alloy in a different environment were noticed. Thus, in order to understand the performance of magnesium alloy in aqueous media and electrochemical properties of AZ80/91 Mg alloys in three different solutions. Accordingly, the current section presents and compares the corrosion behaviour of AZ80/91 Mg alloys in 2.5wt.% NaCl, 3.5wt.% NaCl solution and natural seawater. Influence of corrosion media on coarse and fine-grained AZ80/91 Mg alloys was discussed in the following sections.

### **5.5.1 Corrosion behavior of ECAPed AZ80/91 Mg alloys**

The potentiodynamic polarization curves of all the specimens tested in 2.5wt.% NaCl, 3.5wt.% NaCl and natural seawater (NSW) were shown in figures 5.32 and 5.33 for as-received and ECAPed AZ80 and AZ91 Mg alloys. The Electrochemical test results were obtained from the Tafel extrapolation method and curve-fitting data using Tafel listed in Table 5.3. Figures 5.32 (a)-(c) and 5.33 (a)-(c) represents the polarization curves of as-received, ECAP-2P and ECAP-4P AZ80 and AZ91 Mg samples in 2.5wt.% NaCl, 3.5wt.% NaCl solutions and natural seawater (NSW). This is to analyze the corrosion mechanism of a coarse and fine-grained specimen in 2.5wt.% NaCl, 3.5wt.% NaCl solutions and NSW three different environment. From the experimental results it was observed that as-received samples in all media showed higher corrosion density than the material processed through ECAP for both AZ80 and AZ91 Mg alloys as shown in figures 5.32, 5.33 and Table 5.3 Here, AZ80/91 Mg alloys which are having finer grain size act as noble, whereas coarse grain structured AZ80/91 Mg alloys act as active. This is because of uniform distribution of  $\beta$ -secondary phases after two and four passes of equal channel angular process. Along with this fine grain, ECAPed AZ80/91 Mg alloys have an improved re-passivation capacity, similar observations were noticed by song et al. (2016).

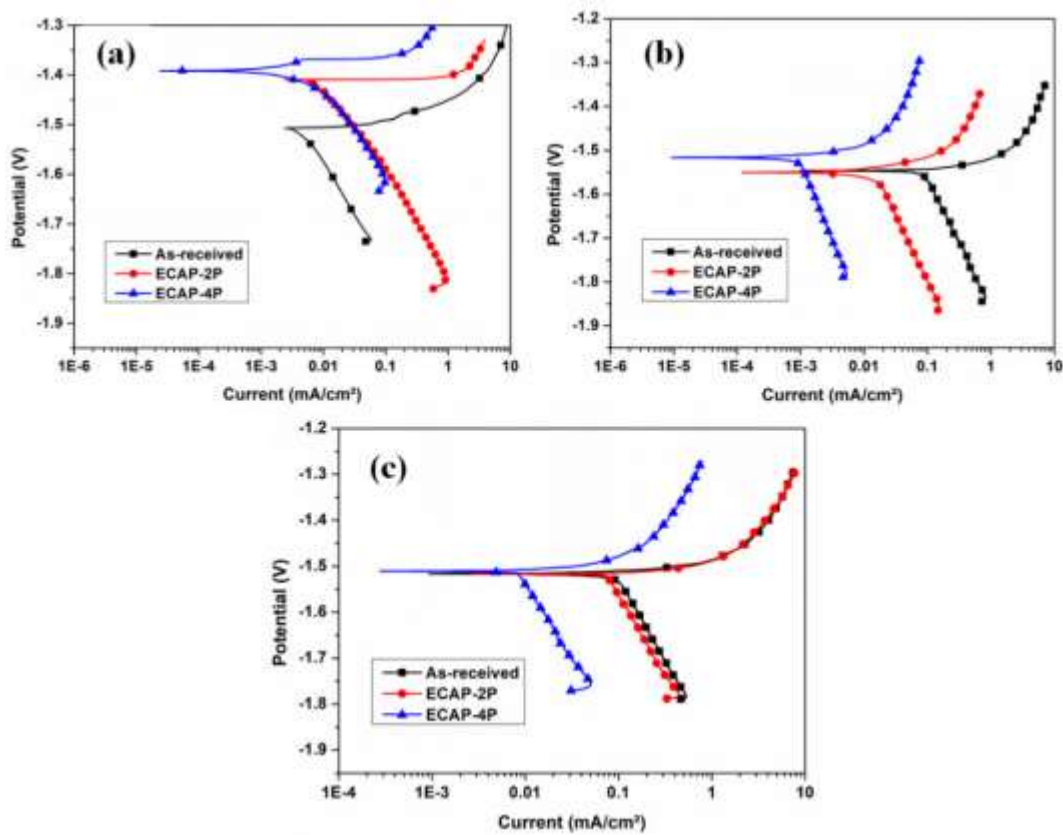


Figure 5.32 Potentiodynamic polarization curves for ECAPed AZ80-Mg alloys in a) 2.5wt.% NaCl b) 3.5wt.% NaCl and c) Natural Seawater

The pitting corrosion behaviour is quite common in magnesium-based alloys (Xin et al., 2010). As noted above, in our research work ECAP-4P AZ80 and AZ91 Mg alloy in 2.5wt.% NaCl solution had the highest corrosion potential ( $E_{corr}$ ) of  $-1.402 V_{SCE}$  and  $-1.401 V_{SCE}$ , whereas as-received AZ80 and AZ91 Mg alloys in NSW solution have the lowest corrosion potential of  $-1.517 V_{SCE}$  and  $-1.510 V_{SCE}$ . This means that ECAP-4P specimens of AZ91 Mg alloys are resistant to pitting corrosion. Table 5.3 also includes the values of the corrosion current density and corrosion rate obtained from the polarization curves. The current density ( $I_{corr}$ ) of ECAP-4P AZ80 fine-grain specimen increased to  $0.0525 \text{ mA/cm}^2$ , whereas ECAP-4P AZ91 Mg alloy current density ( $I_{corr}$ ) increased to  $0.0303 \text{ mA/cm}^2$  in NSW. Here, grain refinement and its uniform distribution of fine grains in the samples were the most influencing factors. Along with this,  $Mg_{17}Al_{12}$  secondary phases played an important role towards corrosion inhibition of AZ80/91 Mg alloys of all the three corrosion media.



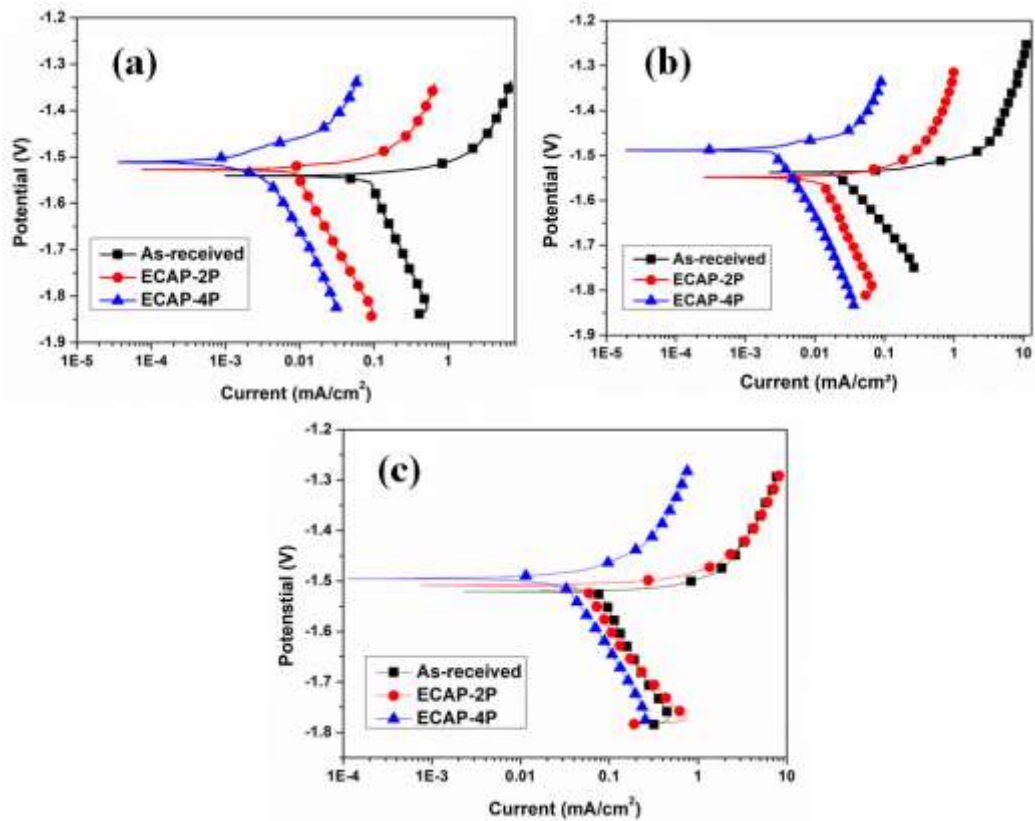


Figure 5.33 Potentiodynamic polarization curves for ECAPed AZ91-Mg alloys in a) 2.5wt.% NaCl b) 3.5wt.% NaCl and c) Natural Seawater

The findings of the work showed greater corrosion resistance with fine grain structure and distribution of secondary phases in the AZ80/91 Mg alloy, which was typical holds for AZ80/91 alloys exposed to containing 2.5wt.% NaCl, 3.5wt.% NaCl and natural seawater. However, grain refinement and secondary-phase precipitation were found to be essential for the differences observed between the corrosion media. Also, polarization results revealed that the corrosion attack of all test AZ80/91 Mg alloys increased with the increase in chloride ion concentration and decreased with the ECAP passes. This is due to the partial breakdown of the passive layer with increasing chloride ion concentration and decreased corrosion attack for ECAPed sample mainly due to fine and distributed grain structure (Ambat et al., 2000; Sun et al.2007; Xin et al. 2011).

### 5.5.2 Corrosion Morphology

The study of SEM morphologies of ECAP-4P specimens of AZ80 and AZ91 Mg alloys after corrosion test in three different environments such as 2.5wt.% NaCl, 3.5wt.% NaCl and NSW are reported. Here, the corrosion attack was observed on the surface of ECAP-4P AZ80/91 samples after electrochemical corrosion in three different media are shown in Figures 5.34 and 5.35. It can be seen from Figures 5.34 and 5.35 that the presence of chloride ion affects the magnesium alloys strongly which is evidently shown (Acharya et al., 2019). At a concentration of 3.5wt.% NaCl and NSW severe pitting corrosion occurs and specimen demonstrates deep corrosion attack over the surface compare to specimen tested in 2.5wt.% NaCl solution for both AZ80/91 Mg alloys. The ECAP-4P AZ80/91 alloy revealed uniform corrosion and pitting corrosion attack with the creation of an irregular passive film, which is composed of  $Mg(OH)_2$ . The uniform distribution of  $Mg_{17}Al_{12}$  secondary phases in the fine-grained AZ80/91 Mg alloy led to pitting corrosion in their vicinity without the development of deep pits for all corrosion media (Cheng et al., 2009; Shaw et al., 2003).

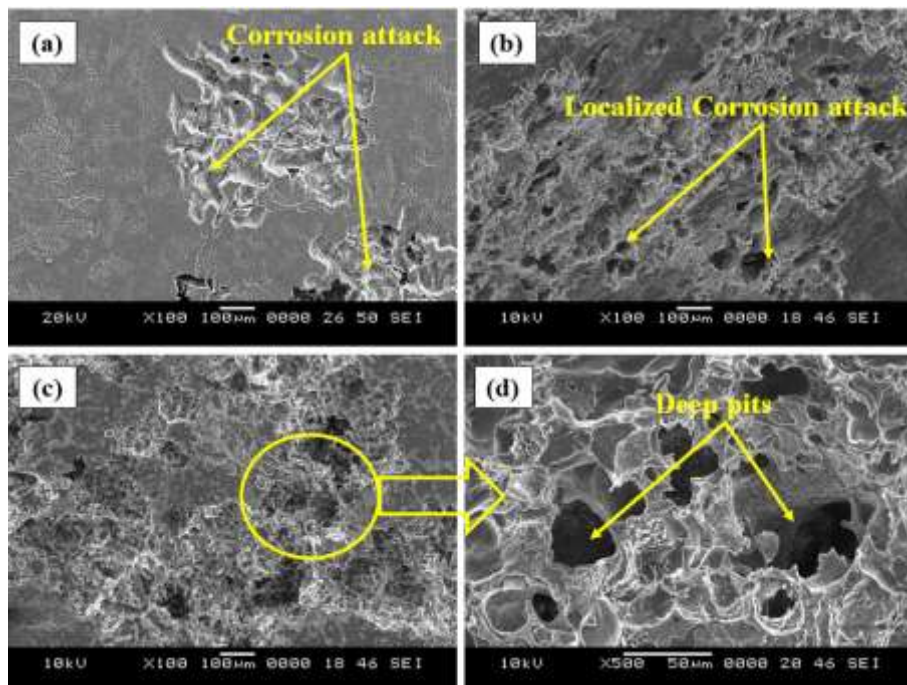


Figure 5.34 Corrosion morphologies of AZ80 Mg alloys ECAP processed at 4P a) 2.5wt.% NaCl b) 3.5wt.%NaCl c) NSW and d) NSW at higher magnification

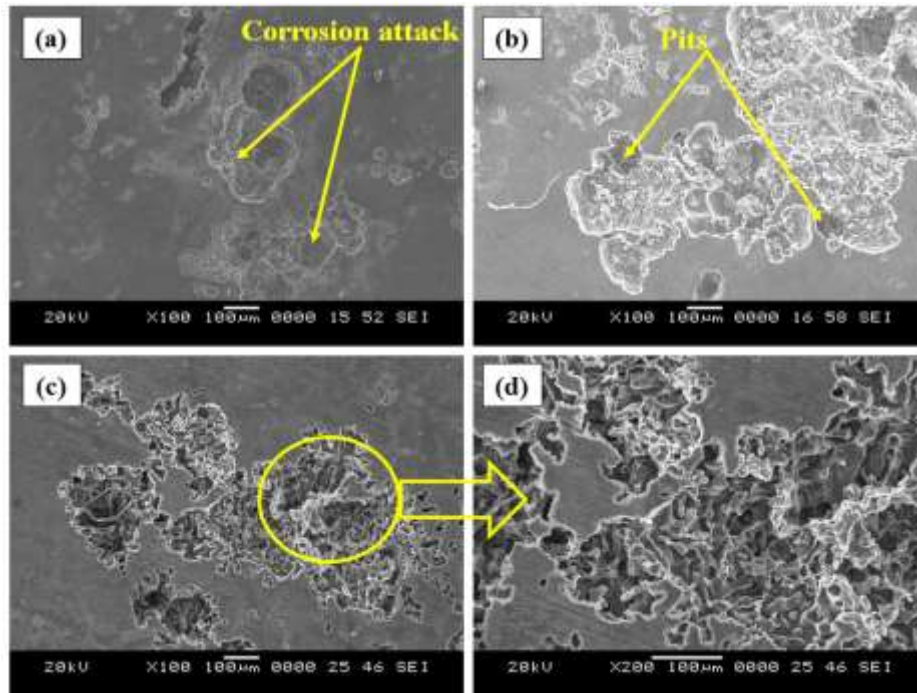


Figure 5.35 Corrosion morphologies of AZ91 Mg alloys ECAP processed at 4P  
 a) 2.5wt.% NaCl b) 3.5wt.% NaCl c) NSW and d) NSW at higher magnification

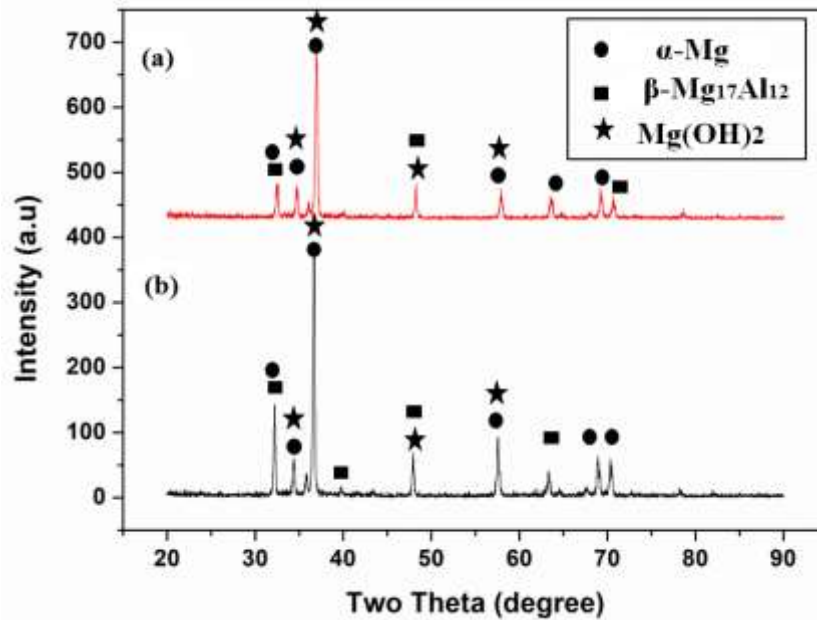


Figure 5.36 XRD for corroded ECAP-4P specimen a) AZ80: 2.5wt.% NaCl  
 and b) AZ91: 2.5wt.% NaCl

Table 5.3 Data Sheet of as-received and ECAPed AZ80/91 Mg alloy after testing in three different environments

Various Environment	As-received		ECAP-2P		ECAP-4P	
	I <sub>corr</sub> (mA/cm <sup>2</sup> )	CR (mm/y)	I <sub>corr</sub> (mA/cm <sup>2</sup> )	CR (mm/y)	I <sub>corr</sub> (mA/cm <sup>2</sup> )	CR (mm/y)
AZ80 Magnesium alloy						
2.5wt.% NaCl	0.136	6.211	0.0111	0.507	0.0057	0.260
3.5wt.% NaCl	0.2972	13.572	0.0295	1.347	0.0084	0.384
Natural sea water	0.404	18.450	0.0789	3.603	0.0525	2.398
AZ91 Magnesium alloy						
2.5wt.% NaCl	0.129	5.891	0.0124	0.566	0.0031	0.142
3.5wt.% NaCl	0.263	12.010	0.0224	1.023	0.0026	0.119
Natural sea water	0.366	16.714	0.0554	2.530	0.0303	1.384

The formation of pits in AZ80/91 Mg alloys due to degradation of the  $\alpha$ -Mg grains and corrosion inhibition mainly due to fine-grain structure and distributed secondary phase, revealed insignificant corrosion attack with the formation of a thin Aluminum rich passive layer, which was observed through SEM morphology and XRD analysis. The presence of Mg(OH)<sub>2</sub> corrosion product were evidently shown through x-ray diffraction analysis for ECAP-4P AZ80/91 Mg alloy in 2.5wt. % NaCl solution as shown in figure 5.36.

## 5.6 SUMMARY

The effect of annealing and aging treatment on the corrosion behavior of the as-received and ECAPed AZ80/91 magnesium alloy processed by equal channel angular pressing was investigated. The annealing and aging treatment were conducted at 523K, 623K and 723K for 6h and 12h. Further, the effect of heat treatment on microstructure and corrosion resistance have been studied. Along with this study, the influence of 316 stainless steel coating on microhardness and corrosion behaviour of as-received and

ECAPed AZ80/91 Mg alloys by HVOF technique were discussed and reported. Also, studied on the corrosion behaviour of as-received and ECAPed AZ80/91 Mg alloys in 2.5wt.% NaCl, 3.5wt.% NaCl and Natural Sea Water at room temperature. The effect of these environmental variables on corrosion resistance was investigated and the surface morphologies of the alloys were observed. Based on the experimental results and discussion, the following conclusions were drawn.

1. During annealing and aging treatments, the size and volume fraction of secondary phase very sensitive to temperature. The volume fraction increased with increasing annealing temperature and aging time.
2. The  $\beta$ -Mg<sub>17</sub>Al<sub>12</sub> secondary phases precipitate and dispersed as fine particles during annealing and aging treatment which descends the corrosion rate of the AZ80 and AZ91 Mg alloy due to reduction of cathodic sites.
3. Annealing temperature at 723 K–6h, 12h aging contributed a desirable improvement in the corrosion resistance according to electrochemical polarization measurements, owing to more homogenous distribution of secondary phases. Therefore, the treatment at 723 K for 6 h, 12 h is treated as an optimized annealing process for the as-received and ECAPed AZ80 Mg alloys respectively.
4. Precipitates of  $\beta$ -Mg<sub>17</sub>Al<sub>12</sub> increased the rate of corrosion resistance with increasing ECAP passes, annealing temperature and aging time. As a result, AZ91 Mg alloy solution treated at 723 K for 12 h and ECAP-4P-processed had enhanced corrosion resistance compared to AZ80 heat treated. Similar observations was made on ZK60 Mg alloys after ECAP and solution treatment by Xian et al. (2015).
5. The microhardness of as-received and ECAPed AZ80/91 Mg alloys improved by HVOF spray coating of 316 stainless steel. The result shows that approximately  $80 \pm 5$   $\mu\text{m}$  thick layer of 316 stainless steel powder improve the microhardness noticeably. In specific, the microhardness has gone up to 402 HV from 65 HV and 68 HV for AZ80 and AZ91 Mg alloy respectively. Also, the coating and substrate interface exhibited slightly higher microhardness.

Similar observations are made by García-Rodríguez et al. (2016) on un-ECAPed ZE41 Mg alloy.

6. The HVOF 316 stainless steel coating on 4P- ECAP AZ91 Mg alloys exhibited excellent corrosion resistance when compared to the other base alloys.
7. The corrosion resistance of exposed AZ80/91 magnesium alloys deteriorated with the chloride ion concentration and salinity and could be related to the cracks in corrosion product layers and the chemistry of corrosion products. AZ91 Mg alloy had the highest corrosion resistance compared to AZ80 Mg alloy.
8. A secondary phase  $Mg_{17}Al_{12}$  and its uniform distribution in ECAPed AZ80/91 Mg alloys improves corrosion resistance in 2.5wt.% NaCl, 3.5wt.% NaCl and Natural Sea Water at room temperature.
9. The current density and corrosion rates of the as-received and ECAPed AZ80/91 Mg alloys increased with an increase in the chloride ion concentration and decreased with ECAP passes. Similar observation were made by Xin et al. (2011) on ECAPed Mg alloys.

## CHAPTER 6

### CONCLUSIONS AND SCOPE FOR FUTURE WORK

#### 6.1 CONCLUSIONS

Equal channel angular extrusion was accomplished on AZ80/91 Mg alloy at a processing temperature of 533K, 598K and 663K using route R. Effects of ECAE process on microstructure, mechanical properties and corrosion behaviour for die A and die B were investigated. Further enhancement of corrosion resistance was achieved through annealing treatment and after 316 stainless steel coating by HVOF coating. Furthermore, the effectiveness of corrosion resistance of as-received and ECAPed AZ80/91 Mg alloys were investigated in three different environments such as 2.5 wt.% NaCl, 3.5 wt.% NaCl and Natural Sea Water and following conclusions are summed up based on the achieved outcome.

- The microstructure stability of fine-grained AZ80/91 magnesium alloy was shown that the Mg alloy processed through die A and die B at 533K using a four ECAP pass exhibited a high degree of grain refinement of about  $\sim 5.35 \mu\text{m}$  and  $\sim 8.64 \mu\text{m}$  respectively for ECAPed AZ80 Mg alloy and mean grain size of ECAPed AZ91 Mg alloy decreased to  $\sim 4.36 \mu\text{m}$  through die A and  $\sim 5.28 \mu\text{m}$  through die B.
- The thermo-mechanical treatment of AZ80/91 Mg alloy remarkably improves the microhardness with respect to a number of passes. The results showed a 24 % and 22 % enhancement in the microhardness of AZ80/91 Mg alloy for an ECAP processed with die A and die B respectively.
- The ECAPed AZ80 Mg alloy exhibited the UTS of  $\sim 451.01 \text{ MPa}$  and achieved highest tensile elongations of  $\sim 21.36 \%$  after 4P with die A. It was observed that the UTS and ductility has been improved by 11 % and 69% respectively. The ECAPed AZ91 Mg alloy exhibited the UTS of  $\sim 432.81 \text{ MPa}$  and achieved tensile elongations of  $\sim 19.13 \%$  after 4P with die A. here, enhancement of UTS and ductility was observed by 14 % and

59 % respectively. Also, tensile fractography revealed that void formation, coalescence and decohesion of secondary phase was dominant which leads to quasi-cleavage fractures.

- Potentiodynamic polarization test results showed reduced corrosion current density ( $I_{corr}$ ) which indicates higher corrosion resistance for the ECAP processed samples due to the presence of equiaxed fine grain microstructure and homogeneously distributed secondary phases ( $Mg_{17}Al_{12}$ ). Corrosion current density of as-received AZ80 Mg alloy is  $0.297 \text{ mA/cm}^2$  ( $13.56 \text{ mm/y}$ ), which is reduced to  $0.0084 \text{ mA/cm}^2$  ( $0.384 \text{ mm/y}$ ) after processing through die A-4P at 598K. Also, Corrosion current density of as-received AZ91 Mg alloy is  $0.263 \text{ mA/cm}^2$  ( $12.01 \text{ mm/y}$ ), which is reduced to  $0.0026 \text{ mA/cm}^2$  ( $0.119 \text{ mm/y}$ ) after processing through die A-4P at 598K.
- The uniformity of grain distribution, enhancement in mechanical properties and corrosion resistance of the AZ80/91 Mg alloy was significantly improved after processing through ECAP-die A at 598K. Therefore, ECAP-die having  $90^\circ$  channel angle is considered as optimum processing die.
- Annealing temperature at 723K and 12h aging contributed a desirable improvement on the corrosion resistance from electrochemical polarization measurements including the corrosion morphology. Therefore, the treatment at 723K for 12h is considered as optimized annealing process for ECAPed AZ80/91 Mg alloy. The corrosion current density of ECAP-4P AZ80 Mg alloy is  $0.0084 \text{ mA/cm}^2$  ( $0.384\text{mm/y}$ ), which is reduced to  $0.0011\text{mA/cm}^2$  ( $0.050\text{mm/y}$ ). Further, corrosion current density of ECAP-4P AZ91 Mg alloy is  $0.0026 \text{ mA/cm}^2$  ( $0.119\text{mm/y}$ ), which is reduced to  $0.0011\text{mA/cm}^2$  ( $0.050\text{mm/y}$ ) respectively.
- Microhardness increases from substrate to the outer most layer of coating and it was noticed to be maximum as it approaches interface zone because the interface layer of HVOF coating is denser and more compact than the inner and outer layer. As a result, interface of SS coated ECAP-4P samples



of AZ80/91 Mg alloy have shown 3.6% and 3.8% higher than the average microhardness of 316 SS coating on ECAP-4P samples of AZ80 and AZ91 Mg alloy respectively. Further, SS coating contributed a desirable improvement on the corrosion resistance. Which reduces the corrosion current density from  $0.297\text{mA/cm}^2$  (13.56mm/y) to  $0.00010\text{mA/cm}^2$  (0.005mm/y). Similarly, HVOF coating on ECAPed AZ91 Mg alloys reduces the corrosion current density from  $0.263\text{ mA/cm}^2$  (12.01mm/y) to  $0.00009\text{ mA/cm}^2$  (0.004mm/y) and it might be suitable for manufacturing of automobile and marine components.

- Corrosion attack on ECAPed AZ80/91 Mg alloys under 2.5wt.% NaCl, 3.5wt.%NaCl and natural seawater, increased with an increase of chloride concentration and decreased with ECAP passes. The corrosion current density decreased in the different environment of order NSW > 3.5wt.% NaCl > 2.5wt.%NaCl and observation might be beneficial to chemical industries.

## **6.2 CHALLENGES IN ECA EXTRUSION OF MAGNESIUM ALLOYS**

For decades equal channel angular extrusion has been efficiently utilized to process many engineering materials. However, ECA processing of magnesium alloy offers many challenges that have to be overcome by continued research.

1. The basal and prismatic planes in the magnesium HCP structure provides two independent slip systems each. Since Von Mises criteria dictates five independent slip system to allow free plastic deformation, it is quite apparent that Mg alloys has an inherent limitation in the plastic deformability. Due to above said reason the chances of formation of surface cracks on Mg samples during ECAP are more while processing at room temperature and below recrystallization temperature.
2. The yield stress of magnesium alloys is usually decreased by ECAP processing after few number passes because it follows inverse Hall-Patch effect.

3. Further, the size of component that can be pressed using ECAP depends upon the size of the die and loading capacity of pressing machine, which require huge investments to commercialize.

### **6.3 SCOPE FOR FUTURE WORK**

AZ series magnesium alloys were processed through equal channel angular extrusion (ECAE) up to four passes using route R. ECAP processed samples showed significant grain refinement and increased strength and hardness properties. Improvement in corrosion resistance was achieved for ECAP processed samples even after annealing and HVOF coating. Apart from these features, the following various aspects can be considered for future work.

- Microstructural investigations can be conducted further by texture analysis using pole figures to study the influence of texture on mechanical properties and corrosion resistance of material after ECAP through route R.
- Long term aging studies can be conducted for ECAPed samples to know the behavior of ECAP processed material at long time aging.
- Fatigue behavior of ECAPed samples can be examined to determine the behavior of material under fluctuating loads.
- Corrosion resistance of ECAPed samples can be investigated after metal arc oxidation coating/PEO-coating.
- Stress corrosion cracking studies can be observed for ECAPed specimens under constant or varying load.

## REFERENCES

- Abbasi, S., Aliofkhazraei, M., Mojiri, H., Amini, M., Ahmadzadeh, M., & Shourgeshty, M. (2017). "Corrosion behavior of pure Mg and AZ31 magnesium alloy." *Protection Met. Phy. Chem. Surf.*, 53(3), 573-578.
- Acharya, M. G., & Shetty, A. N. (2019). "The corrosion behavior of AZ31 alloy in chloride and sulfate media—A comparative study through electrochemical investigations." *J. Magnes. Alloys*, 7(1), 98-112.
- Agarwal S., J. Curtin, B. Duffy, S. Jaiswal. (2016). "Biodegradable magnesium alloys for orthopaedic applications: A review on corrosion, biocompatibility and surface modifications." *Mater. Sci. Engg.: C*, 68, 948–963.
- Aghion E, B. Bronfin. (2000). "Magnesium Alloys Development towards the 21st Century." *Mater. Sci. Forum*, 19, 350–351.
- Agnew, S. R. (2004). "Wrought magnesium: A 21st century outlook." *Jom*, 56(5), 20-21.
- Agwa, M. A., Ali, M. N., & Al-Shorbagy, A. E. (2016). "Optimum processing parameters for equal channel angular pressing." *Mech. Mater.*, 100, 1-11.
- Alaneme, K. K., & Okotete, E. A. (2019). "Recrystallization mechanisms and microstructure development in emerging metallic materials: A review." *J. Sci. Adv. Mater. Devices*, 4(1), 19-33.
- Alvarez-Lopez, M., Pereda, M. D., Del Valle, J. A., Fernandez-Lorenzo, M., Garcia-Alonso, M. C., Ruano, O. A., & Escudero, M. L. (2010). "Corrosion behaviour of AZ31 magnesium alloy with different grain sizes in simulated biological fluids." *Acta Biomater.*, 6(5), 1763-1771.

Ambat, R., Aung, N. N., & Zhou, W. (2000). "Studies on the influence of chloride ion and pH on the corrosion and electrochemical behaviour of AZ91D magnesium alloy." *J. Appl. Electroch.*, 30(7), 865-874.

Arab, S. M., & Akbarzadeh, A. (2013). "The effect of Equal Channel Angular Pressing process on the microstructure of AZ31 Mg alloy strip shaped specimens." *J. Magnes. Alloys*, 1(2), 145-149.

Argade G.R., S.K. Panigrahi, R.S. Mishra. (2012). "Effects of grain size on the corrosion resistance of wrought magnesium alloys containing neodymium." *Corr. Sci.*, 58, 145–151.

Arpacay, D., Yi, S. B., Janeček, M., Bakkaloglu, A., & Wagner, L. (2008). "Microstructure evolution during high pressure torsion of AZ80 magnesium alloy." *Mater. Sci. Forum*, 584, 300-305.

Atrens A, GL Song, F Cao, Z Shi, PK Bowen. (2013). "Advances in Mg corrosion and research suggestions." *J. Magnes. Alloys*, 1, 177-200.

Avvari, M., & Able, M. (2016). "Microstructure evolution in AZ61 alloy processed by equal channel angular pressing." *Adv. Mech. Eng.*, 8(6), 1687814016651820.

Avvari, M., Narendranath, S., & Nayaka, H. S. (2015). "A review on wrought magnesium alloys processed by equal channel angular pressing." *Int. J. Mater. Prod. Tech.*, 51, 139-164.

Avvari, M., & Narendranath, S. (2018). "Effect of secondary Mg 17 Al 12 phase on AZ80 alloy processed by equal channel angular pressing (ECAP)." *Silicon*, 10(1), 39-47.

Avvari, M., & Narendranath, S. (2014). "Influence of Route-R on wrought magnesium AZ61 alloy mechanical properties through equal channel angular pressing." *J. Magnes. Alloys*, 2(2), 159-164.

Avvari, M., Narendranath, S., & Nayaka, H. S. (2014). "Effect of Processing Routes on AZ31 Alloy Processed By Severe Plastic Deformation." *Proc. Mater. Sci.*, 5, 1560-1566.

Azushima, R. Kopp, A. Korhonen, D.Y. Yang, F. Micari, P. Groche, J. Yanagimoto, N. Tsuji, A. Rosochowski, A. Yanagida, G.D. Lahoti. (2008). "Severe plastic deformation (SPD) processes for metals." *Manuf. Tech.*, 57 (1), 716–735.

Bao, L, Z. Zhang, Q. Le, S. Zhang, J. Cui. (2017) "Corrosion behavior and mechanism of Mg-Y-Zn-Zr alloys with various Y / Zn mole ratios," *J. Alloys Comp.*, 712, 15–23.

Bahmani, A., Arthanari, S., & Shin, K. S. (2019). "Improved corrosion resistant and strength of a magnesium alloy using multi-directional forging (MDF)." *Int. J. Adv. Manuf. Tech.*, 105(1-4), 785-797.

Bakhsheshi-Rad, H. R., Abdellahi, M., Hamzah, E., Ismail, A. F., & Bahmanpour, M. (2016). "Modelling corrosion rate of biodegradable magnesium-based alloys: The case study of Mg-Zn-RE-xCa (x= 0, 0.5, 1.5, 3 and 6 wt%) alloys." *J. Alloys Comp.*, 687, 630-642.

Bettles, Colleen, and Mark Gibson. (2005)."Current wrought magnesium alloys: strengths and weaknesses." *Jom*, 57 (5), 46-49.

Bennett, J. W., Grinberg, I., Davies, P. K., & Rappe, A. M. (2010). "Pb-free semiconductor ferroelectrics: A theoretical study of Pd-substituted Ba (Ti<sub>1-x</sub>Ce<sub>x</sub>)O<sub>3</sub> solid solutions." *Phy. Review B*, 82(18), 184106.

Birbilis, N., Ralston, K. D., Virtanen, S., Fraser, H. L., & Davies, C. H. J. (2010). "Grain character influences on corrosion of ECAPed pure magnesium." *Corr. Eng. Sci. Tech.*, 45(3), 224-230.

Blawert, C., Hort, N., & Kainer, K. U. (2004). "Automotive applications of magnesium and its alloys." *Trans. Indian Inst. Met.*, 57(4), 397-408.

Brunner J.G, J. May, H.W. Höppel, M. Göken, S. Virtanen. (2010). "Localized corrosion of ultrafine-grained Al – Mg model alloys." *Electrochimica Acta*, 55, 1966–1970.

Cáceres, C. H., & Rovera, D. M. (2001). "Solid solution strengthening in concentrated Mg–Al alloys." *J. Light Metals*, 1(3), 151-156.

Chen Y., Z. Xu, C. Smith, J. Sankar. (2014). "Recent advances on the development of magnesium alloys for biodegradable implants." *Acta Biomater.*, 10, 4561–4573.

Chen, Q., Shu, D., Hu, C., Zhao, Z., & Yuan, B. (2012). "Grain refinement in an as-cast AZ61 magnesium alloy processed by multi-axial forging under the multi temperature processing procedure." *Mater. Sci. Engg.,: A*, 541, 98-104.

Cheng Xu, Steven Schroeder, Patrick B. Berbon, Terence G. Langdon. (2010). "Principles of ECAP–Conform as a continuous process for achieving grain refinement: Application to an aluminum alloy." *Acta Mater.*, 58 (1), 1379–1386.

Cheng, W. L., Tian, Q. W., Yu, H., Zhang, H., & You, B. S. (2014). "Strengthening mechanisms of indirect-extruded Mg–Sn based alloys at room temperature." *J. Magnes. Alloys*, 2(4), 299-304.

Cheng, Y. L., Qin, T. W., Wang, H. M., & Zhang, Z. (2009). "Comparison of corrosion behaviors of AZ31, AZ91, AM60 and ZK60 magnesium alloys." *Trans. nonferrous met. Soc. China*, 19(3), 517-524.

Chiu, C., & Huang, H. M. (2018). "Microstructure and Properties of Mg-Zn-Y Alloy Powder Compacted by Equal Channel Angular Pressing." *Mater.*, 11(9), 1678.

Chun, J. S., & Byrne, J. G. (1969). "Precipitate strengthening mechanisms in magnesium zinc alloy single crystals." *J. Mater. Sci.*, 4(10), 861-872.

Davies, C., & Barnett, M. (2004). "Expanding the extrusion limits of wrought magnesium alloys." *JOM*, 56(5), 22-24.

Ding, R., Chung, C., Chiu, Y., & Lyon, P. (2010). "Effect of ECAP on microstructure and mechanical properties of ZE41 magnesium alloy." *Mater. Sci. Engg.: A*, 527(16-17), 3777-3784.

Dieter, G. E., & Bacon, D. (1986). "Mechanical metallurgy" (Vol. 3). New York: McGraw-hill.

Ding, S. X., Chang, C. P., & Kao, P. W. (2009). "Effects of processing parameters on the grain refinement of magnesium alloy by equal-channel angular extrusion." *Metallurgical and Materials Transactions A*, 40(2), 415.

Del Valle, J. A., Carreño, F., & Ruano, O. A. (2006). "Influence of texture and grain size on work hardening and ductility in magnesium-based alloys processed by ECAP and rolling." *Acta Materialia*, 54(16), 4247-4259.

Djavanroodi F., M. Ebrahimi. (2010). "Effect of die parameters and material properties in ECAP with parallel channels." *Mater. Sci. Engg.: A*, 527, 7593-7599.

Djavanroodi, F., Omranpour, B., Ebrahimi, M., & Sedighi, M. (2012). "Designing of ECAP parameters based on strain distribution uniformity." *Prog. Nat. Sci.: Mater. Int.*, 22(5), 452-460.

Doiphode, R. L., Murty, S. N., Prabhu, N., & Kashyap, B. P. (2015). "Grain growth in calibre rolled Mg–3Al–1Zn alloy and its effect on hardness." *J. Magnes. Alloys*, 3(4), 322-329.

Dziubińska, A., Gontarz, A., Dziubiński, M. and Barszcz, M. (2016). "The forming of magnesium alloy forgings for aircraft and automotive applications." *Adv. Sci. Tech. Res. J*, 10, 158–168.

Edward Ghali, Wolfgang Dietzel, and Karl-Ulrich Kainer. (2004). "General and Localized Corrosion of Magnesium Alloys: A Critical Review," *JMEP*, 13, 7-23.

Esmaily M, D.B. Blücher, J.E. Svensson, M. Halvarsson, L.G. Johansson. (2016). "New insights into the corrosion of magnesium alloys-The role of aluminium." *Scripta Mater.*, 115, 91–95.

Esmaily M, M. Shahabi-navid, J. Svensson, M. Halvarsson, L. Nyborg, Y. Cao, L. Johansson. (2015). "Influence of temperature on the atmospheric corrosion of the Mg – Al alloy AM50." *Corr. Sci.*, 90, 420–433.

Esmaily, M., Svensson, J. E., Fajardo, S., Birbilis, N., Frankel, G. S., Virtanen, S, & Johansson, L. G. (2017). "Fundamentals and advances in magnesium alloy corrosion." *Prog. Mater. Sci.*, 89, 92-193.

Estrin Y, A. Vinogradov. (2013). "Extreme grain refinement by severe plastic deformation: A wealth of challenging science." *Acta Mater.*, 61 (1) 782–817.

Fan, Q., Liang, W., Bian, L. P., & Cheng, M. Q. (2013). "Effect of ECAP Pass on Corrosion Behavior of High-Al Content Magnesium Alloys." *Mater. Sci. Forum*, 747, 270-275.

Figueiredo, R. B., & Langdon, T. G. (2010). "Grain refinement and mechanical behavior of a magnesium alloy processed by ECAP." *J. Mater. Sci.*, 45(17), 4827-4836.



Figueiredo, Roberto B., Flávia SJ Poggiali, Cláudio LP Silva, Paulo R. Cetlin, and Terence G. Langdon. (2016). "The influence of grain size and strain rate on the mechanical behavior of pure magnesium." *J. Mater. Sci.*, 51 (6), 3013-3024.

Froes, F. H., Eliezer, D., & Aghion, E. (1998). "The science, technology, and applications of magnesium." *Jom*, 50, 30-34.

Furuno, K., Akamatsu, H., Oh-ishi, K., Furukawa, M., Horita, Z. and Langdon, T. G. (2004). "Microstructural development in equal-channel angular pressing using a 60° die." *Acta Mater.*, 52(9), 2497-2507.

Furukawa, M., Horita, Z., & Langdon, T. G. (2001). "Developing ultrafine grain sizes using severe plastic deformation." *Adv. Eng. Mater.*, 3(3), 121-125.

Gajanan, M. N., Narendranath, S., & Kumar, S. S. (2019). "Effect of grain refinement on mechanical and corrosion behavior of AZ91 magnesium alloy processed by ECAE." *IOP Conf. Series: Mater. Sci. Eng.* 591(1), 012015.

García-Rodríguez, S., López, A. J., Torres, B., & Rams, J. (2016). "316L stainless steel coatings on ZE41 magnesium alloy using HVOF thermal spray for corrosion protection." *Surf. Coat. Tech.*, 287, 9-19.

Gao, L., Chen, R. S., & Han, E. H. (2009). "Effects of rare-earth elements Gd and Y on the solid solution strengthening of Mg alloys." *J. Alloys Comp.*, 481(1-2), 379-384.

Gao, X., & Nie, J. F. (2007). "Characterization of strengthening precipitate phases in a Mg–Zn alloy." *Scripta Mater.*, 56(8), 645-648.

Geng, Z., Xiao, D., & Chen, L. (2016). "Microstructure, mechanical properties, and corrosion behavior of degradable Mg-Al-Cu-Zn-Gd alloys." *J. Alloys Comp.*, 686, 145-152.

Gnedenkov, S. V., Sinebryukhov, S. L., Mashtalyar, D. V., & Imshinetskiy, I. M. (2015). "Composite fluoropolymer coatings on Mg alloys formed by plasma electrolytic oxidation in combination with electrophoretic deposition." *Surf. Coat. Tech.*, 283, 347-352.

Ghader Faraji, Alireza Babaei, Mahmoud Mosavi Mashhadi, Karen Abrinia. (2012). "Parallel tubular channel angular pressing (PTCAP) as a new severe plastic deformation method for cylindrical tubes." *Mater. Letters* 77, 82–85.

Ghader Faraji, Mahmoud Mosavi Mashhadi, Soo-Hyun Joo and Hyoung Seop Kim. (2012) "The Role of Friction In Tubular Channel Angular Pressing." *Rev. Adv. Mater. Sci.* 31, 12-18.

Ghali, Edward, Wolfgang Dietzel, and Karl-Ulrich Kainer. (2004). "General and localized corrosion of magnesium alloys: a critical review." *JMEP*, 13, 7-23.

González, S., Pellicer, E., Fornell, J., Blanquer, A., Barrios, L., Ibáñez, E., & Sort, J. (2012). "Improved mechanical performance and delayed corrosion phenomena in biodegradable Mg–Zn–Ca alloys through Pd-alloying." *J. mech. behavior biomedical mater.*, 6, 53-62.

Gobara, M., Shamekh, M., & Akid, R. (2015). "Improving the corrosion resistance of AZ91D magnesium alloy through reinforcement with titanium carbides and borides." *J. Magnes. Alloys*, 3(2), 112-120.

Gopi, K. R., Nayaka, H. S., & Sahu, S. (2016). "Investigation of microstructure and mechanical properties of ECAP-processed AM series magnesium alloy." *JMEP*, 25(9), 3737-3745.

Gopi, K. R., & Nayaka, H. S. (2017). "Tribological and corrosion properties of AM70 magnesium alloy processed by equal channel angular pressing." *J. Mater. Res.*, 32(11), 2153-2160.

Gray, J., & Luan, B. (2002). "Protective coatings on magnesium and its alloys—a critical review." *J. Alloys Comp.*, 336(1-2), 88-113.

Gu, X. N., Li, N., Zheng, Y. F., Kang, F., Wang, J. T., & Ruan, L. (2011). "In vitro study on equal channel angular pressing AZ31 magnesium alloy with and without back pressure." *Mater. Sci. Eng.: B*, 176(20), 1802-1806.

Guo, K. W. (2010). "A review of magnesium/magnesium alloys corrosion and its protection." *Recent Patents on Corr. Sci.*.

Han, J. H., Chang, H. J., Jee, K. K., & Oh, K. H. (2009). "Effects of die geometry on variation of the deformation rate in equal channel angular pressing." *Met. Mater. Int.*, 15(3), 439-445.

Hadzima, B., Janeček, M., Suchý, P., Müller, J., & Wagner, L. (2008). "Microstructure and corrosion properties of fine-grained Mg-based alloys." *Mater. Sci. Forum*, 584, 994-999.

Hao-Miao Yang, Nan-Yi Zhang, Na Liu, Wei-Dong Xie, Xiao-Dong Peng. (2016). "Microstructure, mechanical properties, and corrosion resistance of Mg–9Li–3Al–1.6Y alloy." *Rare Metals*, 35, 374-379.

Hamu, G. B., Eliezer, D., & Wagner, L. (2009). "The relation between severe plastic deformation microstructure and corrosion behavior of AZ31 magnesium alloy." *J. Alloys Comp.*, 468(1-2), 222-229.

Hono K, C.L. Mendis, T.T. Sasaki. (2010). "Towards the development of heat-treatable high-strength wrought Mg alloys." *Scripta. Mater.*, 63, 710–715.

Hosaka, T., Yoshihara, S., Amanina, I., & MacDonald, B. J. (2017). "Influence of grain refinement and residual stress on corrosion behavior of AZ31 magnesium alloy processed by ECAP in RPMI-1640 medium." *Proc. Eng.*, 184, 432-441.

Hoog, C., Birbilis, N., & Estrin, Y. (2008). "Corrosion of pure Mg as a function of grain size and processing route." *Adv. Eng. Mater.*, 10(6), 579-582.

Huang, X., Suzuki, K., & Saito, N. (2009). "Microstructure and mechanical properties of AZ80 magnesium alloy sheet processed by differential speed rolling." *Mater. Sci. Engg.: A*, 508(1-2), 226-233.

Huang, S. J., Chiu, C., Chou, T. Y., & Rabkin, E. (2018). "Effect of equal channel angular pressing (ECAP) on hydrogen storage properties of commercial magnesium alloy AZ61." *Int. J. Hydrogen Energy*, 43(9), 4371-4380.

Ishikawa, K., Watanabe, H., & Mukai, T. (2005). "High strain rate deformation behavior of an AZ91 magnesium alloy at elevated temperatures." *Mater. Lett.*, 59(12), 1511-1515.

Jiang, J., Yin, L., Lu, F., Ma, A., Song, D., Zhang, L., & Chen, J. (2014). "Microstructure and corrosion behaviour of Mg-2Gd-1Y-1Zn-0.2Zr (at-%) alloy processed by equal channel angular pressing." *Corr. Eng. Sci. Tech.*, 49(4), 316-320.

Jiang, J., Zhou, Q., Yu, J., Ma, A., Song, D., Lu, F., & Chen, J. (2013). "Comparative analysis for corrosion resistance of micro-arc oxidation coatings on coarse-grained and ultra-fine grained AZ91D Mg alloy." *Surf. Coat. Tech.*, 216, 259-266.

Kakiuchi T, Y. Uematsu, Y. Hatano, M. Nakajima. (2015). "Effect of hydrogen on fatigue crack propagation behavior of wrought magnesium alloy AZ61 in NaCl solution under controlled cathodic potentials." *Eng. Fracture Mech.*, 137, 88-96.

Kang, Feng, Jin Qiang Liu, Jing Tao Wang, and Xiang Zhao. (2010). "Equal channel angular pressing of a Mg–3Al–1Zn alloy with back pressure," *Adv. Eng. Mater.*, 12, 730-734.

Kappes, Mariano, Mariano Iannuzzi, and Ricardo M. Carranza. (2013). "Hydrogen embrittlement of magnesium and magnesium alloys: a review," *J. Electrochemical Soc.*, 160, 168-178.

Kiyotaka Nakashima, Zenji Horita, Minoru Nemoto And Terence G. Langdon. (1998). "Influence of Channel Angle on The Development of Ultrafine Grains In Equal-Channel Angular Pressing." *Acta Mater.*, 46 (5), 1589-1599.

Kim, W. J., Hong, S. I., Kim, Y. S., Min, S. H., Jeong, H. T., & Lee, J. D. (2003). "Texture development and its effect on mechanical properties of an AZ61 Mg alloy fabricated by equal channel angular pressing." *Acta Mater.*, 51(11), 3293-3307.

Kočiško, R., Kvačkaj, T., & Kováčová, A. (2014). "The influence of ECAP geometry on the effective strain distribution." *J Achiev. Mater. Manuf. Eng.*, 62, 25-30.

Koneshlou, M., Asl, K. M., & Khomamizadeh, F. (2011). "Effect of cryogenic treatment on microstructure, mechanical and wear behaviors of AISI H13 hot work tool steel." *Cryogenics*, 51(1), 55-61.

Kumar, D. Sameer, C. Tara Sasanka, K. Ravindra, and K. N. S. Suman. (2015). "Magnesium and its alloys in automotive applications—a review," *American J. Mater. Sci. Tech.*, 4, 12-30.

Kulekci, M. K. (2008). "Magnesium and its alloys applications in automotive industry." *Int. J. Adv. Manuf. Tech.*, 39(9-10), 851-865.

Leiva, D. R., Fruchart, D., Bacia, M., Girard, G., Skryabina, N., Villela, A. C., & Botta, W. J. (2009). "Mg alloy for hydrogen storage processed by SPD." *Int. J. Mater. Res.*, 100(12), 1739-1746.

Letzig, D., Swiostek, J., Bohlen, J., & Kainer, K. U. (2005). "Magnesium Wrought Alloy Properties of the AZ- Series." *Magnes. Tech.*, 55-59.

Liu, L. J., & Schlesinger, M. (2009). "Corrosion of magnesium and its alloys." *Corr. Sci.*, 51(8), 1733-1737.

Li, L., Jiang, W., Guo, P. T., Yu, W. B., Wang, F., & Pan, Z. Y. (2017). "Microstructure evolution of the Mg-5.8 Zn-0.5 Zr-1.0 Yb alloy during homogenization." *Mater. Res.*, 20(4), 1063-1071.

Li, M. C., Xin, S. S., & Wu, M. Y. (2010). "Electrodeposition behavior of Mg with Zn from acidic sulfate solutions." *J. Solid State Electrochemistry*, 14(12), 2235-2240.

Li, W., Huang, X., & Huang, W. (2017). "Effects of Ca, Ag addition on the microstructure and age-hardening behavior of a Mg-7Sn (wt%) alloy." *Mater. Sci. Eng.: A*, 692, 75-80.

Liu, X. B., Shan, D. Y., Song, Y. W., & Han, E. H. (2010). "Effects of heat treatment on corrosion behaviors of Mg-3Zn magnesium alloy." *Trans. Nonferrous Met. Soc. China*, 20(7), 1345-1350.

Lunder, O., Lein, J. E., Hesjevik, S. M., Aune, T. K., & Nişancıoğlu, K. (1994). "Corrosion morphologies on magnesium alloy AZ 91." *Mater. Corr.*, 45(6), 331-340.

Luo, A., & Pekguleryuz, M. O. (1994). "Cast magnesium alloys for elevated temperature applications." *J. Mater. Sci.*, 29(20), 5259-5271.

Luo, A. A., Mishra, R. K., & Sachdev, A. K. (2011). "High-ductility magnesium–zinc–cerium extrusion alloys." *Scripta Mater.*, 64(5), 410-413.

Ma, X. Q., Gandy, D. W., & Frederick, G. J. (2008). "Innovation of ultrafine structured alloy coatings having superior mechanical properties and high temperature corrosion resistance." *J. Ther. Spray Tech.*, 17(5-6), 933-941.

Mardali, M., Salimijazi, H., Karimzadeh, F., Luthringer-Feyerabend, B. J., Blawert, C., & Labbaf, S. (2018). "Fabrication and characterization of nanostructured hydroxyapatite coating on Mg-based alloy by high-velocity oxygen fuel spraying." *Ceramics Int.*, 44(12), 14667-14676.

Maruyama, K., Sawada, K., & Koike, J. I. (2001). "Strengthening mechanisms of creep resistant tempered martensitic steel." *ISIJ international*, 41(6), 641-653.

Makar, G. L., & Kruger, J. (1993). "Corrosion of magnesium." *Int. mater. reviews*, 38(3), 138-153.

Mezbahul-Islam, M., Mostafa, A. O., & Medraj, M. (2014). "Essential magnesium alloys binary phase diagrams and their thermochemical data." *J. Mater.*

Minárik, P., Král, R., Pešička, J., Daniš, S., & Janeček, M. (2016). "Microstructure characterization of LAE442 magnesium alloy processed by extrusion and ECAP." *Mater. Charact.*, 112, 1-10.

Minárik, P., Král, R., & Hadzima, B. (2012). "Substantially higher corrosion resistance in AE42 magnesium alloy through corrosion layer stabilization by ECAP treatment." *Acta Physica Polonica-Series A General Physics*, 122(3), 614.

Minárik, P., Král, R., & Janeček, M. (2013). "Effect of ECAP processing on corrosion resistance of AE21 and AE42 magnesium alloys." *Appl. Sur. Sci.*, 281, 44-48.

Mostaed, E., Fabrizi, A., Dellasega, D., Bonollo, F., & Vedani, M. (2015). "Microstructure, mechanical behavior and low temperature superplasticity of ECAP processed ZM21 Mg alloy." *J. Alloys Comp.*, 638, 267-276.

Mostaed, E., Vedani, M., Hashempour, M., & Bestetti, M. (2014). "Influence of ECAP process on mechanical and corrosion properties of pure Mg and ZK60 magnesium alloy for biodegradable stent applications." *Biomatter*, 4(1), 28283.

Muralidhar, A., Narendranath, S., & Nayaka, H. S. (2013). "Effect of equal channel angular pressing on AZ31 wrought magnesium alloys." *J. Magnes. Alloys*, 1(4), 336-340.

Nagasekhar and Tick-Hon Yip. (2005). "Finite Element Study of Multi pass Equal Channel Angular Extrusion/Pressing." *Int. J. Nanosci.*, 4(4), 745-751.

Naik, Gajanan M., Gopal D. Gote, S. Narendranath, and SS Satheesh Kumar. (2018). "The impact of homogenization treatment on microstructure microhardness and corrosion behavior of wrought AZ80 magnesium alloys in 3.5 wt% NaCl solution." *Mater. Res. Express*, 5, 086513.

Naik Gajanan, M, Narendranath, S., & Kumar, S. S. (2019). "Influence of ECAP processing routes on microstructure mechanical properties and corrosion behavior of AZ80 Mg alloy." *AIP Conf. Proc.*, 2082 (1), 030016.

Naik, G. M., Gote, G. D., & Narendranath, S. (2018). "Microstructural and Hardness evolution of AZ80 alloy after ECAP and post-ECAP processes." *Mater. Today: Proc.*, 5(9), 17763-17768.

Naik, G. M., Gote, G. D., Narendranath, S., & Kumar, S. S. (2018). "Effect of grain refinement on the performance of AZ80 Mg alloys during wear and corrosion." *Adv. Mater. Res.*, 7(2), 105-118.



Naik, G. M., Narendranath, S., & Kumar, S. S. (2019). "Effect of ECAP Die Angles on Microstructure Mechanical Properties and Corrosion Behavior of AZ80 Mg Alloy." *J. Mater. Eng. Perform.*, 28(5), 2610-2619.

Nikulin, I., Kipelova, A., Malopheyev, S., & Kaibyshev, R. (2012). "Effect of second phase particles on grain refinement during equal-channel angular pressing of an Al-Mg-Mn alloy." *Acta Mater.*, 60(2), 487-497.

Ning, H., Yu, Y., Lin, K., Wen, L., & Liu, C. (2016). "Superplastic Properties of AZ31 and AZ31-1.0 Y-1.3 Sr Alloy Produced by Twin-Roll Casting and Sequential Hot Rolling." *J. Mater. Eng. Perform.*, 25(2), 635-641.

Noor, E A, A.H. Al-moubaraki. (2008). "Corrosion Behavior of Mild Steel in Hydrochloric Acid Solutions." *Int. J. Electrochem. Sci.*, 3, 806–818.

Oksa, M., Turunen, E., Suhonen, T., Varis, T., & Hannula, S. P. (2011). "Optimization and characterization of high velocity oxy-fuel sprayed coatings: techniques, materials, and applications." *Coatings*, 1(1), 17-52.

Orlov, D., Todaka, Y., Umemoto, M., Beygelzimer, Y., Horita, Z., & Tsuji, N. (2009). "Plastic flow and grain refinement under simple shear-based severe plastic deformation processing." *Mater. Sci. Forum*, 604, 171-178.

Parco, M., Zhao, L., Zwick, J., Bobzin, K., & Lugscheider, E. (2006). "Investigation of HVOF spraying on magnesium alloys." *Surf. Coat. Tech.*, 201(6), 3269-3274.

Pardo A., M.C. Merino, A.E. Coy, R. Arrabal, F. Viejo, E. Matykina.(2008). "Corrosion behaviour of magnesium / aluminium alloys," *Corr. Sci.*, 50, 823–834.

Pardo, A., Casajús, P., Mohedano, M., Coy, A. E., Viejo, F., Torres, B., & Matykina, E. (2009). "Corrosion protection of Mg/Al alloys by thermal sprayed aluminium coatings." *Appl. Surf. Sci.*, 255(15), 6968-6977.

Park, J. W., & Suh, J. Y. (2001). "Effect of die shape on the deformation behavior in equal-channel angular pressing." *Metall. Mater. Transactions A*, 32(12), 3007.

Pathak, S. S., Mendon, S. K., Blanton, M. D., & Rawlins, J. W. (2012). "Magnesium-based sacrificial anode cathodic protection coatings (Mg-rich primers) for aluminum alloys." *Metals*, 2(3), 353-376.

Patil, B. V., Chakkingal, U., & Kumar, T. P. (2015). "Effect of geometric parameters on strain, strain inhomogeneity and peak pressure in equal channel angular pressing—A study based on 3D finite element analysis." *J. Manuf. Proc.*, 17, 88-97.

Pawar S., T.J.A. Slater, T.L. Burnett, X. Zhou, G.M. Scamans, Z. Fan, G.E. Thompson, P.J. Withers. (2017). "Crystallographic effects on the corrosion of twin roll cast AZ31 Mg alloy sheet," *Acta Materialia*, 133, 90-99.

Pezzato, L., Brunelli, K., Babbolin, R., Dolcet, P., & Dabalà, M. (2017). "Sealing of PEO coated AZ91 magnesium alloy using La-based solutions." *Int. J. Corr.*,.

Poddar, P., Kamaraj, A., Murugesan, A. P., Bagui, S., & Sahoo, K. L. (2017). Microstructural features of Mg-8% Sn alloy and its correlation with mechanical properties. *J. Magnes. Alloys*, 5(3), 348-354.

Poinern, G. Eddy Jai, Sridevi Brundavanam, and Derek Fawcett. (2012). "Biomedical magnesium alloys: a review of material properties, surface modifications and potential as a biodegradable orthopaedic implant," *American J. Biomedical Eng.*, 2, 218-240.

Poggiali, F. S. J., Silva, C. L. P., Pereira, P. H. R., Figueiredo, R. B., & Cetlin, P. R. (2014). "Determination of mechanical anisotropy of magnesium processed by ECAP." *J. Mater. Res. Tech.*, 3(4), 331-337.

Profile T., L. Alloys, F.O.R. Marine, E., M. Engineers, C. (1945) "Light Alloys For Marine Engines". *Transactions of the Marine Engineers*.

Przondziono, J., Walke, W., Szala, J., Hadasik, E., & Wieczorek, J. (2011). "Evaluation of corrosion resistance of casting magnesium alloy AZ31 in NaCl solutions." In *IOP Conf. Series: Mater. Sci. Eng.*, 22 (1), 012017.

Qi, Y., Lapovok, R., & Estrin, Y. (2016). "Microstructure and electrical conductivity of aluminium/steel bimetallic rods processed by severe plastic deformation." *J. mater. Sci.*, 51(14), 6860-6875.

Qiao, J., Zheng, L., Ji, J., Bian, F., He, M., & Niu, T. (2018). "High temperature tensile behavior of Mg-2Al and Mg-6Al alloys." *Int. J. Mater. Res.*, 109(1), 28-33.

Rajeshkumar, R., Jayaraj, J., Srinivasan, A., & Pillai, U. T. S. (2017). "Investigation on the microstructure, mechanical properties and corrosion behavior of Mg-Sb and Mg-Sb-Si alloys." *J. Alloys Comp.*, 691, 81-88.

Robson, J. D., Stanford, N., & Barnett, M. R. (2011). "Effect of precipitate shape on slip and twinning in magnesium alloys." *Acta Materialia*, 59(5), 1945-1956.

Rossi S., P.L. Bonora, R. Pasinetti, L. Benedetti, M. Draghetti, E. Sacco. (1998) "Laboratory and Field Characterization of a New Sacrificial Anode for Cathodic Protection of Offshore Structures," *Corr.*, 54, 1018–1025.

Rossouw, D., Langelier, B., Scullion, A., Danaie, M., & Botton, G. A. (2016). "Multivariate-aided mapping of rare-earth partitioning in a wrought magnesium alloy." *Scripta Materialia*, 124, 174-178.

Ruzi, H. M., Norhamidi, M., Bakar, S. A., Khairur, R. J., Hafiez, M. N., Sufizar, A., & Murtadhahadi, I. M. H. (2009). "A review of workability of wrought magnesium alloys." *Adv. Manuf. Res. Group*, 9.

Sabirov, M.T. Perez-Prado M. Murashkin, J.M. Molina-Aldareguia, E.V. Bobruk, N.F. Yunusova, R.Z. Valiev. (2010). "Application of Equal Channel Angular Pressing With Parallel Channels For Grain Refinement In Aluminium Alloys And Its Effect On Deformation Behavior." *Int. J. Mater. Form*, 3 (1), 411 – 414.

Sahu G. (2015). "A Brief Review on Mg Alloys their Properties and Application," *Int. J. Adv. Res. Sci. Eng.*, 8354, 65–71.

Sekar, P., Sanna, N., & Desai, V. (2019). "Enhancement of resistance to galvanic corrosion of ZE41 Mg alloy by equal channel angular pressing." *Mater. Corr.*, 1–14.

Shaeri M.H., Ebrahimi, M.T. Salehi, S.H. Seyyedein. (2016). " Materials International Effect of ECAP temperature on microstructure and mechanical properties of Al – Zn – Mg – Cu alloy." *Prog. Nat. Sci. Mater. Int.*, 26, 182–191.

Shaw, Barbara A. (2003). "Corrosion resistance of magnesium alloys," *ASM handbook*, 13, 692-696.

Shahar, I. A., Hosaka, T., Yoshihara, S., & Macdonald, B. J. (2017). "Mechanical and Corrosion Properties of AZ31 Mg Alloy Processed by Equal-Channel Angular Pressing and Aging." *Proc. Eng.*, 184, 423-431.

Shahzad, M., & Wagner, L. (2009). "Influence of extrusion parameters on microstructure and texture developments, and their effects on mechanical properties of the magnesium alloy AZ80." *Mater. Sci. Eng.: A*, 506(1-2), 141-147.

Shen J., V. Gärtnerová, L.J. Kecskes, K. Kondoh, Q. Wei. (2016). "Residual stress and its effect on the mechanical properties of Y-doped Mg alloy fabricated via back-pressure assisted equal channel angular pressing (ECAP-BP)," *Mater. Sci. Eng. A*, 669, 110–117.

Shen, J., Gärtnerová, V., Kecskes, L. J., Kondoh, K., Jäger, A., & Wei, Q. (2016). "Residual stress and its effect on the mechanical properties of Y-doped Mg alloy fabricated via back-pressure assisted equal channel angular pressing (ECAP-BP)." *Mater. Sci. Eng.: A*, 669, 110-117.

Shen, Z., Ma, A., Jiang, J., Song, D., & Lu, F. (2012). "Electrochemical corrosion behavior of ultrafine-grained Mg alloy ZE41A through severe plastic deformation." *Proc. Eng.*, 27, 1817-1822.

Shahzad, M., & Wagner, L. (2009). "Influence of extrusion parameters on microstructure and texture developments, and their effects on mechanical properties of the magnesium alloy AZ80." *Mater. Sci. Eng.: A*, 506(1-2), 141-147.

Sidhu, T. S., Prakash, S., & Agrawal, R. D. (2005). "Studies on the properties of high-velocity oxy-fuel thermal spray coatings for higher temperature applications." *Mater. Sci.*, 41(6), 805-823.

Silva, E. P. D., Batista, L. F., Callegari, B., Buzolin, R. H., Warchomicka, F., Requena, G. C., & Pinto, H. C. (2014). "Solution and ageing heat treatments of ZK60 magnesium alloys with rare earth additions produced by semi-solid casting." *Mater. Res.*, 17(6), 1507-1512.

Singh, I. B., Singh, M., & Das, S. (2015). "A comparative corrosion behavior of Mg, AZ31 and AZ91 alloys in 3.5% NaCl solution." *J. Magnes. Alloys*, 3(2), 142-148.

Sukiman, N. L., Zhou, X., Birbilis, N., Hughes, A. E., Mol, J. M. C., Garcia, S. J., & Thompson, G. E. (2012). "Durability and corrosion of aluminium and its alloys:

overview, property space, techniques and developments.” *Aluminium Alloys-New Trends in Fabrication and Applications*, 47-97.

Song, D., Ma, A., Jiang, J., Lin, P., Yang, D., & Fan, J. (2010). “Corrosion behavior of equal-channel-angular-pressed pure magnesium in NaCl aqueous solution.” *Corr. Sci.*, 52(2), 481-490.

Song, D., Ma, A. B., Jiang, J. H., Lin, P. H., Yang, D. H., & Fan, J. F. (2011). “Corrosion behaviour of bulk ultra-fine grained AZ91D magnesium alloy fabricated by equal-channel angular pressing.” *Corr. Sci.*, 53(1), 362-373.

Song G, A Atrens. (1999). “Corrosion mechanisms of magnesium alloys.” *Adv. Eng. Mater.*, 1, 11-33.

Song, G., Bowles, A. L., & St. John, D. H. (2004). “Corrosion resistance of aged die cast magnesium alloy AZ91D. *Mater. Sci. Eng.: A*, 366(1), 74-86.

Song G, A Atrens. (2003).“Understanding magnesium corrosion mechanism: a framework for improved alloy performance,” *Adv. Engg. Mater.*, 5, 837-858.

Sun, H. Q., Shi, Y. N., Zhang, M. X., & Lu, K. (2007). “Plastic strain-induced grain refinement in the nanometer scale in a Mg alloy.” *Acta Mater.*, 55(3), 975-982.

Sunil, B. R., Kumar, T. S., Chakkingal, U., Nandakumar, V., Doble, M., Prasad, V. D., & Raghunath, M. (2016). “In vitro and in vivo studies of biodegradable fine grained AZ31 magnesium alloy produced by equal channel angular pressing.” *Mater. Sci. Eng.: C*, 59, 356-367.

Suh, J., Victoria-Hernández, J., Letzig, D., Golle, R., & Volk, W. (2016). “Effect of processing route on texture and cold formability of AZ31 Mg alloy sheets processed by ECAP.” *Mater. Sci. Eng.: A*, 669, 159-170.

Sundararajan, G., & Krishna, L. R. (2003). "Mechanisms underlying the formation of thick alumina coatings through the MAO coating technology. *Surf. Coat. Tech.*, 167(2-3), 269-277.

Tan, Qiyang, Andrej Atrens, Ning Mo, and Ming-Xing Zhang. (2016). "Oxidation of magnesium alloys at elevated temperatures in air: A review." *Corr. Sci.*, 112,734-759.

Tański, T., Snopiński, P., Pakieła, W., Borek, W., Prusik, K., & Rusz, S. (2016). "Structure and properties of Al-Mg alloy after combination of ECAP and post-ECAP ageing." *Archiv. Civil Mech. Eng.*, 16(3), 325-334.

Tong, L. B., Zhang, Q. X., Jiang, Z. H., Zhang, J. B., Meng, J., Cheng, L. R., & Zhang, H. J. (2016). "Microstructures, mechanical properties and corrosion resistances of extruded Mg–Zn–Ca–xCe/La alloys." *J. Mech. Behavior Biomedical Mater.*, 62, 57-70.

Upadhyay, S., Li, H., Bowen, P., & Rabiei, A. (2018). "A study on tensile properties of Alloy 709 at various temperatures." *Mater. Sci. Eng.: A*, 733, 338-349.

Vrátná J, B. Hadzima, M. Bukovina, and M. Janeček. (2013). "Room temperature corrosion properties of AZ31 magnesium alloy processed by extrusion and equal channel angular pressing," *J. Mater. Sci.*, 48, 4510–4516.

Verlinden, B. (2018). "Severe plastic deformation of metals." *Metallurgical and Mater. Eng.*,.

Valiev, R. Z., & Langdon, T. G. (2006). "Principles of equal-channel angular pressing as a processing tool for grain refinement." *Prog. Mater. Sci.*, 51(7), 881-981.

Wang, C., Xin, R., Li, D., Song, B., Wu, M., & Liu, Q. (2017). "Enhancing the age-hardening response of rolled AZ80 alloy by pre-twinning deformation." *Mater. Sci. Eng.: A*, 680, 152-156.

Wang Y, H. Choo. (2014). "Influence of texture on Hall – Petch relationships in an Mg alloy." *Acta Materialia.*, 81, 83–97.

Wang, L., Mostaed, E., Cao, X., Huang, G., Fabrizi, A., Bonollo, F. & Vedani, M. (2016). "Effects of texture and grain size on mechanical properties of AZ80 magnesium alloys at lower temperatures." *Mater. Des.*, 89, 1-8.

Waizy, H., Seitz, J. M., Reifenrath, J., Weizbauer, A., Bach, F. W., Meyer-Lindenberg, A & Windhagen, H. (2013). "Biodegradable magnesium implants for orthopedic applications." *J. Mater. Sci.*, 48(1), 39-50.

Wei, F., Zhang, W., Zhang, T., & Wang, F. (2017). "Effect of variations of Al content on microstructure and corrosion resistance of PEO coatings on Mg-Al alloys." *J. Alloys Comp.*, 690, 195-205.

Wenming, T. I. A. N., Songmei, L. I., Jianhua, L. I. U., Mei, Y. U., & Yujie, D. U. (2017). "Preparation of bimodal grain size 7075 aviation aluminum alloys and their corrosion properties." *Chinese J. Aero.*, 30(5), 1777-1788.

Wu, W., Qiao, H., An, K., Guo, X., Wu, P., & Liaw, P. K. (2014). "Investigation of deformation dynamics in a wrought magnesium alloy." *Int. J. Plasticity*, 62, 105-120.

Xiaodong, R., Xuesong, L., Yue, Y., You, Y., & Hua, W. (2017). "Corrosion Behavior and Electrochemical Properties of As-cast Mg-2Zn-0.5 Ca-Y Series Magnesium Alloys in Hank's Solution and NaCl Solution." *Rare Met. Mater. Eng.*, 46(1), 45-50.

Xie, Q., Ma, A., Jiang, J., Cheng, Z., Song, D., Yuan, Y., & Liu, H. (2017). "Stress corrosion cracking behavior of fine-grained AZ61 magnesium alloys processed by equal-channel angular pressing." *Met.*, 7(9), 343.



Xin, L. I., Jiang, J. H., Zhao, Y. H., WEN, D. J., & ZHU, Y. T. (2015). "Effect of equal-channel angular pressing and aging on corrosion behavior of ZK60 Mg alloy." *Trans. Nonferrous Met. Soc. China*, 25(12), 3909-3920.

Yunchang, Tao Hu, and Paul K. Chu. (2010). "Influence of test solutions on in vitro studies of biomedical magnesium alloys." *J. Electrochemical Society*, 157 (7), 238-243.

Xin, L. I., Jiang, J. H., Zhao, Y. H., WEN, D. J., & ZHU, Y. T. (2015). "Effect of equal-channel angular pressing and aging on corrosion behavior of ZK60 Mg alloy." *Trans. Nonferrous Met. Soc. China*, 25(12), 3909-3920.

Xin, Y., Hu, T., & Chu, P. K. (2011). "In vitro studies of biomedical magnesium alloys in a simulated physiological environment: a review." *Acta biomater.*, 7(4), 1452-1459.

Xu, D., Zhao, K., Yang, C., Li, H., & Zhang, J. (2018). "Effect of Heat Treatment on Microstructure and Mechanical Properties of the AZ31/WE43 Bimetal Composites." *Met.*, 8(11), 971.

Yan, Y., Cao, H., Kang, Y., Yu, K., Xiao, T., Luo, J & Dai, Y. (2017). "Effects of Zn concentration and heat treatment on the microstructure, mechanical properties and corrosion behavior of as-extruded Mg-Zn alloys produced by powder metallurgy." *J. Alloys Comp.*, 693, 1277-1289.

Yasi, J. A., Hector Jr, L. G., & Trinkle, D. R. (2010). "First-principles data for solid-solution strengthening of magnesium: From geometry and chemistry to properties." *Acta Mater.*, 58(17), 5704-5713.

Yongdong, X., Shengsun, H., Song, L., Donglang, C., & Xiurong, Z. (2011). "Influence of heat treatment on the microstructure and property of Mg-Nd-Gd-Zn-Zr alloy." *Rare Met. Mater. Eng.*, 40(7), 1133-1137.

Yu, X., Li, Y., & Li, L. (2015). "Fracture mechanism of AZ31 magnesium alloy processed by equal channel angular pressing comparing three point bending test and tensile test." *Eng. Failure Analysis*, 58, 322-335.

Yun, Y., Dong, Z., Lee, N., Liu, Y., Xue, D., Guo, X., & Sundaramurthy, S. (2009). "Revolutionizing biodegradable metals." *Mater. Today*, 12(10), 22-32.

Yuan, Y., Ma, A., Gou, X., Jiang, J., Arhin, G., Song, D., & Liu, H. (2016). "Effect of heat treatment and deformation temperature on the mechanical properties of ECAP processed ZK60 magnesium alloy." *Mater. Sci. Eng.: A*, 677, 125-132.

Yuan, Y., Ma, A., Jiang, J., Lu, F., Jian, W., Song, D., & Zhu, Y. T. (2013). "Optimizing the strength and ductility of AZ91 Mg alloy by ECAP and subsequent aging." *Mater. Sci. Eng.: A*, 588, 329-334.

Zeng, Rong-chang, Jin Zhang, Wei-jiu Huang, W. Dietzel, K. U. Kainer, C. Blawert, and K. E. Wei. (2006). "Review of studies on corrosion of magnesium alloys." *Trans. Nonferrous Met. Soc. China*, 16, 763-771.

Zengin, H., Turen, Y., Ahlatci, H., Sun, Y., & Kara, I. H. (2017). "Microstructure and corrosion properties of homogenized Mg-4Zn-1La magnesium alloy." *Key Eng. Mater.*, 750, 118-123.

Zhang, T., Shao, Y., Meng, G., Cui, Z., & Wang, F. (2011). "Corrosion of hot extrusion AZ91 magnesium alloy: I-relation between the microstructure and corrosion behavior." *Corr. Sci.*, 53(5), 1960-1968.

Zhao, C. Y., Pan, F. S., & Pan, H. C. (2016). "Microstructure, mechanical and bio-corrosion properties of as-extruded Mg-Sn-Ca alloys." *Trans. nonferrous met. Soc. China*, 26(6), 1574-1582.

Zhao, C., Pan, F., Zhang, L., Pan, H., Song, K., & Tang, A. (2017). "Microstructure, mechanical properties, bio-corrosion properties and cytotoxicity of as-extruded Mg-Sr alloys." *Mater. Sci. Eng.: C*, 70, 1081-1088.

Zhao, D., Wang, Z., Zuo, M., & Geng, H. (2014). "Effects of heat treatment on microstructure and mechanical properties of extruded AZ80 magnesium alloy." *Mater. Des.*, 56, 589-593.

Zhang, J., Kang, Z., & Wang, F. (2016). "Mechanical properties and biocorrosion resistance of the Mg-Gd-Nd-Zn-Zr alloy processed by equal channel angular pressing." *Mater. Sci. Eng.: C*, 68, 194-197.

Zhang, C., Guan, S., Wang, L., Zhu, S., & Chang, L. (2017). "The microstructure and corrosion resistance of biological Mg-Zn-Ca alloy processed by high-pressure torsion and subsequently annealing." *J. Mater. Res.*, 32(6), 1061-1072.

Zhao, D., Wang, Z., Zuo, M., & Geng, H. (2014). "Effects of heat treatment on microstructure and mechanical properties of extruded AZ80 magnesium alloy." *Mater. Des.*, 56, 589-593.

Zhang, F., Ma, A., Jiang, J., Xu, H., Song, D., Lu, F., & Nishida, Y. (2013). "Enhanced biodegradation behavior of ultrafine-grained ZE41A magnesium alloy in Hank's solution." *Prog. Nat. Sci.: Mater. Int.*, 23(4), 420-424.

Zhang, J., Zhang, K. S., Hwai-Chung, W., & Yu, M. H. (2009). "Experimental and numerical investigation on pure aluminum by ECAP." *Trans. Nonferrous Met. Soc. China*, 19(5), 1303-1311.

Zhang, Z., Liu, X., Hu, W., Li, J., Le, Q., Bao, L., & Cui, J. (2015). "Microstructures, mechanical properties and corrosion behaviors of Mg-Y-Zn-Zr alloys with specific Y/Zn mole ratios." *J. Alloys Comp.*, 624, 116-125.

Zheng, Y. F., Gu, X. N., & Witte, F. (2014). "Biodegradable metals." *Mater. Sci. Engg.: R: Reports*, 77, 1-34.

Zengin, H., Turen, Y., Ahlatci, H., Sun, Y., & Kara, I. H. (2017). "Microstructure and corrosion properties of homogenized Mg-4Zn-1La magnesium alloy." *Key Eng. Mater.*, 750, 118-123.

Zhongyu Cui, Xiaogang Li, Kui Xiao, Chaofang Dong. (2013). "Atmospheric corrosion of field-exposed AZ31 magnesium in a tropical marine environment," *Corr. Sci.*, 76, 243–256.

Zhao, X., Li, S., Xue, Y., & Zhang, Z. (2019). "An Investigation on Microstructure, Texture and Mechanical Properties of AZ80 Mg Alloy Processed by Annular Channel Angular Extrusion." *Mater.*, 12(6), 1001.

Zhu, T., Chen, Z. W., & Gao, W. (2010). "Dissolution of eutectic  $\beta$ -Mg 17 Al 12 phase in magnesium AZ91 cast alloy at temperatures close to eutectic temperature." *J. Mater. Eng. Perform.*, 19(6), 860-867.

Zhu, Y. T., & Lowe, T. C. (2000). "Observations and issues on mechanisms of grain refinement during ECAP process." *Mater. Sci. Engg.: A*, 291, 46-53.

Zhu, S., Liu, Z., Qu, R., Wang, L., Li, Q., & Guan, S. (2013). "Effect of rare earth and Mn elements on the corrosion behavior of extruded AZ61 system in 3.5 wt% NaCl solution and salt spray test." *J. Magnes. Alloys*, 1(3), 249-255.

Živić, F., Grujović, N., Manivasagam, G., Richards, C., Landoulsi, J., & Petrović, V. (2014). "The Potential of Magnesium Alloys as Bioabsorbable/Biodegradable Implants for Biomedical Applications." *Tribology in Industry*, 36(1).

Zrnik J, S. V Dobatkin. (2008). "Processing of Metals By Severe Plastic Deformation (SPD) – Structure And Mechanical Properties Respond," *Metalurgija*, 47, 211–216.

**List of Publications based on PhD Research Work**

<b>Sl. No.</b>	<b>Title of the paper</b>	<b>Authors</b> (in the same order as in the paper. Underline the Research Scholar's name)	<b>Name of the Journal/ Conference/ Symposium, Vol., No., Pages</b>	<b>Month &amp; Year of Publication</b>	<b>Category *</b>
1	Effect of annealing and ageing treatment on pitting corrosion resistance of fine-grained Mg-8%Al-0.5%Zn alloy	<u>Gajanan M Naik</u> , Narendranath S, S. S. Satheesh Kumar, Sandeep sahu,	Journal of The Minerals, Metals & Materials JOM (2019). <a href="https://doi.org/10.1007/s11837-019-03769-1">https://doi.org/10.1007/s11837-019-03769-1</a>	2019	1
2	Effect of ECAP Die angles on Microstructure Mechanical properties and corrosion behaviour of AZ80 Mg alloy	<u>Gajanan M Naik</u> , Narendranath S, S. S. Satheesh Kumar	Journal of Materials Engineering and Performance 28(5):1-10	2019	1
3	Corrosion of ECAPed Magnesium alloys and its background: A Review	<u>Gajanan M Naik</u> , Narendranath S, S. S. Satheesh Kumar	Journal of Metals Materials and Minerals Vol.29 No.2 pp.1-20, 2019	2019	1
4	Effect of grain refinement on material properties of Mg-8%Al-0.5%Zn alloy after the combined processes of Multi-Direction Forging and Equal Channel Angular Pressing	<u>Gajanan M Naik</u> , Anjan B N, Narendranath S, S. S. Satheesh Kumar, , Preetham Kumar G V	Mater. Res. Express 6 (2019) 096538 <a href="https://doi.org/10.1088/2053-1591/ab2ddf">https://doi.org/10.1088/2053-1591/ab2ddf</a>	2019	1
5	Effect of grain refinement on the performance of AZ80 Mg alloys during wear and corrosion	<u>Gajanan M Naik</u> , Gopal D Gote, Narendranath S, S. S. Satheesh Kumar	Advances in Materials Research, Vol. 7 No. 2 (2018) 105-118. <a href="https://doi.org/10.12989/amr.2018.7.2.83-96">https://doi.org/10.12989/amr.2018.7.2.83-96</a>	2019	1
6	The impact of homogenization treatment on Microstructure Microhardness and Corrosion behavior of wrought AZ80 magnesium alloys	<u>Gajanan M Naik</u> , Gopal D Gote, Narendranath S, S. S. Satheesh Kumar	Materials. Research. Express 5 (2018) 086513. <a href="https://doi.org/10.1088/2053-1591/aad31f">https://doi.org/10.1088/2053-1591/aad31f</a> .	2018	1

7	Magnesium alloys and its Applications: A Short Review	Gajanan M Naik, Gopal D Gote, Narendranath S	Journal of Global Engineering Problems & Solutions, vol. 3, no. 1, pp. 1-4, 2017	2017	1
8	Effect of die parameters and coefficient of friction on equivalent plastic strain during ECAP	<u>Gajanan M Naik</u> , Gopal D Gote, Narendranath S, S. S. Satheesh Kumar	Modeling and optimization, Advances in Modeling and Analysis-A	<b>Under Review</b>	1
9	Corrosion behavior of ECAPed AZ91 Mg alloys	<u>Gajanan M Naik</u> , Narendranath S, S. S.	Journal of Magnesium and alloys	<b>Under Review</b>	1
10	Saltwater corrosion behavior of equal channel angular pressed AZ80 Mg alloys	<u>Gajanan M Naik</u> , Narendranath S, S. S. Satheesh Kumar	International Journal of Lightweight Materials and Manufacture	<b>Under Review</b>	1
11	Modelling of ECAP Process to Study the Effect of Die Parameters and Friction Coefficient on Equivalent Plastic Strain	Gopal D Gote, <u>Gajanan M Naik</u> , Narendranath S,	International Conference on Contemporary Design and Analysis of Manufacturing and Industrial Engineering. (CDAMIES2018), <b>NIT-Tiruchirappalli</b> , Tamil Nadu, 18-20 Jan 2018.	2018 <b>(Received Best Paper Award)</b>	3
12	Microstructural and Hardness evolution of AZ80 alloy after ECAP and post-ECAP processes	<u>Gajanan M Naik</u> , Gopal D Gote, Narendranath S,	8 <sup>th</sup> International Conference of Material Processing and Characterization (ICMPC-2018) Gokaraju Rangaraju Institute of Engineering and Technology-Hyderabad during 16 <sup>th</sup> -18 <sup>th</sup> March 2018, <b>Materials Today: Proceedings 5 (2018) 17763–17768</b>	2018	3

13	Influence of chloride content and exposure time on corrosion behaviour of AZ80 wrought Mg alloy	Gopal D Gote, <u>Gajanan M Naik</u> , Narendranath S,	First International Conference on Energy and Environment: Global Challenges (ICEE - 2018), NIT- Calicut, March 9 & 10, 2018. © Springer Nature Singapore Pte Ltd. 2020 <b>V. Sivasubramanian and S. Subramanian (eds.), Global Challenges in Energy and Environment, Lecture Notes on Multidisciplinary Industrial Engineering,</b> <a href="https://doi.org/10.1007/978-981-13-9213-9_6">https://doi.org/10.1007/978-981-13-9213-9_6</a>	2018	3
14	Microstructure and Corrosion behavior of wrought AZ80 Mg alloys after the combined processes of ECAP and Hot Rolling	<u>Gajanan M Naik</u> , Gopal D Gote, Narendranath S, S. S. Satheesh Kumar	International Conference on Advances in Materials and Manufacturing Applications (IconAMMA-2018), AMRITA University-Bengaluru, 16-18 <sup>th</sup> Aug. 2018. <b>IOP conf. series: Mater. Sci. Eng.</b> 577 (2019) 012110, <a href="https://doi.org/10.1088/1757-899X/577/1/0121102">doi:10.1088/1757-899X/577/1/0121102</a>	2019	3
15	Influence of ECAP Processing Routes on Microstructure Mechanical Properties and Corrosion Behavior of AZ80 Mg alloy	<u>Gajanan M Naik</u> , Narendranath S, S. S. Satheesh Kumar	3 <sup>rd</sup> International Conference on Optoelectronic and Nano Materials for Advanced Technology (IcONMAT-2019) Cochin University of Science and Technology, Kochi, Kerala. 2 <sup>nd</sup> -5 <sup>th</sup> January-2019. <b>American Institute of Physics Conference Proceedings</b> 2082, 030016 (2019); <a href="https://doi.org/10.1063/1.5093834">https://doi.org/10.1063/1.5093834</a> .	2019 <b>(Received Best Poster Award)</b>	3

16	The Role of Processing Temperature in Equal Channel Angular Extrusion: Microstructure Mechanical properties and Corrosion resistance	<u>Gajanan M Naik</u> , Narendranath. S, S.S. Satheesh Kumar	International Conference on Design, Materials, Cryogenics and Constructions ICDMC 2019 Vel Tech Rangarajan Dr Sagunthala R and D Institute of Science and Technology, Chennai, Tamil Nadu, 28-29th March 2019 <b>Springer Lectures Notes in Mechanical Engineering - ISSN 2195-4356,</b> <a href="https://doi.org/10.1007/978-981-15-3631-1_25">https://doi.org/10.1007/978-981-15-3631-1_25</a>	2019 <b>(Received Best Paper Award)</b>	3
17	Effect of grain refinement on mechanical and corrosion behaviour of AZ91 magnesium alloy processed by ECAE	<u>Gajanan M Naik</u> , Narendranath. S, S.S. Satheesh Kumar	International Conference - Modern Technologies in Industrial Engineering - Lasi-Romania, Ramada Hotel, June 19-22, 2019. <b>IOP Conf. Series: Materials Science and Engineering 591 (2019) 012015.</b>	2019	3
18	Flipping Type-ECAP Die	<u>Gajanan M Naik</u> , Narendranath. S, S.S. Satheesh Kumar	<b>Copyrights</b> Diary Number: 14668/2018-CO/L. Reg. No: L-79923/2018	2019 <b>(Granted)</b>	5
19	A novel approach to improve the corrosion resistance of AZ80 Mg alloy through ECAP	<u>Gajanan M Naik</u> , Narendranath. S, S.S. Satheesh Kumar	An active participant in “ <b>Dr. K V Rao Research Awards</b> ”, for the year 2019 in Chemistry.	23 <sup>rd</sup> March 2019	5
20	Promoting Material Properties of Magnesium alloys using Equal Channel Angular Press	<u>Gajanan M Naik</u> , Narendranath. S, S.S. Satheesh Kumar	Research Outreach-Online Magazine	2020 <b>(Published)</b>	5

\* Category:1 : Journal paper, full paper reviewed      2 : Journal paper, Abstract reviewed  
3 : Conference/Symposium paper, full paper reviewed      4 : Conference/Symposium paper, abstract reviewed  
5 : others (including papers in Workshops, NITK Research Bulletins, Short notes etc.(copyrights/patents, Awards, Research Magazine) (If the paper has been accepted for publication but yet to be published, the supporting documents must be attached.)

Research Scholar: **Gajanan M Naik**

Research Supervisor: **Dr. Narendranath S**



**Mr. GAJANAN M NAIK BE, PGDBA, M Tech (NITK). [Ph.D. (NITK)]**

**PERMANENT ADDRESS:**

**Gajanan M Naik  
S/o. Manjunath R Naik  
Konalli Po, Kumta Tq.  
Karwar Dist. 581323**



**PERSONAL PROFILE:**

Date of Birth : 07/03/1989  
Sex : Male  
Nationality : Indian  
Mother Tongue : Kannada

**Mob. No: +917760006193**

**Email: [gajamnaik@gmail.com](mailto:gajamnaik@gmail.com) , [gajanan@mite.ac.in](mailto:gajanan@mite.ac.in) [gajananmnaik@yahoo.com](mailto:gajananmnaik@yahoo.com)**

**QUALIFICATION**

DEGREE	YEAR	INSTITUTE	DISCIPLINE	AGGREGATE
Ph.D.	Pursuing	National Institute of Technology Karnataka Surathkal, Karnataka, India	Mechanical Engineering	77.3% (Course work) [8.23points] [FCD]
M. Tech.	2016	National Institute of Technology Karnataka Surathkal, Karnataka, India	Manufacturing Engineering	73.33% [7.83points] [FCD]
PGDBA	2013	Sikkim Manipal University Directorate of Distance Education, Karnataka, India	Business Administration	Grade-C
B.E	2011	Moodlakatte Institute of Technology Kundapur , Udupi, VTU-Belagavi, Karnataka, India	Mechanical Engineering	70.92% [FCD]

**PROFESSIONAL EXPERIENCE:**

ORGANIZATION/INSTITUTE	DESIGNATION	DURATION
Mangalore Institute of Technology and Engineering (MITE), Moodbidri	Assistant Professor	July 2019- Till date
National Institute of Technology Karnataka (NITK) Surathkal	Senior Research Fellow (SRF)-NRB Project	November 2018- July 2019
National Institute of Technology Karnataka (NITK) Surathkal	Junior Research Fellow (JRF) NRB Project	November 2016- Nov-2018
Srinivas School of Engineering, Mukka	Assistant Professor	August 2016- November 2016
Prasanna College of Engineering and Technology, Belthangady (PCET)	Lecturer	April 2012- August 2014
Kamath Institute of Technology, Kundapur (KIT Polytechnic)	Lecturer	July 2011-April 2012

**DECLARATION:**

I hereby declare that the above-mentioned information is true to best of my knowledge.

**Date: 05-06-2020**

**Place: Moodbidri**

**(GAJANAN M NAIK)**